University of Sussex

Transient Modelling of a Diesel Engine and Air-path Control

Li Cheng

Submitted for the degree of Doctor of Philosophy

University of Sussex

March 2015

Declaration

I hereby declare that this thesis has not been and will not be submitted in whole or in part to another University for the award of any other degree.

Signature:

Li Cheng

UNIVERSITY OF SUSSEX

Li Cheng, Doctor of Philosophy

Transient Modelling of a Diesel Engine and Air-path Control

Summary

Due to the inherent nonlinearity of the diesel engine, real-time control of the variable geometry turbocharger (VGT) and exhaust gas recirculation (EGR) valve still remains a challenging task. A controller has to be capable of coping with the transient operating condition of the engine, the interactions between the VGT and EGR, and also the trade-off effect in this control problem. In this work, novel real-time fuzzy logic controllers (RFLC) were developed and tested. Firstly, the proposed controllers were calibrated and validated in a transient diesel engine model which was developed and validated against the Caterpillar 3126B engine test bed located at the University of Sussex. The controllers were then further tested on the engine test bed. Compared to conventional controllers, the proposed controllers can effectively reduce engine emissions as well as fuel consumption. Experimental results show that compared to the baseline engine running on the Nonroad Transient Cycle (NRTC), mean values of the exhaust gas opacity and the nitrogen oxides (NOx) emission production were reduced by 36.8% and 33%, respectively. Instant specific fuel consumption of the RFLC engine was also reduced by up to 50% compared to the baseline engine during the test. Moreover, the proposed fuzzy logic controllers can also reduce development time and cost by avoiding extensive engine mapping of inlet air pressure and flow. When on-line emission measurements were not available, on-board emission predictors were developed and tested to supply the proposed fuzzy logic controller with predictions of soot and NOx production. Alternatively, adaptive neuro fuzzy inference system (ANFIS) controllers, which can learn from fuzzy logic controllers, were developed and tested. In the end, the proposed fuzzy logic controllers were compared with PI controllers using the transient engine model.

Acknowledgments

Upon finishing this thesis, I would like to take this opportunity to express my gratitude to Dr. William Wang, my supervisor, for his valuable guidance and support during the last two years of my PhD studies. Without his supervision, this thesis could not have been completed. I must also thank Dr. Jun Peng, my former supervisor, who guided me through the first two years of PhD studies with his teaching and consistent encouragement. I would also like to thank Dr. Julian Dunne and Dr. Tai Yang for their constructive suggestions as my annual review interviewers. And I have to thank our technicians Ian and Barry. Without their help and technical support, this work would not have been possible. Moreover, I would like to thank all my colleagues in the Dynamics Control and Vehicle (DCV) research group, especially Pavlos, Colin, Pattarapong, and Jun for their help, and it is their companionship that has made this an enjoyable journey.

I must also thank Prof. Abdel Aitouche and Dr. Jerome Bosche for their guidance and support during my visits to France, and Issam, Boulaid, Olena, and Ines for all the inspiring discussions and fruitful cooperation. It has been a pleasure working with you all.

Lastly, I have to give my utmost thanks to my dear father, mother, and my beloved wife for their continuous encouragement and unconditional support over the years.

I also acknowledge and appreciate the European Regional Development Fund through INTERREG IVA.

Dedication

This thesis is dedicated to my dear father, mother and my beloved wife Ning.

Contents

List of Tables

List of Figures

Nomenclature

ADC analog digital converter

AFR air-fuel ratio

ANFIS adaptive neuro fuzzy inference system

BMEP brake mean effective pressure

BSFC brake specific fuel consumption

CD combustion duration

CFD computational fluid dynamics

CO carbon monoxide

CRA crank angle

DAC digital analog converter

FIS fuzzy inference system

HC hydrocarbons

IC internal combustion

MAF mass air flow

MAP mass air pressure

NRTC nonroad transient cycle

PWM pulse-width modulation

RFLC real-time fuzzy logic control

RMSE root mean square error

SOC start of combustion

TPU time processor unit

BDC bottom dead center

CAT Caterpillar

ECU engine control unit

EGR exhaust gas recirculation

EPA environmental protection agency

FIE fuel injection equipment

MRAC model reference adaptive controllers

NOx nitrogen oxides

RFLC real-time fuzzy logic control

SFC specific fuel consumption

SMC sliding mode control

TDC top dead center

VGT variable geometry turbocharger

WHDC world-wide harmonized heavy-duty certification

Chapter 1

Introduction

1.1 Background

Since the 19th century, diesel engine-powered vehicles have dramatically changed the modes of transport. Because of their inherently high thermal efficiencies, diesel engines have been fitted in a large variety of vehicles, ranging from large marine vehicles, earth movers, road trucks to small passenger cars and scooters [45]. Its applications cover not only transportation, but also utility vehicles used for landscaping, gardening and cleaning. Although the contribution to our society made by diesel engines is far-reaching, the environmental issues such as climate change and human health introduced by diesel engines have drawn increasing public attention [53]. In recent years, engine manufacturers in the automotive sector have undertaken increasing pressure to deliver diesel engines with less harmful emissions and fuel consumption levels to meet the requirements of further stringent legislation [16]. This requires further development of diesel engine technologies.

Smart Control and Diagnosis for Economic and Clean Engine (SCODECE) is a collaborative project funded by the EU 2 Seas Programme. It was initiated at the University of Sussex with two other participating universities in France. The project aims to develop new technologies that would make diesel engines cleaner, more economic and more reliable. Scientific research covering diesel engine modelling, air-path control, fuel-path research, and control system diagnosis was carried out by the project partners. The performance and emissions of diesel engines running on bio-diesel were also investigated.

As a part of this project, this work mainly focuses on the transient modelling and air-path control of the diesel engine. The major air-path components of the Caterpillar 3126B engine test bed are listed in Fig. 1.1. The water-cooled intake air with boosted pressure from the variable geometry turbocharger (VGT) flows into the cylinders through

the inlet manifold during the intake stroke and mixes with injected diesel fuel vapour at the end of the compression stroke. Prior to the piston reaching top dead centre (TDC), the combustion of the air-fuel mixture takes place. The combustion then releases a significant amount of heat during the power stroke after self-ignition of the diesel vapour. The piston is pushed down towards bottom dead centre (BDC) from TDC. After the power stroke, the exhaust gas, which is a by-product of the combustion, is pushed out of the cylinder by the piston moving toward TDC through the exhaust valve during the exhaust stroke. The exhaust gas then flows through the turbine and propels the turbine wheel to spin. The compressor wheel driven by the turbine wheel starts to compress the air. In this way, by recycling part of the exhaust gas energy, the compressor can provide a certain amount of boosted pressure to the engine. The exhaust gas recirculation (EGR) valve is located between the exhaust manifold and the inlet manifold. When the EGR valve is opened, part of the exhaust gas is allowed to flow back into the inlet manifold when there is enough positive pressure gradient across the valve. Consequently, the recirculated exhaust gas will replace part of the fresh air sucked into the cylinder. As a result, nitrogen oxides (NOx) production can be effectively reduced due to reduced combustion temperature caused by the diluted oxygen concentration and some thermal effects [51].

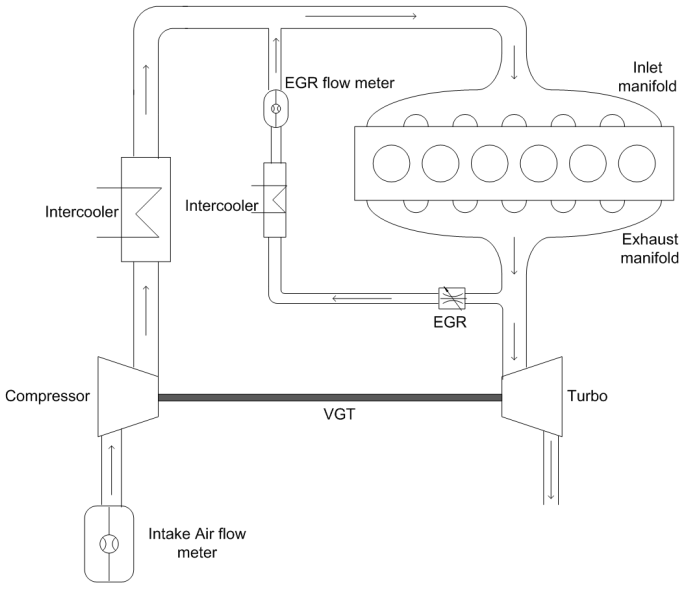

Figure 1.1: Diesel engine air-path

As described above, turbochargers and EGR valves are widely equipped on diesel engines and have proven to be effective ways to reduce harmful emissions as well as to improve engine performance [12]. However, due to the inherent nonlinearity of the diesel engine, real-time control of the variable geometry turbocharger (VGT) and exhaust gas

recirculation (EGR) valve still remains a major challenge. An adequate controller has to be capable of coping with the transient running condition of the engine, the interactions between the VGT and EGR, and also the trade-off effect existing in this control problem.

A turbocharger, which consists of a turbine and a compressor, can generate boost pressure in the inlet manifold. The turbine is driven by a portion of the exhaust gas that comes out of the engine. The compressor is then driven by the turbine to produce the required boost pressure in the inlet manifold. The boost pressure generated by the turbocharger can increase the volumetric efficiency of an internal combustion engine; also, pumping loss can be eliminated. As a result, engine efficiency can be increased. However, fixed geometry turbochargers often suffer from turbo lag, especially for those installed on heavy-duty diesel engines, which are normally large. These turbochargers are normally optimised by full load and high engine speed conditions [18]. Thus, under low load and low engine speed conditions, the efficiency of the turbocharger is low, which, in turn, will influence the engine performance and emissions. To address this problem, one of the possible solutions is to replace the ordinary turbocharger with a VGT, which has a variable geometry design. Compared to the fixed geometry turbochargers, a VGT has movable vanes that surround the turbine wheel (Fig. 1.2) so that they have the flexibility to adjust themselves according to different engine working conditions. The alteration of the distance between each vane can significantly change the direction of the exhaust gas flow towards the turbine wheel and speed. In the VGT closed position (Fig.1.2b), that is, when the vanes are adjusted close to one another, the speed of the exhaust gas is accelerated and the gas will hit the turbine wheel at a more efficient angle. As a result, the turbine wheel will respond faster and will be able to drive the compressor more effectively when required. This is particularly useful at low load and low engine speed conditions. Additionally, the VGT can preclude use of a waste-gate by closing the vanes to produce required back pressure to assist EGR [64].

EGR can reduce nitrogen oxides efficiently at relatively low cost [59], so it is widely adopted by heavy-duty diesel engine applications [85]. The inside of the EGR valve installed on the test bed is illustrated in Fig. 1.3. By reintroducing a certain amount of exhaust gas into the inlet manifold, NOx production can be reduced due to a lower peak combustion temperature [51]. The amount of exhaust gas that flows back into the inlet manifold can be controlled by a movable piston valve. However, recirculating excessive EGR gas will have a negative effect on soot emissions, engine performance and stability.

In the light of ever-stricter emissions legislation, much research has focused on the

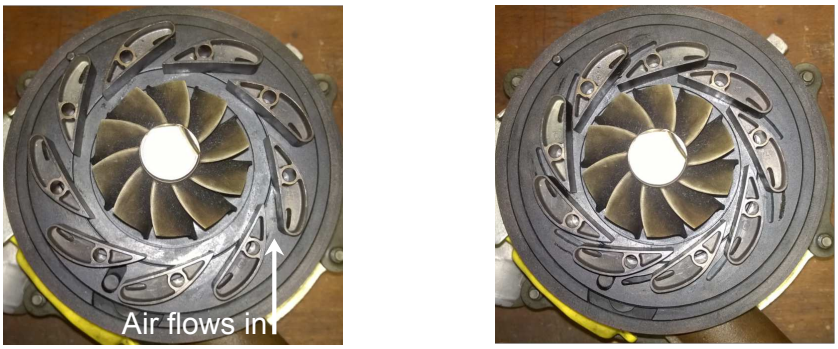

(a) (b)

Figure 1.2: Inside of a Garrett GT3782VA 84 Trim *090A/R variable geometry turbocharger. (a) Fully opened vanes, (b) Fully closed vanes.

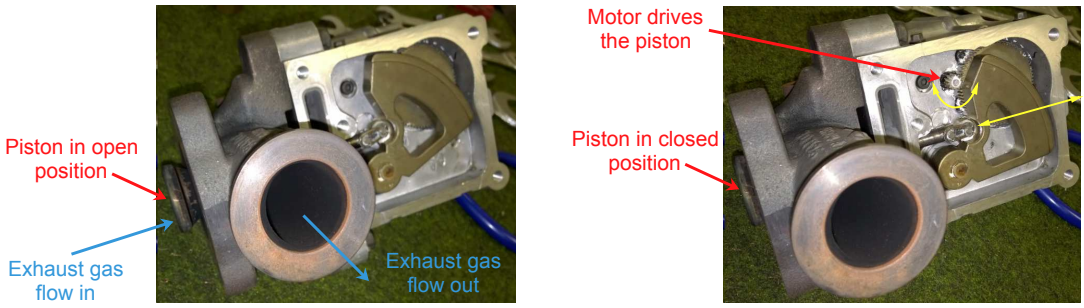

(a) (b)

Figure 1.3: Inside of an EGR valve. (a) EGR valve in open position, (b) EGR valve in closed position.

control of VGT and EGR in diesel engines; for example, works include [84, 36, 81, 62, 15, 66, 6]. In this study, novel real-time controllers for VGT and EGR control were developed using PI control, fuzzy logic control and adaptive neuro fuzzy inference system (ANFIS) modelling techniques. The controllers were firstly developed and validated in a 1-D engine model built based in a Caterpillar 3126B engine test bed located at the University of Sussex, and then they were tested on this real engine test bed.

1.2 Aim and Objectives

The overall aim of this work is to reduce soot and NOx emissions of heavy-duty diesel engines by transient engine modelling and develop real-time controllers for the control of VGT and EGR in a heavy-duty diesel engine under transient running conditions. The following objectives are listed in a logical sequence, and each of them contributes to the overall aim of the work. The objectives of the work are to

1. Comprehensively review of diesel engine fundamentals, air-path in particular, engine modelling techniques, and existing control algorithms for the control of VGT and EGR in a diesel engine;

2. Build a transient diesel engine model based on the Caterpillar 3126B engine using AVL-BOOST, and validate the model against the experimental results acquired from the test bed;

3. Investigate diesel engine air-path behaviour using the 1D engine model and test bed;

4. Develop the real-time controllers using PI control, fuzzy logic control, and ANFIS modelling techniques, and validate the real-time controllers using the 1D engine model before testing them in the real engine;

5. Develop on-board emission predictors using ANFIS modelling technique;

6. Test the real-time controllers on the Caterpillar 3126B engine test bed using the Nonroad Transient Cycle (NRTC) predefined by CP engineering;

7. Carry out repeatability and robustness tests of the fuzzy logic controller;

8. Compare the fuzzy logic controller with PID controller and ANFIS controller, and compare fuzzy logic controller with real emission analyser and fuzzy logic controller with on-board emission predictor.

1.3 Outline of Thesis

This thesis consists of the following chapters:

Chapter 1 Introduction In the first chapter, the background of this research is given. It also states the aim and objectives.

Chapter 2 Review of diesel engine modelling, and control In this chapter, at first, a thorough study of major diesel engine emissions is given with a focus on how these emissions are produced and controlled. Then, current diesel engine modelling and control technologies are discussed, followed by a detailed review of the VGT and EGR control problem in the literature.

Chapter 3 Diesel engine modelling This chapter describes the transient engine model developed using AVL-BOOST for realizing PI control, fuzzy logic control and ANFIS control. Model configurations are summarized in detail and the model has been validated against the Caterpillar (CAT) 3126B engine with details given at the end of the chapter.

Chapter 4 Diesel engine air-path control In this chapter, the developments of real-time VGT and EGR controllers using PI control, fuzzy logic control and ANFIS control techniques are given respectively. The details of on-board emission predictors developed using the ANFIS modelling technique are also presented.

Chapter 5 Robustness Evaluation In this chapter, a robustness evaluation of the fuzzy logic controller is carried out using the transient engine model. The evaluation includes sudden air leak tests and turbocharger mechanical efficiency deterioration tests.

Chapter 6 Comparison and discussion In this chapter, the performance of the fuzzy logic controller is compared with that of the PID controller and ANFIS controller. The tests were performed using the transient engine model and the CAT3126B test bed where possible. All of the tests were carried out under transient running conditions. The tests carried out on the test bed were run on the NRTC cycle and hence the robustness of the controllers can also be assessed. After evaluation on the test bed, the performance of the on-board emission predictors is also presented and discussed.

Chapter 7 Conclusion and Outlook This chapter derives conclusions followed by a brief discussion about future work.

Appendix Appendix A concludes that the work has been done using a test bed experimental setup with detailed information about the hardware and software required to carry out this research.

Appendix B is a list of publications.

Appendix C shows photos of the CAT3126B test bed.

Chapter 2

Review of diesel engine modelling, and control

2.1 Major Diesel Engine Emissions

2.1.1 Diesel combustion

The combustion of diesel fuel not only releases heat energy to power the engine, but also inevitably produces harmful emissions. Currently, nitrogen oxides, carbon monoxide (CO), total hydrocarbons (HC), particulates and visible smoke are regulated in legislation relating to diesel engines [18]. Table 2.1 shows the EU emission standards for a heavy-duty diesel engine running under steady-states and transient conditions, respectively.

A main component of fossil fuel is carbon, comprising about 85% by weight (Fig. 2.1 a). The general chemical formula of fuel can be written as C_nH_{2n+2} [33] which has a structure illustrated in Fig. 2.1 c. Ideally, the complete combustion of pure diesel can be described by the following chemical reaction Eq. 2.1 which only produces H_2O and CO_2. [12]. In reality, there are other components in the exhaust gas, which, due to ideal conditions, are difficult to produce either due to the air-fuel mixing problem or the impureness of the fuel. Fig. 2.2 shows the untreated exhaust gas composition of diesel engines under different air-fuel ratios (AFR) conditions.

$$n_1C_xH_{2x+2} + m_1O_2 \rightarrow n_2H_2O + m_2CO_2 \tag{2.1}$$

Table 2.1: EU emission standards for heavy-duty diesel engines. (a) Steady-state testing, a - PM = 0.13 g/kWh for engines smaller 0.75 dm^3swept volume per cylinder and a rated power speed above 3000 min^{-1}, (b) Transient testing, a - for gas engines only (Euro III-V: NG only; Euro VI: NG + LPG) ; b - not applicable for gas-fuelled engines at the Euro III-IV stages; c - PM = 0.21 g/kWh for engines smaller than 0.75 dm^3 swept volume per cylinder and a rated power speed above 3000 min^{-1}; d - THC for diesel engines; e - for diesel engines, PN limit for positive ignition engines TBD. [28]

Stage	**Date**	**Test**	**CO**	**HC**	**NOx**	**PM**	**PN**	**Smoke**
			g/kWh				*1/kWh*	*1/m*
Euro I	1992, ≤ 85 kW	ECE R-49	4.5	1.1	8.0	0.612		
	1992, > 85 kW		4.5	1.1	8.0	0.36		
Euro II	1996.10		4.0	1.1	7.0	0.25		
	1998.10		4.0	1.1	7.0	0.15		
Euro III	1999.10 EEV only	ESC & ELR	1.5	0.25	2.0	0.02		0.15
	2000.10		2.1	0.66	5.0	0.10[a]		0.8
Euro IV	2005.10		1.5	0.46	3.5	0.02		0.5
Euro V	2008.10		1.5	0.46	2.0	0.02		0.5
Euro VI	2013.01	WHSC	1.5	0.13	0.40	0.01	8.0×10^{11}	

(a)

Stage	**Date**	**Test**	**CO**	**NMHC**	**CH_4[a]**	**NOx**	**PM[b]**	**PN[e]**
			g/kWh					1/kWh
Euro III	1999.10 EEV only	ETC	3.0	0.40	0.65	2.0	0.02	
	2000.10		5.45	0.78	1.6	5.0	0.16[c]	
Euro IV	2005.10		4.0	0.55	1.1	3.5	0.03	
Euro V	2008.10		4.0	0.55	1.1	2.0	0.03	
Euro VI	2013.01	WHSC	4.0	0.16[d]	0.5	0.46	0.01	6.0×10^{11}

(b)

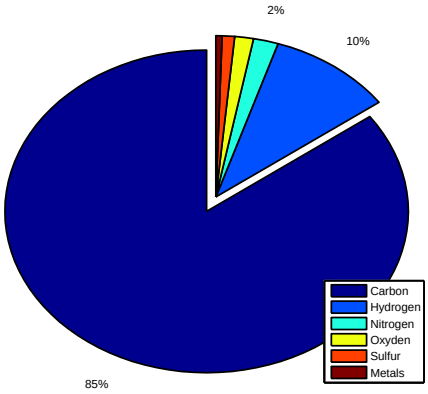

(a)

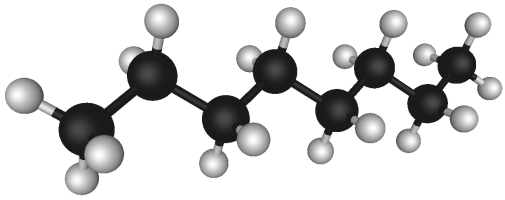

(b)

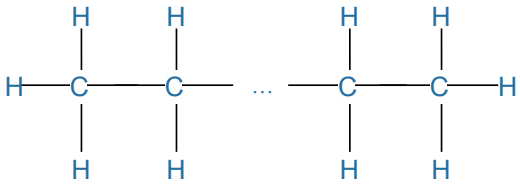

(c)

Figure 2.1: Fuel composition. (a) fuel components by weight [69], (b) a 3D molecule of octane, and (c) chemical structure of hydrocarbon.

2.1.2 Formation of carbon dioxide (CO_2)

As shown in the chemical formula of diesel combustion (see Eq. 2.1), CO2 is a natural product of complete diesel combustion. The proportion of CO2 in the exhaust gas depends on the operating conditions of the engine. The amount of converted CO2 in the exhaust gas is directly proportional to fuel consumption and, hence, the only way to reduce CO2 emission when using standard fuel is to reduce fuel consumption [12]. Because CO2 is a natural component of atmospheric air, it is not classified as a pollutant. However, CO2 contributes to the greenhouse effect and global climate change and, since 1920, CO2 in the atmosphere has risen continuously from roughly 300 ppm to 450 ppm in 2001 [12]. This has become the motivation to reduce CO2 and fuel consumption in the automotive industry.

2.1.3 Formation of carbon monoxide (CO)

CO is produced mainly due to incomplete combustion when there is not enough air to burn with the injected fuel; the burning of fuel droplets that fail to vaporize also contributes to it [12]. It is also produced when there is excessive air, but the concentration is minimal. CO is an odourless and tasteless gas and, and hence, it is almost undetectable by people. But it prevents the blood from absorbing oxygen, which leads to asphyxiation. Hence, it is both harmful and dangerous.

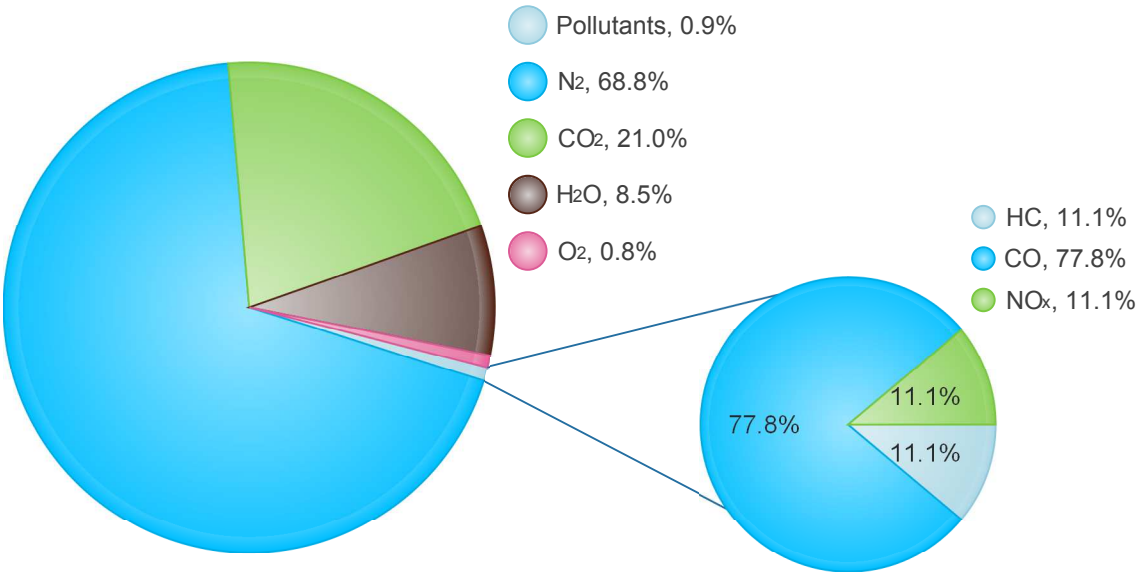

(a)

Composition of exhaust gas	AFR = 76.9	AFR = 50	AFR = 34.5	AFR = 25.6	AFR = 17.9	AFR = 14.3	AFR = 11.9	AFR = 10.6
CO2, % by volume	2.74	4.19	6.22	8.36	12.40	13.8	12.1	10.2
O2, % by volume	17.14	15.13	12.20	9.26	3.44	0.8	0.3	0.3
CO, % by volume	0.041	0.028	0.024	0.027	0.058	0.7	3.3	6.0
H2, % by volume	-	-	-	-	-	0.1	1.3	3.0
CH4, % by volume	-	-	-	-	0.03	0.1	0.3	0.4
N2, % by volume	80.08	80.65	81.56	82.35	84.07	84.5	82.7	80.1
NOx, ppm by volume	167	267	378	448	364	346	277	186
Aldehydes, ppm by volume	4	1	1	1	4	1	2	0

(b)

Figure 2.2: Composition of untreated exhaust gas of internal combustion engines. (a) engine running at $\lambda = 1$ [12], (b) comparison of diesel engine exhaust gas composition under different AFR conditions under 1440rpm. [67].

2.1.4 Formation of HC

HC, which stands for hydrocarbons, is a generic designation for the entire range of chemical compounds uniting hydrogen H with carbons C. It is also mainly produced during incomplete combustion when an engine is running in a rich fuel mixture. Incomplete combustion produces new hydrocarbon compounds that do not initially present in the fuel [12]. Not all hydrocarbons are odourless; for example, cyclic aromatic hydrocarbons emit a discernible odour. Partially oxidized hydrocarbons can also emit an unpleasant odour. It is s harmful gas with the potential to cause cancer.

2.1.5 Formation of NOx

Nitrous oxides, or oxides of nitrogen, is the generic term encompassing chemical compounds consisting of nitrogen and oxygen. They result from secondary reactions that occur in all combustion processes where air containing nitrogen is burned [12]. The primary forms that occur in the exhaust gases of internal-combustion engines are nitrogen oxide (NO) and nitrogen dioxide (NO2), with dinitrogen monoxide (N2O) also present in minute concentrations. NO is colourless and odourless. In atmospheric air, it is gradually converted to nitrogen dioxide (NO2). Pure NO2 is a poisonous reddish-brown gas with a penetrating odour. NO2 can induce irritation of the mucous membranes when present in concentrations found in highly polluted air. Nitrous oxides contribute to forest damage and also act in combination with hydrocarbons to generate photochemical smog.

Most of the NOx emissions result from a chemical kinetic process, known as the Zeldovich [38] Thermal NOx emission mechanism, where:

$$N_2 + O = NO + N \tag{2.2}$$

$$N + O_2 = NO + O \tag{2.3}$$

The rate constants for the two reactions are exponential functions of the temperatures in the combustion chamber [75]. These temperatures depend on the thermodynamic processes that occur during compression and combustion, as well as on the adiabatic flame temperature of the fuel-air mixture.

2.1.6 Formation of Particulates

The problem of particulate emissions is primarily associated with diesel engines. Levels of particulate emissions from gasoline engines with multipoint injection systems are neg-

ligible. Particulates result from incomplete combustion. Unburned and partly combusted hydrocarbons form deposits on the soot, where they are joined by aldehydes, with their penetrating odour. Aerosol components and sulphates bond to the soot. The sulphates result from the sulphur content in the fuel. Consequently, these pollutants do not occur if sulphur-free fuel is used.

Soot formation is a very complex chemical process that is affected by the physical processes that occur during the fuel mixing and combustion processes. A simplistic view of the diesel diffusion-burning process involves a relatively thin flame front formed at the interface between the fuel and air. In this view, the fuel is on one side of the flame and air on the other. The initial soot formation reactions include thermal breakdown (pyrolysis) of the fuel before it enters the flame. Under these conditions, the soot precursor reactions (leading to greater soot formation potential) favour high temperature and long residence times. More soot precursors are formed if the mixing rates are slow and the temperatures are high. Higher temperatures also lead to higher soot oxidation rates. The level of PM emissions from a given diesel engine is the result of the difference between the formation rate and the oxidation rate. In general, higher temperatures tend to lead to lower soot and PM emissions, due primarily to the effect of the increased temperature of the PM oxidation rate.

Diesel particulate matter is defined by regulatory bodies as anything collected in a specific filter that is maintained at 125 F [75]. The collection procedure involves dilution of the exhaust sample with fresh air. The method has been defined by the United States environmental protection agency (EPA) to simulate what occurs when diesel exhaust is emitted into the atmosphere.

The diesel engine designer faces a conflict between PM and NOx emissions. High temperatures are desirable for PM emission control, but they also lead to high NOx emissions. It is this trade-off that constitutes one of the primary concerns of modem diesel engine design.

2.2 Diesel Engine Modelling

2.2.1 Why modelling

Experimental tests are crucial to scientific research, especially for automotive engine research. Firstly, necessary data can be collected and analysed using appropriate scientific methods and new findings can be possibly discovered; secondly, new theories and tech-

nologies have to be validated by relevant experiments before they can be approved and put into practice. However, experimental tests can be expensive and time-consuming processes. Some experiments can even be unpredictable and, thus there is a risk of accident. Instead of carrying out experimental tests in a real-world engine test bed, such tests can be conducted in a virtual engine model that represents the correlative real-world engine. Using the virtual model, expensive experimental work can be reduced and any modifications to the engine system can be easily validated and assessed before they can finally be applied to the real engine. Furthermore, the virtual model can also be used to predict the performance of a real plant, and this can be used for control and diagnostic purposes. However, virtual models often make a simplified reduction of the complexity of the original system with well-defined boundary conditions [71], so the virtual model has to be validated against the real plant.

2.2.2 Modelling techniques

With the rapid development of computing technology, it has been possible to build sophisticated engine models and engine modelling has become more and more important in automotive engine research. Different engine modelling technologies have been developed and used by researchers in this field. In order to deeply understand the engine modelling topic, several modern modelling techniques have been reviewed and discussed.

The computational fluid dynamics (CFD) technique is fundamentally based on the governing equations of fluid dynamics. It is also called 3D simulation because it is able to investigate the dynamics of flow in three dimensions and, and hence, it can provide results in great detail with relatively high accuracy [78]. However, in some cases, 2D simulation is sufficient and can be selected to reduce computing effort. A very important concept in CFD is mesh (also called grid). A mesh can be either 2D or 3D and it divides the target space into small elements. The differential equations governing the behaviour of each element are then solved to predict the dynamics of the fluid such as temperature, pressure, flow speed and direction, and so on. It has been widely adopted to study the dynamics of air and fuel flows in internal combustion (IC) engine research. Dickmann et al. [27] developed a CFD model of a turbocharger compressor stage impeller. Two operating points at off-design conditions were analysed under transient conditions. This work has demonstrated that it is possible to simulate unsteady flows through complex centrifugal compressor geometries for off-design conditions. Cui et al. [23] used CFD simulation to study the intake port structure optimization. An intake port model was created using the

AVL-Fire platform, and the previous intake port structure was optimized to improve intake port performance. This study shows that CFD simulation is an efficient way to design engine intake port where air flow condition is complex. The effect of the fuel injection timing and intake pressure in a direct injection diesel engine was studied by Jayashankara and Ganesan [44] using the CFD method. The performance and emissions characteristics of the engine such as pressure, temperature, heat release, NOx and soot were investigated under transient conditions. The study shows how advanced and retarded injection time would affect the in-cylinder pressure, temperature, heat-release rate and emissions of the engine and optimum injection timing. However, due to the numerous calculations involved in the CFD method, especially in the 3D model, the CFD-based solution cannot run fast enough with the current control task. It would usually take more than 10 hours to solve two strokes of one diesel cycle; for the transient running condition, it would take months of constant running to finish just one test.

It is possible to neglect the cyclic variation of the diesel cycle to use a so-called 'mean value' model instead. Calculations needed to solve the solution are largely reduced and, and hence, it is possible to simulate the engine running for a considerably longer duration. Poloni et al. [61] developed an augmented observable mean value engine model of a turbocharged diesel engine to compute the mass flows for different places. Cieslar et al. [20] reported a particular implementation of model predictive control based in a corresponding mean value engine model. The work is focused on the transient response of a light-duty automotive diesel engine and aims to properly assess the full potential of a given hardware configuration. Watanabe et al. [83], Tan et al. [73], Tao et al. [74], Bolla et al. [14], Grahn et al. [35] and Cheng et al. [19] also reported diesel engine studies based on mean-value models.

1D CFD models have the advantage of a mean value model and give the mathematical model a length dimension. Sophisticated commercial software is available such as Ricardo WAVE, GT-POWER and AVL-BOOST, which can provide reliable solutions for many applications of automotive research. 1D simulation has become a significant part of the engine development process in the automotive industry. Cornolti et al. [22] carried out a detailed analysis of the unsteady flows in the intake and exhaust systems of a diesel engine using a 1D CFD model they built. The model was created based in a modern four-cylinder turbocharged diesel engine with different EGR circuits. Experimental test data has been used to validate the model, and the two main lay-out of external EGR systems has been studied in this model. Ahmed et al. [3] developed a 1D CFD model of the exhaust flow

using Navier-Stokes equations. The model was then used for simulating the effects of exhaust gas flow through the variable turbine geometry section of a variable geometry turbocharger. The model shows good compliance with experimental results. Lopez et al. [50] studied the spray characteristics, mixing and autoignition process using diesel fuel and gasoline, respectively, with a 1D model. The experimental results have confirmed the 1D spray model calculations. Zhou and Chen [88] studied exhaust noise reduction using a 1D engine model built in AVL-BOOST. After coupling the modified muffler model to the 1D engine model, the simulation results show that the modified muffler is superior to the former design.

1D/3D-coupled simulation can join a 1D model with a 3D model to provide more accuracy when required. Bohbot et al. [13] combined 1D and 3D models to study the effect of injection parameters on the combustion behaviour of a single-cylinder diesel engine. In their coupled model, the 1D model was used in the gas exchange system and fuel injection system and to provide necessary inputs such as volumetric efficiency, thermodynamic state, mixture composition and mass flow rate for 3D model. The 3D model was used in the combustion chamber to ensure an accurate description of the combustion process. The simulation results are in good agreement with experimental results. Mtui [54] used a 1D/3D coupled model to investigate the performance of a dual fuel diesel engine running with added natural gas at 600 rpm under varied load conditions. The 1D model was created in GT-Power, and the 3D model was built using KIVA-3. The coupled model is able to accurately predict engine performance and emissions running with different percentages of substitutions of natural gas. However, as 3D simulation is involved, the computing time is considerably longer compared to that of 1D-only simulation.

Models can also be built with artificial intelligence methods such as neural network or ANFIS. The main feature of these artificial intelligence modelling techniques is the ability to learn and predict the desired outputs so they are very good at predicting the dynamics of a non-linear system [39]. Once trained by appropriate selected data sets, the neural network and ANFIS model are able to predict the outputs based on the input values without any explicit mathematical representation. To build such models, necessary experimental tests are needed to acquire the required data sets for training and testing processes. The chosen data set used to train an ANFIS should include all representative features of a system. Uzun [80] developed a neural network model to determine the effects of inter-cooling process in a performance-charged diesel engine's air intake mass flow. It shows that the neural network model is quicker, more secure and robust. Based on the

experimental data collected from a single-cylinder CRDI engine, Roy et al. [65] developed a neural network model to predict brake- specific fuel consumption, brake thermal efficiency, CO2, NOx and PM with load, fuel injection pressure, EGR and fuel injected per cycle as input parameters. The developed neural network model was capable of predicting the performance and emissions of the experimental engine with excellent agreement as observed in the experimental test results.

In this work, considering the real-time control of the VGT and EGR under transient running conditions, AVL-BOOST 1D simulation was used to build the required diesel engine model based on the Caterpillar 3126B engine. In order to build the model, necessary studies in diesel engine air and fuel system components are needed.

2.3 Engine Control Techniques

2.3.1 Controller main components

The control system of an engine is designed to maintain the performance and emissions of the engine within specified limits [18]. In a modern control system, three components are essential to complete a control task: sensor, processor, and actuator (Fig. 2.3).

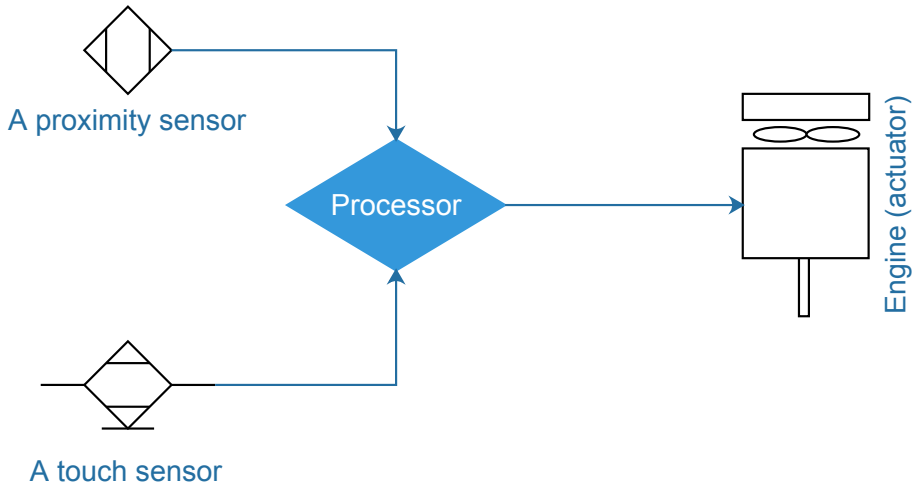

Figure 2.3: Sensors, processor, and actuator in a control loop

A sensor obtains a measurement of a physical variable through a direct measurement or a combination of measurement and computation. A 'soft sensor' delivers a value through an intermediate computation. Sensors can be specified to measure a range of physical and chemical quantities at the speed of response needed even by a high speed diesel engine. Several factors limit those that prove acceptable in a production engine including cost and durability.

A processor calculates a control action that will keep system performance at the required level. The processor does not have to be electronic and indeed the most widely known form of speed control in engines uses a purely mechanical system. The centrifugal governor uses the position of fly weights to set the required fuelling and was first applied to engines by James Watt, although the principle came from earlier windmill technology. The majority of control systems fitted to today's engines are electronic and are usually programmable.

An actuator is set by the processor to induce the required control action. Fuel injection equipment (FIE) is the most fundamental actuator on the engine and is the means of supplying energy to the cylinders. Historically the control system has adjusted the fuel rack which has adjusted fuelling in parallel to all the cylinders. Modern FIE systems permit fully flexible timing control and where there are unit injectors controlled by individual cylinders. Other actuators include the EGR valve, variable geometry devices, and the turbocharger waste gate.

2.3.2 Structures of control systems

Basically, there are two control structures (Fig 2.4) depending on whether a feedback signal of the control target variable presents in the control loop. When there is a feedback signal available and it has been used as a reference point for the controller to adjust its relevant control input variables, it is called closed loop control or feedback control. When there is no feedback of the control target variable and the instantaneous status of the system is unknown to the controller, it is called open loop control. Obviously, the closed loop control is superior to the open loop control because the closed loop control is able to precisely control the target.

A purely open loop control system has no embedded feedback mechanism, and relies on external agents, normally people, to make corrections. Fig. 2.4 shows a scheduled control is part way between pure open loop control and closed loop control.

A closed loop controller calculates a control action on the basis of the error between a demand signal and the value measured from the system under control. In order to compensate for a measured disturbance, feed-forward technique is added to the control action. In Fig. 2.4, a closed loop is formed when a measurement m is compared with a demand r. The error e is calculated as r-m, and then included in a simple calculation to form the control signal u. In a simple feedback system u is sent direct to an actuator whose position is set accordingly. For feed-forward measurement, d is in effect advance warning

of a coming change. A computation of the effect of this variable is done and delivers a value f, which is the amount by which the actuator must be moved to compensate for the change implied by the measurement d.

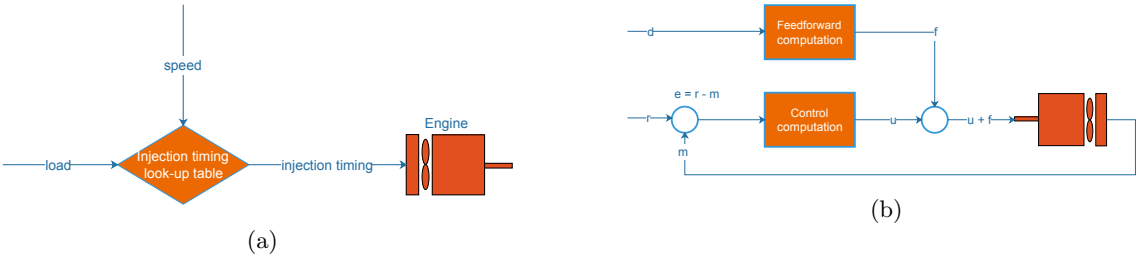

Figure 2.4: Control loop. (a) open loop control, (b) closed loop control with feedback signal 'm'.

2.4 Literature Review of Diesel Engine Air-path Control

2.4.1 Overview

Air and fuel system are the most important components of a diesel engine system. In a diesel engine, atomized diesel fuel is injected into the cylinder at the end of the compression stroke in the form of spray. Because of the self-ignition properties of the diesel fuel, the combustion takes place immediately when the fine fuel drops meet the previously compressed air in the cylinder. The combustion then spreads rapidly so that all injected fuel burns completely usually with an air-fuel ratio well above of the stoichiometric value (around 14.9). In the literature, several different types of closed-loop controllers have been developed to solve this control problem.

2.4.2 PID based control

PID control (also called three-term control) has been widely applied throughout engine control applications in the automotive industry. Fig. 2.5 shows a typical PID controller structure. It is a typical closed loop control method because it takes the feedback of the system to be controlled into account. The three terms P, I, and D refers to proportional, integral, and derivative. At each control step, the error between the feedback and the reference set-point will be calculated. The P term offers the speed of response, the I term ensures that there is no control error in the steady state, and the D term ensures that the control signal is modified if the error changes quickly [18]. For linear control problems, a PID controller can offer excellent speed of response, stability and accuracy and these

are achieved by properly tuning of the three coefficients (K_P, K_I, and K_D in Fig. 2.5) in each terms described before. The P term produces a multiple of the current error. When the error grows, the control amplitude increases correspondingly, and the error can be eliminated more quickly. The I term accumulates the control error over time. If this term keeps growing, it will produce a stronger correction action on the control signal. The D term calculates the derivative of the measurement and subtracts the result from the control output. This tends to damp the control response and acts as a stabilizing influence on the control action.

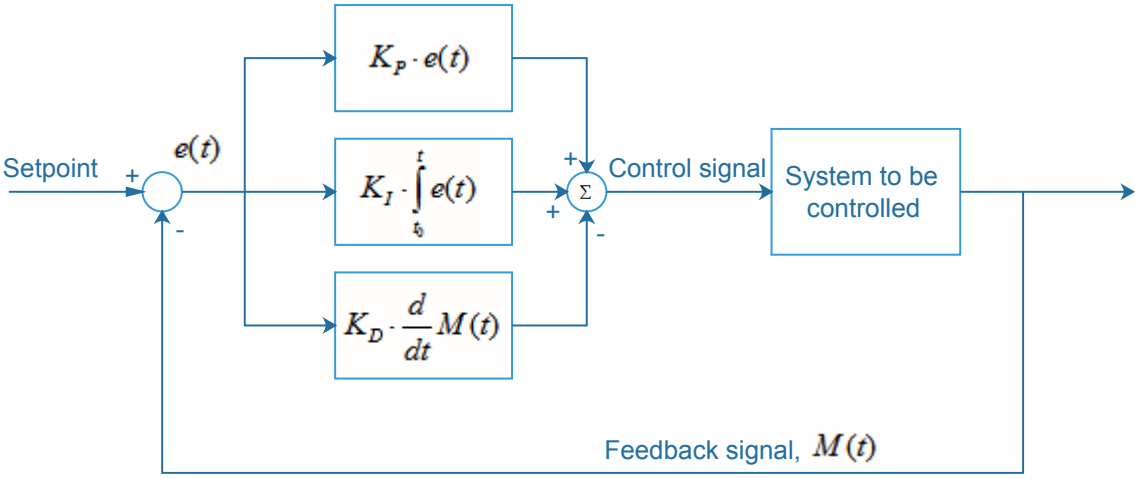

Figure 2.5: PID control structure [52]

The simplicity of PID controllers has made themselves very popular in diesel engine control applications in automotive industry. However, due to it is generally a linear controller, so the control performance is often sacrificed.

PID-based controllers have been widely used in mass-produced passenger cars [7]. According to the authors, such a control system is often based on the dual-loop PID structure shown in Fig. 2.6. This controller is trying to regulate the mass air pressure (MAP) and mass air flow (MAF) based on the set-points generated from two predefined maps. One loop uses a feedback signal from the inlet air pressure sensor to control the VGT position; the other uses a feedback signal from the air flow meter to control the EGR position. However, these two loops cannot work simultaneously due to the highly coupled nature of inlet pressure and flow. In another word, only one of the control targets can be achieved depending on the operating condition of the engine. Another drawback of this control method is a map of PID gains has to be generated in order to cope with the inherent nonlinearity of the diesel engine system, and this would further increase the development as well as hardware cost.

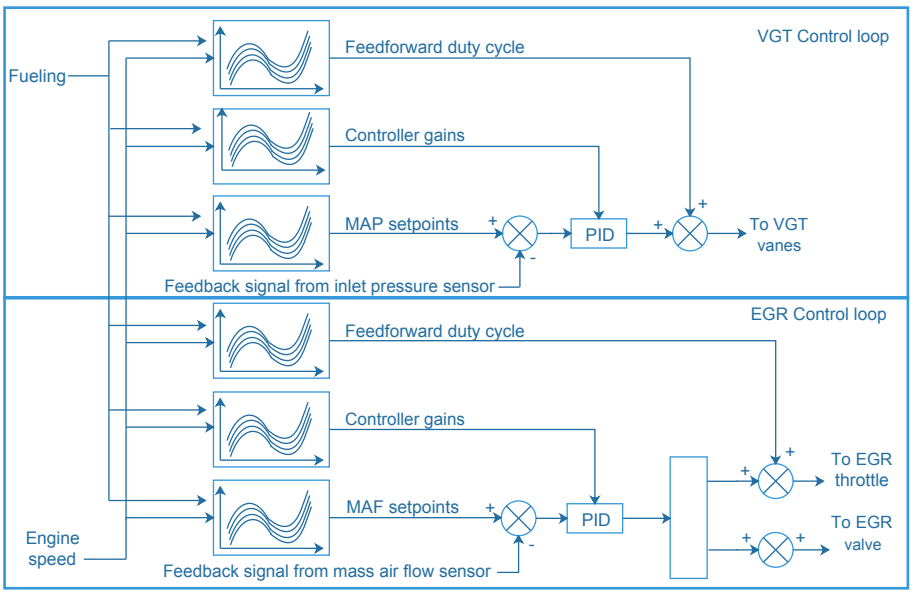

Figure 2.6: Structure of dual-loop PID controller

2.4.3 Model based control

A mathematical model represents the target system can be built to compute the control actions. This approach is good at solving nonlinear control problems. Diesel engines are highly nonlinear systems so model-based control has been widely adopted in diesel engine control related research. Zhang et al. [86] developed a model-based control scheme to address the cold-start speed control in spark ignition engines with the aim to improve the transient performance of the starting engine speed. dAmbrosio et al. [26] developed a control-oriented real-time semi-empirical model for predicting the NOx emissions in diesel engines under both steady state and transient conditions. Similarly, Finesso et al. [31] developed a semi-empirical model for estimating the particulate matter in diesel engines. Alfieri and Alois Amstutz [4] proposed a gain-scheduled model-based feedback control of the air/fuel ratio in diesel engines.

Model-based controllers, such as predictive controllers [77] and robust controllers [21] [70], are able to cope with the nonlinearity of a system well, but they are relatively more difficult to apply in a large production scale due to the high variability of engine parameters. Apart from this, mathematical models such as state-space models have to be simplified in order to reduce computing time. Jankovic et al. [42] built a mean value diesel engine model based on the conservation of mass and energy and the ideal gas law, but the heat transfer to the surroundings was neglected in the model. Additionally, the author stated that several nonlinear functions in the controller had to be held constant in order to simplify the controller for implementation. Abidi et al. [2] also developed a

state-space diesel engine model for the control of VGT and EGR. For the same reason, the inlet temperature was neglected in their model in order to reduce computing effort. Such simplifications sacrificed the accuracy of the models.

Kim et al. [46] in their work developed a 5th order control oriented model with input-output linearization technique for the controlling of the air-path of a diesel engine with dual-loop EGR and VGT. However, several assumptions have been made in controller design. According to the authors, these assumptions include:

- burnt gas fraction states which are difficult to measure and not directly coupled with other dynamics are omitted;
- transition of temperature of which dynamics is relatively slow is ignored;
- temperatures of all flows in the same location are in the same level. Full model can be found in the paper.

The controller has been verified by simulations carried out in a full engine model, and the simulation results show that the control states (intake manifold pressure, exhaust manifold pressure, and mass air flow) have tracked the desired trajectories with few overshoot or oscillatory behaviours. The authors mentioned their future work would include the experimental verification of the control system.

Kuzmych et al. [48] previously developed a robust nonlinear controller based on control Lyapunov function. The obtained controller gain guarantees the global convergence of the system and regulates the intake flow and EGR flow in order to minimize emissions. Simulation results have shown the effectiveness of this approach. However, due to the nature of this control it is difficult to apply in a real engine test bed.

2.4.4 Robust control

Robust control mainly deals with uncertainty. A robust controller should function correctly when uncertain parameters or unexpected disturbances are present in the system under control. In model based control system, due to unintentionally or intentionally excluded dynamics and/or wear-and-tear effects upon the plant, a model will never completely and truly describe the dynamic behaviour of the actual system [76]. On the other hand, the industrial control systems operating in the real world are vulnerable to external disturbances and measurement noises. For this reason, the controller should be able to keep the control system stable as well as maintain a desired performance level even in the presence of unexpected and undefined disturbances.

Nelson-Gruel et al. [55] developed a robust controller using CRONE control methodology [58] to adapt the air-path and fuel-path of a diesel engine and minimize NOx emissions. According to the authors, the aim of this approach was to find a decoupling and stabilizing controller for the combustion engine that minimized NOx emission at each operating point considered and during transient of torque and engine speeds. The system is a square multivariable system with three inputs: Exhaust gas recirculation valve, variable geometry turbine, and start of injection; and three outputs: mass air flow, boost pressure and NOx level. Fractional order transfer functions were used to define all the components of the diagonal open-loop transfer matrix, β0. Optimisation gave the best fractional open-loop transfer matrix and, finally, frequency domain system identification was used to find a robust controller $K(s) = G_0^{-1}(s)\beta_0(s)$.

2.4.5 Sliding mode control

In control theory, sliding mode control (SMC) is a nonlinear control method that alters the dynamics of a nonlinear system by application of a discontinuous control signal that forces the system to slide along a cross-section of the system's normal behaviour [79, 60]. The state-feedback control law is not a continuous function of time. Instead, it can switch from one continuous structure to another based on the current position in the state space. Hence, sliding mode control is a variable structure control method. The multiple control structures are designed so that trajectories always move toward an adjacent region with a different control structure, and so the ultimate trajectory will not exist entirely within one control structure. Instead, it will slide along the boundaries of the control structures. The motion of the system as it slides along these boundaries is called a sliding mode [89], and the geometrical locus consisting of the boundaries is called the sliding (hyper) surface. In the context of modern control theory, any variable structure system, like a system under SMC, may be viewed as a special case of a hybrid dynamical system as the system flows through a continuous state space but also moves through different discrete control modes.

Ali et al. [5] proposed a control scheme for controlling the diesel engine air path using the sliding mode control. The controller has been tested on the Jankovic Turbocharged Diesel Engine model, but not yet tested on real engine test bed. The proposed sliding mode controller was compared with the feedback linearization method [41] in the paper. Simulation results show that compared to the feedback linearization method, the performance of the sliding mode controller has not been affected by different values of parametric uncertainties.

2.4.6 Optimal control

In optimal control, the control signals are selected to optimize a cost function. Linear quadratic Gaussian controllers are typical optimal controllers which use a cost function made up of deviation between the demand, the achieved output of the controlled system, and the size of the control signal. The control behavior in operation is determined by the weighting placed on each of the two aspects of cost. If control is expensive then the weighting on control will be high; if error is expensive then the weighting on error will be high. Such an optimal controller is designed from a cost function qualitatively defined as Eq. 2.4 [18], where the sum is formed over a long period the solution for the feedback law converges to a constant value.

$$J = \sum (Qx^2 + Ru^2) \tag{2.4}$$

Flardh et al. [32] developed an optimal control scheme to find optimal open-loop trajectories for the overlap and the VGT position for a fast transient response. This optimization is based on a 1-D simulation model. According to the authors, a generic feedback strategy for controlling the VGT is found based on this optimization and this strategy is implemented and evaluated on an engine and shows good performance. Kolmanovsky and Stefanopoulou [47] demonstrated how the optimal control-based analysis can be very useful in studying feasibility and cost/benifit trade-off for an automotive hardware component.

2.4.7 Adaptive control

If a controller is able to change its design - either structure or parameters - to suit new conditions under which it is operating, it can then be classified as adaptive control. According to Challen and Baranescu [18], adaptive control covers a large number of different algorithms and we can consider them in two broad classes:

- Model reference adaptive controllers (MRAC), keep an internal model of the process under control: if the model changes the controller adapts its design to suit.
- Self-tuning adaptive controllers monitor the behaviour of the system they control by refitting a model at every control step.

The MRAC controller has an inner loop consisting of the controller, the process and the feedback of the process output. An outer loop is responsible for the adjustment of the controller parameters, and is driven by the error between the actual and predicted process output. The error, e, drives the adaptation of the controller.

One of the earliest and best known MRAC laws is the MIT[1] law 2.5 [18]. The MIT law determines the change in the control parameter, ϑ:

$$\dot{\theta} = -\alpha * error * grad_{\theta} * e \tag{2.5}$$

Dambrosio et al. [25] developed an adaptive technique for the control of the VGT in a turbocharged compression ignition engine. The adaptive control is based on a one-step-ahead technique and a least-square parameter estimator algorithm. The paper shows that the one-step-ahead technique is able to improve dramatically the control performance with respect to that provided by a commonly applied PID control technique. However, in the paper there is only simulation results available, the applicability on a real engine remains unclear. Dambrosio et al. [24] also used the one-stop ahead adaptive technique on gas turbine power plants.

2.4.8 Intelligent control

In the literature, intelligent systems have been proposed to overcome the inconvenience of those model-based approaches. A fuzzy logic controller proposed by Arnold et al. [7] is capable of controlling the VGT vanes and EGR valve simultaneously without using a model of the air path system, and it is claimed that the proposed fuzzy logic controller has reduced the usage of electrically erasable programmable read-only memory in the engine control unit (ECU) by reducing the feed-forward maps needed and also has better responding time compared to the dual-loop PID controllers.

The controllers described above aim to achieve the optimal intake pressure and flow set-points by regulating the positions of the VGT vanes and EGR valve. Consequently, these controllers require extensive engine mapping to determine the optimal intake pressure and flow at different engine speeds and loads with respect to engine performance and emissions. This is a time consuming and expensive process. In order to reduce the difficulties in developing the maps, Omran et al. [57] have proposed a mathematical optimization process which can search for the optimal control strategies of the diesel engines under static and dynamic conditions. The proposed optimization process can generate a database which can be used to train a neural network. The neural network can then be used as an online controller loaded into the ECU to predict the optimal control output variables. However, the author stated that this dynamic optimization process cannot be directly integrated into the ECU of a real engine due to the extremely slow computing time.

[1] Massachusetts Institute of Technology

The advantage of fuzzy logic control is that expert knowledge can be included in the form of rules to control a process. The control strategy is made based in a group of control input variables and it is effective to solve nonlinear control problems [43]. In this study, a novel real-time fuzzy logic controller (RFLC) has been developed to search for the trade-off-oriented control strategies under dynamic conditions. Instead of regulating the VGT and EGR positions to attain the optimal set-points of inlet pressure and flow, the proposed controller is able to determine the optimal VGT and EGR positions in real time.

2.5 Chapter Summary and Conclusions

In the beginning of this chapter, a basic chemical explanation of diesel combustion was given and the formations of major diesel engine emissions including CO_2, CO, HC, NOx, and Particulates were discussed. It then followed by descriptions and discussions of diesel engine modelling and controlling techniques. Modelling techniques include CFD modelling, mean value modelling, 1D CFD model, 1D/3D coupling modelling, modelling using artificial intelligence such as fuzzy logic and neural networks or the hybrid of these two: ANFIS. Control techniques include PID control, model based control, intelligent control. How to choose from these techniques were also discussed. After all, a thorough literature review of diesel engine air-path control was given.

Chapter 3

Diesel Engine Modelling

3.1 Engine Model Development

3.1.1 Overall engine model structure

AVL-BOOST advance simulation software was used to create the required transient engine model. AVL-BOOST is an advanced and fully integrated internal combustion engine simulation tool with advanced models for accurately predicting engine performance. With a full range of configurable sub-models (engine, cylinder, pipe, ECU...) provided, a vehicle power train model can be created by correctly connecting all the relevant sub-models and configuring each sub-model according to the design. It can be either used to evaluate a new power train design, or to create a model based on an existing platform. When the model is completed, steady-state tests and transient tests can be performed to evaluate the model. Temperature of gas, pipe, and wall, pressure in pipes, manifold, or cylinder, heat transfer effect, engine power, torque, brake mean effective pressure (BMEP), noise, and emissions results are available in both transients(against cycle number or time) and traces (against crank angle degree) mode.

In this work, two transient engine models (see Fig. 3.1) were created based on the Caterpillar 3126B test bed located in the University of Sussex. The only difference between these two models is that in the first model, the VGT and EGR is controlled by PI controllers, in the other one the VGT and EGR is controlled by the fuzzy logic controllers. Main components of the engine model include an engine (E1), 6 cylinders (C1 to C6), a VGT (TC1), an EGR valve (TH1), 2 inter coolers (CO1 and CO2), a mechanical consumer (MHC1), 26 pipes (1 to 26), 4 plenum (PL1 to PL4), 2 system boundaries (SB1, SB2), 4 junctions (J1 to J4),), 13 measuring points (MP1 to MP13), an ECU (ECU1), a monitor (MNT1), a Matlab interface (API1), and 2 PI controllers (PID1 and PID 2). All

the components including the diameter and length of the pipes were configured according to the test bed.

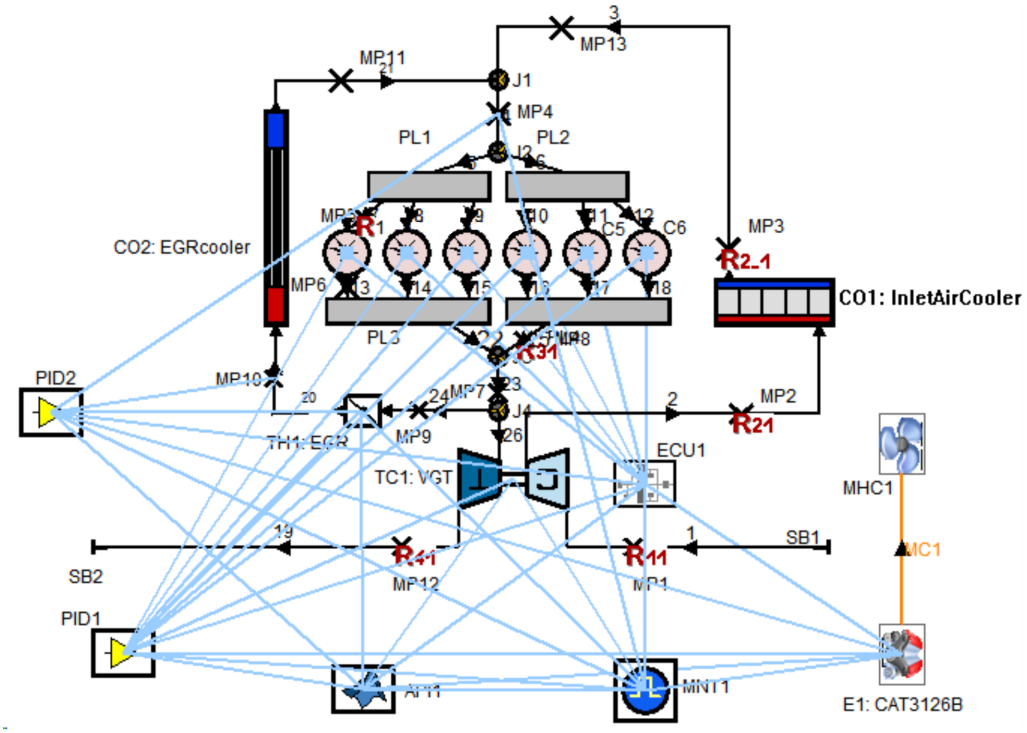

(a)

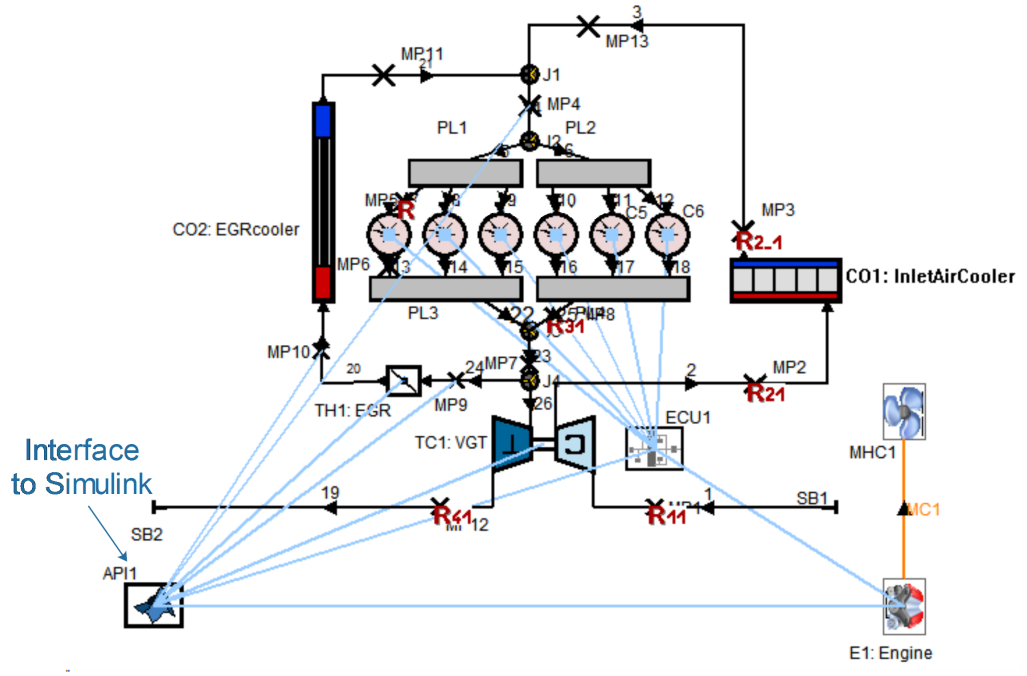

(b)

Figure 3.1: AVL-BOOST models created based on the Caterpillar 3126B engine test bed. (a) PI control, (b) fuzzy logic control/ANFIS control.

3.1.2 Engine & cylinder sub-model configuration

The configurations of sub-model Engine (E1) and Cylinders (C1 to C6) will be described in detail here. The details of the other sub-models can be found in the Appendix section. Table 3.1 shows the configurations for the Engine (E1) sub-model. In this sub-model, the engine speed can be configured either as transient or steady. When transient is chosen, inertia moment of the engine needs to be set ($1.6 kgm^2$). The cylinders were configured as identical cylinders, so later when configuring the Cylinder sub-model, it is only needed to configure one cylinder, the other 5 cylinders will automatically use the same settings.

The engine friction is calculated using the SLM model proposed by Shayler et al. [68]. The friction data of this model was collected from motored engine tests on 4 cylinder diesel engines.

Table 3.1: Sub-model Engine (E1) configuration.

Engine	General	Cycle type	4-stroke
	Cylinder setup	Firing order C1-C2-C3-C4-C5-C6	0 - 480 - 240 - 600 - 120 - 360deg
	Engine friction	Friction model	Shayler, Leong, Murphy model
		Cylinder arrangement	Inline
		Type of valve train	SOHC-rocker arm
		Number of camshafts bearings	6 camshaft bearings
		Maximum valve lift	12mm
		Type of cam follower	Roller follower
		Oil tpye	SAE 15/W40 oil at 80degC
		Injection pump	Ticked

The configuration for Cylinder (C1 to C6) sub-model is listed in Table 3.2 below. As explained above, only C1 was configured here, C2 to C6 will automatically use the configurations for C1.

The combustion model used for this simulation is Vibe 2-Zone. This model will calculate two mass average temperatures (burned and unburned zone), so it provides a more accurate prediction of the pollutants (NOx, CO, Soot). Moreover, this model is capable of predicting the knocking characteristics of the engine. Heat release characteristics are defined by start of combustion (SOC), combustion duration (CD), shape parameter m, and parameter a. The parameter 'a' characterizes the completeness of the combustion. For complete combustion, a value of 6.9 is required [10]. To accurately define these parameters, the chart shown in Fig. 3.2 provided by AVL [10] is needed.

According to the AVL-BOOST user guide, for a turbocharged intercooled heavy- duty DI diesel engine at full load, the CD and shape parameter m are 75 Crank angle (CRA) degrees and 0.9 at rated speed, 60 CRA degrees and 1.0 at half-rated speed, respectively.

Table 3.2: Sub-model Cylinder (C1-C6) configuration.

Cylinder	General	Bore	110mm
		Stroke	127mm
		Compression ratio	16
		Con-Rod length	200mm
		Mean crankcase pressure	1bar
		Scavenge model	Perfect mixing
	Initialization	Initial pressure at exhaust valve open	8.5 bar
		Initial temperature at exhaust valve open	1248.24K
		Ratio type	Air/fuel ratio
		Ratio value	14.7
		Combustion products	0.628
	Combustion	Heat release model	Vibe 2-zone
		Fuel mass/cycle	5.7 e-005kg
		Mixture preparation	internal
		Parameter a	6.9
		NOx kinetic multiplier	0.11
		NOx postprocessing multiplier	0.3
		Soot production constant	200
		Soot consumption constant	900
	Heat transfer	Cylinder model	Woschni 1990
		Ports	Zapf
		Piston surface area	13304.64mm^2
		Piston wall temperature	276.85degC
		Cylinder head surface area	9503.31mm^2
		Cylinder head wall temperature	246.85degC
		Liner surface area (piston at TDC)	432mm^2
		Liner wall temperature (Piston at TDC)	176.85degC
		Liner wall temperature (Piston at BDC)	86.86degC
		Combustion system	Direct injection
		Incylinder swirl ratio nD/nM	1.9

The point of 50% mass fraction burned is at 10 CRA degrees after TDC. According to the chart, the location of 50% mass fraction burned after combustion start related to the combustion duration is 0.4. Thus, the start of combustion can be calculated by Eq. 3.1 below:

$$SOC = 720 + (10 - CD \times CRA\,since\,SOC\,related\,to\,CD) \tag{3.1}$$

where CRA since SOC related to CD can be read from Fig. 3.2. The SOC, CD, and shape parameter m used in this model are listed in Table 3.3 below:

Table 3.3: Vibe 2-Zone combustion model configuration.

Engine speed, rpm	700 (Idling)	1100	2200 (Rated)	2640(Maximum)
SOC @ full load, CRA degree	711.9	710.8	706.8	705.7
CD @ full load, CRA degree	55	60	75	81
Shape parameter @ full load, m, (-)	1.04	1	0.9	0.86

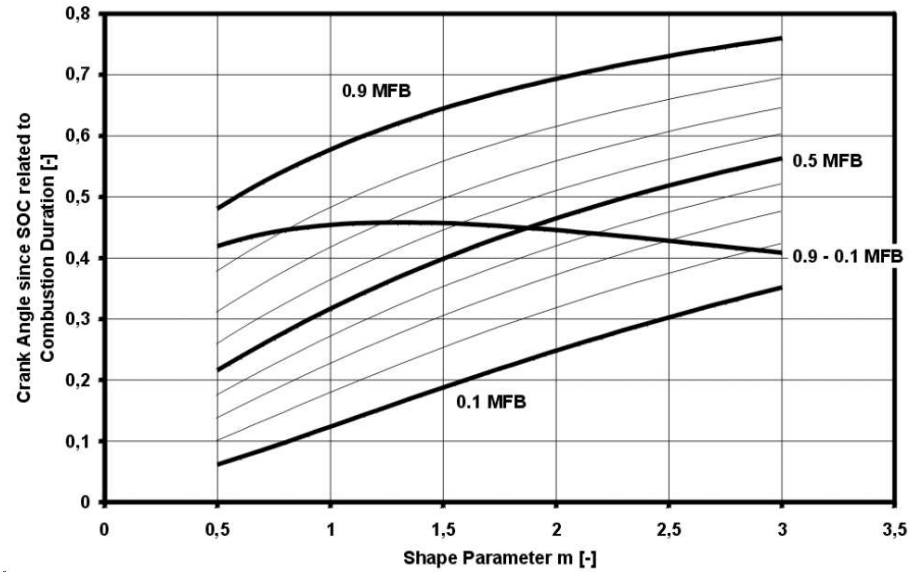

Figure 3.2: Crank angle related to combustion duration.

There are four parameters of the emission models requiring configuration, which are NOx kinetic multiplier, NOx post-processing multiplier, soot production constant, and soot consumption constant. Emission levels of NOx and soot can be calibrated using these four parameters. Fig. 3.3 shows how these four parameters affect the emission levels when the engine model was running at 2400 rpm, 2 bar inlet pressure, and EGR slightly open (10%). It can be seen that NOx level increases as the NOx kinetic, post-processing multipliers increase; soot level increases when the soot production constant increases,

decreases when soot consumption constant increases. Based on the experimental results under the same engine running conditions, a combination of these four parameters was chosen and listed in Table 3.2.

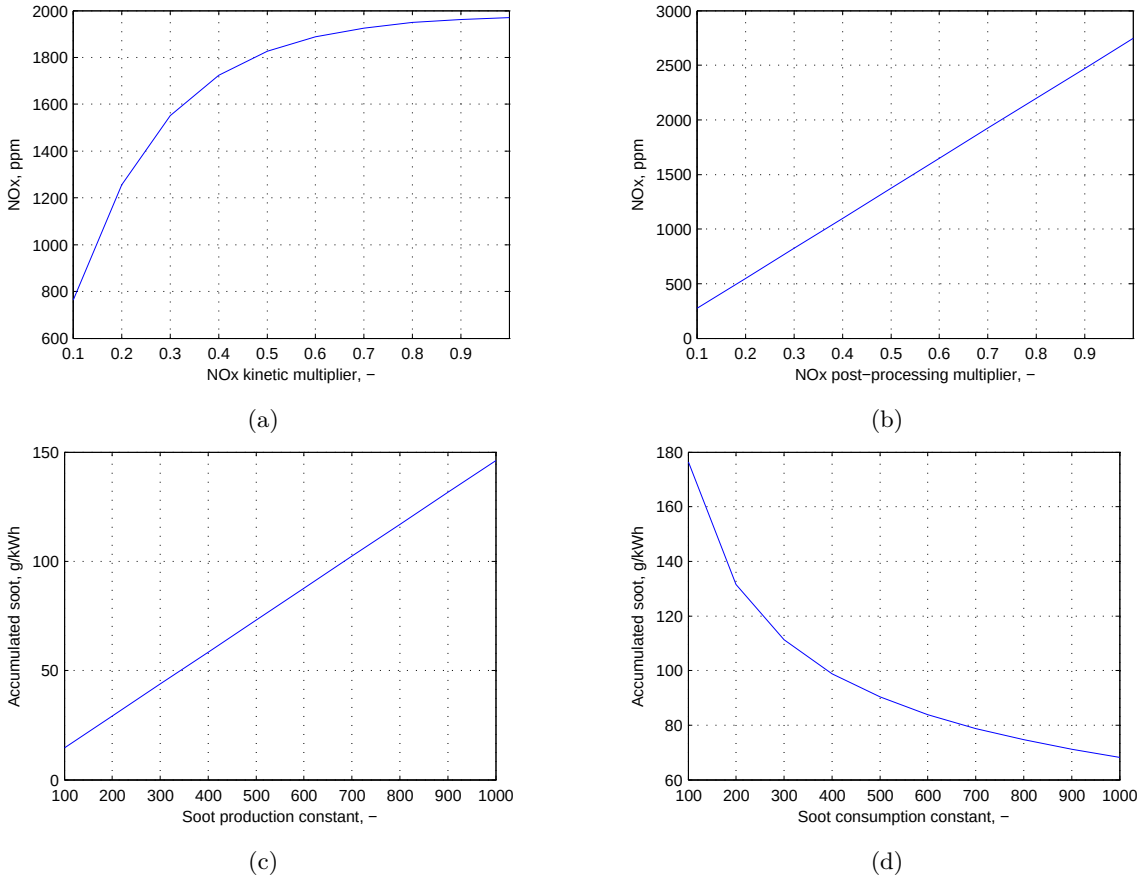

Figure 3.3: Emission model tuning. (a) NOx kinetic multiplier, (b) NOx post-processing multiplier, (c) soot production constant, and (d) soot consumption constant.

A modified Zapf heat transfer model (see Eq. 3.2, Eq. 3.3, and Eq. 3.4 [11]) are used to calculate the heat transfer in the intake and exhaust port.

$$T_d = (T_u - T_w) \cdot e^{\left(-A_w \cdot \frac{\alpha_p}{\dot{m} \cdot c_p}\right)} + T_w \tag{3.2}$$

where α_p denotes the heat transfer coefficient in the port, T_d denotes downstream temperature, T_u denotes upstream temperature, T_w denotes port wall temperature, A_w denotes port surface area, $\dot{m}$ denotes mass flow rate, c_p denotes specific heat at constant pressure.

The heat transfer coefficient, α_p, depends on the direction of the air flow. For air flowing out of the cylinder, Eq. 3.3 [11]is used; for air flowing into the cylinder, Eq. 3.4 [11]is used.

$$\alpha_p = \left[C_4 + C_5 \cdot T_u - C_6 \cdot T_u^2\right] \cdot T_u^{0.44} \cdot \dot{m}^{0.5} \cdot d_{vi}^{-1.5} \cdot \left[1 - 0.797 \cdot \frac{h_v}{d_{vi}}\right] \tag{3.3}$$

$$\alpha_p = \left[C_7 + C_8 \cdot T_u - C_9 \cdot T_u^2\right] \cdot T_u^{0.33} \cdot \dot{m}^{0.68} \cdot d_{vi}^{-1.68} \cdot \left[1 - 0.765 \cdot \frac{h_v}{d_{vi}}\right] \tag{3.4}$$

where h_v denotes valve lift, d_{vi} denotes inner valve seat diameter. The constants values used are $C_4 = 1.2809$, $C_5 = 7.0451\text{e-}004$, $C_6 = 4.8035\text{e-}007$, $C_7 = 1.5132$, $C_8 = 7.1625\text{e-}004$, $C_9 = 5.3719\text{e-}007$.

The configurations for intake and exhaust ports are listed in Table 3.4. Fig. 3.4 shows the intake valve and exhaust valve lift and flow coefficients. The mass flow rates at the intake and exhaust ports are calculated from the equations for isentropic orifice flow under consideration of the flow efficiencies of the ports determined on the steady state flow test rig. From the energy equation for steady state orifice flow, the equation for the mass flow rates can be calculated from Eq. 3.5 to Eq. 3.8 [11].

$$\frac{dm}{dt} = A_{eff} \cdot p_{o1} \cdot \sqrt{\frac{2}{R_o \cdot T_{o1}}} \cdot \Psi \tag{3.5}$$

where $\frac{dm}{dt}$ denotes mass flow rate, A_{eff} denotes effective flow area, p_{o1} denotes upstream stagnation pressure, T_{o1} denotes upstream stagnation temperature, R_o denotes gas constant.

For subsonic flow,

$$\Psi = \sqrt{\frac{\kappa}{\kappa - 1} \cdot \left[\left(\frac{p_2}{p_{o1}}\right)^{\frac{2}{\kappa}} - \left(\frac{p_2}{p_{o1}}\right)^{\frac{\kappa+1}{\kappa}}\right]} \tag{3.6}$$

where p_2 denotes downstream static pressure, κ denotes ratio of specific heats.

and for sonic flow,

$$\Psi = \Psi_{max} = \left(\frac{2}{\kappa + 1}\right)^{\frac{1}{\kappa - 1}} \cdot \sqrt{\frac{\kappa}{\kappa + 1}} \tag{3.7}$$

The actual effective flow area can be determined from measured flow coefficients $\mu\sigma$:

$$A_{eff} = \mu\sigma \cdot \frac{d_{vi}^2 \cdot \pi}{4} \tag{3.8}$$

where $\mu\sigma$ denotes flow coefficient of the port, d_{vi} denotes inner valve seat diameter (reference diameter).

The flow coefficient varies with valve lift and represents the ratio between the actual measured mass flow rate at a certain pressure difference and the theoretical isentropic

mass flow rate for the same boundary conditions. The flow coefficient is related to the cross section area of the attached pipe [11].

The valves timing and lift were calculated from the cam-lobe profiles provided by Caterpillar. However, due to the rocker arm specification is unknown, simulations were carried out to find out the optimal valve lift using the valve opening and closing shift. The values of the shifts shown in Table 3.4 are the optimal values found based on the simulation results (see Fig. 3.5). Results show that 7 deg is the optimal value of intake valve opening shift and 10 deg is the optimal value of exhaust valve opening shift. The closing shift has to be the same as opening shift.

Table 3.4: Sub-model Valve ports configuration.

	Intake port (pipe 7)	Exhaust port (pipe 13)
Surface area	2513.27mm^2	1452.2mm^2
Wall temperature	246.85degC	246.85degc
Inner valve seat diameter	37mm	40mm
Valve clearance	0.38mm	0.64
Scalling factor for effective flow area	1.1	0.55
Valve opening	310deg	82deg
Cam length	298deg	336deg
Valve opening shift	7deg	10deg
Valve closing shift	7deg	10deg

3.1.3 ECU sub-model configuration

A fuelling map needs to be defined in the ECU sub-model. Ideally, the fuelling map should be set as the same as the fuelling map used on the Caterpillar 3126B engine. Due to difficulties in getting access to the ECU settings of the engine, the fuelling map used for the engine model has to be estimated based on the air-intake behaviour of the Caterpillar 3126B engine. Inevitably, this will cause performance differences between the engine model and the real engine. But the error can be minimized to an acceptable level by carefully tuning of the map.

In a petrol engine, because the fuel is premixed with the air, a relatively precise stoichiometric air/fuel ratio around 14.7 has to be maintained under all engine working conditions to ensure a satisfied combustion condition critical to the performance and emissions of petrol engines. If the fuel/air mixture is not mixed at this ratio, either the combustion will not be complete, or the emissions will be high. For this reason, the fuel injection amount is calculated based on the intake air mass rate provided by an air mass meter

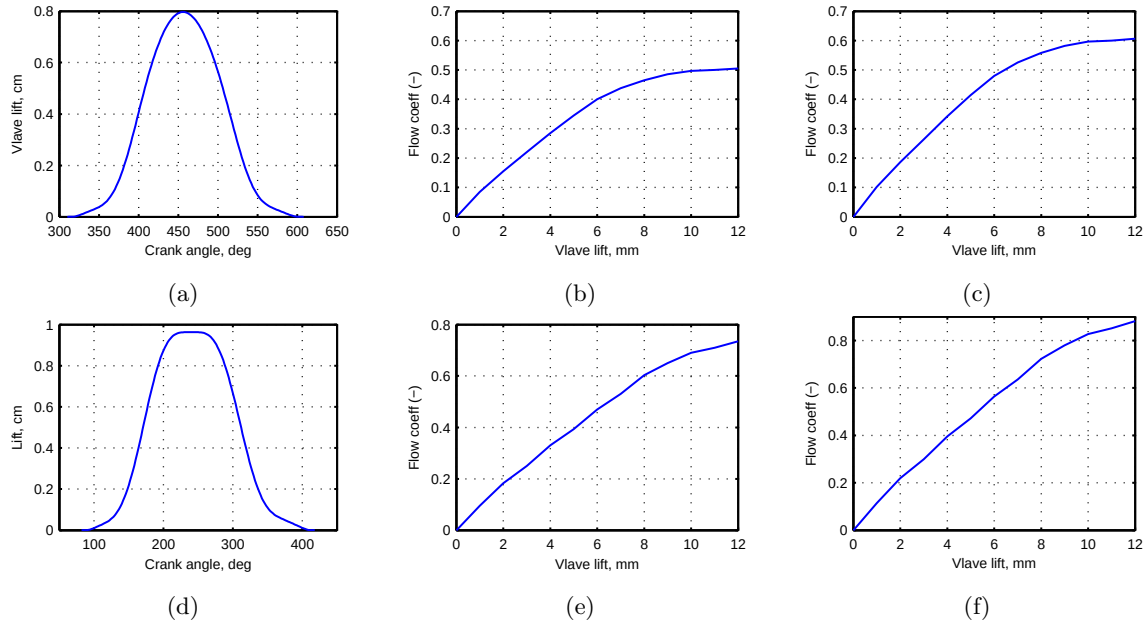

Figure 3.4: Valves lifts and coefficients. (a) intake valve lift, (b) intake valve flow coefficient, pressure ratio* less than 1, (c) intake valve flow coefficient, pressure ratio greater than 1, (d) exhaust valve lift, (e) exhaust valve flow coefficient, pressure ratio less than 1, (f) exhaust valve flow coefficient, pressure ratio greater than 1. * Pressure ratio less than 1 for flow into the cylinder, pressure ratio greater than 1 for flow out of the cylinder.

installed in all petrol engines. The throttle changes the air mass flow rate, and the fuel injection varies with it accordingly.

In a direct injection diesel engine like the Caterpillar 3126B engine, there is no throttle that changes the air mass flow rate, and the fuel injection does not depend on the air mass flow rate, but directly responds to driver demand (controlled by acceleration pedal). Moreover, the fuel is injected separately slightly before the TDC at the very end of the compression stroke. This characteristic makes diesel engines capable of working in a much wider air/fuel ratio range (12 to 140) compared to petrol engines. When idling or cruising at high speed, the air/fuel ratio can be as high as 140, which is 10 times the stoichiometric ratio. When the engine is working under high load or acceleration, the ratio will drop to a normal level: around 15. This is one of the reasons diesel engines have much more efficient fuel consumption in comparison to petrol engines.

As explained above, the fuel injection in diesel engines has to be predefined as a fuelling map. The fuelling map is actually a two-dimensional look-up table with two inputs (engine speed, load) and one output (injected fuel amount per cycle). This map will decide how much fuel will be injected per cycle at any given engine speed and load. Usually, the air/fuel ratio in a diesel engine will not be allowed to drop below 12; hence there is a

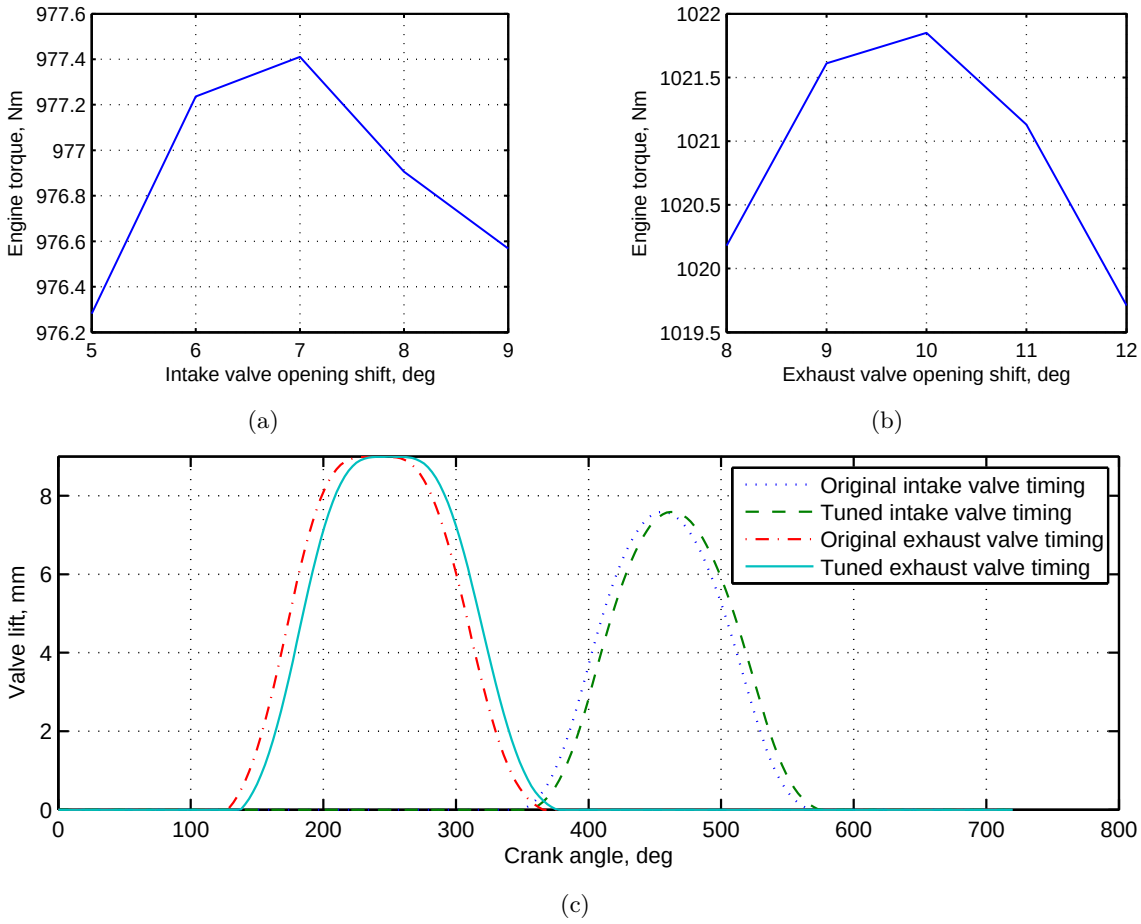

Figure 3.5: Intake and exhaust valve timing tuning. (a) Engine torque against intake valve opening shift, (b) engine torque against exhaust valve opening shift, (c) comparison between original valve timing and tuned.

function built in the ECU limiting the air/fuel ratio above 12.

To build the fuelling map required by this engine model, firstly the air intake behaviour of the engine without either the turbocharger or EGR valve has to be studied. A simplified model has been built in AVL-BOOST (see Fig. 3.6). Using this model, the air mass naturally sucked into each cylinder per cycle at different engine speeds can be investigated. Because we are not going to run this engine model at any engine speed below 500 rpm, only air intake behaviour during 500 rpm and 2640 rpm was studied. It can be seen in Fig. 3.7 a that the air intake starts from about 1.188g per cycle at 500 rpm, reaches its highest level 1.238g at around 1000rpm, and drops slowly to 0.9013g at 2640rpm. Due to the engine speed limit of this engine of 2640 rpm, beyond this engine speed, the air intake amount has been set to 0.

The fuelling map will be developed based on this air intake curve. At first, the stoichiometric fuel injection curve was derived using the Eq. 3.9.

$$F_s = \frac{A_n}{stoichiometric\,ratio} \tag{3.9}$$

where F_s and A_n denote the stoichiometric fuel mass per cycle and nature inspired air mass per cycle respectively, $stoichiometric\,ratio$ is 14.7.

The fuel injection amount not only depends on engine speed, but also depends on throttle position (load demand). Fig. 3.7 b shows that the stoichiometric fuel injection curve overlaps the fuel injection curve at half-load. This is because it is assumed that at half-throttle position, the amount of fuel injected is equal to the stoichiometric value. The figure also shows that at 0.1, 0.25, 0.75, and full throttle position, the amount of fuel injected is set to 0.2, 0.5, 1.5, and 2 times the stoichiometric value, respectively. When the injected fuel volume exceeds the stoichiometric value, boost pressure is required. In the next section, the configurations for the VGT

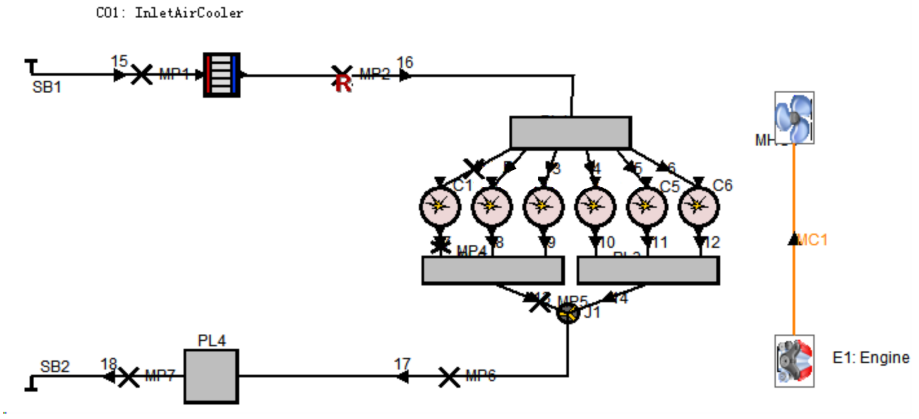

Figure 3.6: Simplified model created in AVL-BOOST for studying the air intake behaviour of the engine without a turbocharger and EGR valve.

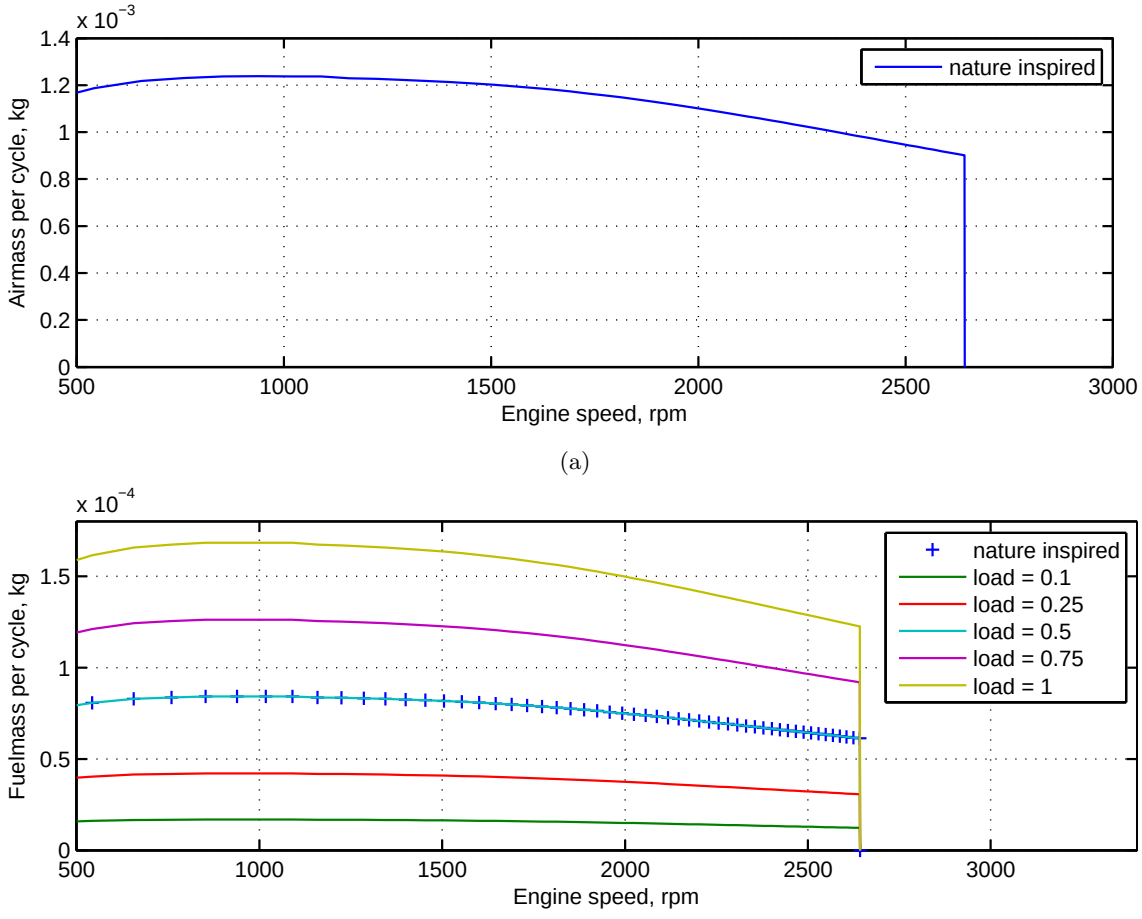

(a)

(b)

Figure 3.7: Air mass and fuel mass entered each cylinder at each cycle at different engine speeds. (a) Air mass naturally sucked into the cylinder, (b) fuelling map developed for different loads.

3.1.4 VGT & EGR sub-model configuration

The VGT sub-model is configured using the 'full model' option. Moment of inertia of this turbo is set as 2e-005 kg.m^2, and initial speed is set as 1e004 rpm. The 'full model' requires a map of the compressor unit and a map of the turbine unit of the turbocharger. The maps have been provided by Garrett®. Fig. 3.8 a and b show the maps of the compressor and turbine used on the engine. It can be seen from the maps that both the compressor and turbine are matched to the operating range of the engine. Based on these maps, the VGT sub-model of the engine model can be configured accordingly. Data points have been carefully taken from these two maps and these data points have been used to created the maps required by the VGT sub-model. Fig. 3.9 shows the compressor map generated in the VGT sub-model based on the Garrett®C117 compressor map. Fig. 3.10 to 3.12 show the turbine maps generated in the VGT sub-model based on the Garrett® GT3782VA turbine at different positions. It can be seen that the maximum corrected turbine mass flow at vanes closed position (VGT position = 0) is about 0.1 kg/s which is about 1/3 of the corrected turbine mass flow at vanes fully open position (VGT position = 1).

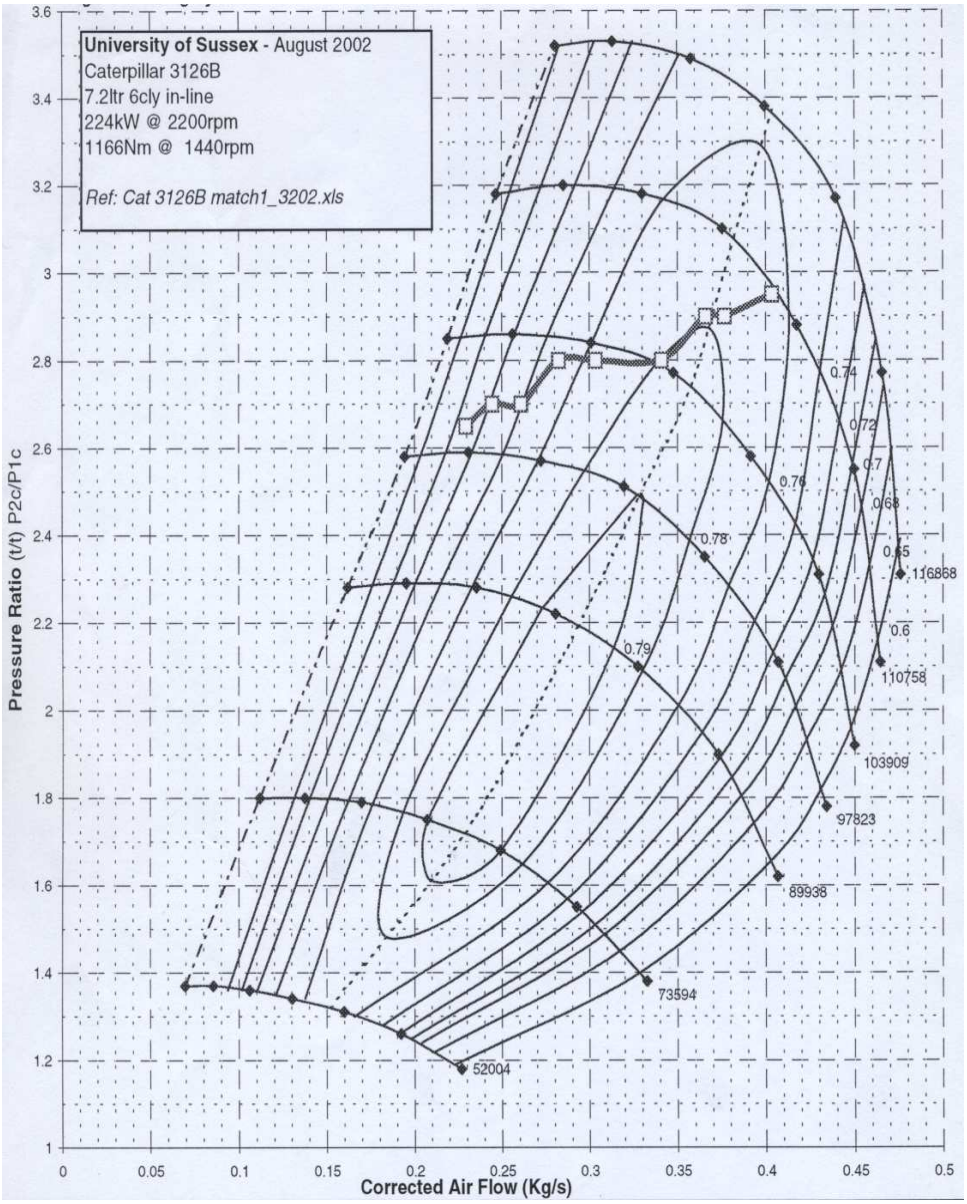

(a)

Figure 3.8: OEM turbocharger maps. (a) Garrett® 82mm 52 trim 72 A/R C117 compressor map, (b) Garrett® GT3782VA 84 trim *090 A/R vanes fully open. (Please note: this document contains proprietary information, and such information may not be disclosed to others for any purpose, or used for manufacturing without written permission from Honeywell Inc.)

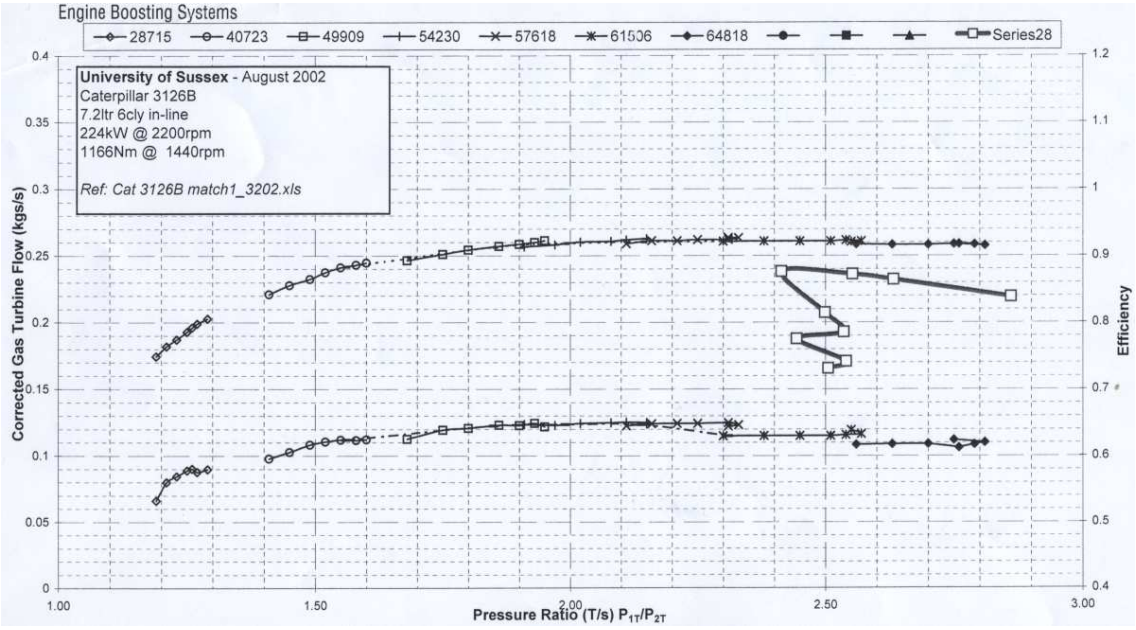

(b)

Figure 3.8: (continued)

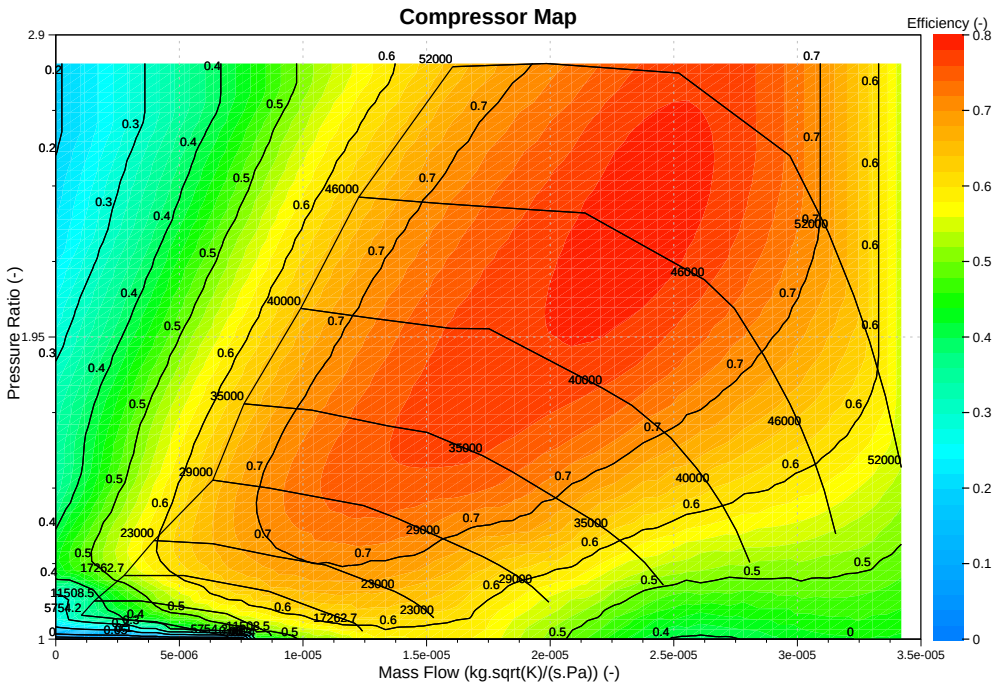

Figure 3.9: Compressor map created in the VGT sub-model based on the Garrett®C117 compressor map.

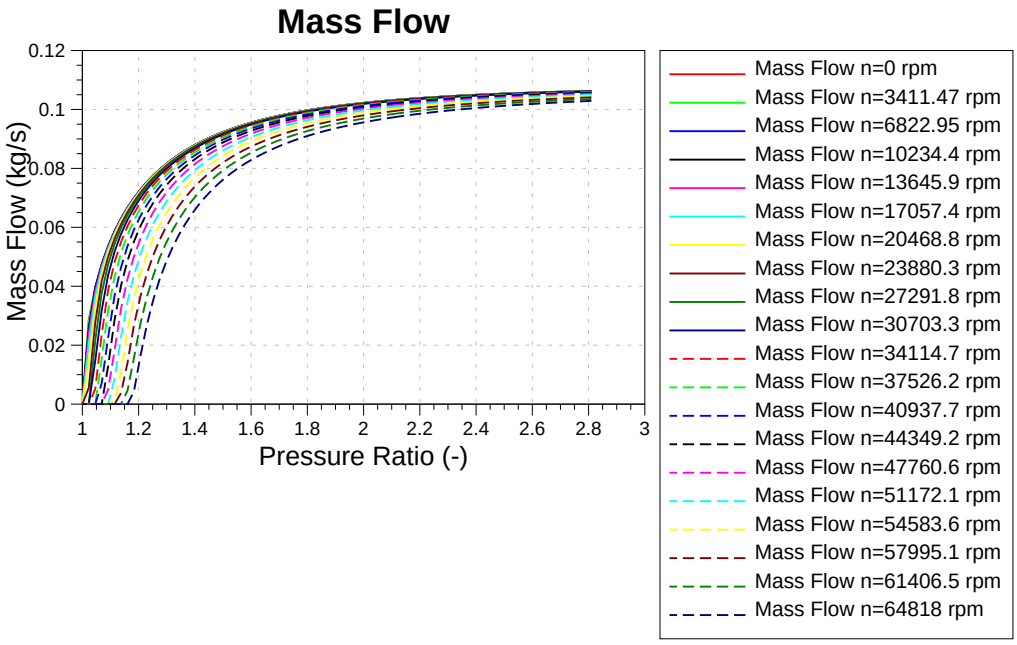

(a)

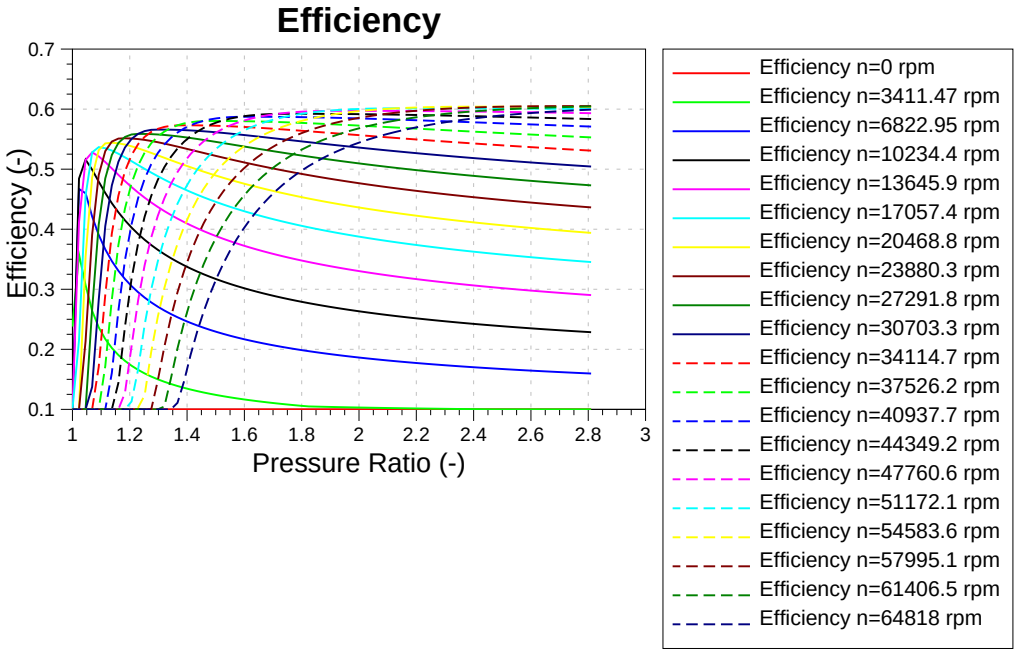

(b)

Figure 3.10: Turbine maps generated in the VGT sub-model based on the Garrett® GT3782VA turbine, vanes position = 0. (a) Corrected mass flow plotted against pressure ratio at different corrected speeds n, (b) efficiency plotted against pressure ratio at different corrected speeds n.

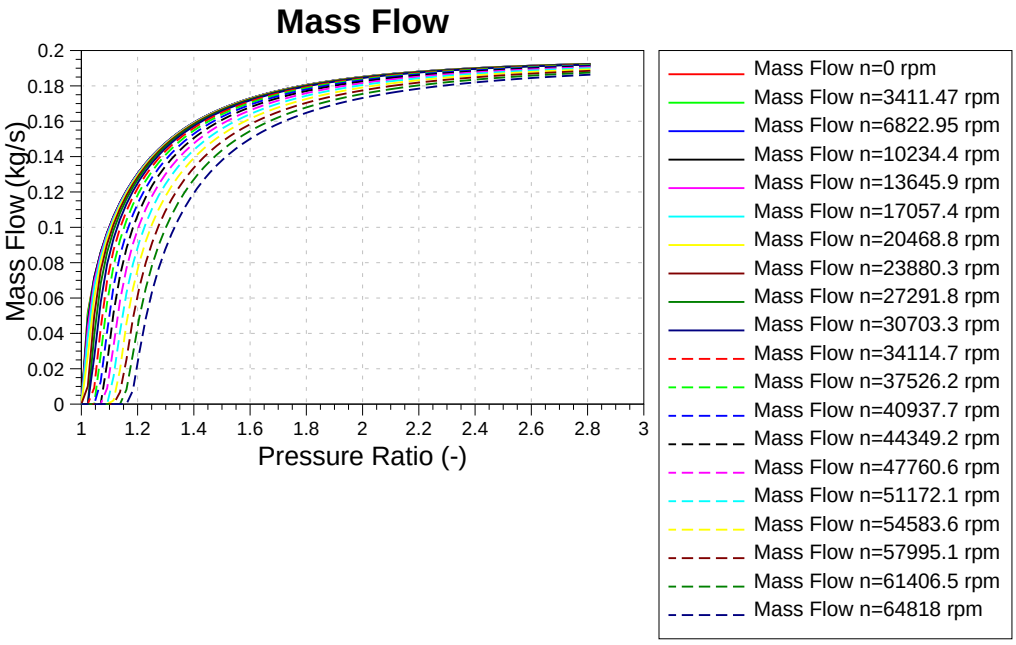

(a)

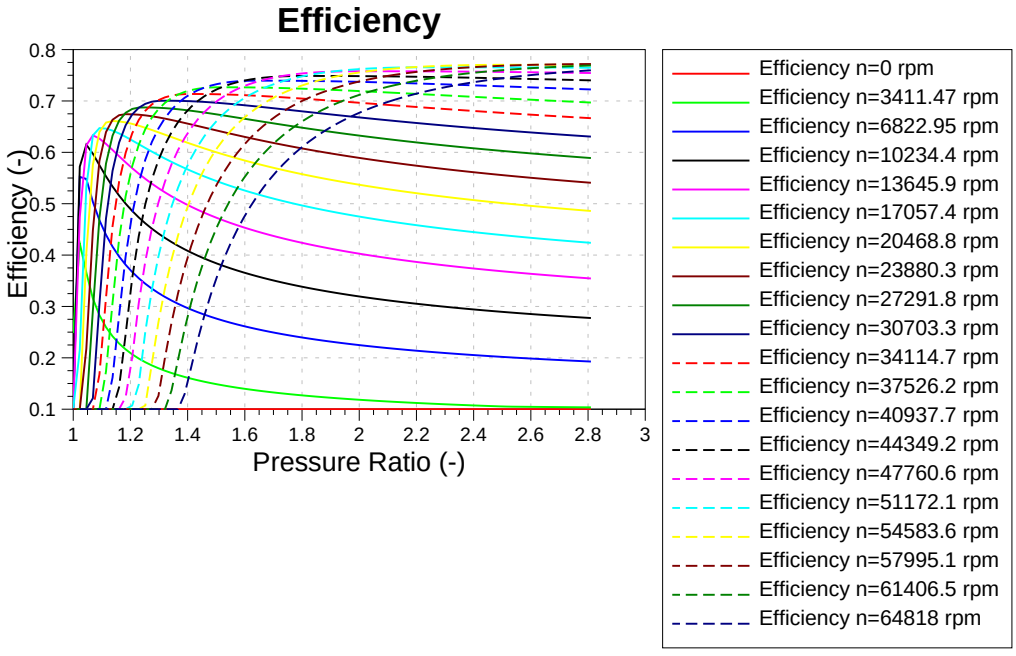

(b)

Figure 3.11: Turbine maps generated in the VGT sub-model based on the Garrett® GT3782VA turbine, vanes position = 0.5. (a) Corrected mass flow plotted against pressure ratio at different corrected speeds n, (b) efficiency plotted against pressure ratio at different corrected speeds n.

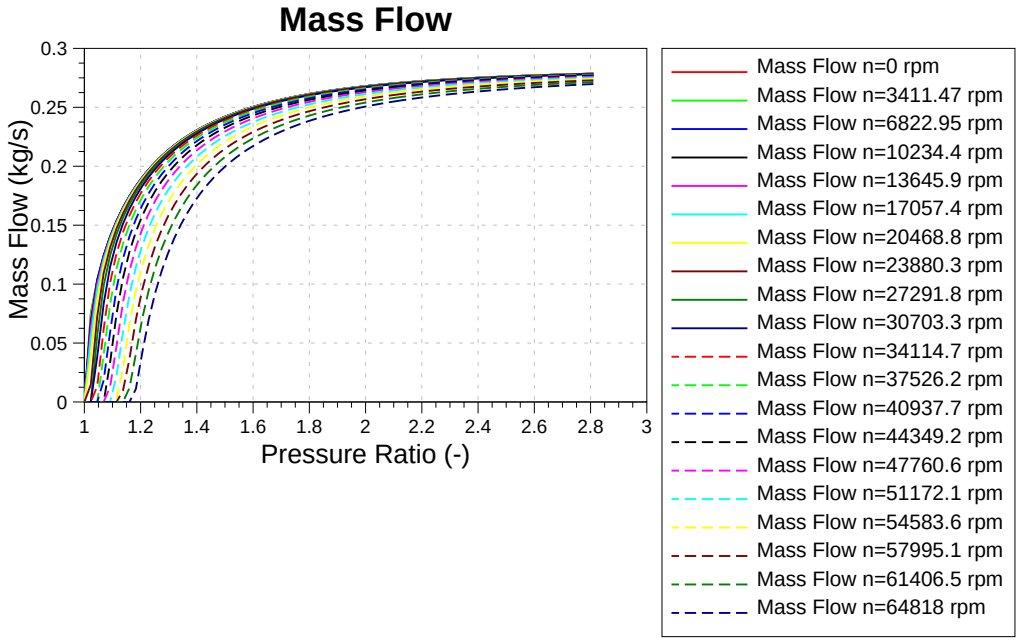

(a)

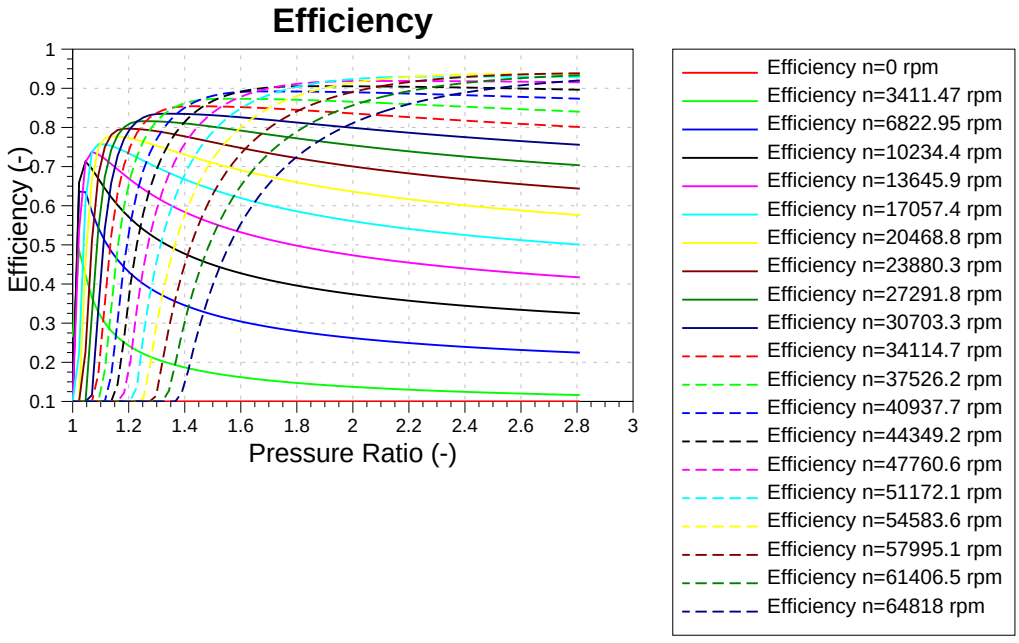

(b)

Figure 3.12: Turbine maps generated in the VGT sub-model based on the Garrett® GT3782VA turbine, vanes position = 1. (a) Corrected mass flow plotted against pressure ratio at different corrected speeds n, (b) efficiency plotted against pressure ratio at different corrected speeds n.

3.2 Model Validation

The engine model was validated against the Caterpillar 3126B engine at various engine running conditions in order to assess the differences between the engine model and the real engine. For this work, the validation of the engine model does not require that simulation results are exactly the same as experimental results, because the engine model does not replace the real engine completely and it is just a platform which used to develop and validate the controllers before they can be tested in the real engine test. However, the model validation should show that the engine model is robust and reliable and has similar performance and behaviour of the real engine.

In order to acquire the data that can be used to validate the engine model, six sets of experimental tests have been carried out on the test bed (see Table 3.5). During each set of the engine tests, engine speed was fixed as 1000 rpm, 1250 rpm, 1440 rpm, 2000 rpm, and 2400 rpm respectively. At each engine speed, the steady-state readings of inlet pressure, intake air flow, fuelling rate, AFR, engine torque, Soot, and NOx were recorded. These are the parameters used to validate the engine model. Simulations were carried out in steady-state mode in two different manners: 1) based on inlet pressure, 2) based on VGT and EGR positions. The simulation results were compared with the experimental one to validate the engine model.

Table 3.5: Experiments carried out on the Caterpillar 3126B engine test bed to collect the data required for the model validation work. '100' means fully open, '0' means fully closed.

	Load, %	VGT position, %	EGR position, %
Set 1	100	100	0
Set 2	100	100	100
Set 3	100	40	0
Set 4	100	40	100
Set 5	75	100	0
Set 6	75	100	100

3.2.1 Model validation based on inlet pressure

In each set of simulations, the load and EGR position of the engine model was set according to the values listed in Table 3.5. At each engine speed, VGT was controlled by a PID controller to achieve the same inlet pressure as it was measured from the engine test bed.

Once the target inlet pressure is achieved and becomes stable, the values of the other 6 parameters were recorded and compared with the experimental results. This validation mainly aims to find out the following:

1. whether the air intake behaviour of the engine model is in good agreement with that of the CAT3126B engine. At the same engine speed, if the inlet pressure is the same, according to the ideal gas law, the air mass flow should be the same, given that the inlet temperature is assumed to be the same;

2. whether the fuel injection map is set correctly compared to the fuel injection of the CAT3126B engine. This can be found out by comparing the mass of fuel injected per second and AFR between the simulation results and the experimental results;

3. whether the emission models for soot and NOx have been calibrated correctly compared to the measurements of soot and NOx from the CAT3126B engine.

Fig. 3.13 shows the model validation based on the same inlet pressures of the AVL-BOOST engine model and CAT3126B engine when the engine is running at 100% load demand, VGT vanes fully open, and the EGR valve under fully closed conditions. It can be seen that the air mass flow (Fig. 3.13 a), fuelling rate (Fig. 3.13 b), and engine torque curves (Fig. 3.13 d) at each engine speed are in good agreement with the experimental results in terms of trend. However, the simulation results of air mass flow and fuelling rate are slightly higher than the experimental results, but this does not cause significant differences in the air fuel ratio comparison (Fig. 3.13 c). The air fuel ratio value at 2400 rpm of the simulation result is higher than that of the experimental results. This is caused by a slightly higher inlet pressure (Fig. 3.13 g) at 2400 rpm compared to the experimental result. The difference of the inlet pressure between the simulation and experiment is because the inlet pressure could not be maintained at the same inlet pressure as the experimental results. It is caused by the performance differences between the VGT sub-model and the real turbocharger installed on the test bed, even the VGT position has been set as low as possible by the PID controller, the inlet pressure still cannot reach the same inlet pressure value of the experimental results. The higher fuelling rate also results in higher engine torque values at each engine speed. The soot mass fraction curve (Fig. 3.13 e) and NOx curve (Fig. 3.13 f) closely match with the experimental results at high, medium and low engine speeds.

Fig. 3.14 shows the model validation based on the same inlet pressures of the AVL-BOOST engine model and CAT3126B engine when the engine is running at 100% load

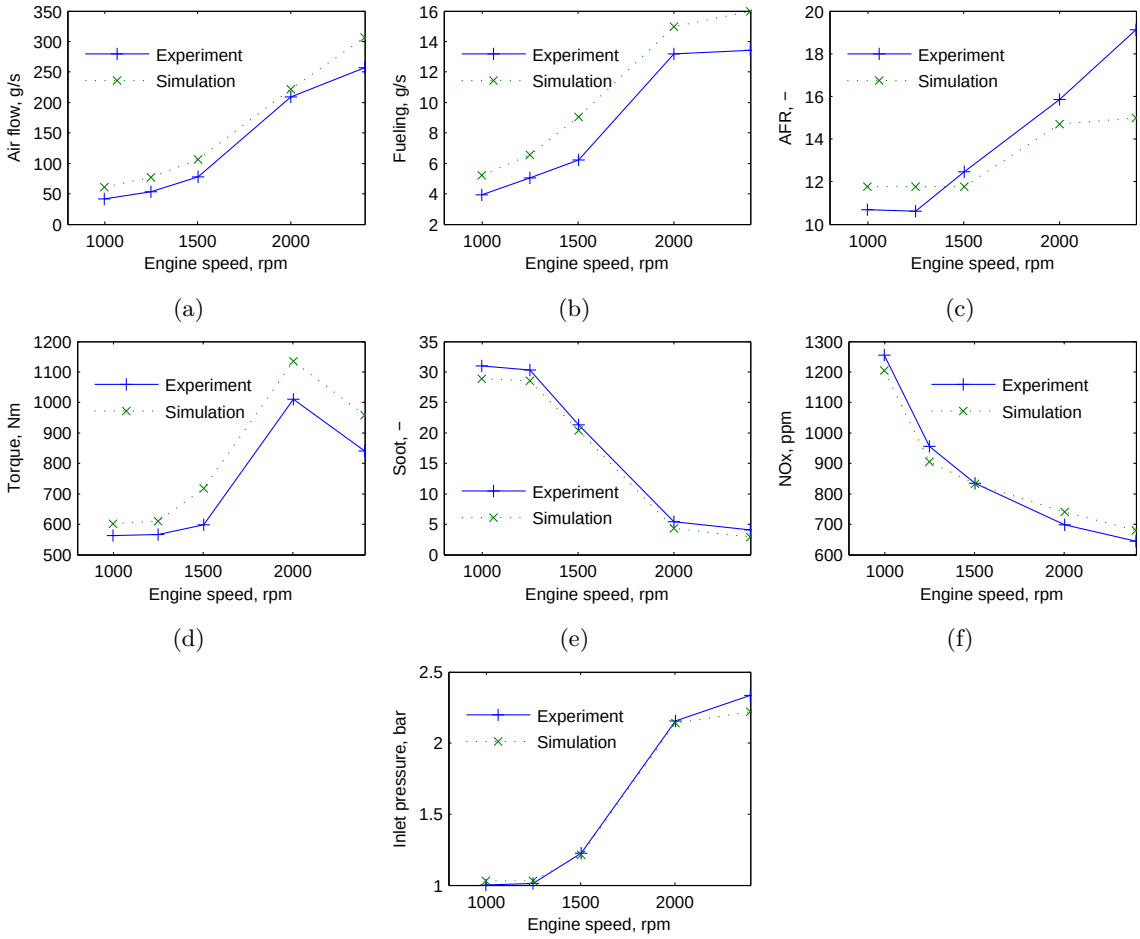

Figure 3.13: Model validation based on inlet pressure. Test bed experiment settings: Load - 100%, VGT - 100%, EGR - 0%, engine model running at the same inlet pressure.

demand, VGT fully open, EGR fully open. At this setting, due to the EGR valve is fully open, the inlet pressure of the experimental results is slightly lower than the inlet pressure of the experimental results when the EGR valve is fully closed (see Fig. 3.14 g) at high engine speed when there is positive pressure differences between the exhaust manifold and inlet manifold. At low engine speed range, because the VGT position is set fully open, there is inadequate energy of the exhaust gas to propel the turbine wheel even when the EGR valve is fully closed. Thus, when the EGR valve is open, the exhaust manifold pressure will affect the inlet manifold pressure which is why the inlet pressure when the EGR valve is fully open is slightly higher than the inlet pressure when the EGR valve is fully closed. The air mass flow (Fig. 3.14 a) and AFR (Fig. 3.14 c) of the simulation results are in good agreement with the air mass flow of the experimental results from 1000 rpm to 2000 rpm. Above 2400 rpm, there is a relatively major difference of the air mass flow and AFR between the simulation results and experimental results. This is caused by the performance difference between the VGT sub-model and the real VGT. However, the trend of the simulation results of fuel injection rate (Fig. 3.14 b), engine torque (Fig. 3.14 d) are in good agreement with the experimental results. The simulation results of soot (Fig. 3.14 e) and NOx (Fig. 3.14 f) are closer to the experimental results of soot and NOx at middle to high engine speeds.

Fig. 3.15 shows the model validation based on the same inlet pressures of the AVL-BOOST engine model and CAT3126B engine when the engine is running at 100% load demand, VGT 40% open, EGR fully closed. Because of the VGT position on the engine is set at 40% open, the inlet pressure is much higher than the previous two running conditions (see Fig. 3.15 g). At this running condition, it can be seen that the validation results are quite similar to that of the previous validations. The trends of intake air flow (Fig. 3.15 a), fuel injection rate (Fig. 3.15 b), AFR (Fig. 3.15 c), and engine torque (Fig. 3.15 d) are all in good agreement with the experimental results of the engine. But there are trivial differences between the simulation results and the experimental results, mainly due to the differences between the fuel injection settings of the engine model and the real engine. The simulation results of soot are quite close to the experimental results of soot at middle to high engine speeds, but the differences at low engine speeds are relatively large (see Fig. 3.15 e). The simulation results of NOx are the same as the experimental results of NOx at about 1500 rpm, but there are relatively small differences at low engine speeds (see Fig. 3.15 f).

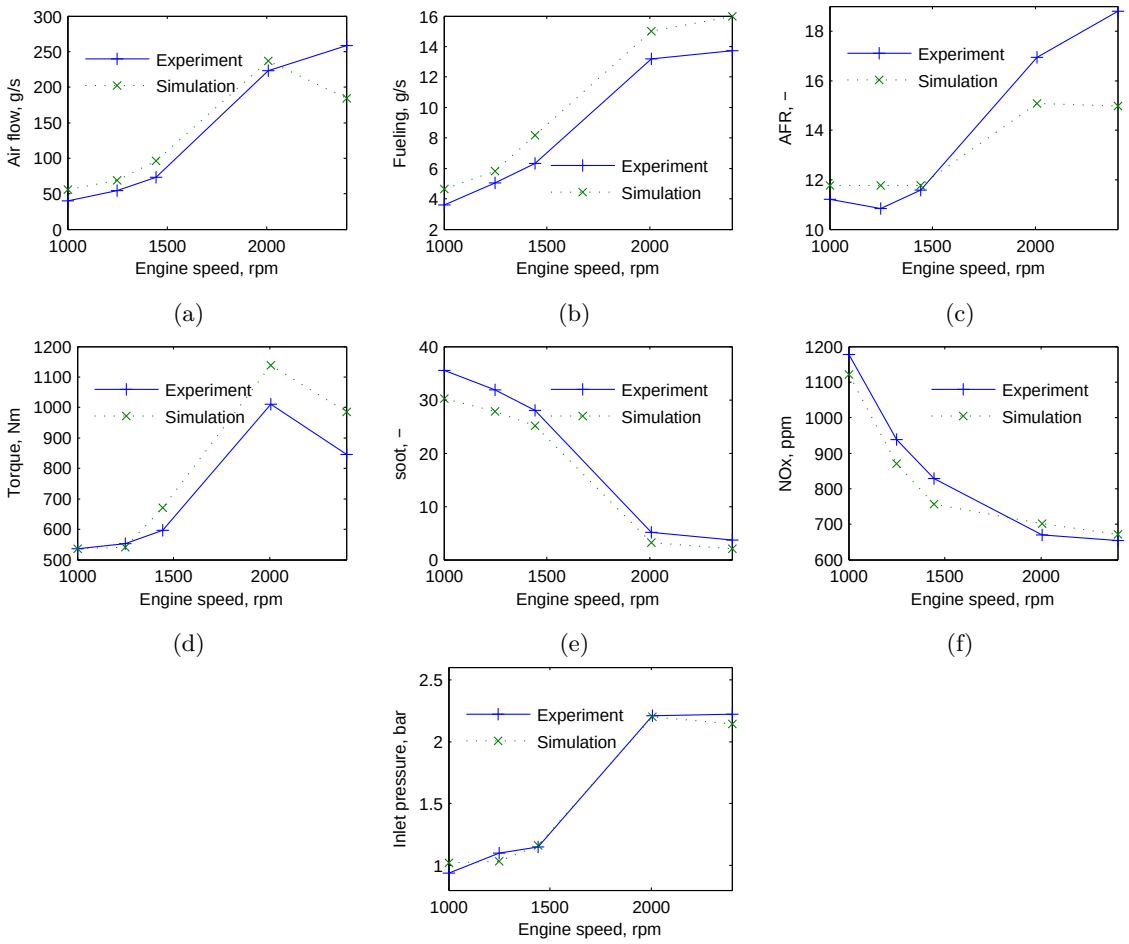

Figure 3.14: Model validation based on inlet pressure. Test bed experiment settings: Load - 100%, VGT - 100%, EGR - 100%, engine model running at the same inlet pressure.

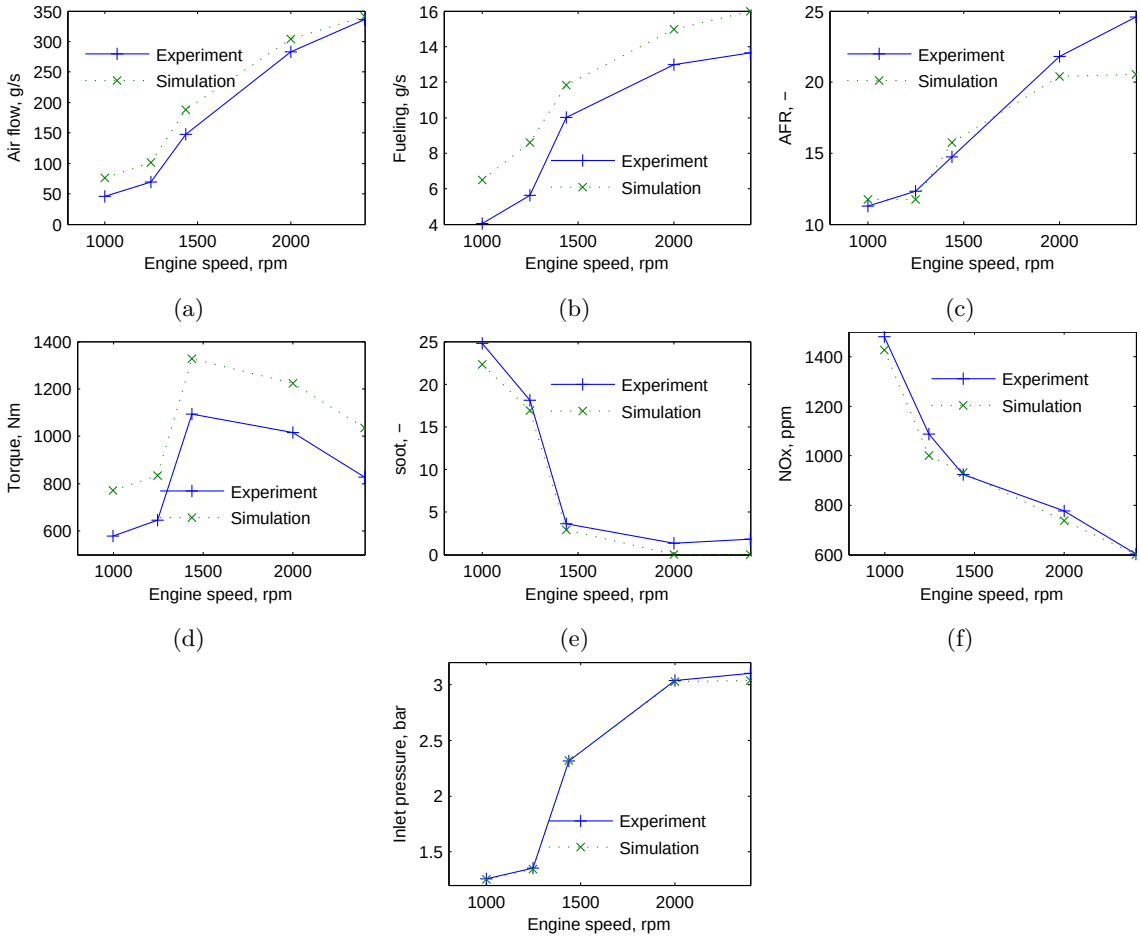

Figure 3.15: Model validation based on inlet pressure. Test bed experiment settings: Load - 100%, VGT - 40%, EGR - 0%, engine model running at the same inlet pressure.

Fig. 3.16 shows the model validation based on the same inlet pressures of the AVL-BOOST engine model and CAT3126B engine when the engine is running at 100% load demand, VGT 40% open, EGR fully open. Because the VGT position is set at 40% open, the position of the EGR valve does not affect the inlet pressure as much as it does the inlet pressure when the VGT position was fully open, especially at low to medium engine speeds (see Fig. 3.16 g). This is because when the VGT position is fully open, the closure of the EGR valve will direct all the exhaust gas to the turbine, and hence the turbine gets more energy and spins faster than it spins when the EGR valve is open. Similar to the validations under previous conditions, the trends of the intake air flow (Fig. 3.16 a), fuel injection rate (Fig. 3.16 b), AFR (Fig. 3.16 c) and engine torque (Fig. 3.16 d) of the simulation results are in good agreement with those of the experimental results measured from the engine. The simulation result of soot (Fig. 3.16 e) is quite close to the experimental result of soot at medium to high engine speeds, and the simulation result of NOx (Fig. 3.16 f) is the same as the experimental measurement between 1250 rpm and 1500 rpm.

Fig. 3.17 and 3.18 show the model validations based on the same inlet pressures of the AVL-BOOST engine model and CAT3126B engine when the engine is running at 75% load demand, VGT 100% open, EGR fully closed, and running at 75% load demand, VGT 100% open, EGR fully open, respectively. It can be seen that both simulation results and experimental results are quite similar between these two running conditions. This is because at 75% load, when the VGT position is fully open, the opening and closing of the EGR valve does not affect the inlet pressure, because there is inadequate positive pressure difference between the exhaust manifold and inlet manifold, and hence there is no exhaust gas flowing back into the inlet manifold even though the EGR valve is open. The simulation results and experimental results of intake air flow (Fig. 3.17 and 3.18 a), fuel injection rate (Fig. 3.17 and 3.18 b), AFR (Fig. 3.17 and 3.18 c) and engine torque (Fig. 3.17 and 3.18 d) are in good agreement at low to medium engine speeds; at high engine speeds from 2000 rpm to 2400 rpm, there is a relatively major difference between the simulation result and experimental result of fuel injection rate and this has caused a relatively major difference between the simulation result and experimental result of AFR at these engine speeds. The simulation result of soot is close to the experimental result of soot at high engine speeds (Fig. 3.17 and 3.18 e), and the simulation result of NOx is close to the experimental result of NOx at medium to high engine speeds (Fig. 3.17 and 3.18 f).

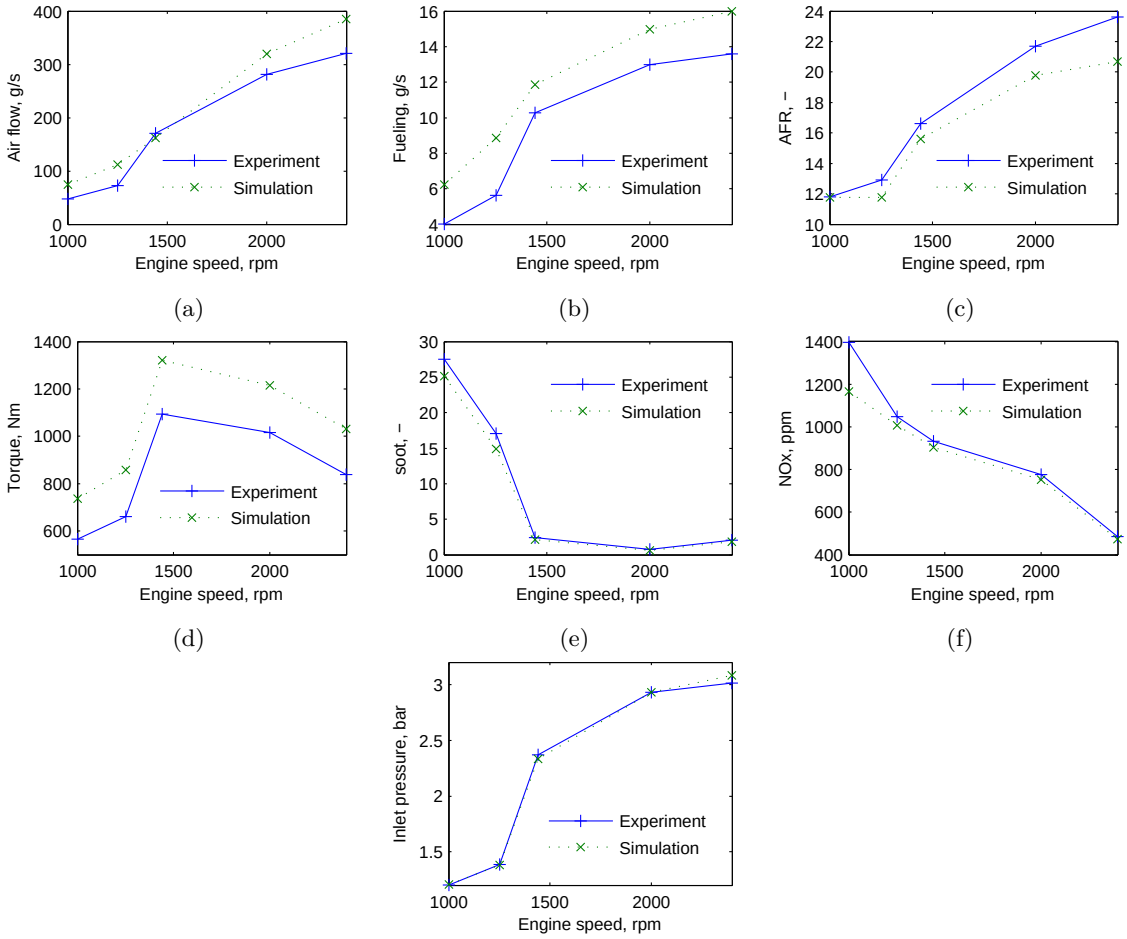

Figure 3.16: Model validation based on inlet pressure. Test bed experiment settings: Load - 100%, VGT - 40%, EGR - 100%, engine model running at the same inlet pressure.

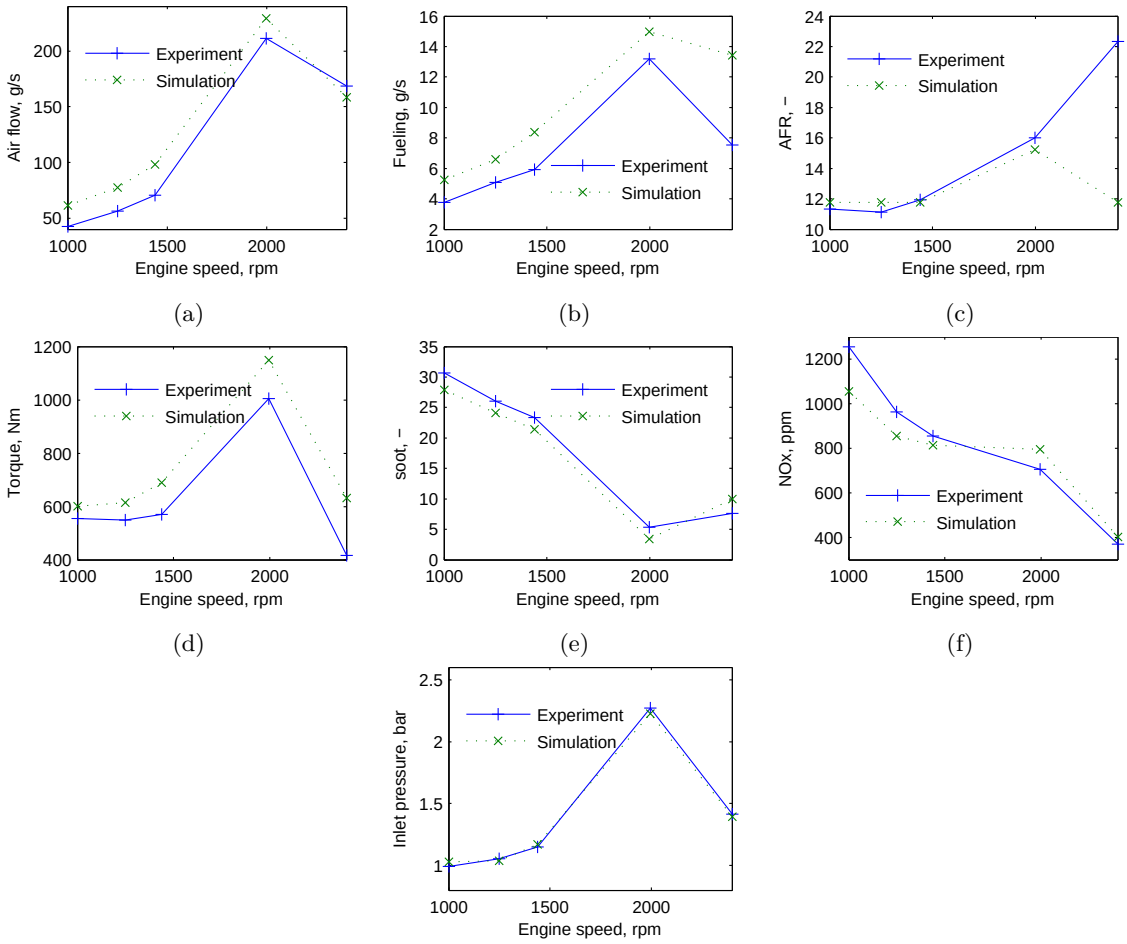

Figure 3.17: Model validation based on inlet pressure. Test bed experiment settings: Load - 75%, VGT - 100%, EGR - 0%, engine model running at the same inlet pressure.

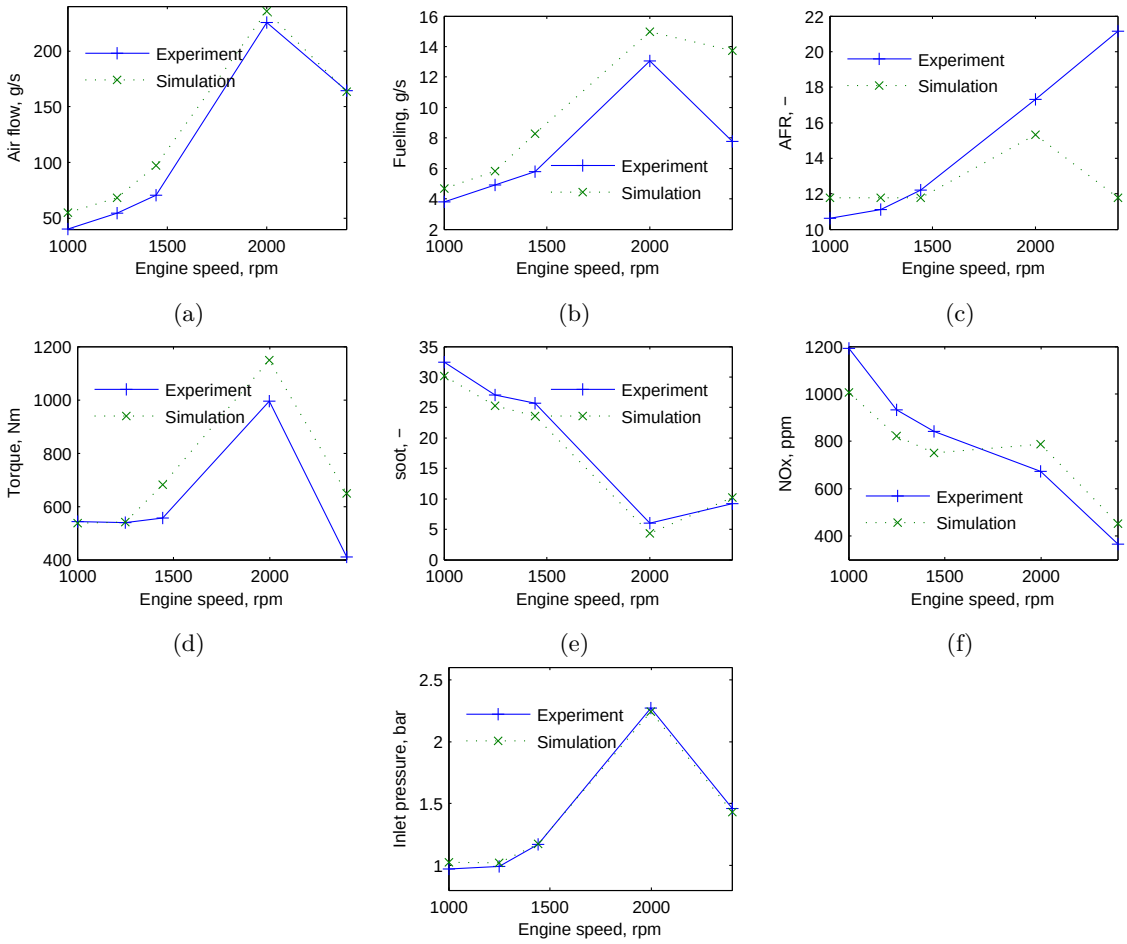

Figure 3.18: Model validation based on inlet pressure. Test bed experiment settings: Load - 75%, VGT - 100%, EGR - 100%, engine model running at the same inlet pressure.

At above running conditions, the simulation results of the engine model are in good agreement with the experimental results collected from the CAT3126B engine test bed at most occasions. This has demonstrated that the air intake behaviour, fuel injection map, and combustion model setup of the transient engine model are appropriated and they are very close to the settings of the real engine. However, there are still differences between the simulation results and the experimental results of the engine because there is still limited information available about the CAT3126B engine. It can be improved by refining the configurations of the engine model with more detailed information of the CAT3126B engine, especially the exact valve timing and lift and the fuel injection map of the ECU. Those details are difficult to cultivate currently. In order to further reduce the differences between the simulation results and the experimental results of the soot and NOx emissions, maps of the soot production constant, soot consumption constant, NOx kinetic multiplier, and NOx post-processing multiplier at different engine running conditions should be developed.

3.2.2 Model validation based on VGT and EGR positions

In each set of simulations, the simulation was carried out using the settings for load demand, VGT position, and EGR position listed in Table 3.5. Inlet pressure, intake air flow, fuelling rate, AFR, engine torque, soot, and NOx were recorded at each engine speed and compared with those measured from the real engine.

Fig. 3.19 shows the validation at 100% load demand, when the VGT vanes are fully open, and when the EGR valve is fully closed. The inlet pressures (Fig. 3.19 g) of the simulation result at each engine speed are slightly higher than that of the experimental result. This is because the VGT sub-model of the engine model tends to produce more pressure compared to the real turbocharger at the same conditions. Similar to that of the steady-state validation, air mass flow (Fig. 3.19 a) and fuelling rate (Fig. 3.19 b) are both slightly higher than that of the experimental result, as well as the torque produced (Fig. 3.19 d), but they follow the same trend as the experimental results. The air fuel ratio curve (Fig. 3.19 c) at medium to high engine speeds is quite close to that of the experimental results. The soot mass fractions (Fig. 3.19 e) at each engine speed of the simulation result are slightly lower than those of the experimental result. The NOx (Fig. 3.19 f) at medium engine speeds is slightly higher than that of the experimental results and slightly lower at low and high engine speeds.

At 100% load demand, VGT vanes are fully open, the EGR valve is fully open (Fig.

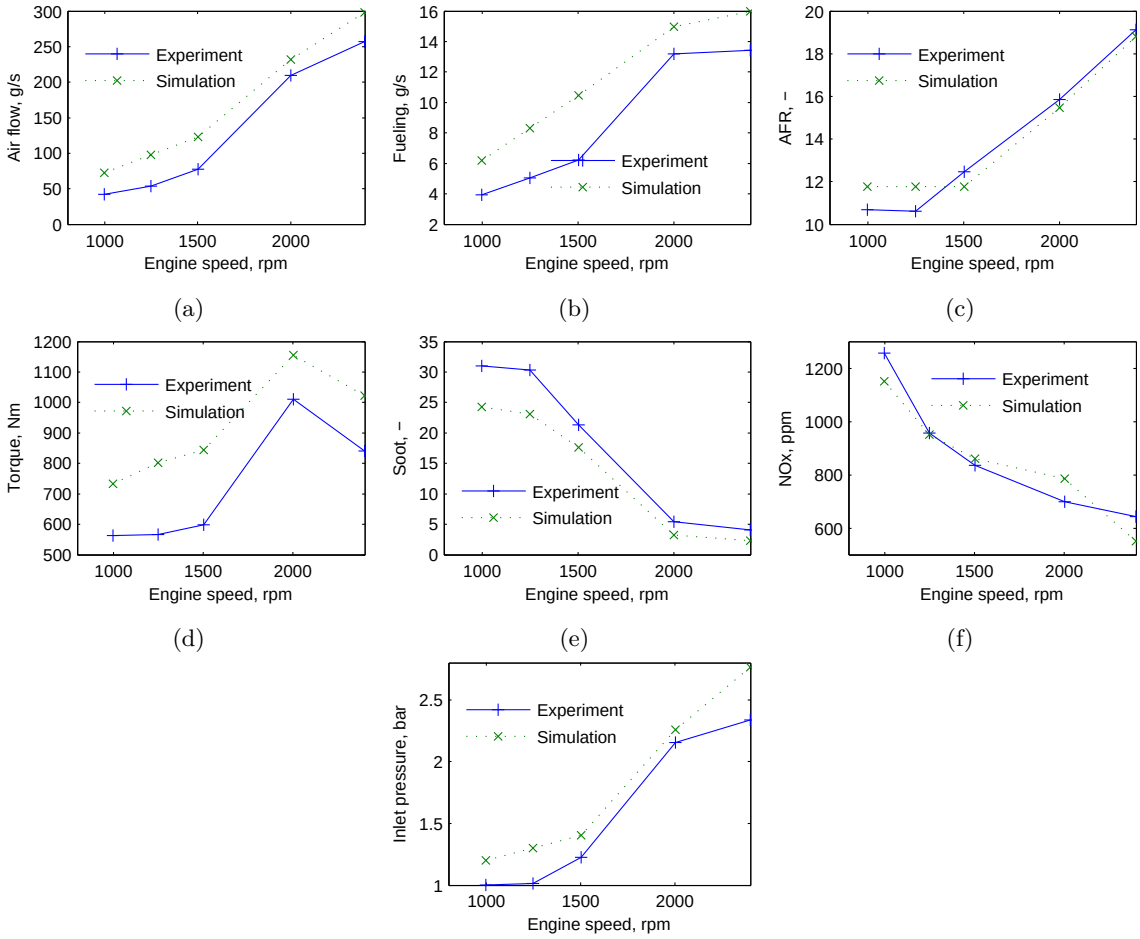

Figure 3.19: Model validation based on VGT and EGR positions. Test bed and engine model settings: Load - 100%, VGT - 100%, EGR - 0%.

3.20), the validation is quite similar to the validation at 100% load demand, when the VGT vanes are fully open, and when the EGR valve is fully closed. This is because the validations of the inlet pressures (Fig. 3.19 g and 3.20 g) under these two conditions are very similar. They are both in good agreement with the experiment results. Similar to the last running condition, the soot mass fractions (Fig. 3.20 e) at each engine speed of the simulation result are slightly lower than those of the experimental result. The NOx (Fig. 3.20 f) at medium engine speeds is slightly higher than that of the experimental results and slightly lower at low and high engine speeds.

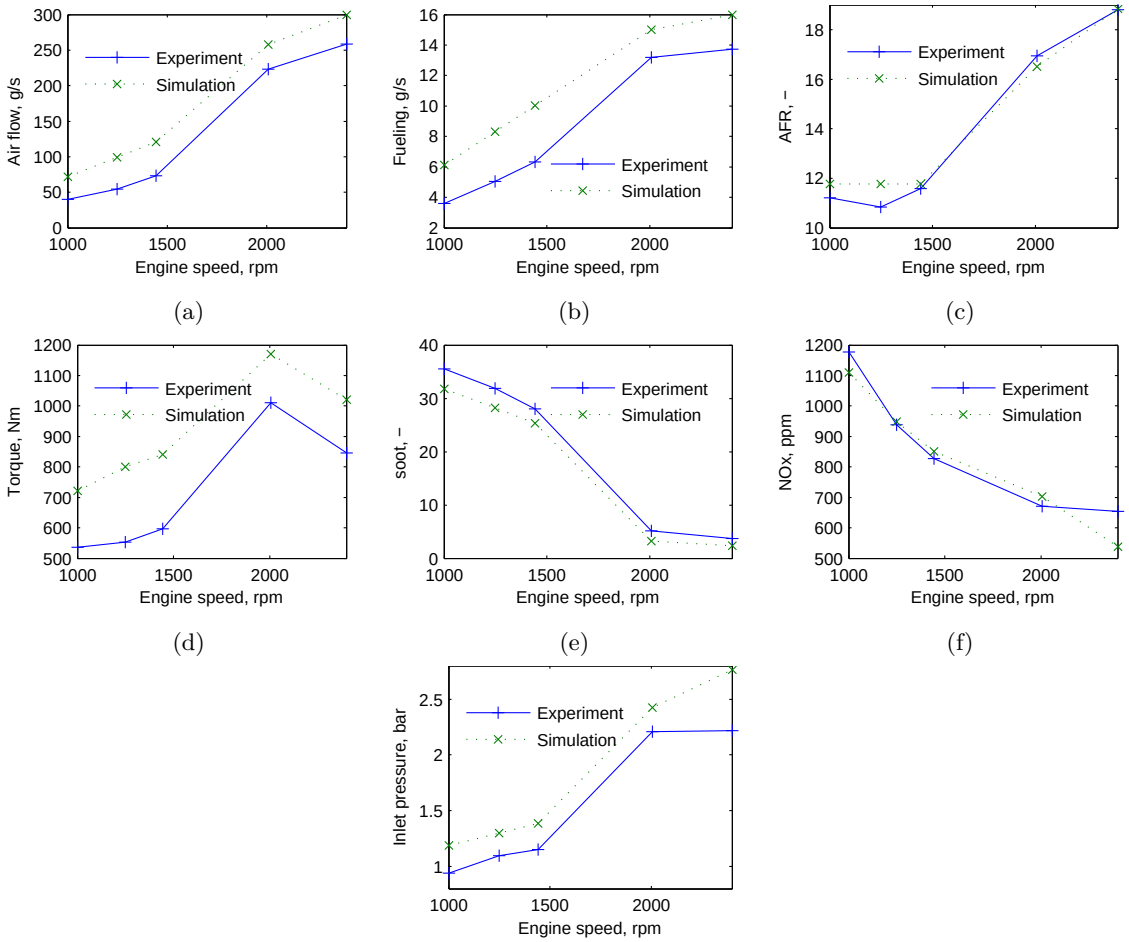

Figure 3.20: Model validation based on VGT and EGR positions.Test bed and engine model settings: Load - 100%, VGT - 100%, EGR - 100%.

Fig. 3.21 and 3.22 shows the validation when the load is 75%, VGT position is 100% with EGR position is fully closed and fully open respectively. The differences between the experimental results of these two running conditions are hardly noticeable and the experimental results also show the highest inlet pressure (Fig. 3.21 g and 3.22 g) is at around 2000 rpm instead of 2400 rpm. This is because compared to full load running

conditions, there is less fuel injected and the exhaust energy is not sufficient to propel the turbine wheel at around 2400 rpm. As a result, the highest intake air flow (Fig. 3.21 a and 3.22 a), fuel injection rate (Fig. 3.21 b and 3.22 b), and engine torque (Fig. 3.21 d and 3.22 d) are all at around 2000 rpm. However, the AFR (Fig. 3.21 c and 3.22 c) of the simulation results is in good agreement with the AFR of the experimental results in terms of trend. Similar to the last running condition, the soot mass fractions (Fig. 3.21 g and 3.22 e) at each engine speed of the simulation result are slightly lower than those of the experimental result. The NOx (Fig. 3.21 g and 3.22 f) at medium engine speeds is slightly higher than that of the experimental results and slightly lower at low and high engine speeds.

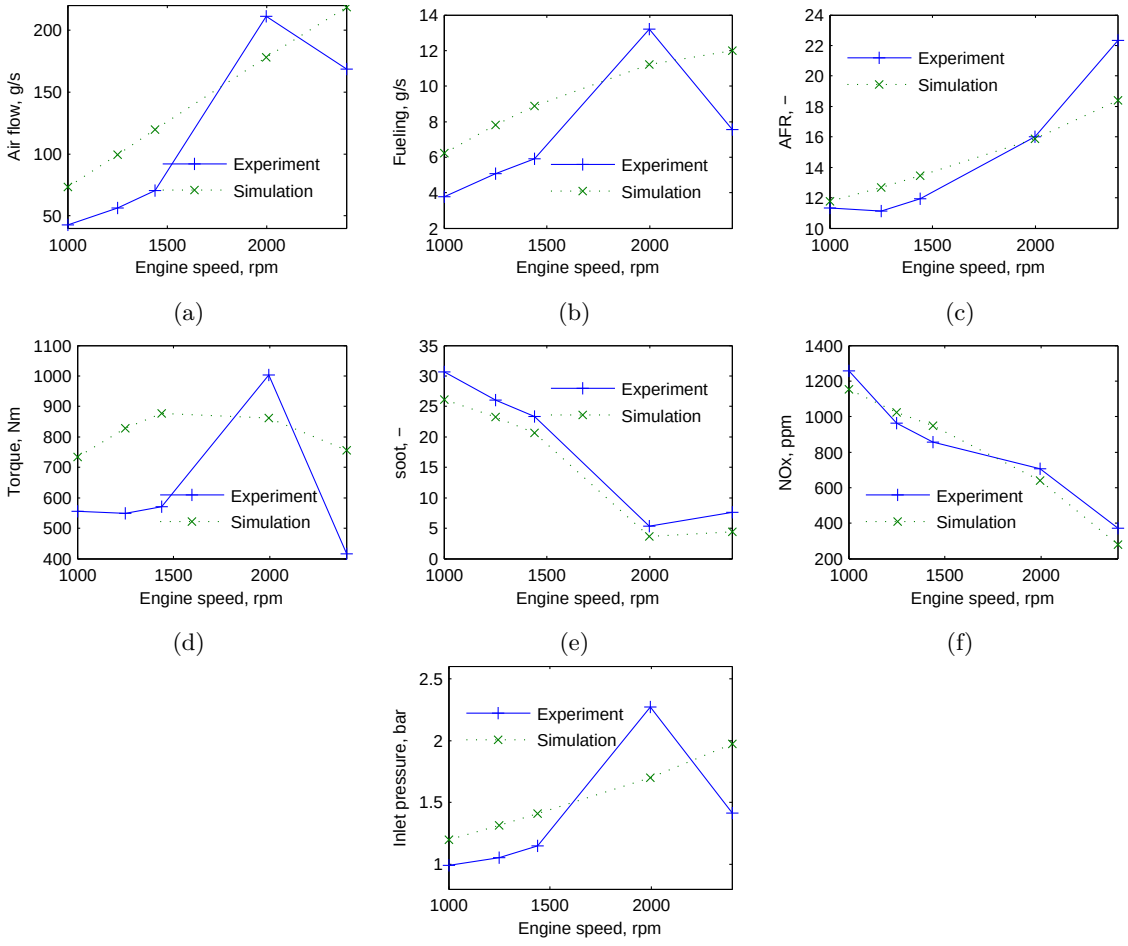

Figure 3.21: Model validation based on VGT and EGR positions.Test bed and engine model settings: Load - 75%, VGT - 100%, EGR - 0%.

The validation based on the VGT and EGR positions shows that when at full load and when the VGT position is fully open, the simulation results are in good agreement with the experimental results. At 75% load, there is a difference between the inlet pressure of

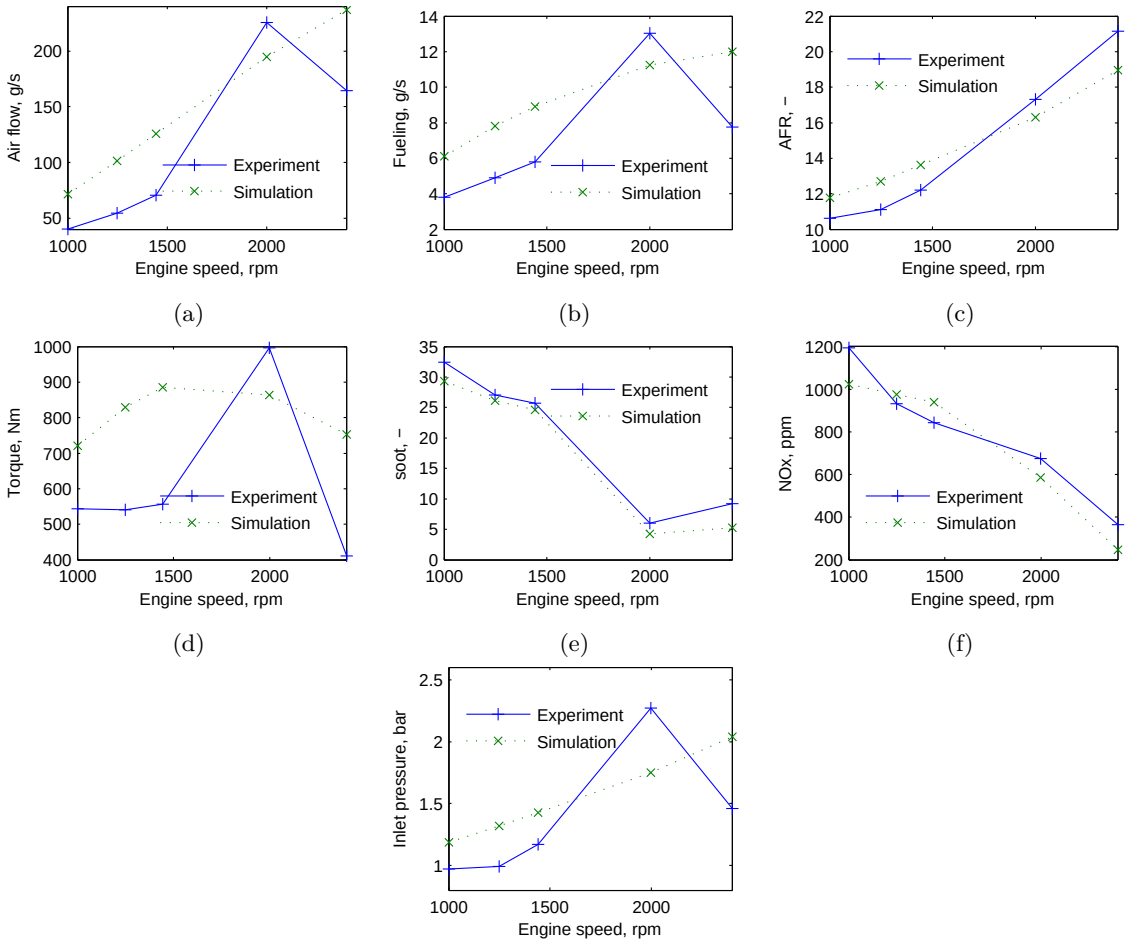

Figure 3.22: Model validation based on VGT and EGR positions.Test bed and engine model settings: Load - 75%, VGT - 100%, EGR - 100%.

the simulation results and experimental results at high engine speeds, mainly due to the performance difference between the VGT sub-model and the real VGT component of the engine. The difference between the inlet pressures has also caused the differences between other parameters such as intake air flow, fuel injection rate, and engine torque. However, the AFR was not affected.

3.3 Chapter Summary and Conclusions

In this chapter, the development of the transient engine model was detailed. The configurations of main sub-models that would largely affect the performance of the engine model are described in detail. These sub-models include engine and cylinders, which include the definition of combustion model, heat release behaviour, and configurations of valve lift and timing and heat transfer, ECU, VGT and EGR. The developed engine model was then validated against the CAT3126B engine. The model was firstly validated by comparing the engine performances and emissions of the engine model and the real engine. Based on the same inlet pressure, the model was also validated by comparing the engine performances and emissions based on the same VGT and EGR positions. The validations show that the engine model is in good agreement with the real engine.

Chapter 4

Diesel Engine Air-path Control

In this chapter, PID controller, fuzzy logic controller, and ANFIS controller for VGT and EGR control were developed and tested under transient running conditions. The performance of the PID controller will be used as a benchmark, so that the performances of the fuzzy logic controller can be compared with the performances of the PID controller.

4.1 PID Control

4.1.1 PID controller development

PID control technique is the most dominating structure of feedback control at present [8]. It is a simple but effective way of keeping process variables as close as possible to desired set-points. In order to compare the proposed fuzzy logic controller with PID controllers, PID controllers for VGT and EGR control have been developed and tested using the AVL-BOOST transient engine model.

Inlet pressure and EGR mass fraction have been selected as process output variables, which will be kept as close as possible to the desired set-points by manipulating the VGT and EGR. Only two terms P and I are used in this work mainly due to the concern that the noise inhabited in the feedback signals will cause oscillations. The performances of the controller that need to be considered include rise time, overshoot, settling time, steady-state error and stability. How each of the three terms affect the control performances is shown in the Table 4.1 below. Table 4.2 shows the tuned coefficients of P and I terms for VGT and EGR control. The structure of the PI controllers developed for VGT and EGR control in this work is shown in Fig. 4.1.

MAP set-points for VGT control are generated by a predefined map that takes engine speed and load demand as input signals; EGR mass fraction set-points for EGR control

Table 4.1: Effects to the control performances of a PID controller by increasing a coefficient independently [87].

Coefficients	Rise time	Overshoot	Settling time	Steady-state error	Stability
P	Decrease	Increase	Small change	Decrease	Degrade
I	Decrease	Increase	Increase	Eliminate	Degrade
D	Minor change	Decrease	Decrease	No effect in theory	Improve if D small

Table 4.2: Tuned coefficients of P and I terms for VGT and EGR controllers.

Coefficients	VGT control	EGR control
P	1	1
I	8	55

are generated by a predefined map, which takes only engine speed as the input signal. The PI controllers for VGT and EGR control then minimize the errors between the feedback signals and set-points by manipulating the VGT vanes and EGR valve.

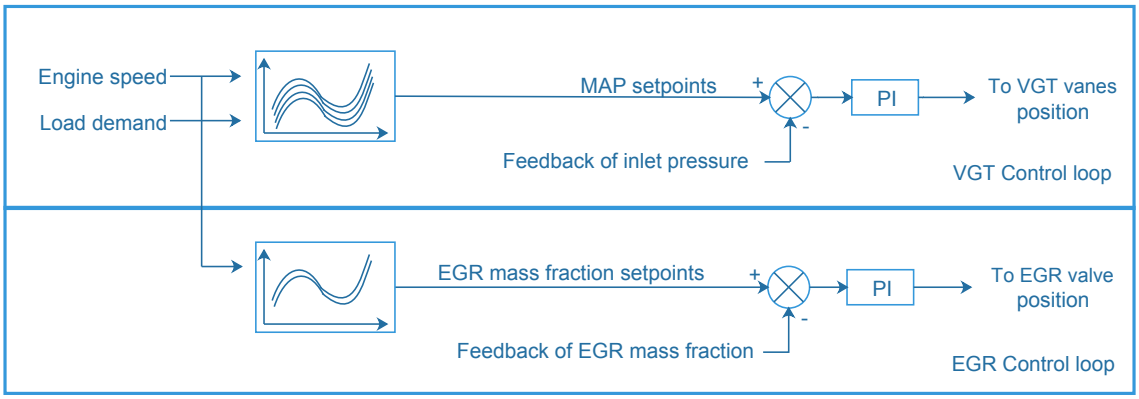

Figure 4.1: PID controller structure.

Fig. 4.2 shows the Simulink model created using Matlab for realizing the PI control. EGR valve will be kept closed at an engine speed below 1400 rpm, at an engine speed above 2200 rpm, or at a load demand greater than 0.5. VGT was controlled dependently; that is VGT will be kept fully open when the EGR valve is open. This is to reduce the interaction between VGT and EGR. These strategies have been reflected by the Simulink model.

Independent control of VGT has also been designed using the Simulink model. In this mode, VGT is controlled by the PID controller regardless of the status of the EGR position. By comparing the VGT-dependent control with Vgt-independent control, the interaction between VGT and EGR can be revealed, which will be discussed in Section

4.1.3.

4.1.2 Set-points generation

In order to generate the required set-points of inlet pressure and EGR mass fraction, investigations of how AFR and EGR mass fraction affect engine performances and emissions have been carried out using the transient engine model.

Fig. 4.3 shows how AFR effect BMEP, brake specific fuel consumption (BSFC), soot and NOx at different engine speeds ranging from low to high. It can be seen that as AFR increasing from about 12 to 15, BMEP increased slightly about 1 bar, BSFC dropped considerably, soot production reduced dramatically, NOx production increased. It can then be concluded that higher AFR can lead to slightly more torque, better fuel consumption, much cleaner exhaust gas, but high NOx level. Therefore a trade-off has to be made. Table. 4.3 shows the set-points of inlet pressure. At these set-points, the AFR would be around 14.9 which is stoichiometric ratio.

Table 4.3: Set-points of inlet pressure.

Engine speed, rpm/Load demand, -	700	2640
0	1	1.15
0.5	1	1.15
1	2	2.15

Fig.4.4 shows how EGR mass fraction affects AFR, in-cylinder temperature, BMEP, BSFC, soot, and NOx at different engine speeds ranging from low to high. It can be seen that as EGR mass fraction increasing from 0 to 16%, AFR decreased from 15 to 13, in-cylinder temperature decreased from 2710 K to 2630 K, BMEP dropped slightly, BSFC increased, soot production increased dramatically, NOx production decreased considerably. Similar to determining the set-points of inlet pressure, a trade-off has to be made. Fig. 4.5 shows the trade-off and set-points of EGR mass fraction at different engine speeds.

4.1.3 Transient PI control test

Transient tests of the PI controllers have been carried out using the transient engine model. The test investigates the responding performance and robustness of the PI controllers.

In transient simulation mode, engine speed is not fixed, but changes depending on the engine torque produced. If the torque produced is greater than the road load torque, engine speed will increase; if the torque produced is the same as the road load torque, the

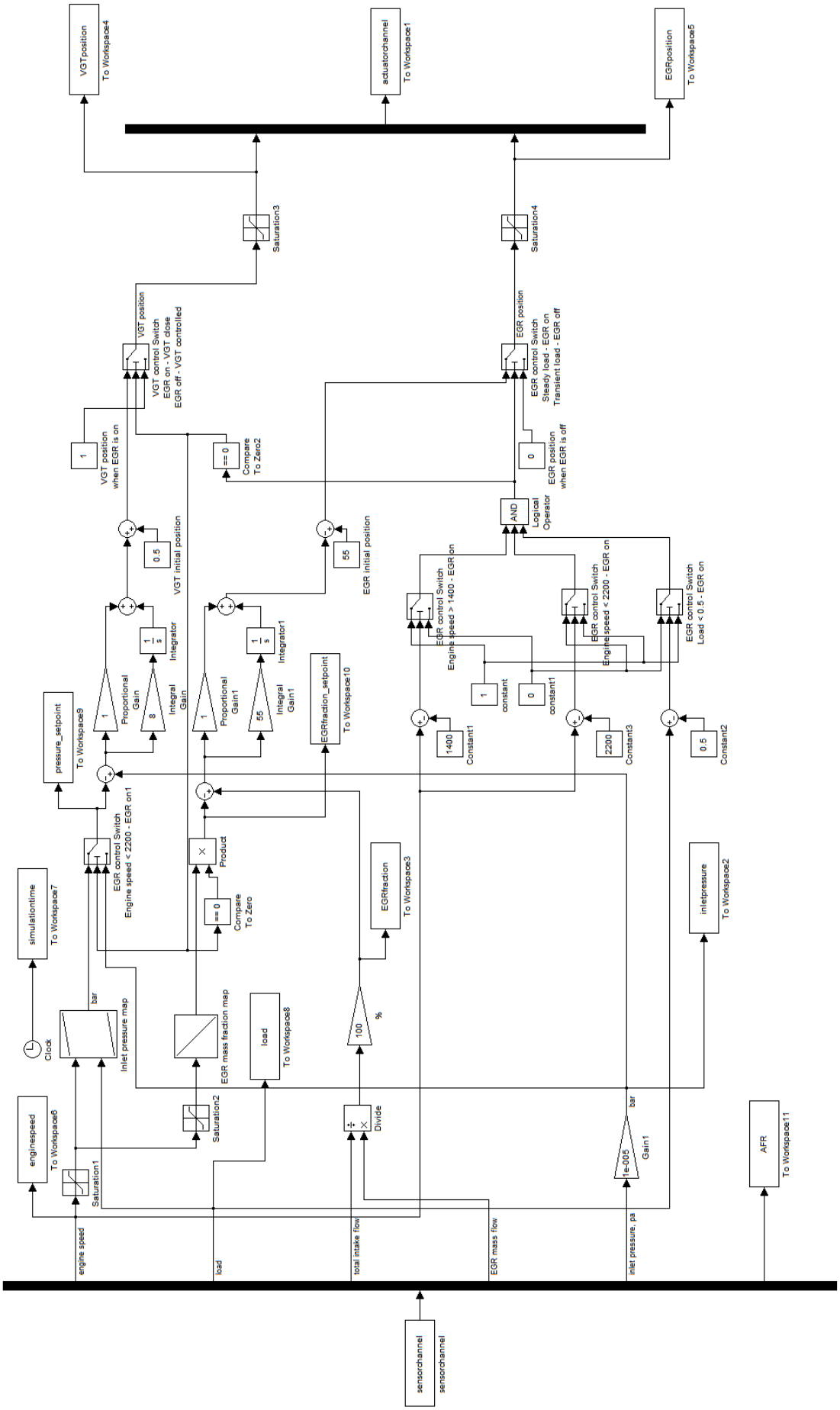

Figure 4.2: Simulink model of the PI controllers for VGT and EGR control.

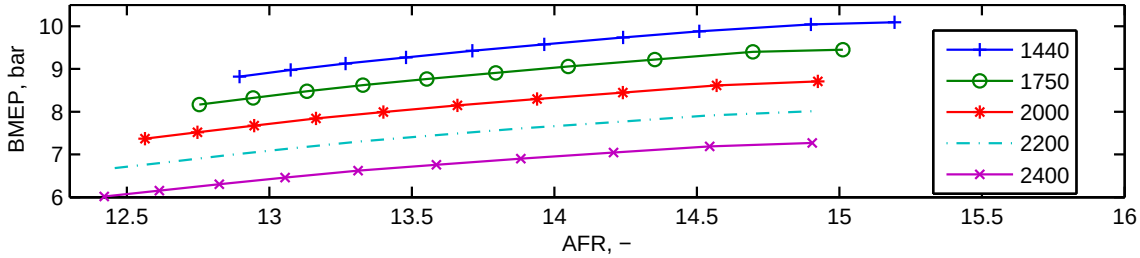

(a)

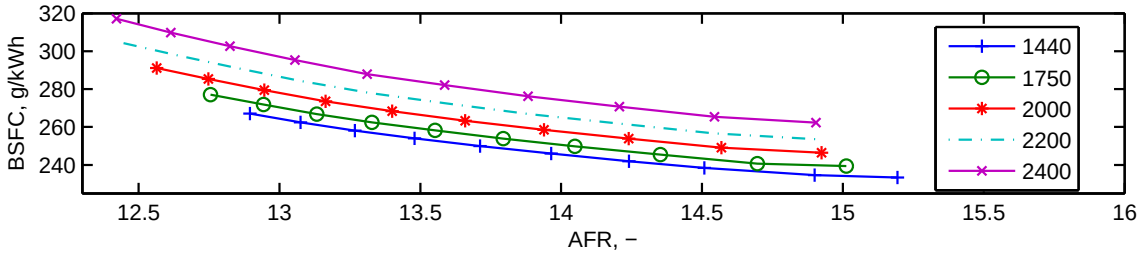

(b)

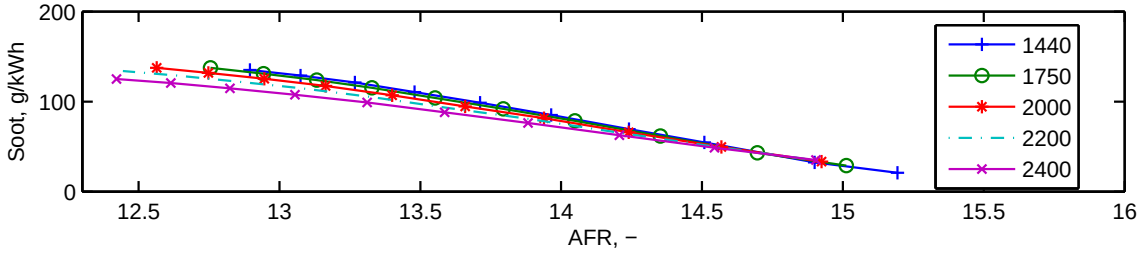

(c)

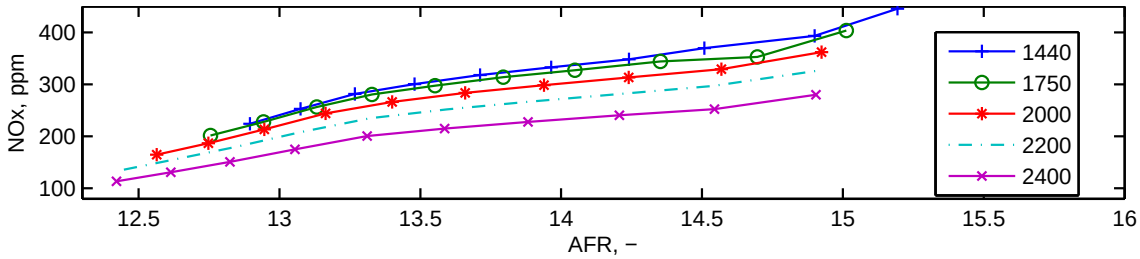

(d)

Figure 4.3: Effect of air fuel ratio to the engine performances and emissions, load = 0.48.

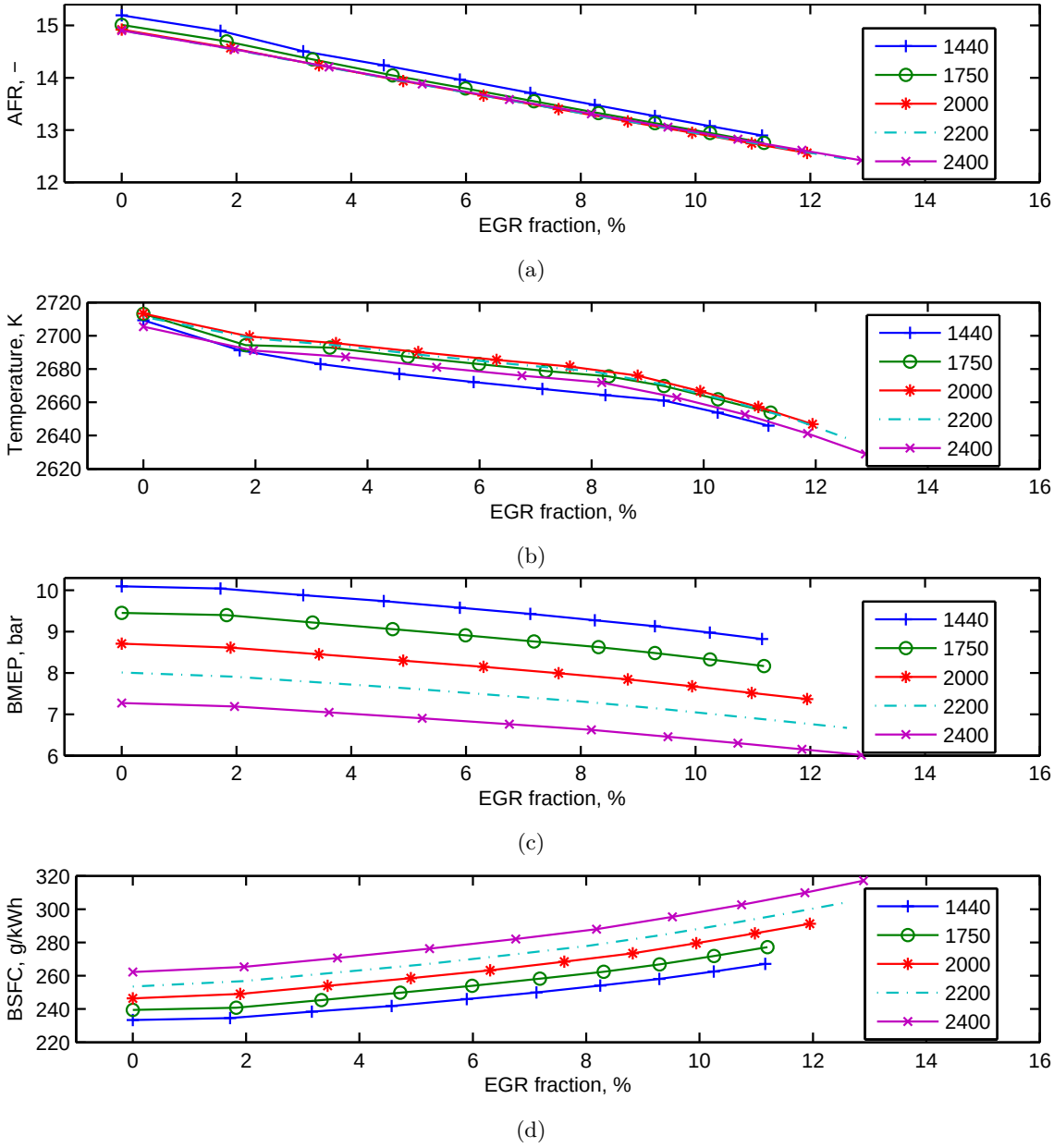

(a)

(b)

(c)

(d)

Figure 4.4: Effect of EGR gas mass fraction in the intake air flow to the engine performances and emissions, load demand = 0.48.

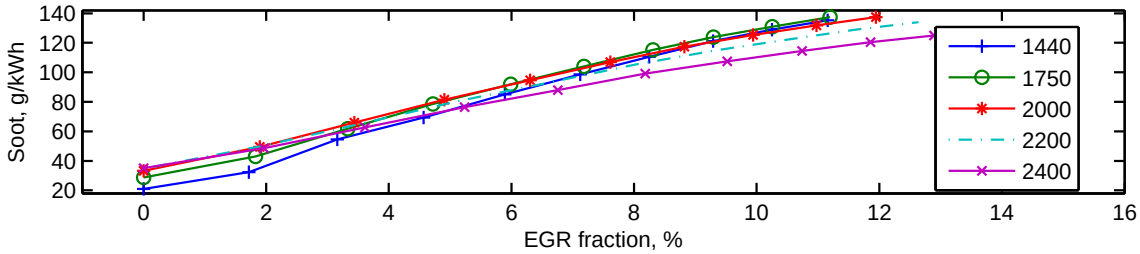

(e)

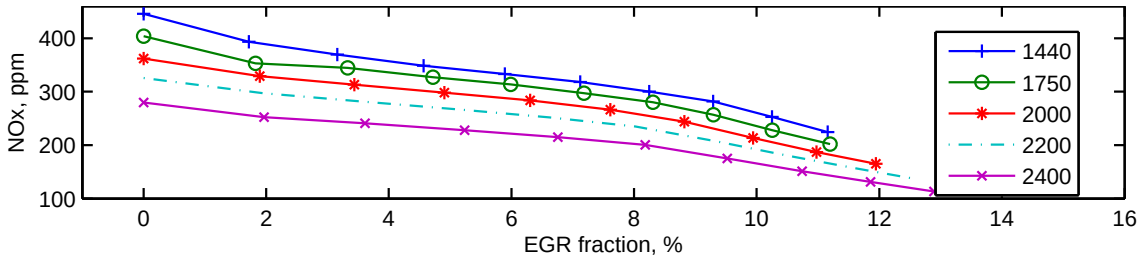

(f)

Figure 4.4: (continued)

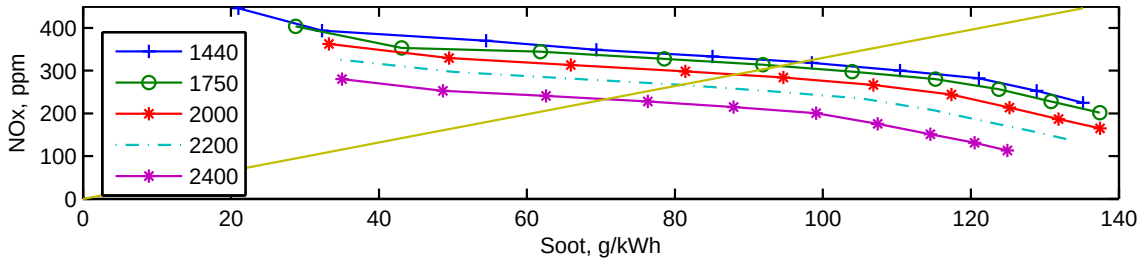

(a)

Engine speed, rpm	EGR mass fraction, %
1440	7.12
1750	5.99
2000	5.6
2200	5.14
2400	4.43

(b)

Figure 4.5: Trade-off between soot and NOx production. (a) the crossing points of the emissions curve and yellow straight line marked the trade-off operating points of the engine, (b) EGR mass fraction at trade-off points.

engine speed will stay the same; if the torque produced is less than the road load torque, the engine speed will start to drop. The road load is simulated by a mechanical consumer sub-model. The load characteristic applied to the mechanical consumer is calculated according to Eq. 4.1:

$$M = \frac{a}{n_c} + b + cn_c + dn_c^2 \tag{4.1}$$

where M is road load torque. a, b, c, d denote load coefficients (unit is Nm.rpm). n_c denotes the rotational speed of the mechanical consumer.

In this simulation, a has been set as -392857, b is 0, c is 0.443, d is 0. This setting will generate low road load torque at low engine speed (700 rpm), high road load torque at high engine speed (2400 rpm).

Fig. 4.6 and 4.7 show the controlled trajectory of inlet pressure and EGR mass fraction compared to the trajectory of set-points. It can be seen that both of the PI controllers have response times of less than 1 second and are stable. However, compared to the VGT-dependent control, the VGT-independent control shows some disturbance around 20 - 30 seconds into the test. This indicates that VGT-dependent control is stabler because it avoids the interaction between VGT and EGR.

Fig.4.8 shows the comparison between the VGT dependent control and Vgt-independent control. It can be seen that compared to PID-independent control, the VGT position of PID-dependent control during 1 - 5 seconds and 20 - 30 seconds of the test has been kept fully open; in order to keep the same EGR mass fraction, the EGR position of the Vgt-independent control has been kept lower than that of the Vgt-independent control. As a result, the inlet pressure of VGT- independent control is slightly higher than that of the Vgt-independent control, as well as the AFR, turbine total efficiency, BSFC. Engine torque is slightly higher too. Soot and NOx production are lower than those of the Vgt-independent control.

It can be concluded that Vgt-independent control is not as stable as Vgt-independent control because of the interactive effect between VGT and EGR, but it is slightly higher than Vgt-independent control in terms of engine performance and emissions because the VGT was controlled all the time.

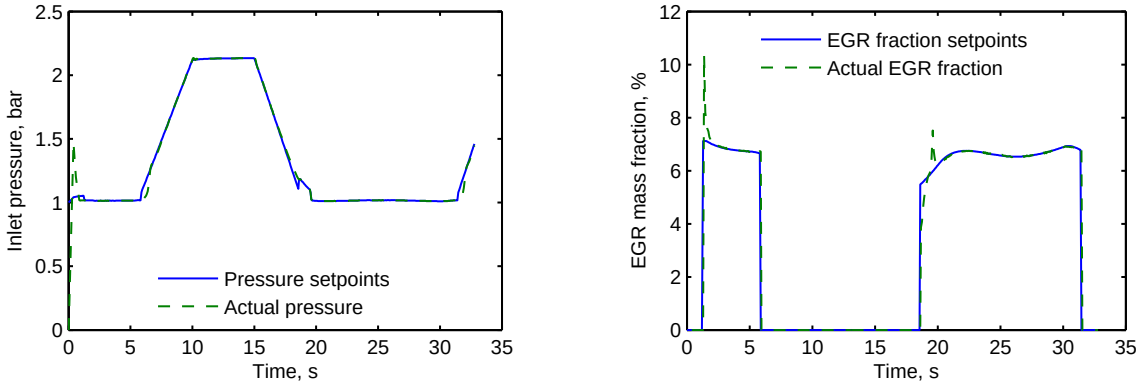

(a) (b)

Figure 4.6: Responding performances of the PID controller 1 (Vgt-independent control). (a) actual inlet pressure against set-points (b) actual EGR mass fraction against set-points.

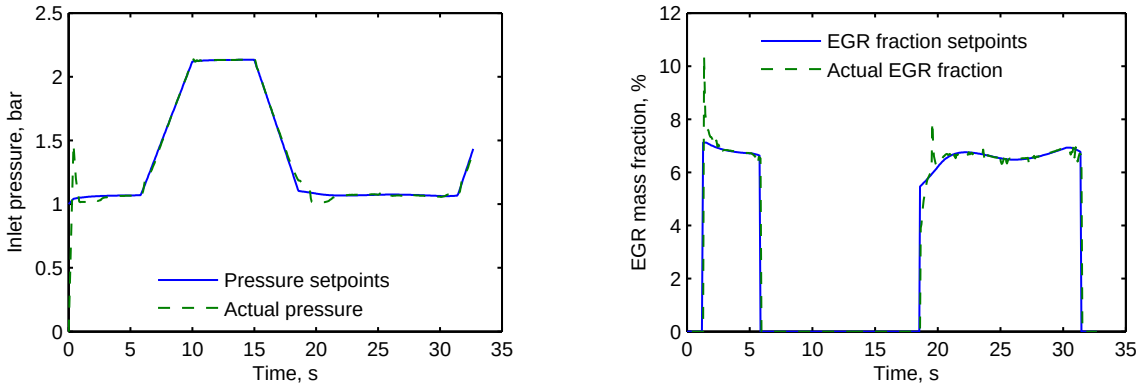

(a) (b)

Figure 4.7: Responding performances of the PI controllers 2 (Vgt-independent control). (a) actual inlet pressure against set-points (b) actual EGR mass fraction against set-points.

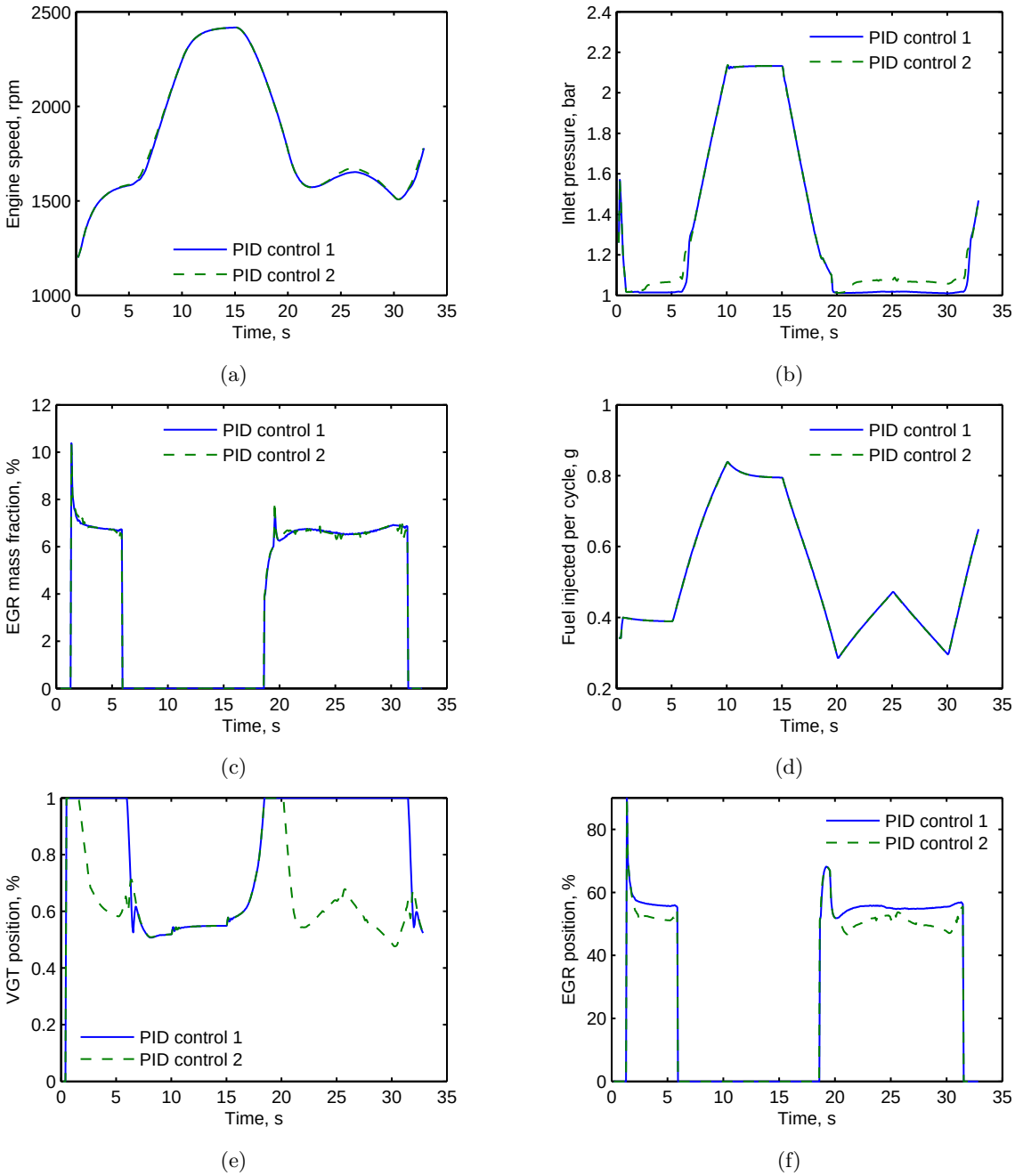

Figure 4.8: Comparison between PID controller 1 (Vgt-independent control) and PID controller 2 (Vgt-independent control).

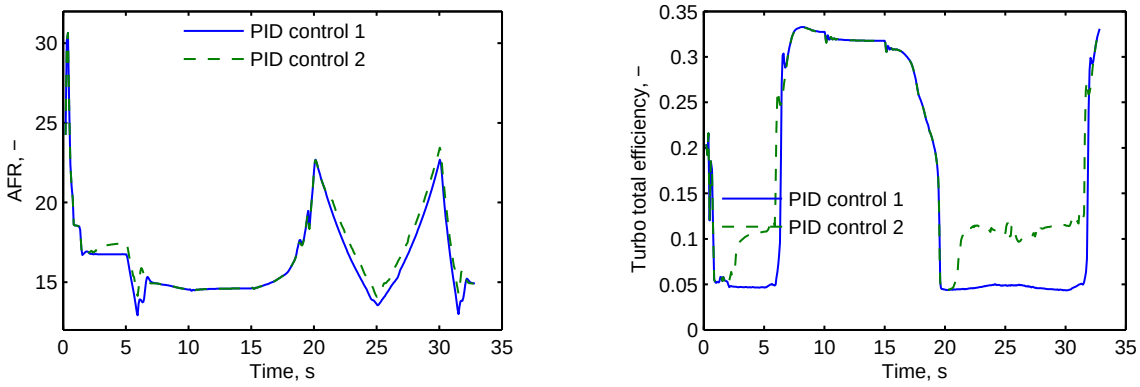

(g)

(h)

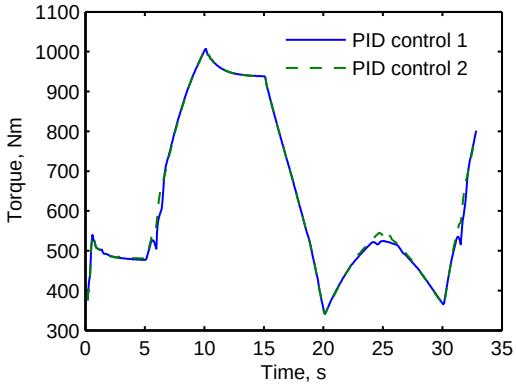

(i)

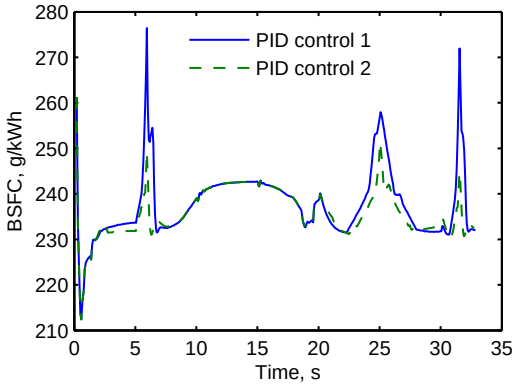

(j)

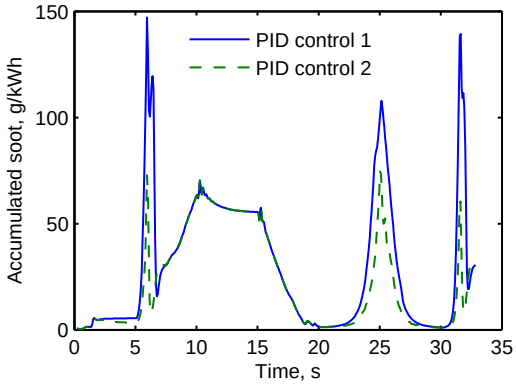

(k)

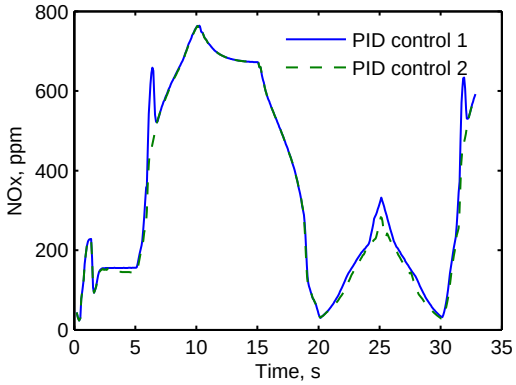

(l)

Figure 4.8: (continued)

4.2 Fuzzy Logic Control

In this study, a novel real-time fuzzy logic controller (RFLC) has been developed to search for the trade-off-oriented control strategies under dynamic conditions. The advantage of fuzzy logic control is that expert knowledge can be included in the form of rules to control a process. The control strategy is based on a group of control input variables, and it can be used to effectively solve nonlinear control problems [43]. Compared to conventional PI controllers, which adjust the VGT and EGR positions to attain the optimal set-points of inlet pressure and flow generated by extensive engine mapping, the proposed controller is able to determine the optimal VGT and EGR positions based on fuzzy logic rules in real time.

4.2.1 Effects of VGT and EGR to diesel engines

In order to create effective fuzzy logic rules for real-time control of the VGT and EGR, experimental tests were carried out to investigate the actual influences of the VGT and EGR to the diesel engine. The interaction effects between the VGT and EGR were also investigated.

Firstly, the influences of the VGT vanes position to the diesel engine was examined. In this experimental test, the engine speed was fixed at 1440 rpm which is about the speed with the highest torque at full throttle. In order to investigate how VGT position affects EGR performance, the EGR valve was kept fully opened. The engine performance and emissions with the VGT gradually opened from 0-100% can be found from Fig. 4.9 below.

As shown in the figure, when the VGT was opened gradually, the torque (Fig. 4.9 a) of the engine dropped from about 1100 Nm to 600 Nm. This is because when the VGT was gradually opened, the inlet pressure (Fig. 4.9 b) gradually dropped from 3 bar to about 1 bar, hence the intake air flow (Fig. 4.9 c) dropped from about 180 g/s to 80 g/s. In order to avoid misfire and excessive emissions, the fuel injection control module restricts the air fuel ratio to above 12 (Fig. 4.9 f). As a result, the fuel injection rate (Fig. 4.9 d) dropped from about 10 g/s to 6 g/s, even though the throttle position has been fixed at 100% (full load condition). The specific fuel consumption (Fig. 4.9 g) also increased about 16% from 0.22 kg/kWh to 0.25 kg/kWh. This indicates that the closed VGT vanes position can effectively reduce the fuel consumption of the engine.

In terms of emissions, when VGT was opened gradually, the opacity of exhaust gas (Fig. 4.9 i) increased from about 1% to 15%, NO_x (Fig. 4.9 j) increased from about 700 ppm to 900 ppm. The increase of opacity was caused by insufficient oxygen supplied to

the combustion which is due to dropped intake air mass flow. The increase of NO_x was caused by reduced EGR flow (Fig. 4.9 h) from about 4 g/s to 0. This is because when the VGT was opened, the pressure at the inlet of the turbine dropped. As a result, there is not enough positive pressure gradient across the EGR valve. Consequently, the exhaust gas was not able to flow through the EGR valve even with the valve fully open. This indicates that to effectively recirculate the exhaust gas , the VGT has to be closed to a certain degree to create the required positive pressure gradient across EGR.

It was also discovered that when the VGT was opened from 30% to 100%, the opacity of exhaust gas dramatically increased from about 0.7% to 18.3% whereas NO_x emissions dropped from 1025 ppm to 875 ppm. This indicates the trade-off effect between the control of the VGT and EGR.

To investigate the influences of EGR on the engine, several tests were conducted with engine speed set at 1000 rpm, 1500 rpm, 2000 rpm, and 2400 rpm respectively under full load conditions. In order to protect the intake manifold, the VGT was kept as closed as possible while at the same time without generating a inlet pressure more than 3 bars. The same VGT position (Fig. 4.10 a) was set for each data point when EGR was opened and closed.

As illustrated in Fig. 4.10, compared to the EGR valve closed at 1000 rpm, NO_x emissions (Fig. 4.10 g) were reduced by 21.6% when the EGR valve was opened. However, (Fig. 4.10 i) the opacity of exhaust gas increased 81.8% and the torque of the engine (Fig. 4.10 h) dropped by 11.3%. This indicates that an open EGR valve at low engine speed can reduce NO_x emissions but will cause a significant increase of soot emissions. Apart from this, it also sacrifices the performance of the engine. It should also be noticed that the inlet pressure is generally lower when EGR is open, this means in order to supply enough air to the cylinder, EGR should be kept as closed as possible when it is not necessary to open. At high engine speed, the figure shows that there is no obvious improvement on NO_x when EGR is open, therefore EGR should be kept closed. In the middle range of the engine speed, when EGR is opened, there is noticeable NO_x reduction compared to when EGR is closed and without much increase of opacity. The influence on the torque of the engine is also not noticeable.

4.2.2 Overall control structure

Sugeno-type fuzzy logic controllers have been developed to control the VGT vanes and EGR valve for improving fuel consumption and reducing emissions under real-time tran-

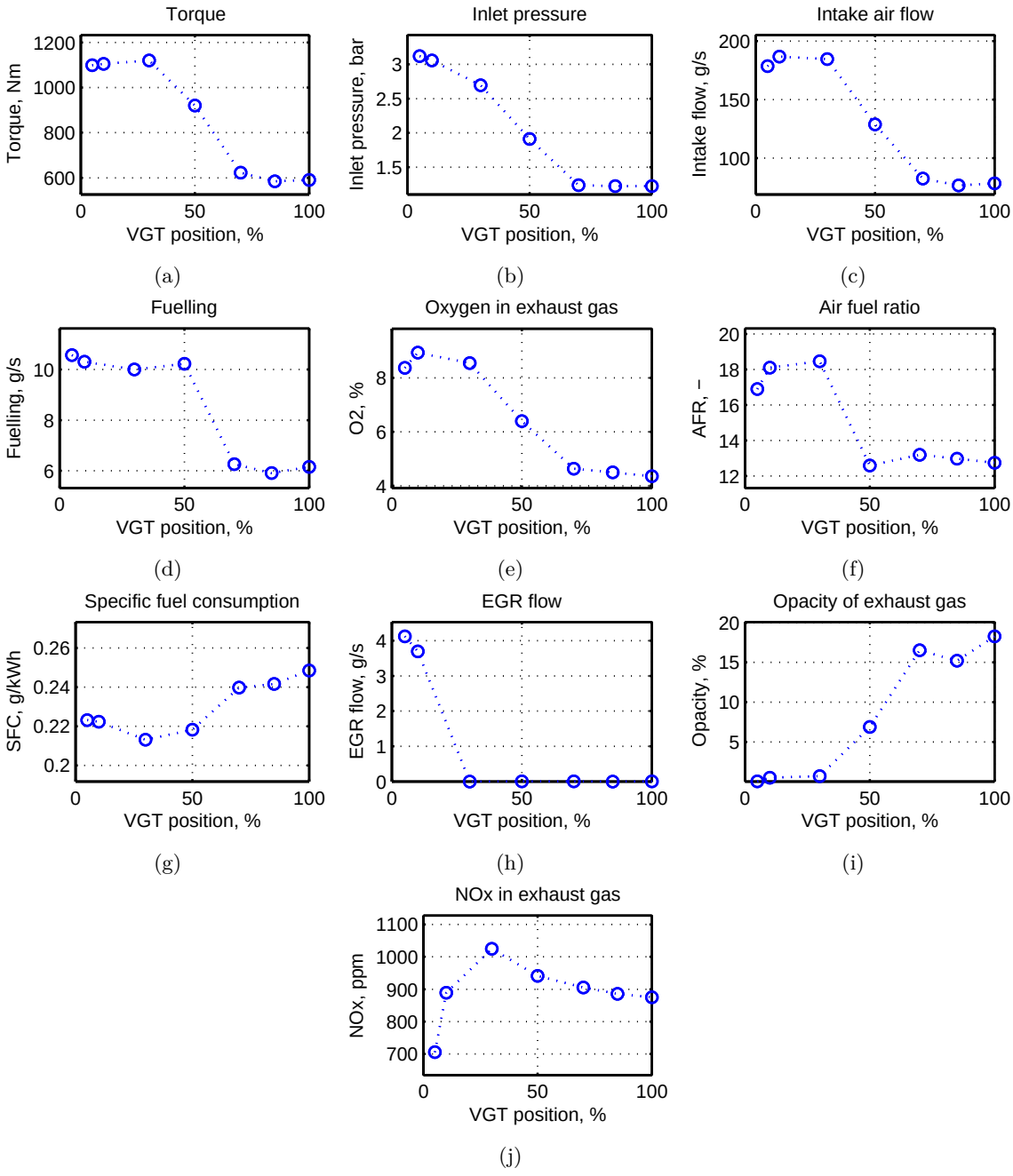

Figure 4.9: The influences of VGT to the engine performance and emissions.

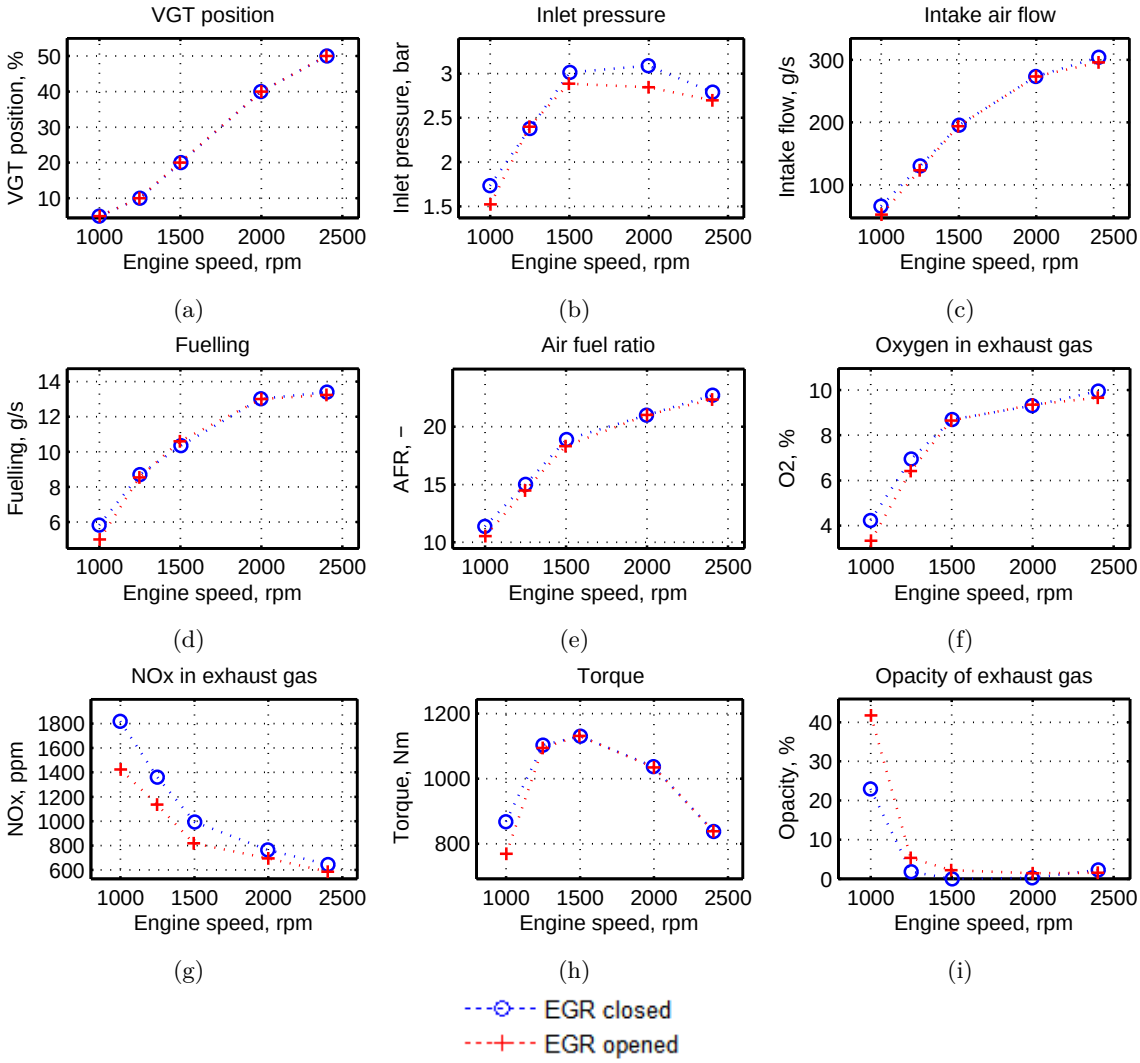

Figure 4.10: The influences of EGR to the engine performance and emissions.

sient running conditions. The overall control structure is shown in Fig. 4.11. The fuzzy logic controller receives real-time transient signals including engine speed, load, inlet pressure, soot, NO_x as input variables, and generates transient vanes and valve position according to the control output signals based on a set of predefined fuzzy rules corresponding to the transient input signals. There are two downstream PID controllers to position the VGT vanes and EGR valves at the required position sent from the fuzzy logic controller upstream.

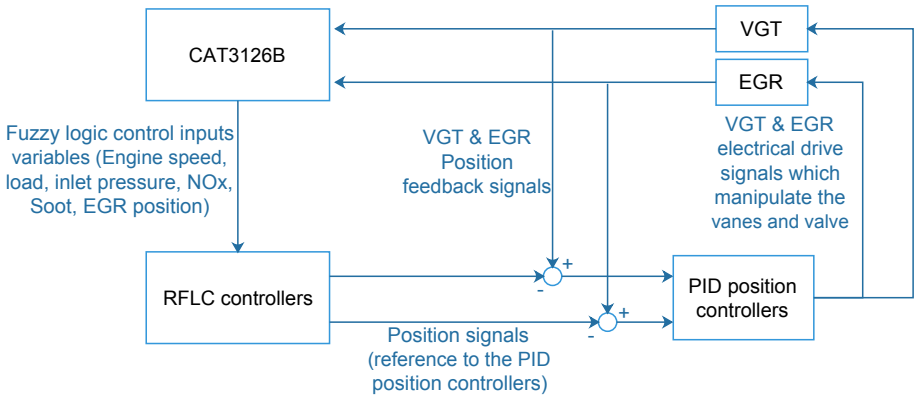

Figure 4.11: Overall closed-loop fuzzy logic control structure

Based on theoretical studies and experimental tests, comprehensive fuzzy logic rules for both VGT and EGR control were created and tested on the test bed. The overall structure of the fuzzy logic controllers for the VGT and EGR were illustrated in Fig. 4.12. The control input and output variables are detailed in the next section.

4.2.3 Definition of control variables and membership functions

To develop a fuzzy logic controller, necessary control input and output variables should be defined. Based on the experimental investigations described in sections 4.2.1, a total of six control input variables have been defined. They are engine speed, load, inlet pressure, opacity, $NO_x$and EGR position. Two control output variables have been defined which are VGT position and EGR position. A symmetric Gaussian function has been used for each control input variable which is defined by two parameters σ and c as given by Eq. 4.2. The output variables membership functions are the Sugeno constant type.

$$f(x;\sigma,c) = e^{\frac{-(x-c)^2}{2\sigma^2}} \tag{4.2}$$

There are three membership functions (Fig.4.13 a) defined by engine speeds, which are low, medium and high. With respect to the engine specifications listed in Table A.1 and

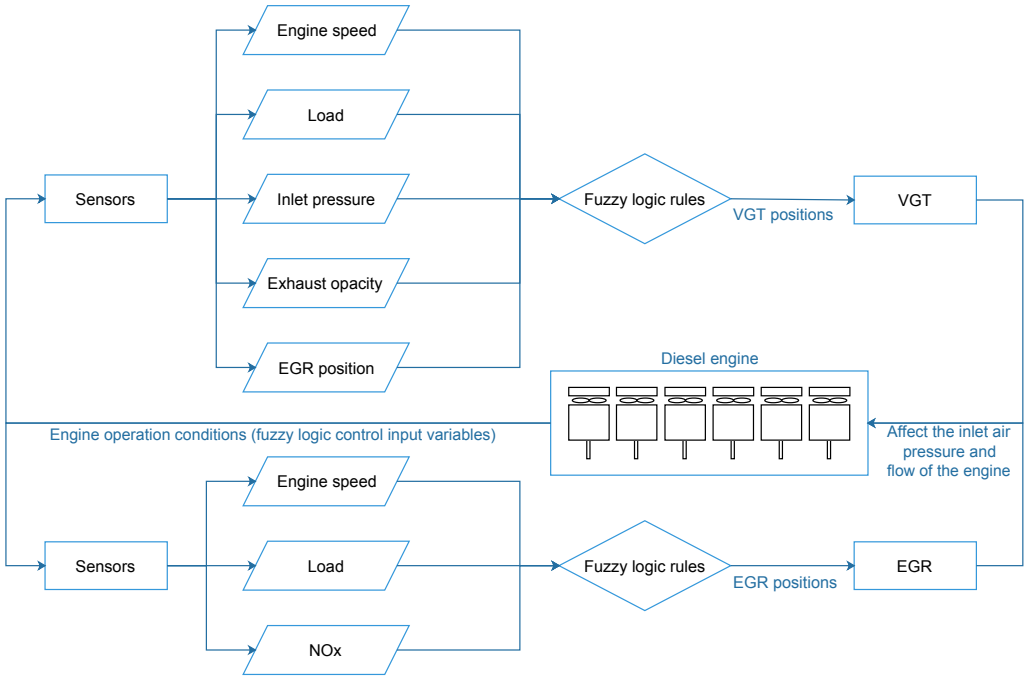

Figure 4.12: Fuzzy logic controller structure

the experimental tests, the speed range is defined from 1250 rpm to 2250 rpm. Any input speed value lower than 1250 will be fed to the controller as 1250rpm; any input speed value higher than 2250 will be fed to the controller as 2250 rpm.

Five membership functions (Fig.4.13 b) are defined for loads, which are very low, low, medium, high, and very high. The load ranges from 0% to 100%.

Similar membership functions (Fig.4.13 c) are defined for inlet pressure, which are very low, low, medium, high, and very high. Any input pressure value below 1.1 will be fed to the controller as 1.1 bar; any input pressure value above 3.2 will be fed to the controller as 3.2 bar.

For exhaust opacity, membership functions defined are very low, low, medium, high and very high as shown in Fig.4.13 d. Any input opacity value higher than 3 will be fed to the controller as 3.

The membership functions (Fig.4.13 e) defined for EGR position are fully closed, closed, middle, opened and wide opened. Any input EGR position value bigger than 50 will be fed to the controller as 50%.

Three membership functions (Fig. 4.13 f) were defined for NO_x, which are low, medium, and high. Any input NO_xvalue higher than 600 will be fed to the controller as 600 ppm.

The parameters of the membership functions defined for the input variables are listed

in Table 4.4.

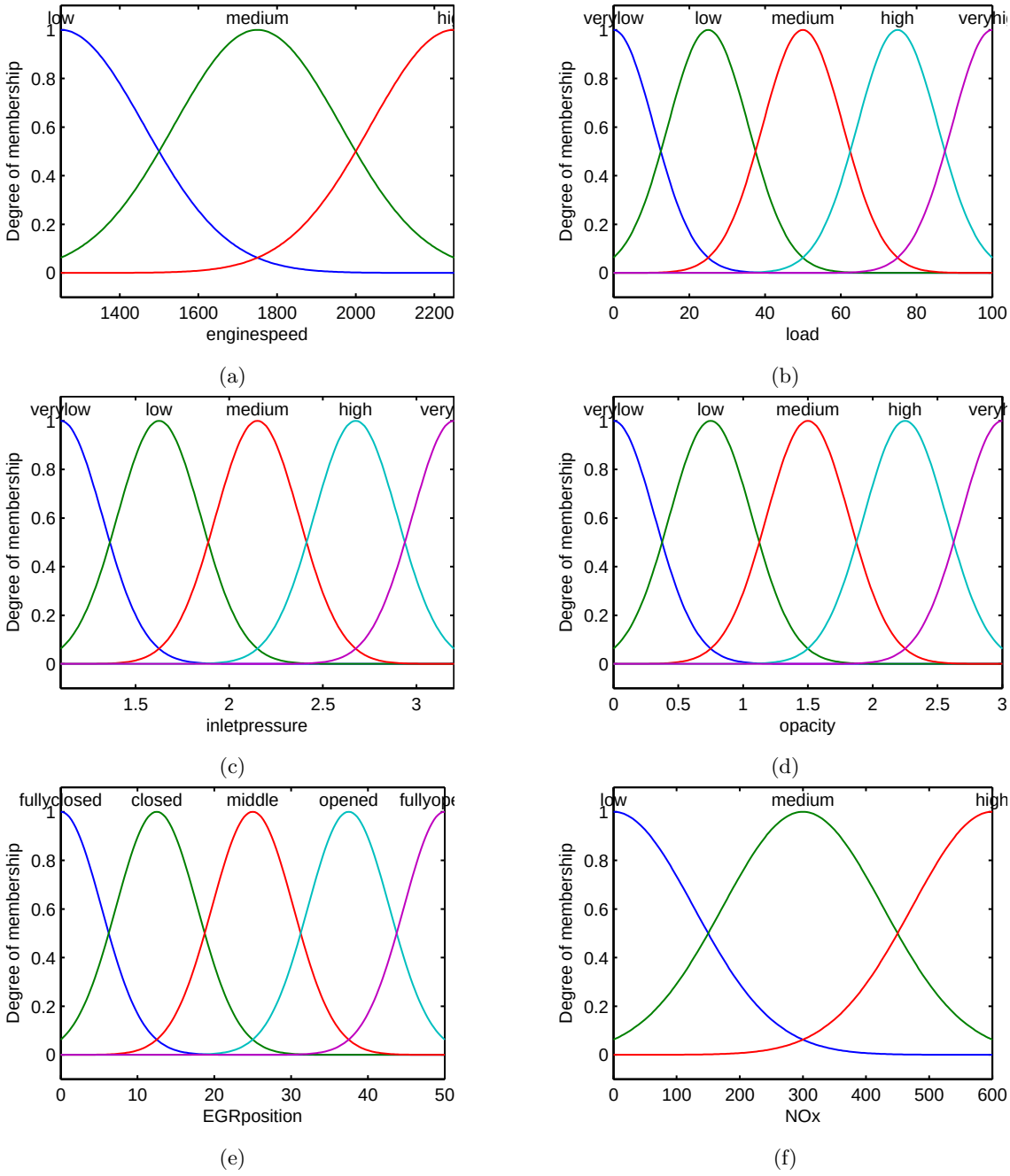

Figure 4.13: Membership functions of control input variables

Five constant membership functions have been defined for the VGT position output variable, which are fully opened, opened, middle, closed and fully closed with parameter 100, 75, 50, 25, and 0 respectively. For the EGR position output variable, three constant membership functions have been defined, which are opened, middle, and closed with parameter 100, 50, and 0 respectively.

Table 4.4: Parameters of the membership functions defined for input variables. (a) input variables with 3 membership functions, (b) input variables with 5 membership functions.

Input variables	Membership functions and parameters		
Engine speed	Low	Medium	High
	σ=212.3, c=1250	σ=212.3, c=1750	σ=212.3, c=2250
NOx	Low	Medium	High
	σ=127.4, c=0	σ=127.4, c=300	σ=127.4, c=600

(a)

Input variables	Membership functions and parameters				
Load	Very low	Low	Medium	High	Very high
	σ=10.62, c=0	σ=10.62, c=25	σ=10.62, c=50	σ=10.62, c=75	σ=10.62, c=100
Inlet pressure	Very low	Low	Medium	High	Very high
	σ=0.223, c=1.1	σ=0.223, c=1.625	σ=0.223, c=2.15	σ=0.223, c=2.675	σ=0.223, c=3.2
Opacity	Very low	Low	Medium	High	Very high
	σ=0.3186, c=0	σ=0.3186, c=0.75	σ=0.3186, c=1.5	σ=0.3186, c=2.25	σ=0.3186, c=3
EGR position	Fully closed	Closed	Middle	Opened	Fully opened
	σ=5.31, c=0	σ=5.31, c=12.5	σ=5.31, c=25	σ=5.31, c=37.5	σ=5.31, c=50

(b)

4.2.4 Control rules and surfaces

Based on the experimental investigations described in the Section 4.2.1, the following fuzzy logic control rules have been proposed for the VGT and EGR control.

VGT control

Another draw back of the existing PID control approach is that the control of the VGT only aims to produce the boosted pressure required without considering the actual working condition of the turbocharger. But actually, the control of the VGT also needs to take the following factors into account.

1. Avoid the compressor working beyond the surge line and chock line. If the compressor keeps working beyond the surge line and chock line, it will cause premature turbo failure. This is addressed by rules 1-3 listed below.

2. Avoid excessively boosted pressure being supplied to the engine. This can protect the engine from unexpected damage. This is addressed by rules 9 and 10 listed below.

3. Keep the VGT as open as possible to reduce unnecessary pumping loss. This is addressed by rules 4-8 and 11-15 listed below.

4. To produce enough back pressure when the EGR valve is open which can help the exhaust gas flow back into the inlet manifold through the EGR valve. This is addressed by rules 16-18 listed below.

Considering all control requirements listed above, a total of 18 fuzzy logic rules have been proposed for VGT control:

1. if ENGINE SPEED is *low*, then VGT POSITION is *fully closed*

2. if ENGINE SPEED is *medium*, then VGT POSITION is *middle*

3. if ENGINE SPEED is *high*, then VGT POSITION is *fully opened*

4. if LOAD is very *low*, then VGT POSITION is *fully opened*

5. if LOAD is *low*, then VGT POSITION is *opened*

6. if LOAD is *medium*, then VGT POSITION is *middle*

7. if LOAD is *high*, then VGT POSITION is *closed*

8. if LOAD is *very high*, then VGT POSITION is *fully closed*
9. if INLET PRESSURE is *very high*, then VGT POSITION is *fully opened*
10. if INLET PRESSURE is *high*, then VGT POSITION is *opened*
11. if OPACITY is *very high*, then VGT POSITION is *fully closed*
12. if OPACITY is *high*, then VGT POSITION is *closed*
13. if OPACITY is *medium*, then VGT POSITION is *middle*
14. if OPACITY is *low*, then VGT POSITION is *opened*
15. if OPACITY is *very low*, then VGT POSITION is *fully opened*
16. if EGR POSITION is *fully opened*, then VGT POSITION is *fully closed*
17. if EGR POSITION is *opened*, then VGT POSITION is *closed*
18. if EGR POSITION is *middle*, then VGT POSITION is *middle*

Rules 1-3 govern the VGT position with respect to engine speed. When selecting a turbocharger, it should match the high engine speed running condition. As a result, when the engine is running in the low speed range, the exhaust flow does not have sufficient energy to propel the turbine wheel if the vanes are wide open. Especially for large turbochargers selected for massive heavy-duty diesel engines. So the VGT position should be in the closed range. When the engine is running in the high speed range, the VGT position should be in the opened range. This action can prevent the compressor from working beyond the chock line which is an indication of deteriorated compressor efficiency. This action can also reduce back pressure which leads to reduced pumping loss.

Rules 4-8 govern the VGT position with respect to load. When the engine is running under a high load condition, the demand for fuel is high, as a result, more oxygen is required. In order to supply the engine with enough oxygen, the VGT position should be in the closed range. When the load is low, the demand for fuel is relatively low, so the oxygen requirement is low as well. The VGT position should be in the opened range to reduce pumping loss.

Rules 9 and 10 set the boosted pressure limit so that when the boosted pressure is approaching the limit, the VGT position will be moved towards being opened accordingly.

Rules 11-15 adjust the VGT position in respect of the opacity of the exhaust gas. This action can make sure that a greater boosted pressure will be produced if the opacity of the exhaust gas exceeds the predefined value which means more oxygen is needed.

Rules 16-18 adjust the VGT position with respect to the EGR valve position. This is to produce the necessary back pressure needed for recirculating part of the exhaust gas to the inlet manifold through the EGR valve.

From the control rules, control surfaces between each variable can be generated, see Fig. 4.14. The control surfaces reflect the fuzzy logic control rules set above.

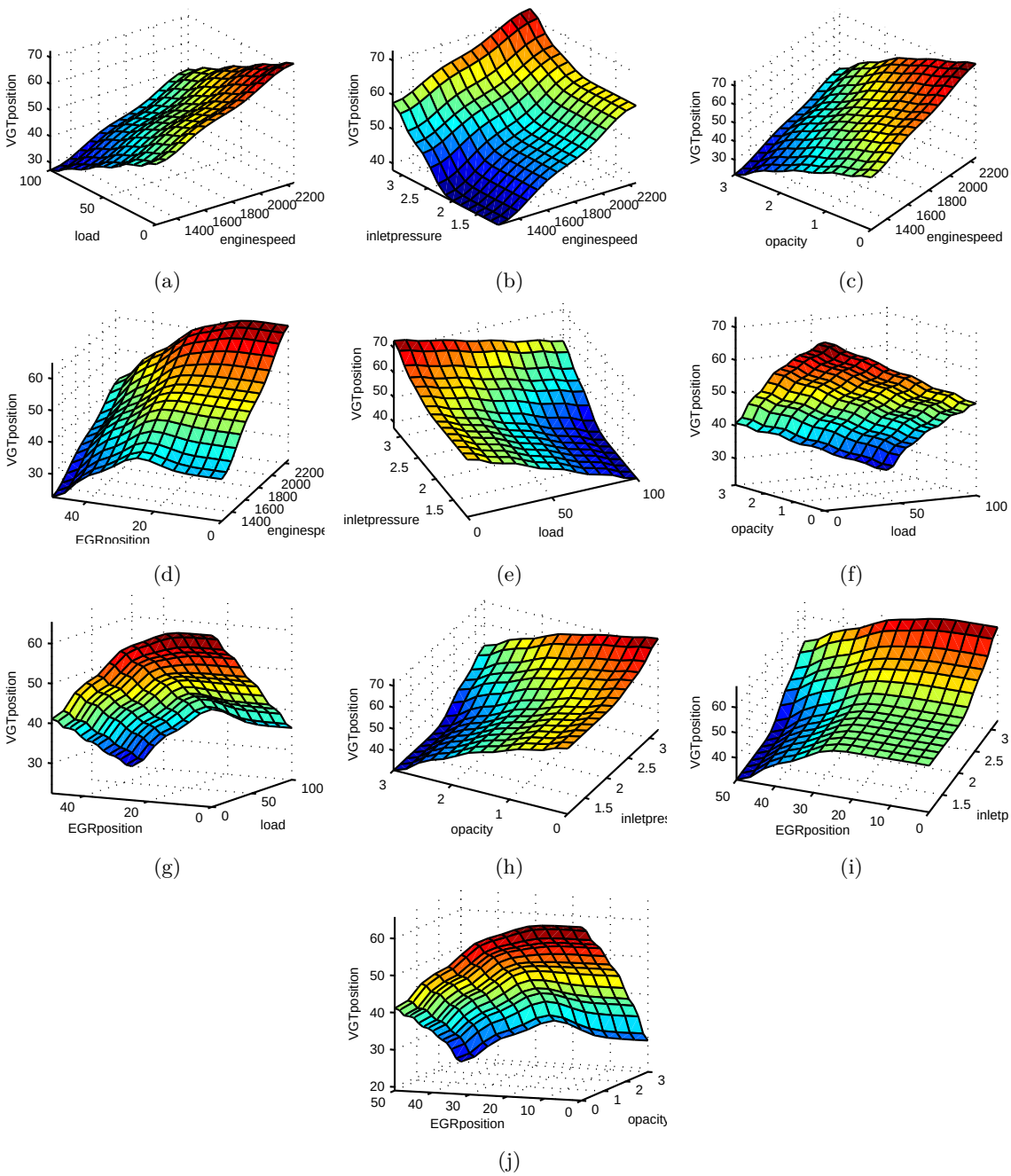

Figure 4.14: VGT fuzzy logic control surfaces

EGR control

Due to the recirculated EGR, gas can have negative effect on the engine performance. The control of EGR should be able to minimise the effect on the performance of the engine while reducing the NOx emission. Based on the discussions in the section 4.2.1, the EGR valve should only be opened during medium engine speed when the NOx emission is high. So the following three fuzzy logic control rules have been proposed for EGR control:

1. if ENGINE SPEED is *medium* and LOAD is *medium* and NO_X is *not low*, then EGR POSITION is *opened*

2. if ENGINE SPEED is *medium* and LOAD is *medium* and NO_X is *low*, then EGR POSITION is *closed*

3. if ENGINE SPEED is *not medium* and LOAD is *not medium*, then EGR POSITION is *closed*

The control surfaces of EGR control derived from the control rules are shown in Fig. 4.15.

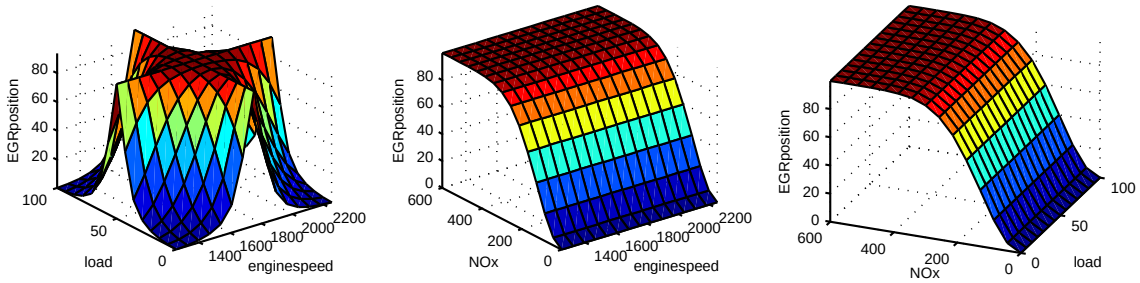

Figure 4.15: EGR fuzzy logic control surfaces

4.2.5 Control decision making

The control decisions are the real-time positions of the VGT and EGR. Each control decision was made by computing the final output of the Sugeno fuzzy inference system. The Sugeno (also known as Takagi-Sugeno) method of fuzzy inference was introduced in 1985 [72] and the output membership functions are either linear or constant. For this controller, because the output variables are the constant type so the fuzzy model has the form below:

If *Input 1* = x, *Input 2* = y,..., *Input n* = r, then the *output* is z = c (c is a constant)

The output level z_i of each rule is weighted by the firing strength w_i of the rule, which can be acquired by Eq. 4.3:

$$w_i = AndMethod(F_1(x), F_2(y), ..., F_n(r)) \tag{4.3}$$

where $F_{1,2,...,n}(.)$ are the membership functions for Inputs 1, 2, ..., n.

The final output of the fuzzy inference system is the weighted average of all rule outputs, which can be computed as Eq. 4.4:

$$Final\,Output = \frac{\sum_{i=1}^{N} w_i z_i}{\sum_{i=1}^{N} w_i} \tag{4.4}$$

where N is the number of rules.

4.2.6 The Nonroad Transient Cycle

The engine was running on a NRTC cycle predefined by Sierra-CP Engineering. According to DieselNet [28], the NRTC test is a transient driving cycle for off-road diesel engines developed by the US EPA in cooperation with the authorities in the European Union (EU). The test is used internationally for emission certification/type approval of off-road engines. NRTC testing is required by a number of emission standards for nonroad engines, including the EU Stage III/IV regulation, the US EPA Tier 4 rule and Japanese 2011/13 regulations.

The engine speed and torque prescribed in the driving cycle are illustrated in Fig. 4.16. The engine speed was governed at the predefined speed set by the driving cycle and the load was controlled by a PID controller to produce the predefined torque. This off-road driving cycle covers all the possible ranges of engine speed and load, and it also allows the controller to be tested while the engine is running in transient mode. The same driving cycle was used in different tests in order to compare the engine performance and emissions with different VGT and EGR control methods.

4.2.7 VGT and EGR position feedback

The VGT and EGR installed on the test bed have feedback channels which tell the current positions of the VGT vanes and EGR valve. Two PID controllers were built to regulate the positions of the VGT vanes and EGR valve. Fig. 4.17 shows the VGT vanes and EGR valve positions against the set points generated by the fuzzy logic controllers. It shows that the VGT and EGR position has followed the position references generated by the proposed fuzzy logic controller with acceptable errors.

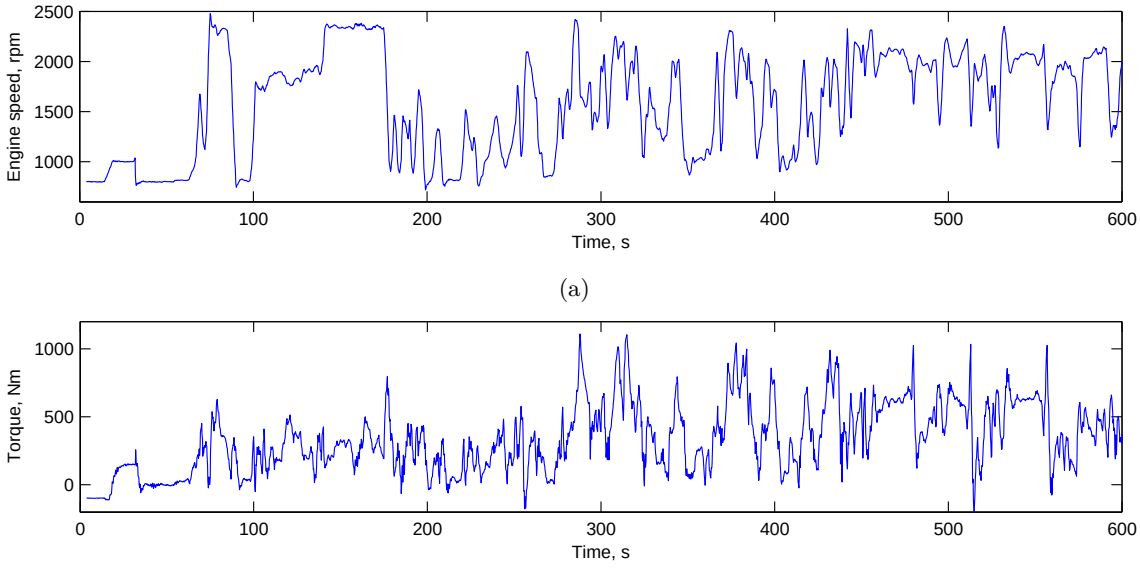

(a)

(b)

Figure 4.16: Half of the profiles of the NRTC cycle used for the tests of the proposed control scheme: (a) engine speed curve, (b) torque demand curve.

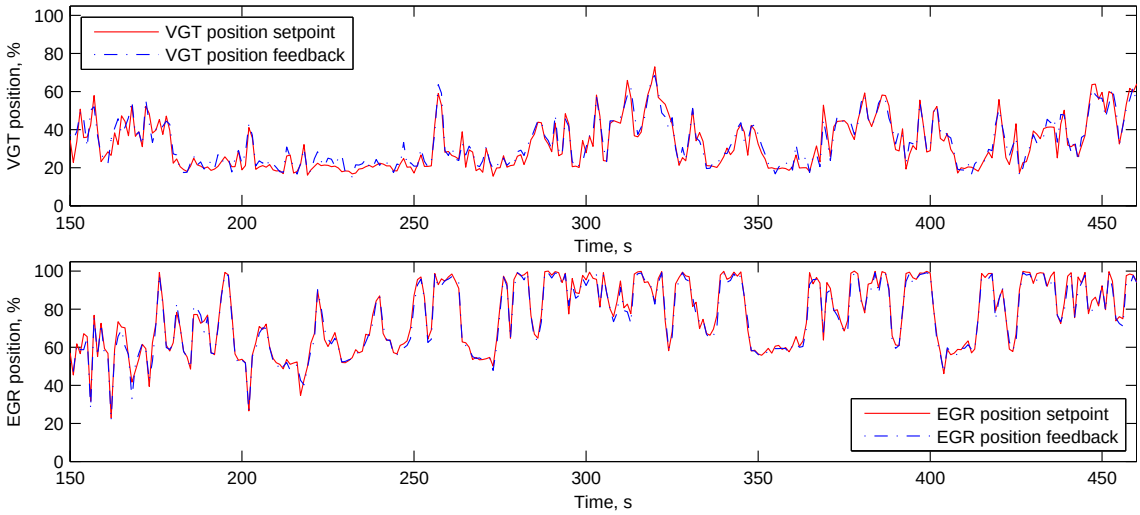

Figure 4.17: Performances of the PID position controllers for the VGT and EGR: (a) VGT actual positions against the set-points generated by the proposed fuzzy logic controller, (b) EGR valve actual positions against the set-points generated by the proposed fuzzy logic controller.

4.2.8 RFLC Engine performance and emissions

The performance and emissions of the RFLC engine were compared with those of the baseline engine. The baseline engine is configured as VGT half opened and EGR fully opened. This comparison aims to investigate whether the proposed controller is able to effectively reduce emissions and fuel consumption and properly address the trade-off effect. Fig. 4.18 and 4.19 show the comparisons of the engine speed, load, torque, specific fuel consumption (SFC) and emissions between the RFLC engine and the baseline engine during 150s to 460s of the test. Due to the limitation of the method used to measure the fuel consumption, SFC cannot be measured continuously during the test[1]. Those invalided SFC results during measuring tank refilling process have been removed. Firstly, it shows that the proposed controller is able to give a rapid response to the transient engine running conditions; secondly, the opacity and NOx emissions have been dramatically reduced compared to that of the baseline engine; thirdly, the inlet pressure has not exceeded the limit (3.2 bar) during the whole test.

In order to examine the results more closely, several segments which reflect some typical running conditions of the test have been selected and analysed in detail.

During 162 s to 164 s of the test, the engine was running in the high speed range at 2400 rpm (Fig. 4.20 a) with 80% load (Fig. 4.20 b). On the RFLC engine, the VGT position was set at about 40% and EGR position was set at about 55%. As a result, the inlet pressure (Fig. 4.20 i) was about 0.5 bar higher than the baseline engine. This is because the closed EGR valve lets more exhaust gas flow through the turbine. Compared to the baseline engine, the figure shows that the RFLC engine produced the same torque (Fig. 4.20 e) required by the driving cycle but produced much less soot and NO_x. At 164 s, opacity (Fig. 4.20 g) was reduced from 18.02% to 3.022% and NO_x (Fig. 4.20 h) was reduced from 616.7 ppm to 182.9 ppm . SFC (Fig. 4.20 f) was slightly reduced from 0.2818 kg/kWh to 0.2282 kg/kWh which indicates that the engine efficiency was slightly improved.

During 230 s to 234 s of the test, the engine was running in the low speed range (Fig. 4.21 a) with the load (Fig. 4.21 b) below 20% . The VGT position (Fig. 4.21 c) was set to about 20% and EGR (Fig. 4.21 d) was set to 60% open by the RFLC controller. Compared to the baseline engine, the figure shows that torque (Fig. 4.21 e) and inlet

[1]Fuel consumption is measured by monitoring the weight reduction rate of the fuel in a measuring tank located after the main fuel tank and low pressure pump. The accuracy of the mass flow rate is guaranteed by using this method, but the tank has to be refilled after it becomes empty during the measurement.

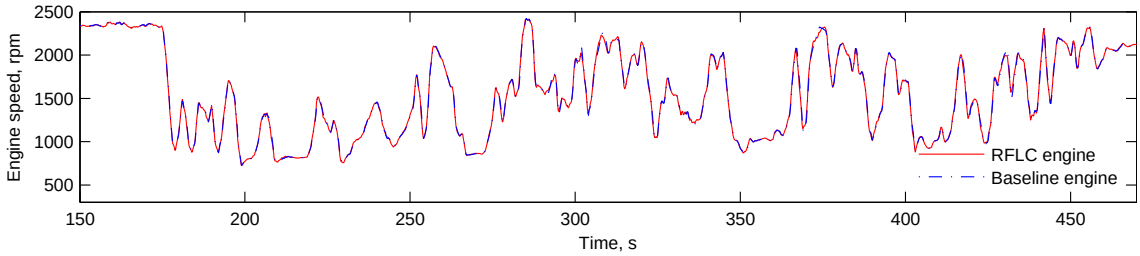

(a)

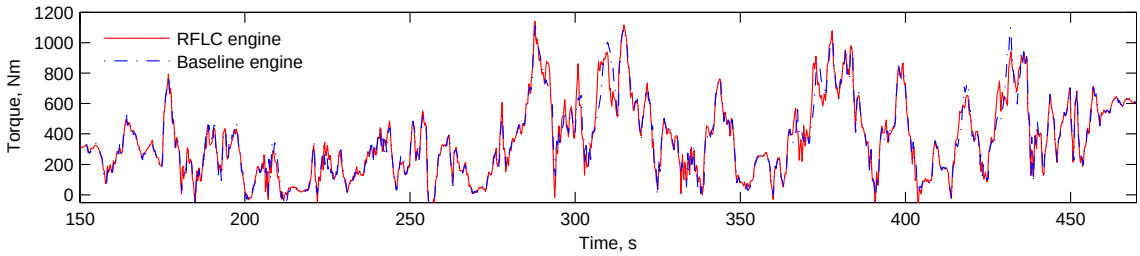

(b)

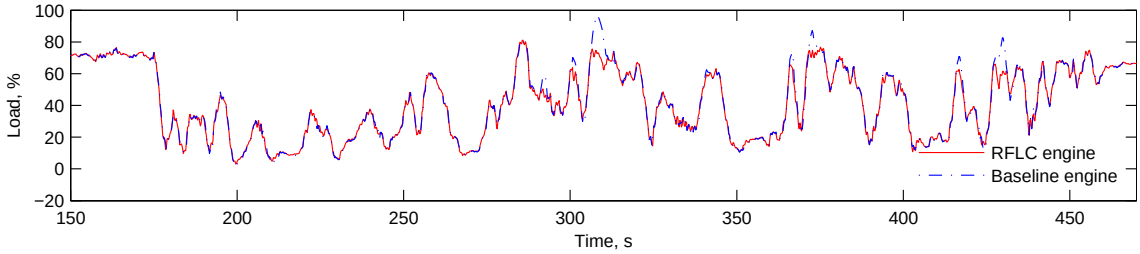

(c)

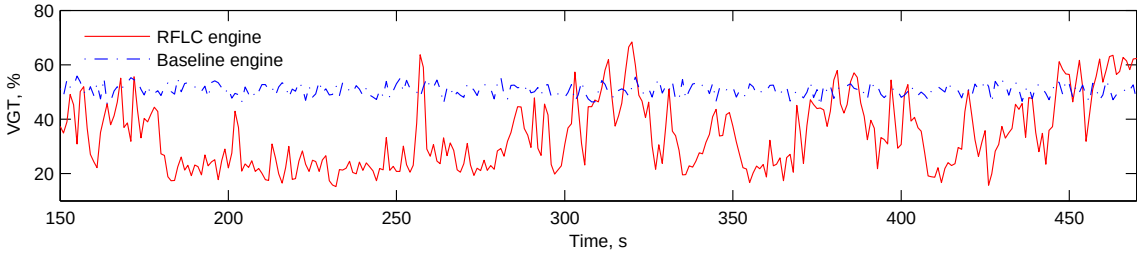

(d)

Figure 4.18: Comparison of experimental results of engine performance and emission between baseline engine and VGT/EGR fuzzy logic controlled during 150s-460s.

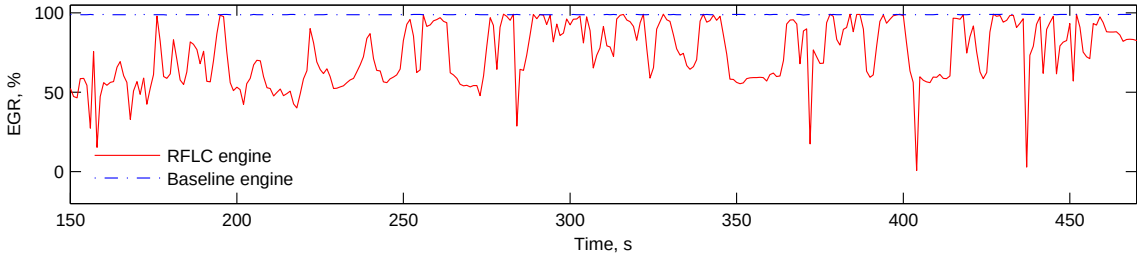

(e)

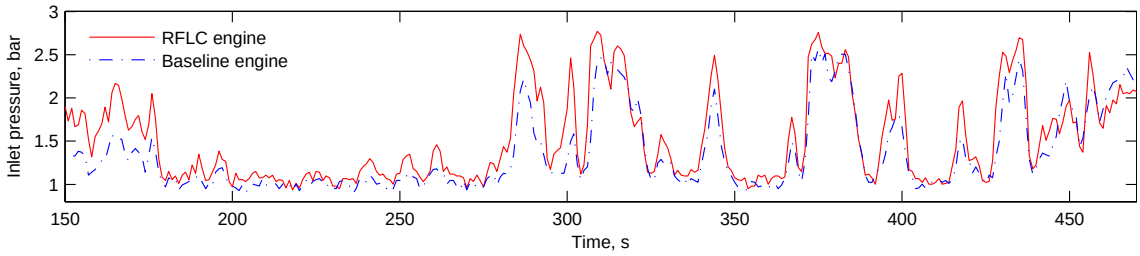

(f)

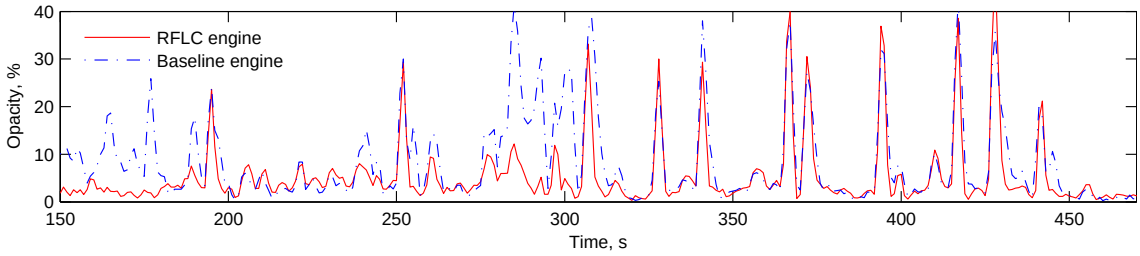

(g)

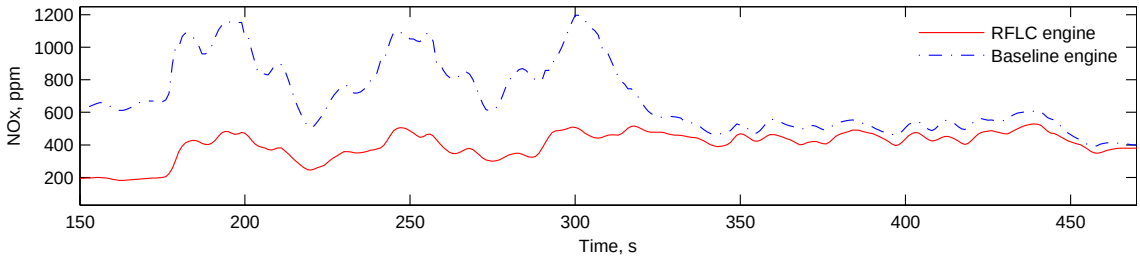

(h)

Figure 4.18: (continued)

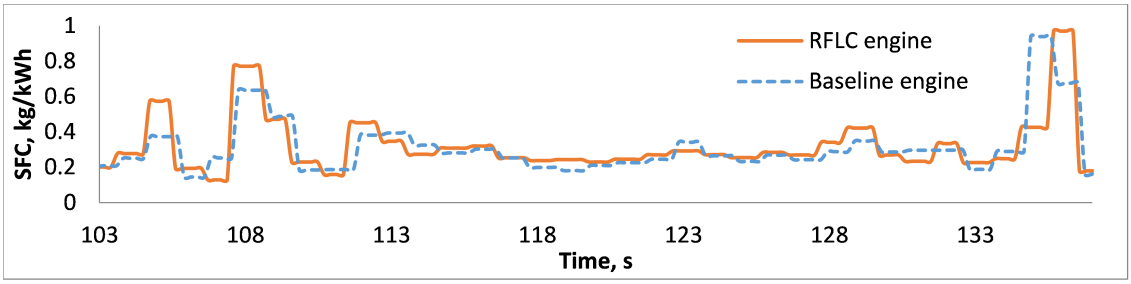

(a)

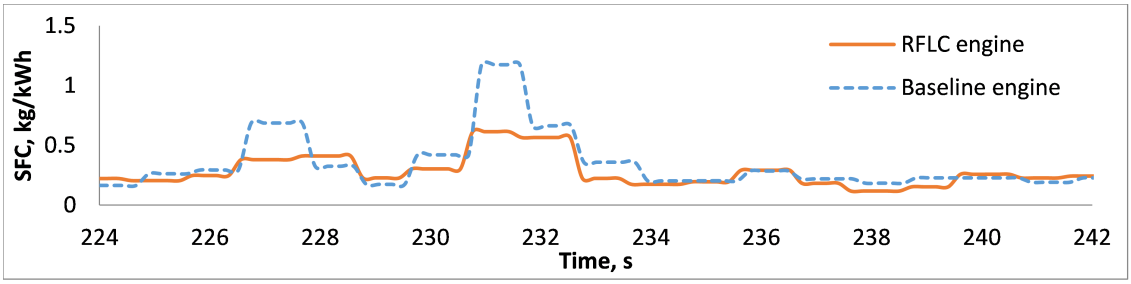

(b)

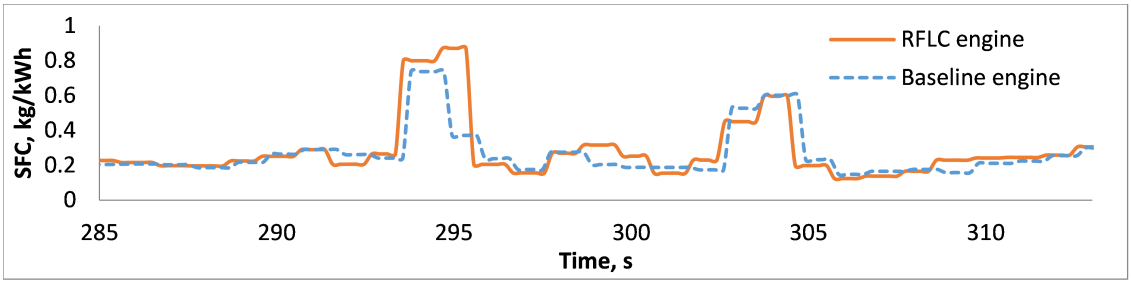

(c)

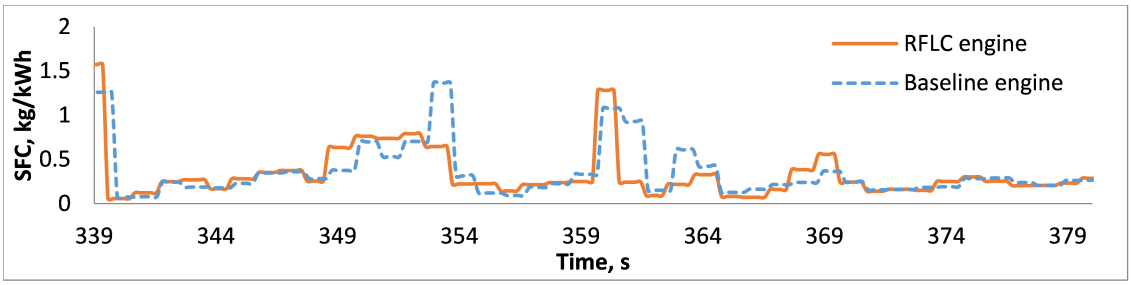

(d)

Figure 4.19: Comparison of experimental results of specific fuel consumption between baseline engine and VGT/EGR fuzzy logic controlled during 150s-460s.

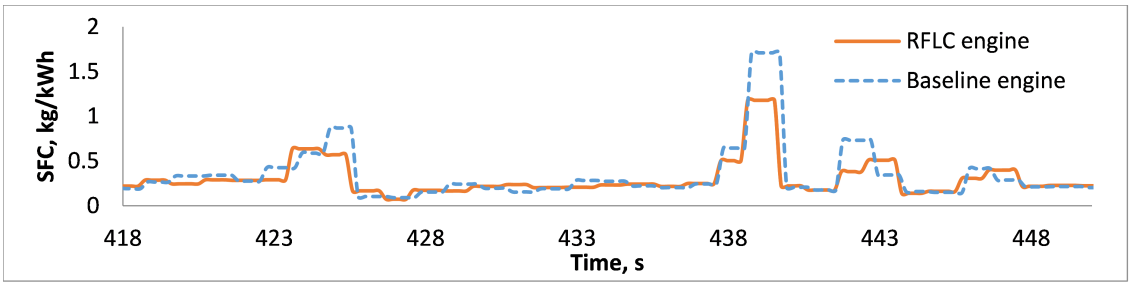

(e)

Figure 4.19: (continued)

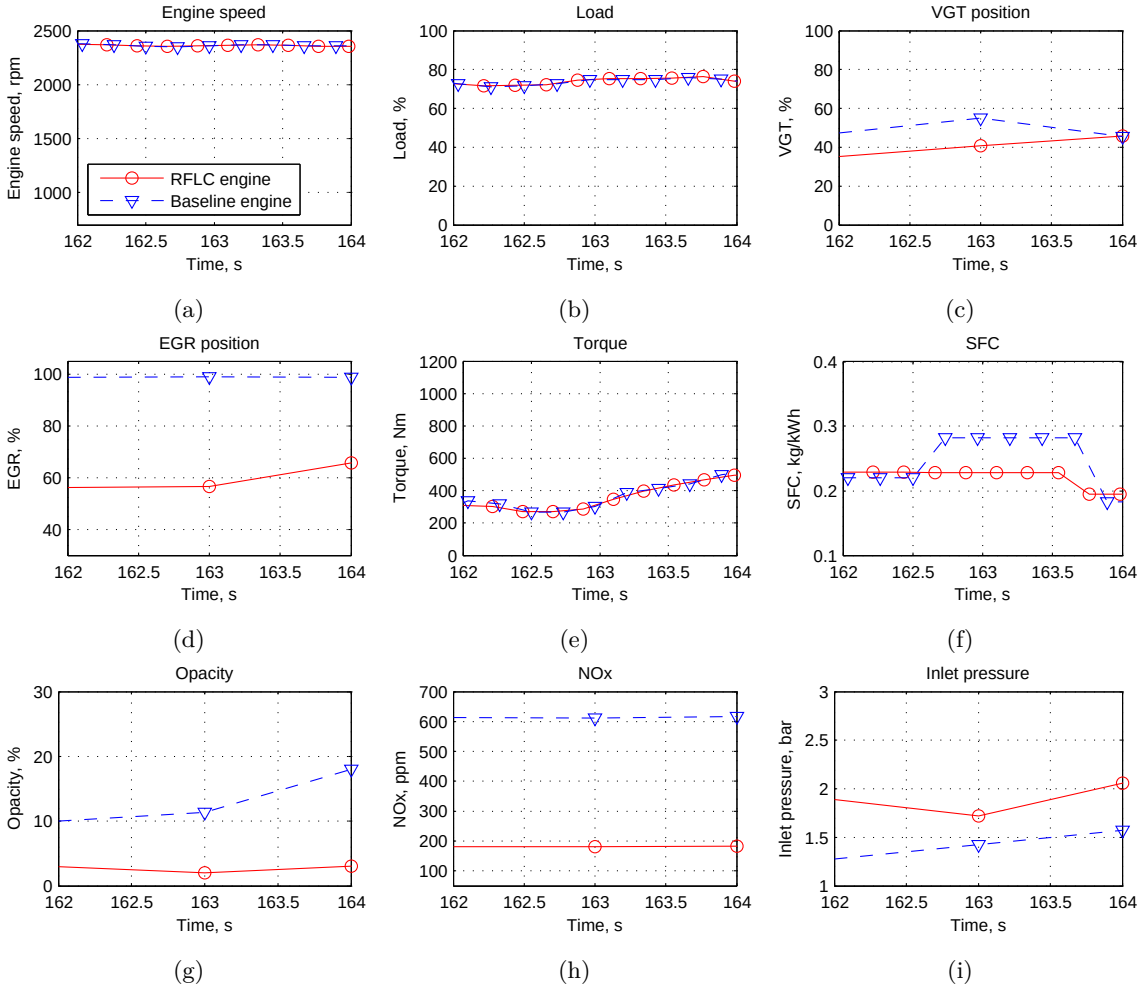

Figure 4.20: Comparison of experimental results of engine performance and emission between baseline engine and VGT/EGR fuzzy logic controlled during162s-164s.

pressure (Fig. 4.21 i) were almost the same, but NO_x (Fig. 4.21 h) was reduced from 763.1 ppm to 231 ppm. However, opacity (Fig. 4.21 g) was slightly increased from 5.261% to 7.038%. This is because the closed VGT can produce more back pressure in the exhaust manifold, the exhaust gas can be effectively recirculated through the EGR valve. As a result, NOx was reduced but soot was slightly increased. Noticeably, SFC (Fig. 4.21 f) was reduced from 1.175 kg/kWh to 0.6146 kg/kWh.

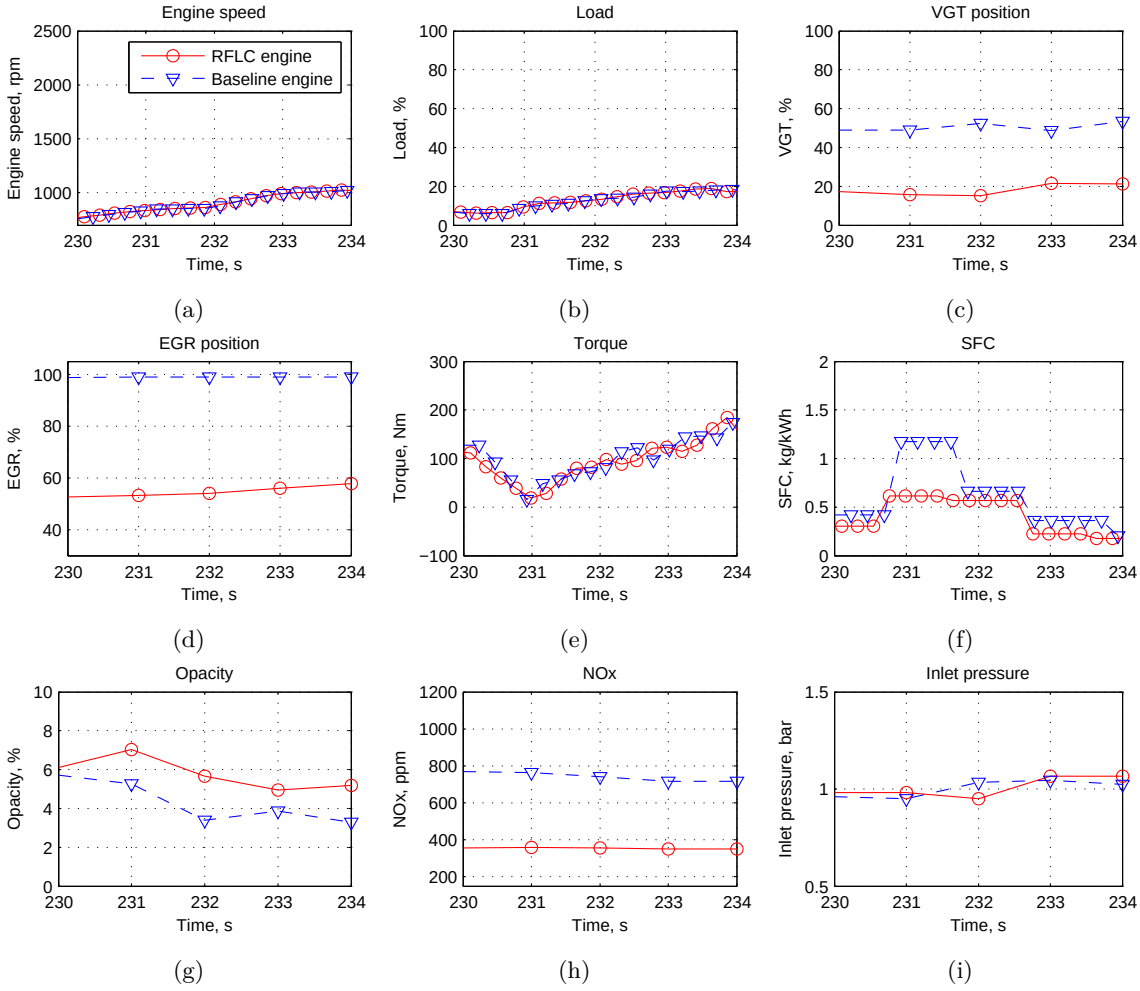

Figure 4.21: Comparison of experimental results of engine performance and emission between baseline engine and VGT/EGR fuzzy logic controlled during 230s-234s.

During 291 s to 293 s, the engine was running at about 1500 rpm (Fig. 4.22 a) which is in the middle speed range. Noticeably, the load (Fig. 4.22 b) of the baseline engine was higher than the load of the RFLC engine. However, the torque (Fig. 4.22 e) produced by the baseline engine was considerably lower than the torque produced by the RFLC engine. This is because there is not enough oxygen in the cylinder due to the relatively low inlet pressure (Fig. 4.22 i) in the baseline engine. So the load was further increased in order to achieve the required torque defined by the driving cycle. However, as mentioned

before, there is a limit for AFR in the fuel control unit, so when the AFR limit (about 12) is reached, no extra fuel is allowed to be injected even with a high load demand. As a result, the required torque cannot be achieved by the baseline engine and due to its rich combustion condition, the opacity (Fig. 4.22 g) was 8 times higher than the RFLC engine. SFC (Fig. 4.22 f) was also much higher (40.9%) than that of the RFLC engine. Additionally, the NO_x (Fig. 4.22 h) produced by the RFLC engine was considerably reduced from 857.9 ppm to 448.4 ppm.

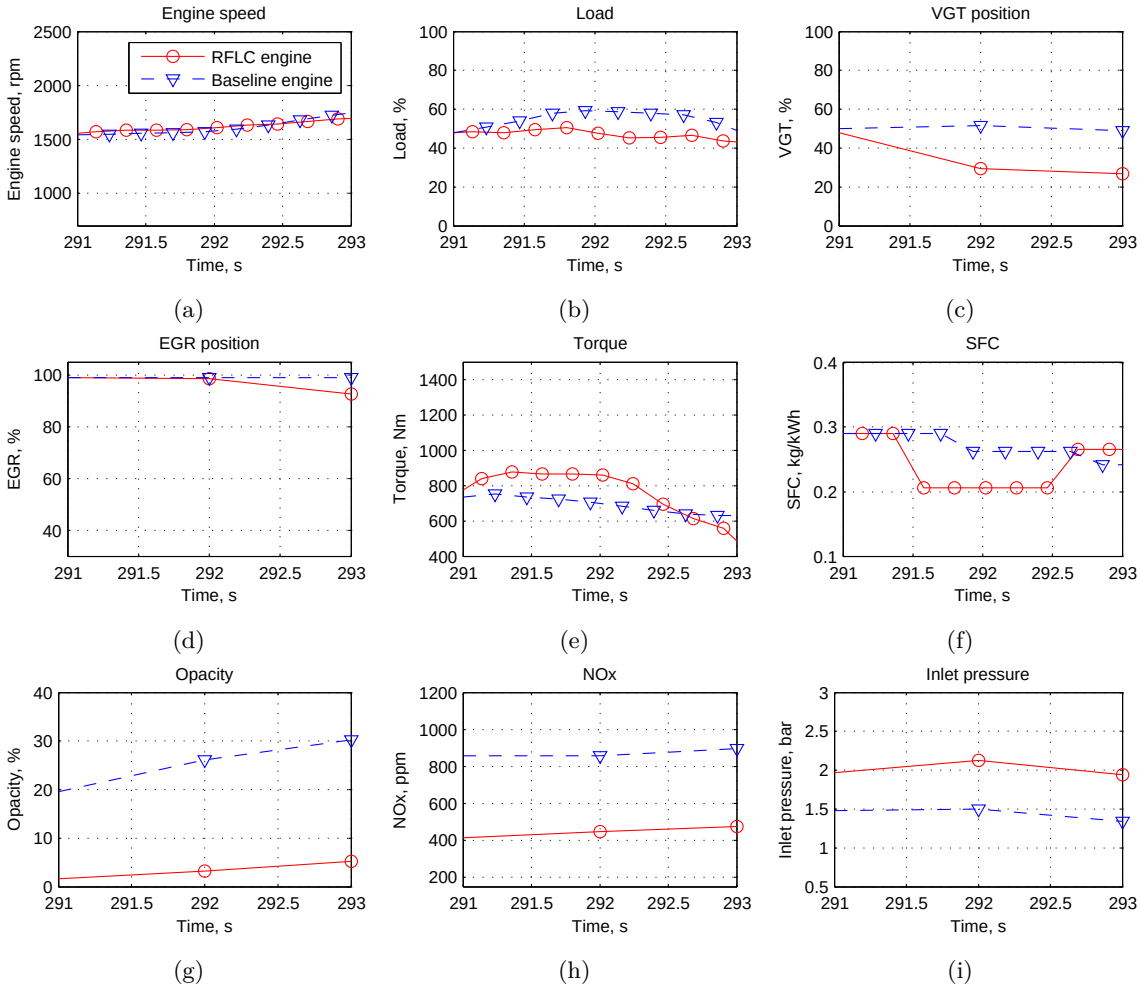

Figure 4.22: Comparison of experimental results of engine performance and emission between baseline engine and VGT/EGR fuzzy logic controlled during 291s -293s.

During 460 s to 465 s, the engine was running at about 2000 rpm (Fig. 4.23 a) with about 65% load (Fig. 4.23 b). Because the opacity (Fig. 4.23 g) at this moment was not high (below 2%), the VGT position (Fig. 4.23 c) was set at about 60% on the RFLC engine which was higher than the baseline engine. The figure shows that the opacity (Fig. 4.23 g) produced by the RFLC engine was slightly higher than the baseline engine due to the lower inlet pressure (Fig. 4.23 i). However, compared to the baseline engine, NO_x

(Fig. 4.23 h) produced by the RFLC engine was 50 ppm lower and SFC (Fig. 4.23 f) was also reduced from about 0.6 kg/kWh to about 0.25 kg/kWh.

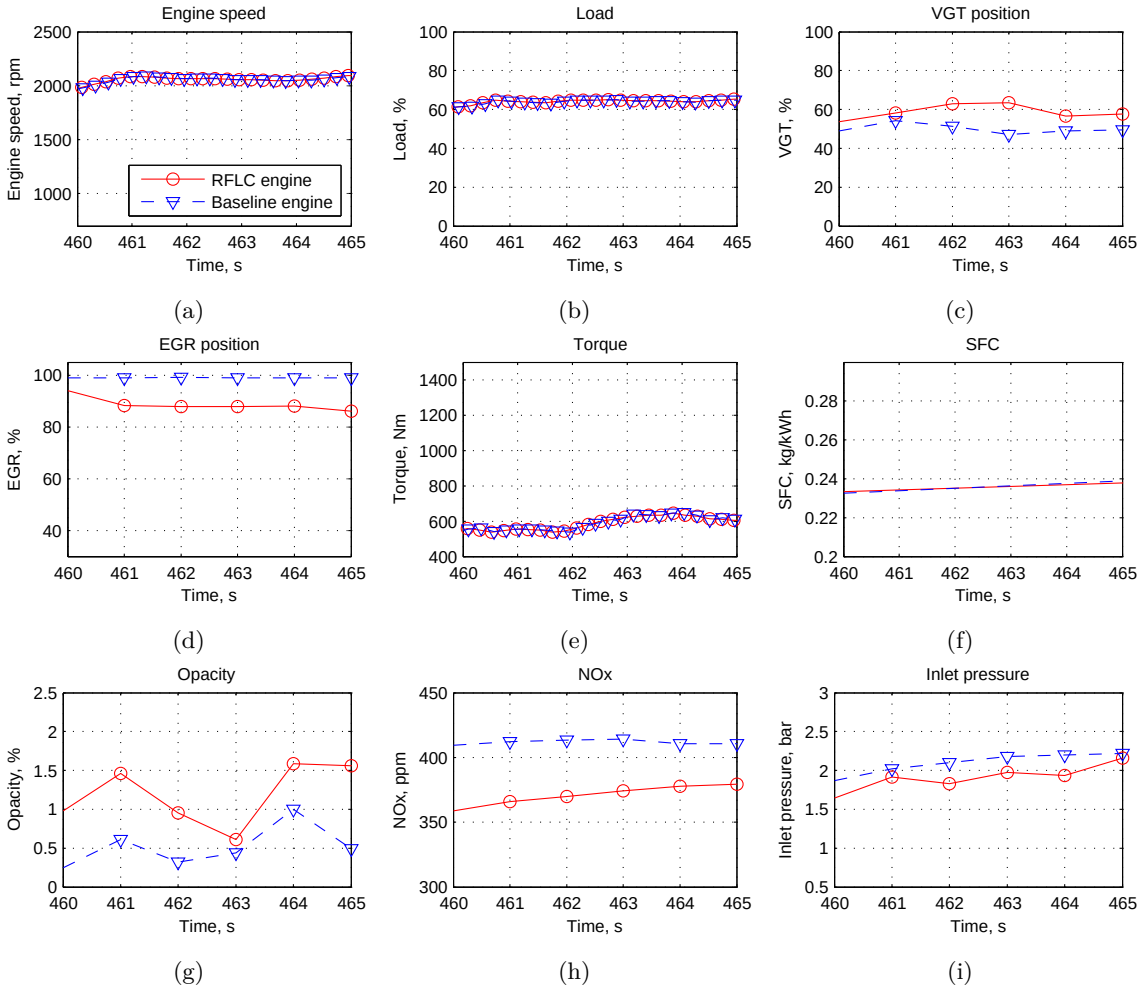

Figure 4.23: Comparison of experimental results of engine performance and emission between baseline engine and VGT/EGR fuzzy logic controlled during 460s-465s.

In order to minimise the influences of measuring errors on the results, the same test was performed three time to calculate the average results. During the whole driving cycle from 0 s to 600 s, compared to the baseline engine, the mean value of exhaust opacity was reduced by 36.8% (from 7.059% to 4.46%) on the RFLC engine, the mean value of NO_x was reduced by 33% (from 573.3 ppm to 384.2 ppm), and the mean value of fueling rate was reduced by 0.85% (from 5.049 g/s to 5.006 g/s).

4.2.9 Repeatability test of fuzzy logic control

In this section, the repeatability test of the fuzzy logic control scheme is reported. The tests were conducted on the CAT3126B engine test bed using the NRTC driving cycle when the engine is fully warmed up. The test was repeated five times.

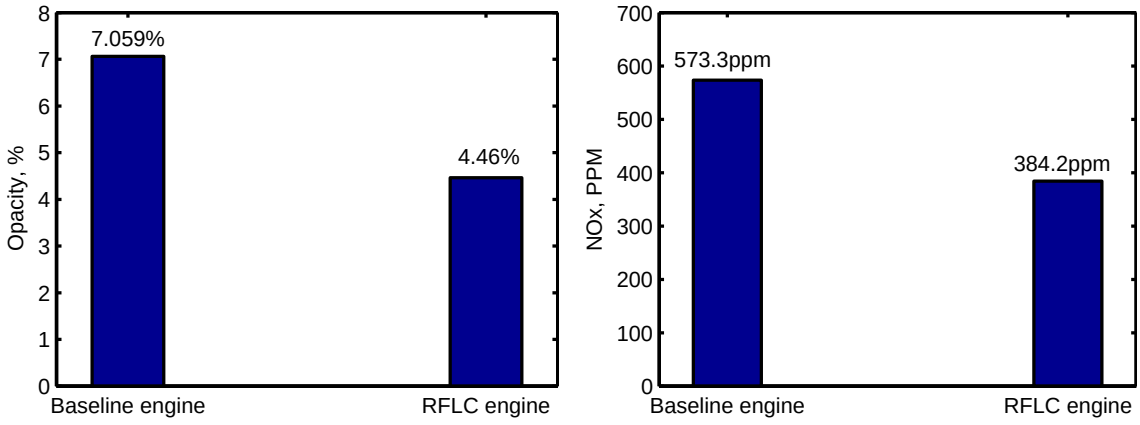

(a) (b)

Figure 4.24: Comparison of the mean value of opacity and NO_x produced during an off-road driving cycle between baseline engine and fuzzy controlled engine: (a) mean value of opacity, (b) mean value of NO_x.

A fraction of the whole NRTC test (from 0 s to 160 s) is extracted, and Fig. 4.25 shows the experimental results of the redundant tests of the fuzzy logic controller. Generally, the redundant test shows good agreement between each repeat, which demonstrates the repeatability of the fuzzy logic control. Engine speed (Fig. 4.25 a) and torque (Fig. 4.25 b) curves are predefined by the NRTC driving cycle. The engine speed is governed by the dynamometer, and torque is achieved by adjusting the pedal position (Fig. 4.25 c) which is controlled by a PID controller. During these five redundant tests, the inlet pressure curves (Fig. 4.25 g), intake air mass flow curves (Fig. 4.25 h), O2 exhaust curves (Fig. 4.25 i), and opacity curves (Fig. 4.25 j) are overlapped most of the test. However, the inlet pressure curves (Fig. 4.25 f) have relatively higher differences between each of them. This might have caused the differences between the VGT position curves (Fig. 4.25 d) and the EGR position curves (Fig. 4.25 e).

Fig. 4.26 shows the mean values of each key engine parameter across the five redundant tests. The differences between the five average values for each engine parameter are trivial, with the standard deviation for each engine parameter shown in Fig. 4.27.

4.3 Fuzzy Logic Control with On-board Emission Predictors

4.3.1 Emission predictors development

The fuzzy logic controllers developed require real-time emission measurement as control input signal, but on-board emission analysers are not currently installed as standard equipments in a vehicle. In order to overcome this problem, on-board emission predictors were

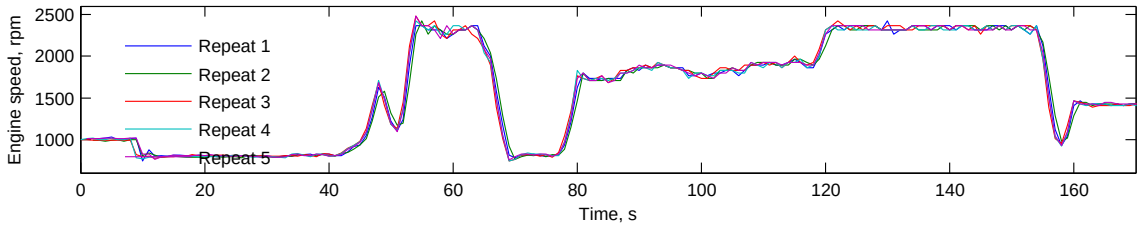

(a)

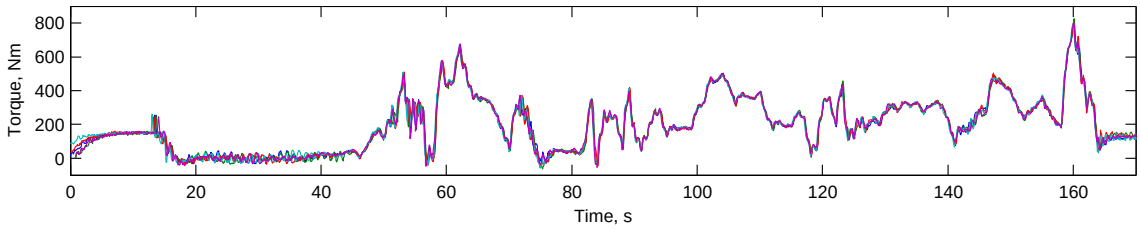

(b)

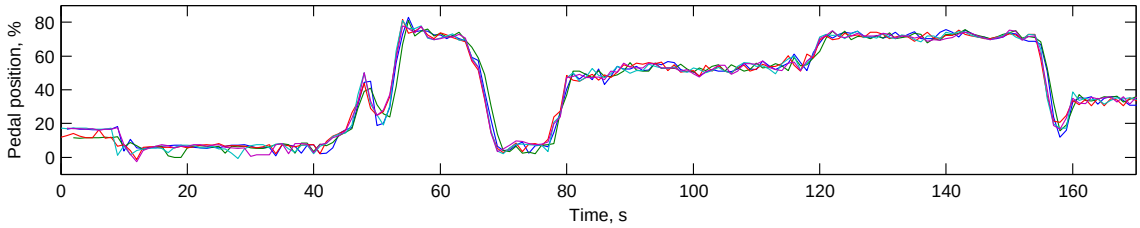

(c)

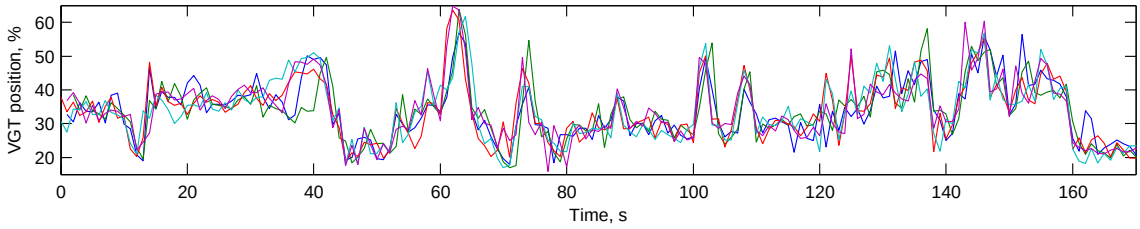

(d)

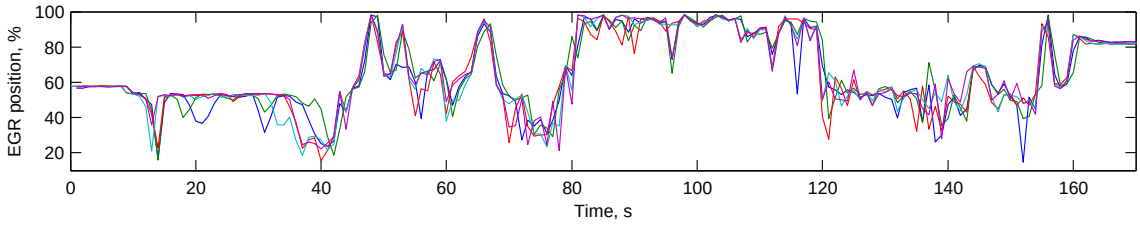

(e)

Figure 4.25: Redundant tests of fuzzy logic controller on CAT3126B engine test bed running on NRTC cycle.

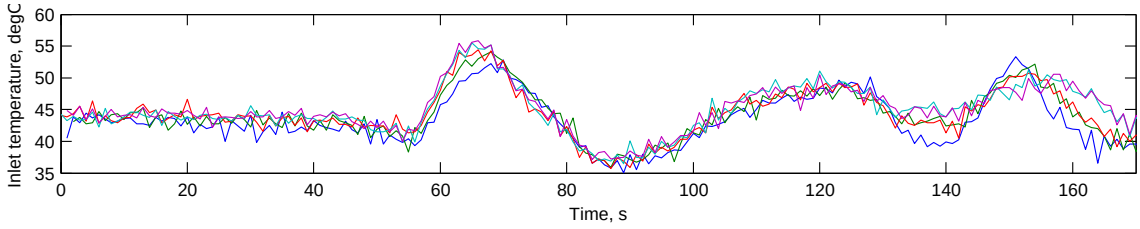

(f)

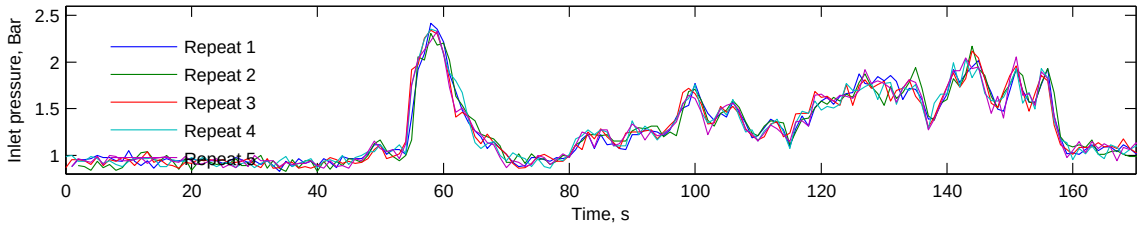

(g)

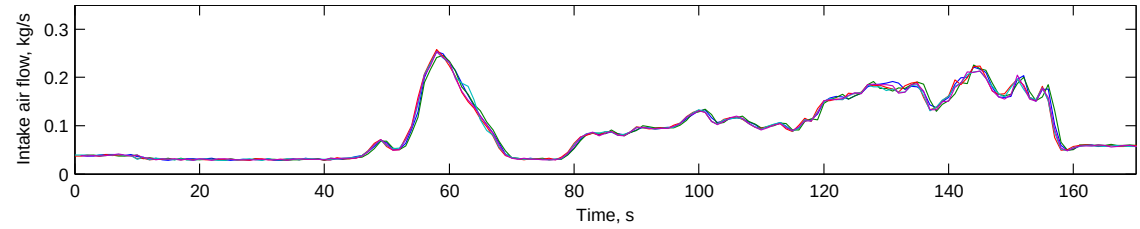

(h)

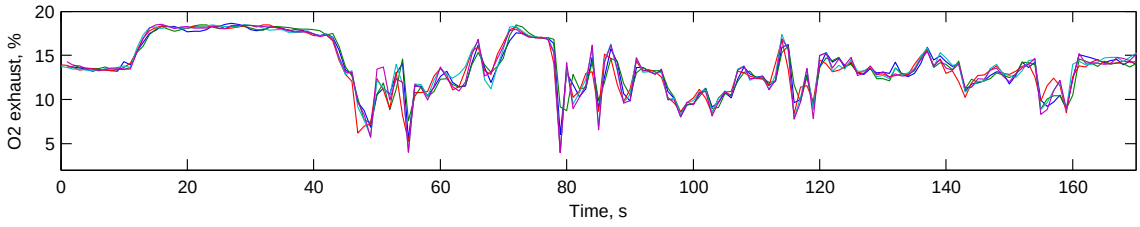

(i)

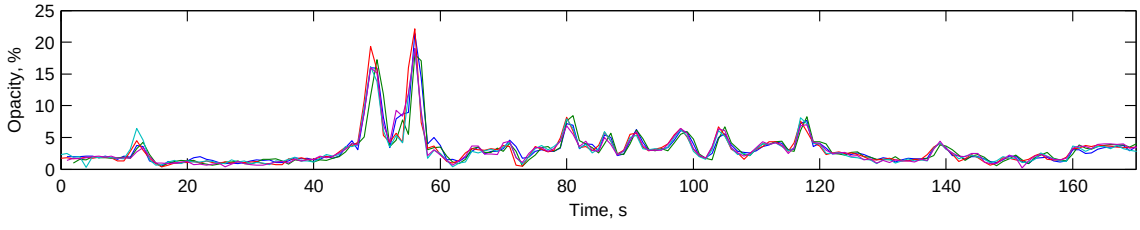

(j)

Figure 4.25: (continued)

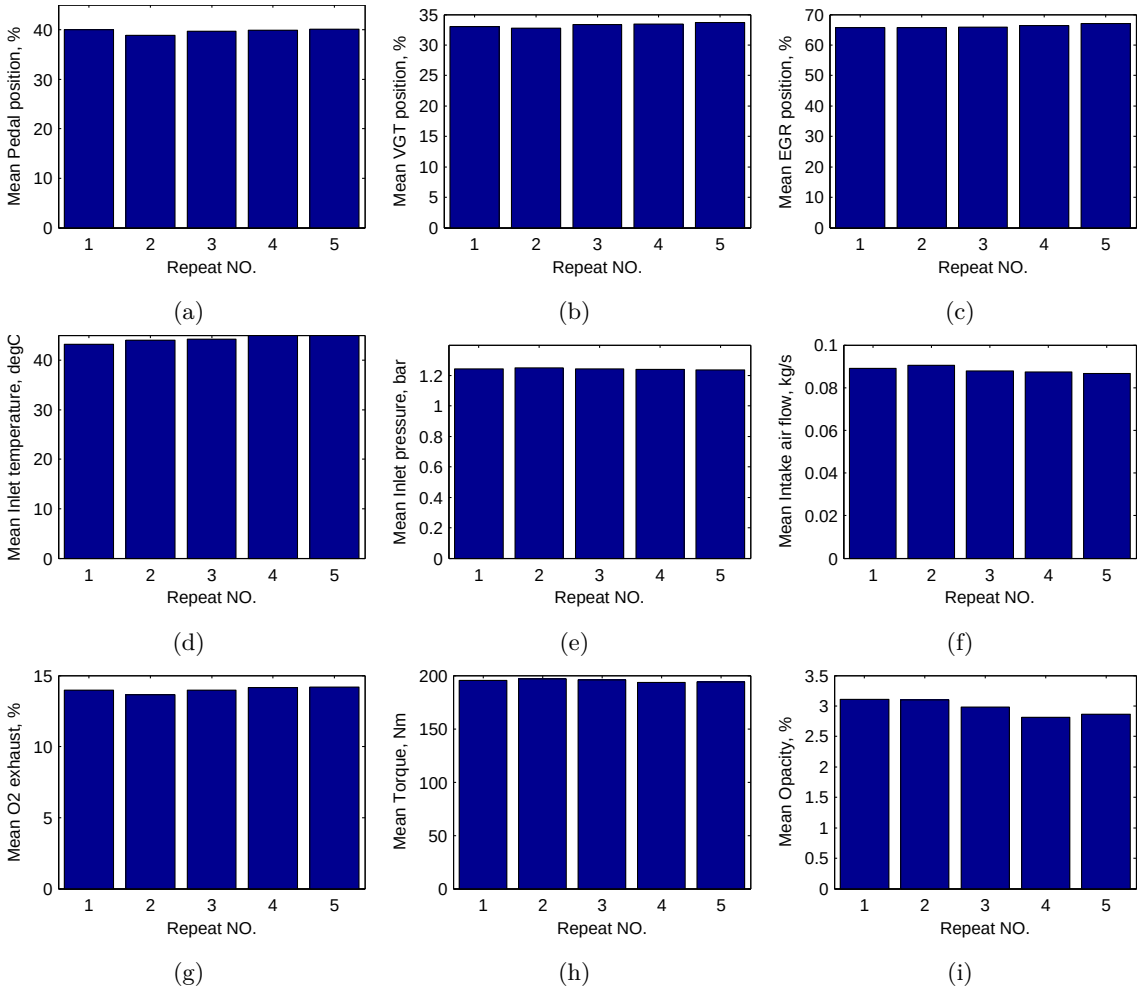

Figure 4.26: Mean value of each engine parameters over five redundant tests.

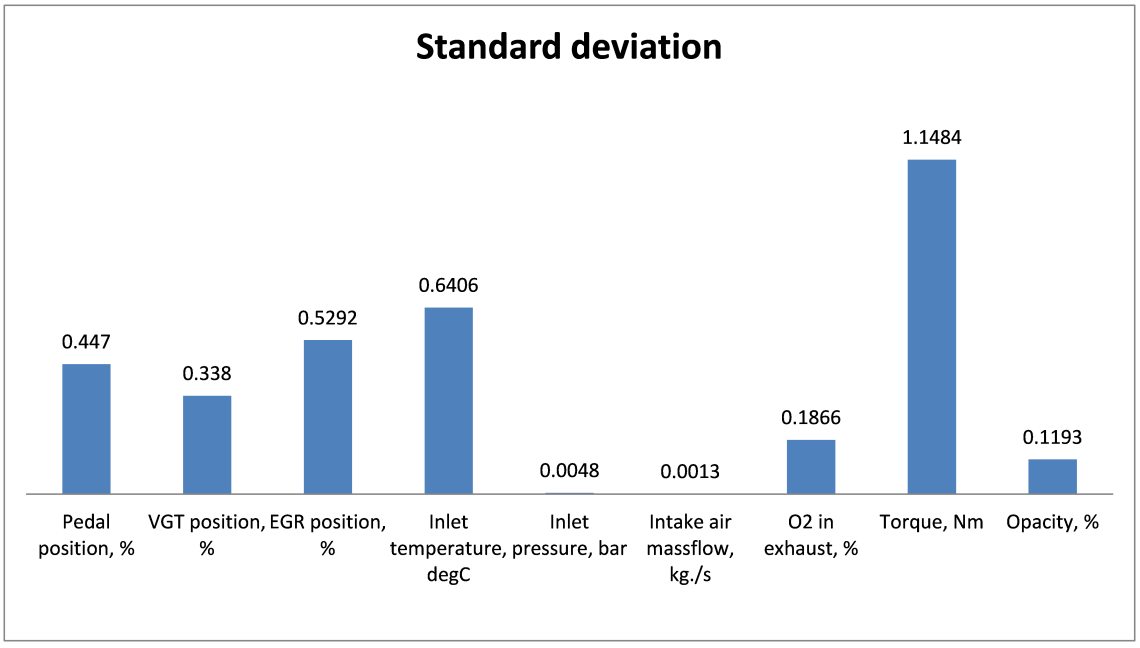

Figure 4.27: Standard deviation of the mean values of each engine parameters.

proposed and developed using ANFIS modelling technique.

The production of soot and NOx by a diesel engine is largely determined by the AFR and combustion temperature, and hence it is possible to predict soot and NOx productions based on the AFR and combustion temperature. AFR and combustion temperature are usually not directly measurable, though they can be reflected in several parameters such as engine speed, oxygen level in inlet manifold, intake air flow, and load demand, which are directly accessible from the ECU. Thus, the emission predictors take engine speed, oxygen level in inlet manifold, intake air flow, and load demand as input signals. Based on these input signals, soot and NOx production can be predicted in real time.

A data set (see Fig. 4.5) includes engine speed, oxygen level in inlet manifold, intake air flow, and the emission measurements required to train the ANFIS. In order to avoid over-fitting during training, the first half of the data set was used as a training data set, the second half of the data set was used as a checking data set. The training data set is selected based on the principle of including representative features as much as possible. The structure of the on-board emission predictor is shown in Fig. 4.28.

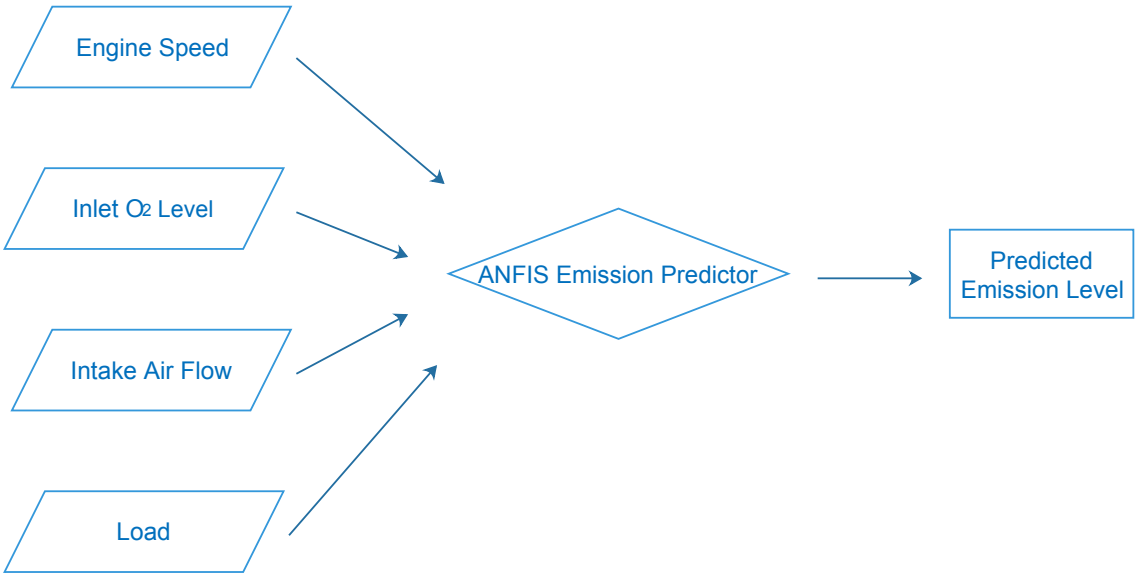

Figure 4.28: The structure of on-board emission predictor.

A fuzzy inference system (FIS) structure has to be generated before training, and this FIS will largely affect the training error. The FIS structure required for training was generated using the 'genfis2' function. This function generates a Sugeno-type FIS structure using subtractive clustering. The syntax of this function is:

$$fismat = genfis2(Xin, Xout, radii) \tag{4.5}$$

Table 4.5: A sample of the data set used to train the on-board emission predictor.

1st column	2nd column	3rd column	4th column	5th column
engine speed, rpm	O2 inlet, %	Intake air flow, kg/s	Load, %	Opacity, %/NOx, ppm
...	...	...		...
1628	12.2	0.177	44.4	1.66
1532	14.8	0.136	37.2	1.05
...	...	...		...
2043	13.8	0.218	57.2	1.34

where $Xin, Xout$ are input and output data sets used for training, respectively. *radii* is a vector that specifies a cluster center's range of influence in each of the data dimensions. If it is a scalar valve, then the value is applied to all data dimensions.

In order to identify the most suitable value of 'radii', multiple values have been used to train the ANFIS for both soot and NOx predictors. After a certain number of training cycles, it should reduce both the training error and checking error as much as possible. Sometimes the training error can be very close to zero, but the checking error increases dramatically. This indicates overfitting, which means the ANFIS gained from this training would not be accurate when it is fed with other data sets apart from the set used to train it. The training and checking errors are normally assessed using root mean square error (RMSEs) [40]. Eq. 4.6 shows the definition of RMSE.

$$RMSE = \sqrt{\frac{\sum (f(x_i) - y_i)^2}{n}} \tag{4.6}$$

where $f(x_i)$ is the predicted data, y_i is the data used to train the ANFIS, n is the number of data points used to train the ANFIS.

On-board soot predictor development

Fig. 4.29 shows the training and checking RMSEs of the soot predictor using 'radii1 - 0.45', 'radii2 - 0.5' and 'radii3 - 0.55' as the ranges of influence of cluster centers. The training and checking RMSEs of 'radii1', 'radii2', and 'radii3' became stable after about 550 epochs and 'radii1' training and checking RMSEs are the lowest among them all and it should be selected to train the ANFIS predictor.

It should also be noticed that the training RMSE of 'radii1' and the training RMSE of 'radii2' become very close after 600 epochs, but the checking RMSE of 'radii2' rises to about 7.6% compared to 7.1% of 'radii1'. This means the predictor is more accurate

when using the training data, but it will become inaccurate when fed with other data sets. This is not preferable because the predictor should be robust enough to work in unknown circumstances.

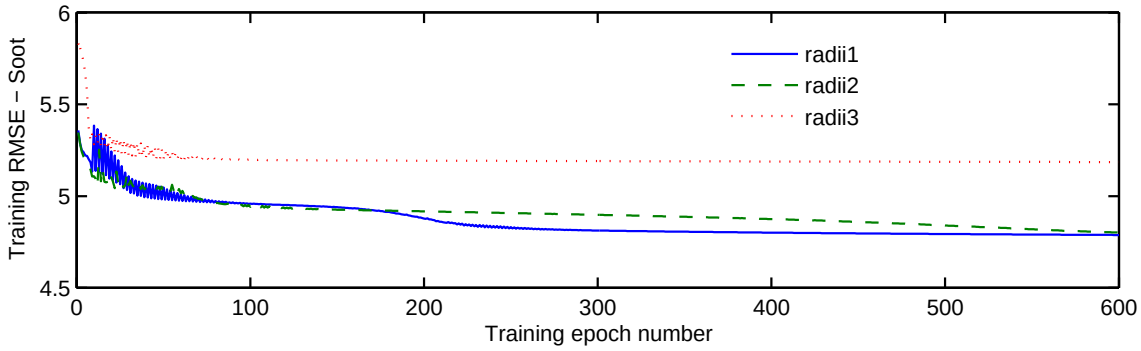

(a)

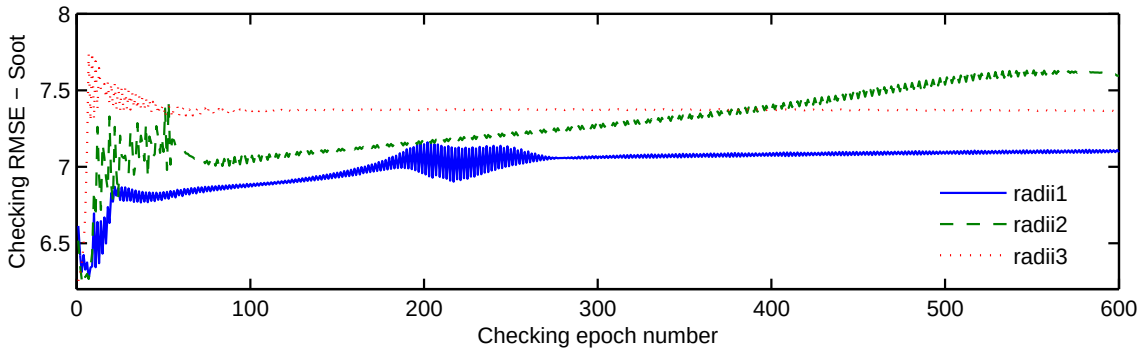

(b)

Figure 4.29: RMSE of the on-board soot predictor. (a) training RMSE (%), (b) checking RMSE (%).

The Soot predictor trained using 'radii1' was evaluated by comparison of the soot level (indicated by opacity) between the measured value and predicted value (Fig. 4.30). It can be seen that, from 0 to 450 seconds, the predicted opacity curves match the measured opacity curve closely. After 450 seconds, the predicted opacity curves are generally higher than those of the measured curve.

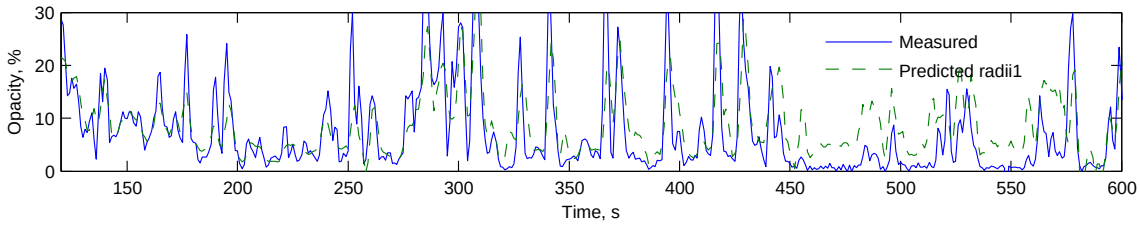

Figure 4.30: Evaluation of the on-board soot predictor trained using 'radii1'.

Fig. 4.31 shows the FIS structure of the on-board soot predictor trained using 'radii1'.

A total of 10 rules have been created during training. in1, in2, in3, and in4 represent the input variables engine speed, intake oxygen percentage, intake air mass flow and load demand, respectively, and out1, which is Sugeno type, represents the predicted opacity. The black curves inside each yellow box illustrate the membership functions created for the corresponding input variable during training.

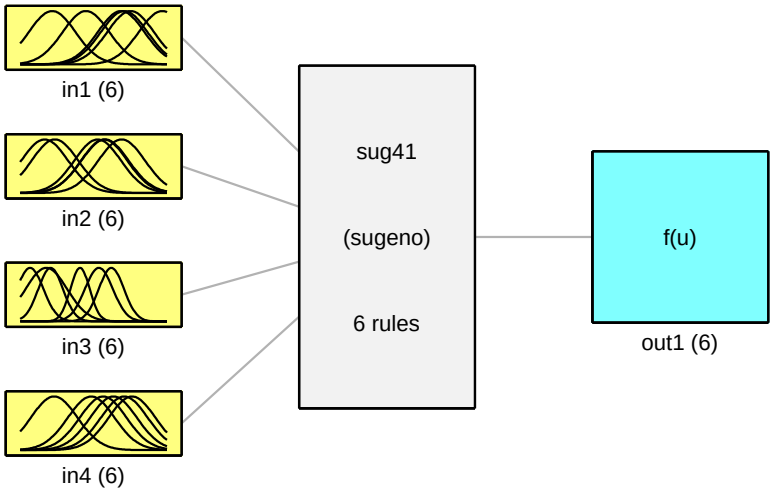

Figure 4.31: FIS structure of on-board soot predictor trained using 'radii1', in1 - engine speed, in2 - intake oxygen percentage, in3 - intake air mass flow, in4 - load demand, out1 - predicted opacity.

Fig. 4.32 shows the surfaces of the on-board soot predictor. These surfaces illustrate how opacity changes with input variables engine speed, intake oxygen percentage, intake air mass flow, and load demand. These surfaces reveal the rules generated for the soot predictor during training. For a given set of values of input variables, an aggregated single output can be calculated by the Sugeno type fuzzy inference method. This single output is the predicted soot production level.

On-board NOx predictor development

Fig. 4.33 shows the training and checking RMSEs of the NOx predictor when trained using 'radii1 - 0.3', 'radii2 - 0.4', and 'radii3 - 0.5' as ranges of influence of cluster centers. All of the training and checking RMSEs become stable after about 600 epochs. When trained using 'radii1', both training and checking errors are the lowest. Hence, it should be selected to train the ANFIS predictor.

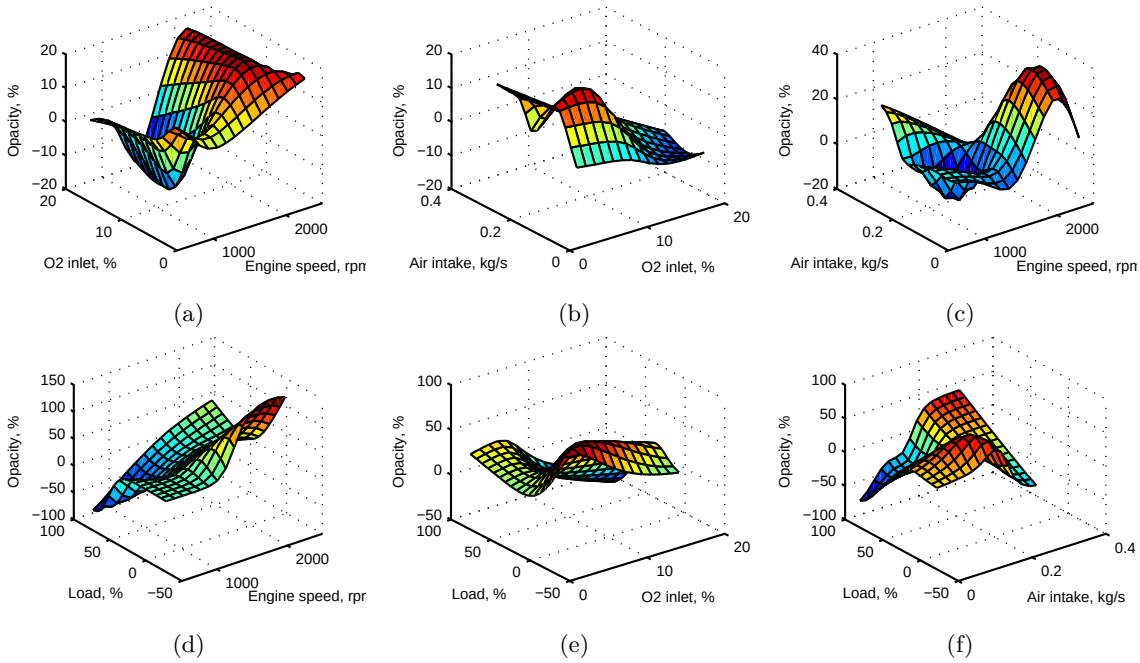

Figure 4.32: Surfaces of the on-board soot predictor trained using 'radii1'.

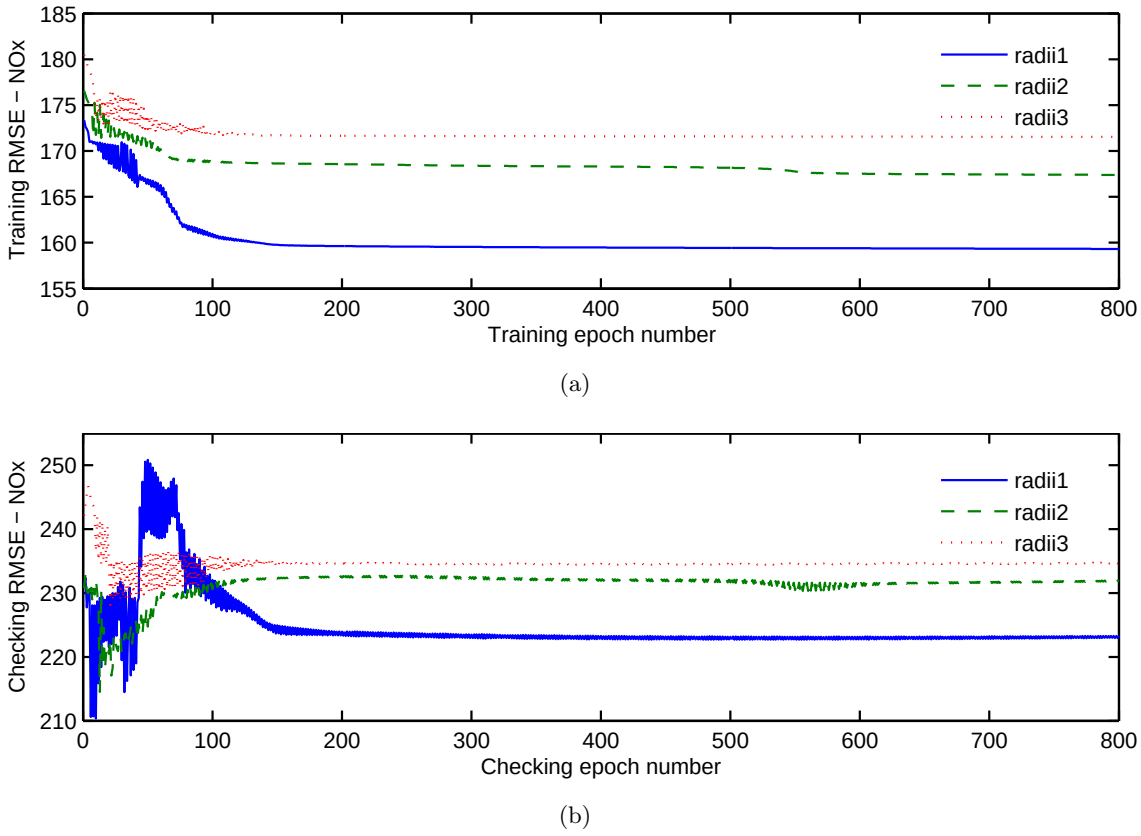

Figure 4.33: RMSE of the on-board NOx predictor. (a) training RMSE (ppm), (b) checking RMSE (ppm).

Fig. 4.34 shows the evaluation of the NOx predictor trained using 'radii1'. Compared to the measured NOx level, the predicted NOx level curve has followed the trend of the measured curve. However, a maximum error of approximately ±200 ppm can be noticed at several time periods.

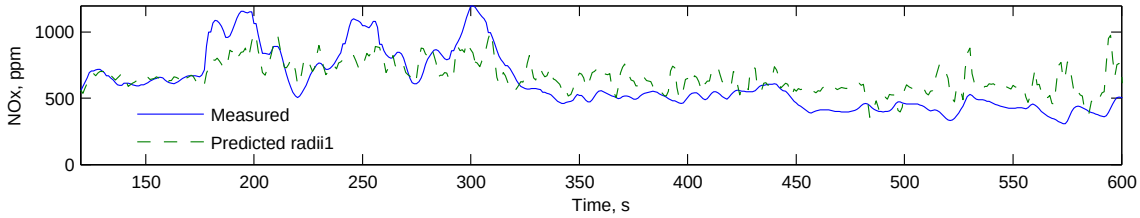

Figure 4.34: Evaluation of the on-board NOx predictor trained using 'radii1'.

Fig. 4.35 shows the FIS structure of the on-board NOx predictor trained using 'radii1'. A total of 10 rules have been created during training. in1, in2, in3, and in4 represent the input variables engine speed, intake oxygen percentage, intake air mass flow and load demand respectively and out1 which is Sugeno type represents the predicted NOx level. The black curves inside each yellow box illustrate the membership functions created for the corresponding input variable during training.

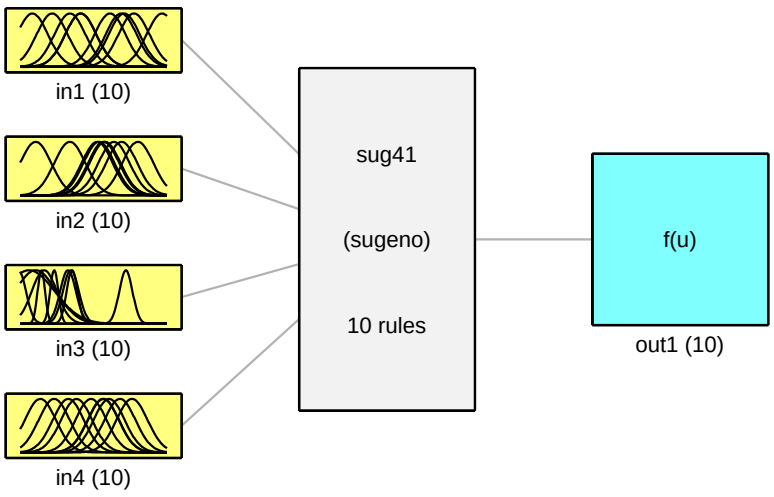

Figure 4.35: FIS structure of on-board NOx predictor trained using 'radii1', in1 - engine speed, in2 - intake oxygen percentage, in3 - intake air mass flow, in4 - load demand, out1 - predicted NOx level.

Fig. 4.36 shows the surfaces of the on-board NOx predictor. These surfaces illustrate how NOx production changes with input variables engine speed, intake oxygen percentage,

intake air mass flow, and load demand. These surfaces reveal the rules generated for the NOx predictor during training. For a given set of values of input variables, an aggregated single output can be calculated by the Sugeno type fuzzy inference method. This single output is the predicted NOx production level.

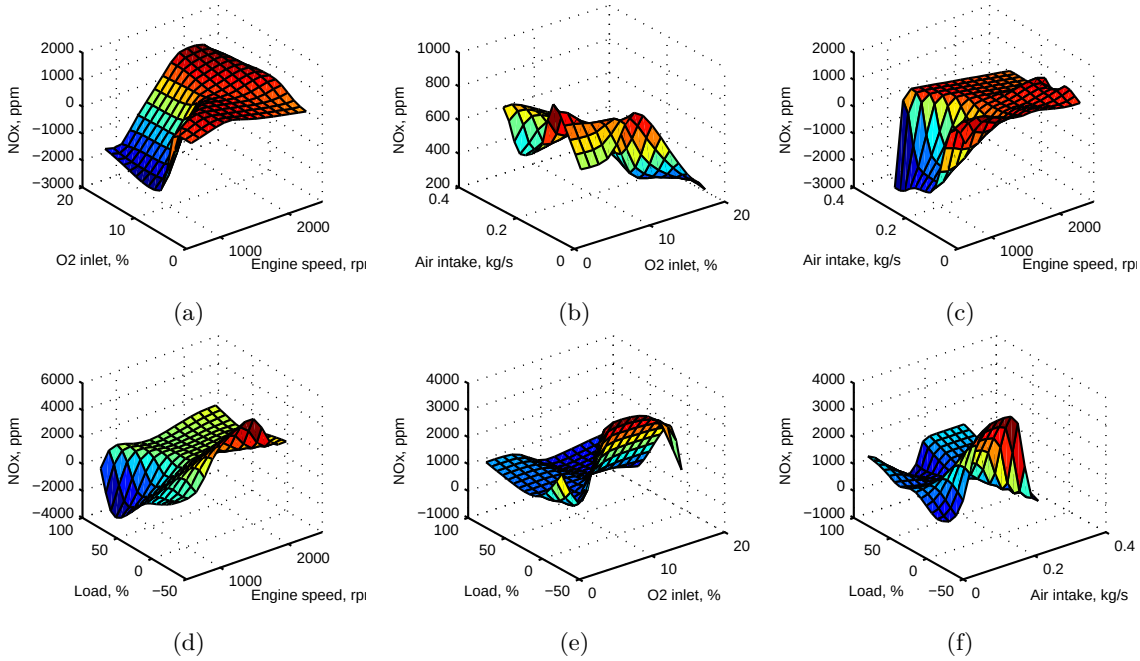

Figure 4.36: Surfaces of the on-board NOx predictor trained using 'radii1'.

4.4 ANFIS Control

4.4.1 Controller development

In the section above, the development of emission predictors using ANFIS modelling technique was described. The emission predictors are capable of predicting soot and NOx productions of a diesel engine in real time. The predicted emissions results can then be fed to the fuzzy logic controllers described in Section 4.2 as input signals in real time. This makes it possible to use the proposed fuzzy logic controllers to control the VGT and EGR when on-board emission analysers are not available.

Alternatively, it is also possible to predict VGT and EGR positions using ANFIS modelling technique by learning a data set created by controlling the VGT and EGR using fuzzy logic controller. After running the engine with EGR and VGT controlled by the fuzzy logic controller (simulation or experiment), several data sets (matrixes) can be created. Apart from the last column, each column of these data sets (matrixes) are the input variables (vectors), such as engine speed, load signal, inlet pressure, etc and the

last column is the controller output variable EGR position or VGT position. The ANFIS controllers are able to learn the relationship between these input variables and the output variable and next time when a set of values of all the input variables are fed to the ANFIS controller, an answer will be given (output control variable) based on the values of the input variables. In this way, an ANFIS can learn the behaviour of a dynamic system. From this point of view, it is possible to remove the NOx and soot from the input variables, and train the ANFIS with the rest of the input variables. Once the ANFIS system has been successfully trained, it will be able to control the EGR and VGT in a vehicle on the road without NOx and soot as input variables.

Similar to the development process of the ANFIS emission predictors, two FIS structures was generated using function 'genfis2' (Eq. 4.5) before training. Two data sets were created: one will be used to train the EGR ANFIS controller; the other will be used to train the VGT ANFIS controller. First half of each data set will be used as training data, the last half of each data set will be used as checking data. As explained before, this is to avoid over-fitting during the training process. In order to include as many different driving patterns (acceleration, deceleration, sharp load change, mild load change, etc) as possible in the training data set, a complex load signal curve was fed to the ECU of the BOOST model. Thus, that the ANFIS can learn as many representative features as possible from different driving patterns. The EGR training data set is composed with engine speed and load signal as the input variables, EGR position as the output; the VGT training data set is composed with engine speed, load signal as well as inlet pressure, current EGR position as the input variables, with the VGT position as the output variable. 'radii1 - 0.4', 'radii - 0.5', and 'radii - 0.6' were used as the ranges of influence of cluster centers for both VGT and EGR ANFIS controllers. The overall structure of the ANFIS control is shown in Fig. 4.37.

When validating the performance of the ANFIS controller, a different load signal curve will be fed to the ECU, which can demonstrate the ANFIS controller is independent of the driving conditions.

VGT ANFIS controller development

Fig. 4.38 shows the training and checking RMSEs of the VGT ANFIS controller after 5 epochs of training using 'radii1', 'radii2', and 'radii3' as cluster center's range of influence. The training RMSEs of 'radii1' and 'radii2' are very close and they have dropped to less than 0.05 after 3 epochs, while the training RMSE of 'radii3' is higher which is about 0.16.

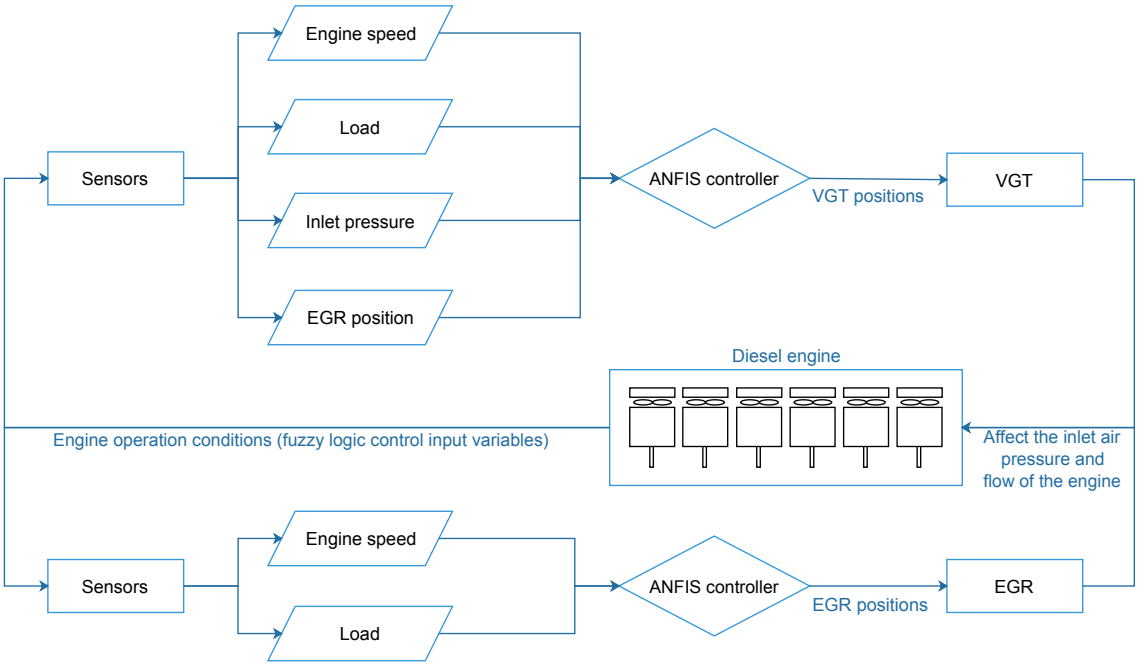

Figure 4.37: ANFIS controller overall structure.

The RMSE of 'radii2' is the lowest among the checking RMSEs of these three. Hence, 'radii2' is selected as the best cluster center's range of influence for the training of VGT ANFIS controller.

After training, the VGT ANFIS controller was evaluated by comparing the predicted output (VGT position) with the output data (VGT position) of fuzzy logic controller which used to train the ANFIS (see Fig. 4.39). It can be seen that the predicted VGT position has followed the VGT position output of the fuzzy logic controller most of the time. During about 6 to 8 seconds and 28 to 30 seconds, there is a maximum of 0.1 difference between the predicted VGT position and the fuzzy logic controller VGT position.

Fig. 4.40 shows the structure of the FIS generated after the training. There is a total of 4 rules generated and the curves of input variables in1, in2, in3, and in4 represent the membership functions generated for input variables engine speed, load demand, inlet pressure, and EGR position respectively, out1 is the predicted VGT position which is Sugeno type.

Fig. 4.41 shows the surfaces of the VGT ANFIS controller between the predicted output and all the input variables. These surfaces reveal the rules generated for the VGT ANFIS controller during training. For a given set of values of input variables, an aggregated single output can be calculated by the Sugeno type fuzzy inference method. This single output is the predicted VGT position.

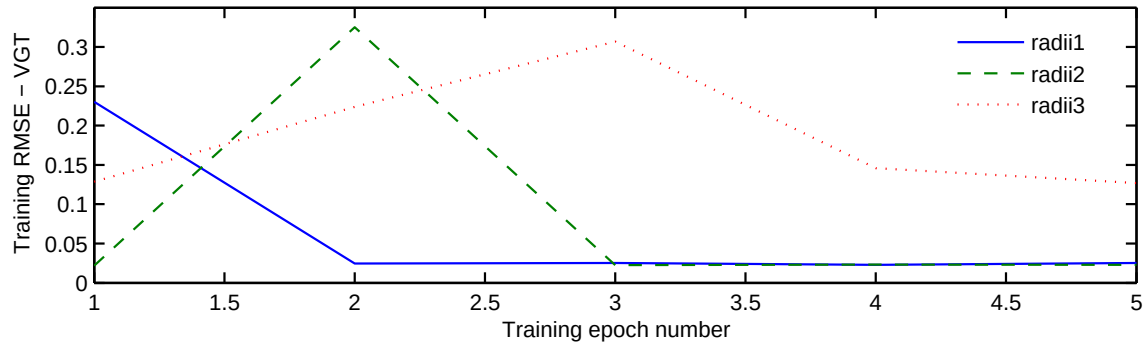

(a)

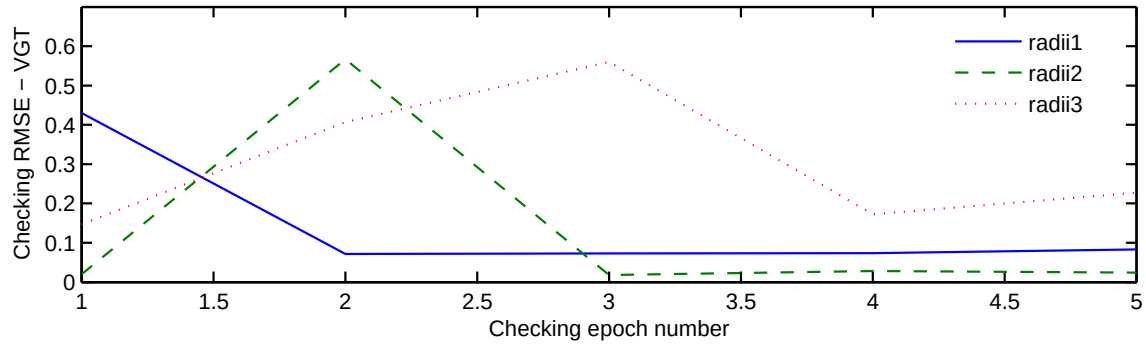

(b)

Figure 4.38: RMSE of VGT ANFIS controller. (a) training RMSE (-), (b) checking RMSE (-).

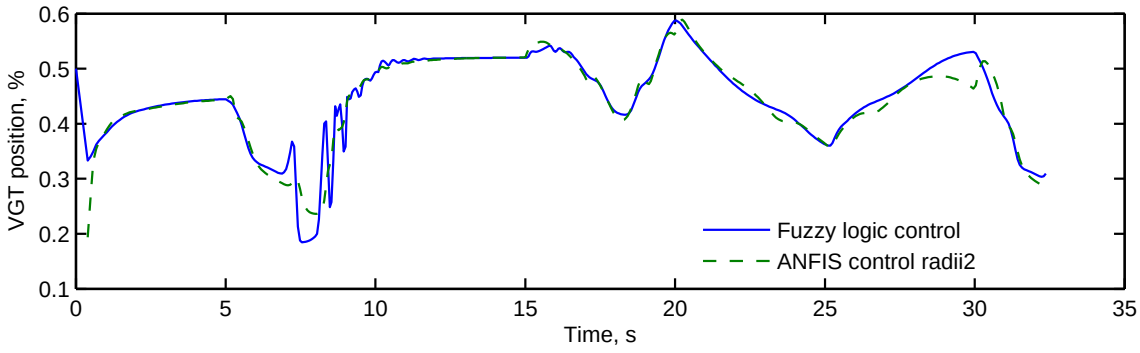

Figure 4.39: Evaluation of the VGT ANFIS controller.

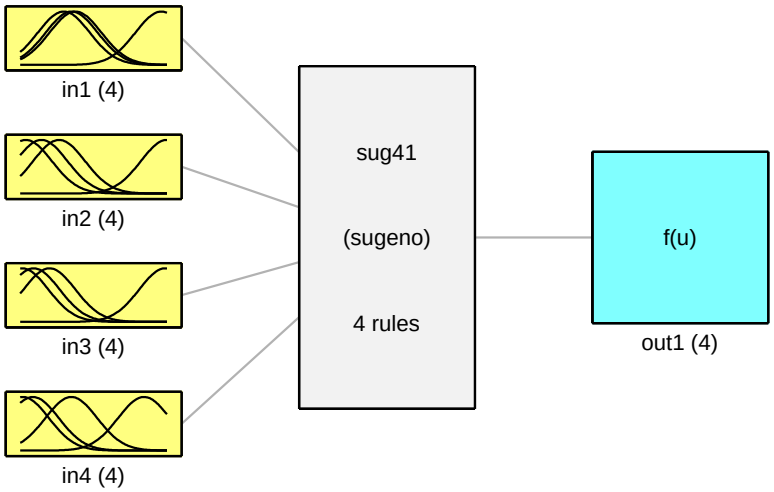

Figure 4.40: FIS structure of VGT ANFIS controller, in1 - engine speed, in2 - load demand, in3 - inlet pressure, in4 - EGR position, out1 - VGT position.

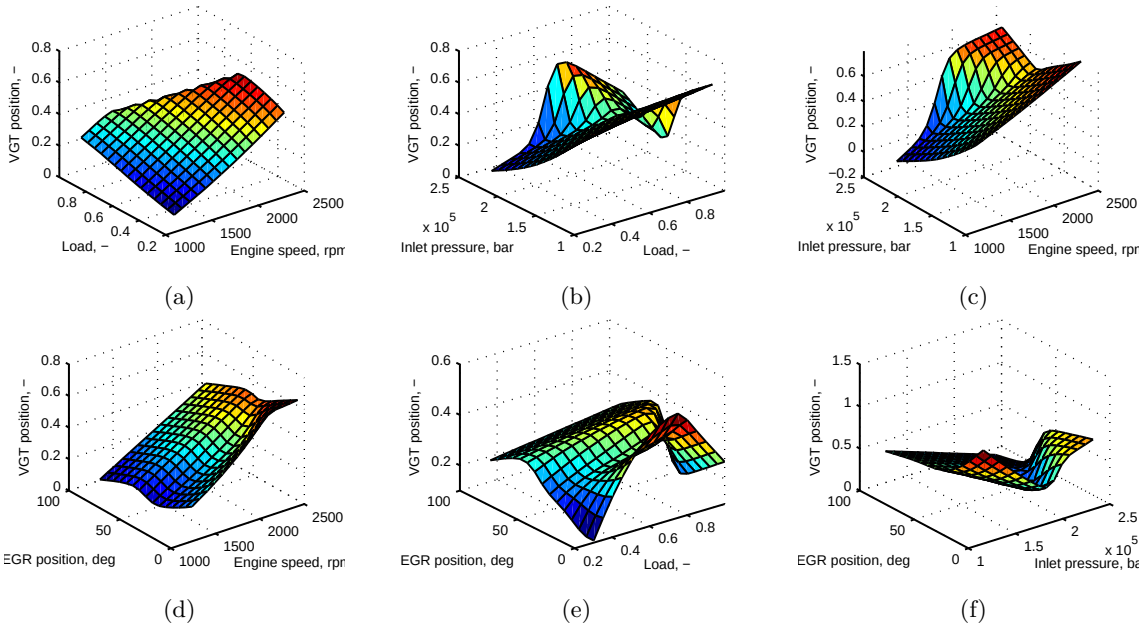

Figure 4.41: Surfaces of the VGT ANFIS controller.

EGR ANFIS controller development

The FIS of EGR ANFIS controller was created using function 'genfis2' as well. Fig. 4.42 shows the training and checking RMSEs when trained using 'radii1', 'radii2', and 'radii3' as ranges of influence of cluster centers. The lowest training RMSE is acquired when trained using 'radii2', which is about 1.5 degree, though the lowest checking RMSE is acquired when trained using 'radii1' and the training RMSE of 'radii1' is very close to that of 'radii2', which is about 3 degrees. Thus, 'radii1' is selected as the best ranges of influence of cluster centers.

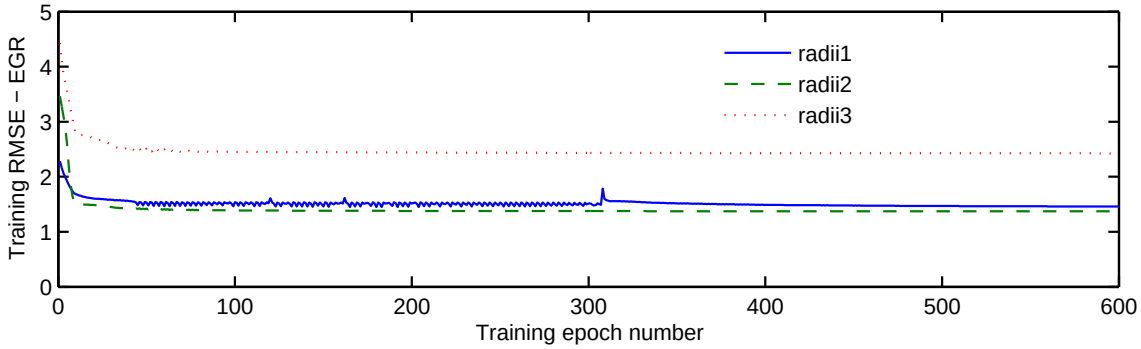

(a)

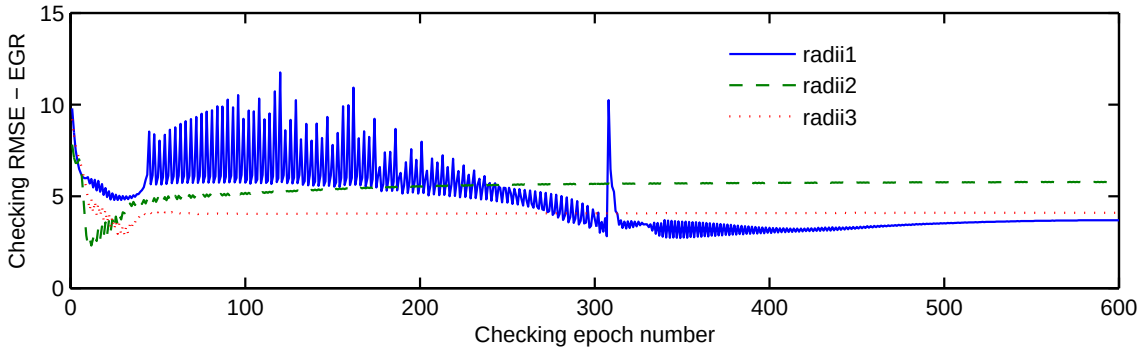

(b)

Figure 4.42: RMSE of EGR ANFIS controller. (a) training RMSE (degree), (b) checking RMSE (degree).

After training of the FIS generated using 'radii1', the ANFIS gained was evaluated by comparing the predicted EGR position with the fuzzy logic-controlled EGR position (see Fig. 4.43). It can be seen that the predicted EGR position has closely followed the EGR position controlled by the fuzzy logic controller most of the time. At around 25 seconds, the predicted EGR position is slightly lower than that of the EGR position controlled by the fuzzy logic controller.

The FIS structure of the EGR ANFIS controller after training is shown in Fig. 4.44. A total of five rules has been created. Blocks in1 and in2 show the membership func-

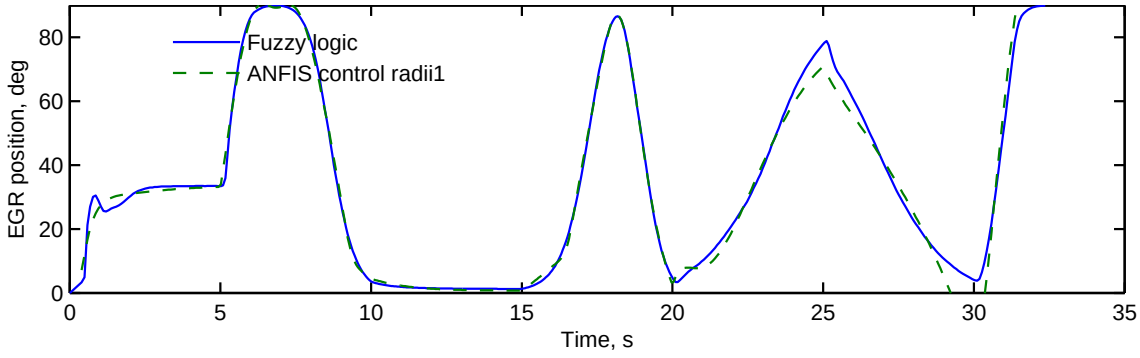

Figure 4.43: Evaluation of the EGR ANFIS controller.

tions generated for input variables engine speed and load demand, respectively, and out1 represents the predicted EGR position, which is Sugeno type.

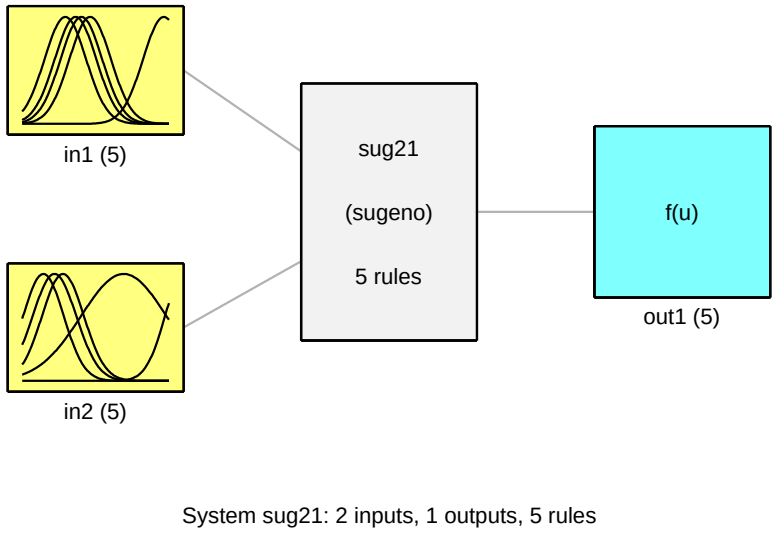

Figure 4.44: FIS structure of EGR ANFIS controller, in1 - engine speed, in2 - load demand, out1 - EGR position.

The surface of the EGR ANFIS controller between the predicted EGR position and input variables is shown in Fig. 4.45. These surfaces reveal the rules generated for the EGR ANFIS controller during training. For a given set of values of input variables, an aggregated single output can be calculated by the Sugeno type fuzzy inference method. This single output is the predicted EGR position.

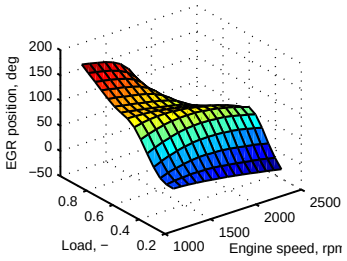

Figure 4.45: Surface of the ANFIS EGR controller.

4.5 Chapter Summary and Conclusions

In this chapter, PID controller, fuzzy logic controller, and ANFIS controller for VGT and EGR control were developed and tested under transient running conditions. Emission predictors using the ANFIS modelling technique were also developed to supply the fuzzy logic controller with predictions of soot and NOx productions when online measurement of the soot and NOx is not available.

To develop the PID controller, set-points of inlet pressure and EGR mass fraction need to be determined first. The set-points should optimise engine operation and minimise emissions to the lowest level. There is a trade-off between soot and NOx productions, which has to be taken into account when determining the set-points. After the determination of the set-points, the coefficients of the PID controller have to be carefully tuned in order to achieve an ideal response time and settling time. In this application, only the P term and I term are enough to achieve an acceptable control performance.

Instead of determining the set-points required by the PID controller, fuzzy logic rules are required by the fuzzy logic controller. The fuzzy logic control rules are written based on experimental investigations of the VGT and EGR. How VGT and EGR positions affect the engine performances and emissions under different engine running conditions were investigated on the CAT3126B test bed. After this, membership functions of each input and output variables have to be defined based on either physical limitations of the test bed and experimentally determined values. The developed fuzzy logic controller was then tested on the test bed running in an NRTC driving cycle, and the engine performances and emissions when controlled by the fuzzy logic controller have been compared with the baseline engine performance and emissions.

A repeatability test of the fuzzy logic controller has been carried out on the CAT3126B test bed. Experimental results show that each redundant test has good agreement with each other and the standard deviation of the mean values of each key engine parameter are trivial. This demonstrates that this control scheme is repeatable and reliable.

The ANFIS controller is developed by learning from a data set that is generated by running the engine with the fuzzy logic controller. The ANFIS controller is able to control the VGT and EGR without online emission measurements. The initial FIS for training was generated using the function 'genfis2', the key parameter is 'radii', which is a vector that specifies a ranges of influence of cluster centers in each of the data dimensions. In order to find most suitable value of 'radii', different values of 'radii' have been tried during training. RMSE is used to assess the fitness of training and checking of the ANFIS. When the RMSEs of training and checking are both small, the ANFIS acquired can be selected to control. If the RMSE of training is small but the RMSE of checking is high, overfitting has occurred and this is what should be avoided.

Emission predictors for soot and NOx are also developed using ANFIS modelling technique. The predictors can be used to provide the fuzzy logic controller with predicted soot and NOx levels when online emission measurement is not available. Similar to that of the ANFIS controller, the emission predictor was developed by learning from an experimental data set which includes soot and NOx measurements. After training, the predictor is able to estimate emission productions of soot and NOx based on instant engine speed, inlet oxygen level, intake air flow, and load demand in real time. Again, the initial FIS of training was generated by the function 'genfis2', and the fitness of the training is assessed by RMSEs of the training and checking.

Chapter 5

Robustness Evaluation

Uncertainties may suddenly or gradually happen while a dynamic system, such as diesel engine, is operating and this will affect the running conditions of the system. A real-time controller should have the ability or tolerance to allow this to happen. Ideally, the controller should be able to self-adapt to these uncertainties and changes. For this reason, it is necessary to evaluate the robustness of the fuzzy logic controller. In this chapter, the robustness evaluation of the fuzzy logic controller is given. The evaluation would include a test of sudden air leak [17, 29, 56, 82] of the inlet pipe and a test of mechanical efficiency drop of the VGT. Because it's more convenient to design and simulate these tests, these evaluations were performed using the transient engine model.

5.1 Sudden air leakage

5.1.1 Simulation design

A sudden air leakage in the air inlet pipe area may suddenly happen without notice due to material deterioration. In the lifecycle of engines, leakages can occur in the intake manifold, which will result in mismatches between the mixture in the cylinder and the reference mixture. These mismatches can have dramatic effects. For example, they generate extra pollution and can also result in loss of horsepower. A controller should be able to make necessary adjustments in response to the sudden change of inlet pressure and flow.

To simulate the sudden air leak around the inlet pipe area, a few modifications have been made to the engine model. A restriction element has been added into the intake pipe after the inter-cooler (see Fig. 5.1).

The restriction element represents the site of the air leak, and by varying the flow coefficient of the restriction it is possible to change the magnitude of the leak. In this

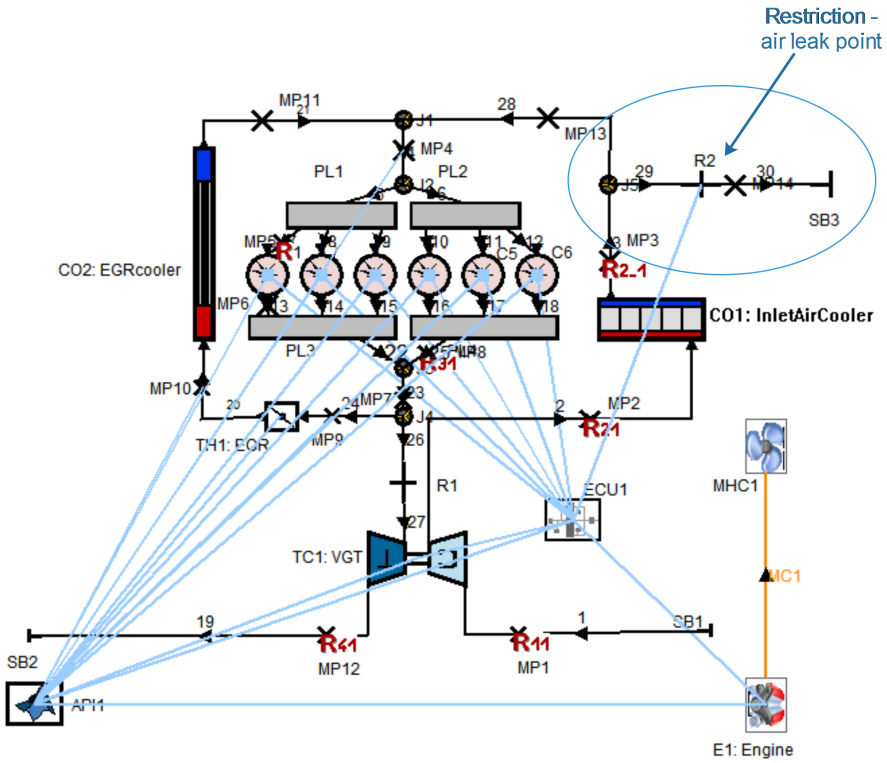

Figure 5.1: Engine model modified with air leak around intake pipe area.

study, three different flow coefficients have been applied and tested and the simulation has been performed under engine acceleration, deceleration and cruise states.

5.1.2 Simulation results

Acceleration

The simulation results of sudden air leak tests with three different amplitudes of air leak are compared with the simulation results of a scenario in the absence of an air leak. The flow coefficient set for air leak tests are listed in Table. 5.1 below.

Table 5.1: Flow coefficients set for 3 different amplitudes of air leak.

Sudden air leak 1	0.175
Sudden air leak 2	0.35
Sudden air leak 3	0.5

Fig. 5.2 shows the air leak tests under engine acceleration state. It can be seen that during 4 s and 8 s of the test, load demand (Fig. 5.2 a) increases from 0.6 to 1, correspondingly engine speed increases from 1800 rpm to 2300 rpm. A sudden air leak

happens at 5.5 s and the air leak ratio[1] gradually increases since that time (see Fig. 5.2 b). The air leak ratios of sudden air leak tests 1, 2, and 3 jump from 0% to about 2%, 4%, and 5% respectively and then continue to increase gradually afterwards. Due to the air leak, inlet pressure drops accordingly. Responding to this disturbance, the fuzzy logic controller has adjusted the VGT and EGR positions to compensate the pressure loss due to the air leak. The VGT position is lower after the happening of air leak compared to the VGT position when there is no air leak, and the more severe the air leak, the lower the VGT position (see Fig. 5.2 c). Because the engine speed is over 2000 rpm after the air leak happens, the EGR position has been kept low by the fuzzy logic control rules, and it does not actively respond to the NOx change (Fig. 5.2 d). Because of the active adjustment of the VGT position, engine torque does not drop noticeably after the air leak happens, and at 8 s in the simulation, all the engine torques of air leak tests 1, 2, and 3 mimicked the values of engine torque in the absence of air leak. Similar results can be found with soot. Due to the EGR valve not being under active control when engine speed is high, there is no obvious improvements in NOx.

Deceleration

Fig. 5.3 shows a sudden air leak happens while the engine is deceleration. As load demand (Fig. 5.3 a) is decreasing from 0.9 s to 0.5 s of the test, engine speed (Fig. 5.3 j) is gradually decreasing from about 2300 rpm to 2000 rpm. The sudden air leak happens at about 5.5 s, it can be seen that the air leak ratio (Fig. 5.3 b) of these 3 tests at 5.5 s suddenly jump from 0 to about 2%, 4.5%, and 6.5% respectively. As the load demand is decreasing, the air leak ratio starts to drop once reaches its maximum value. In order to compensate for the air leak which would cause inlet pressure (Fig. 5.3 e) drop, the fuzzy logic controller has adjusted the VGT position and EGR position accordingly. VGT position (Fig. 5.3 c) has been set lower and lower as the amplitude of the air leak increases and the adjustments start once the air leak happens. The adjustments of EGR position (Fig. 5.3 d) follow the same trend as the adjustments of the VGT position, however, they only start at about 6.8 s when the engine speed has dropped to about 2100 rpm. This is because one of the fuzzy logic rules of EGR control only allow it to operate the EGR valve in the medium engine speed range. Because of the adjustments, the engine torque (Fig. 5.3 g) has not been affected by the sudden air leak, soot (Fig. 5.3 h) and NOx (Fig. 5.3i) increases slightly

[1] $$air\ leak\ ratio = mass\ of\ air\ leakage / mass\ of\ total\ intake\ air$$

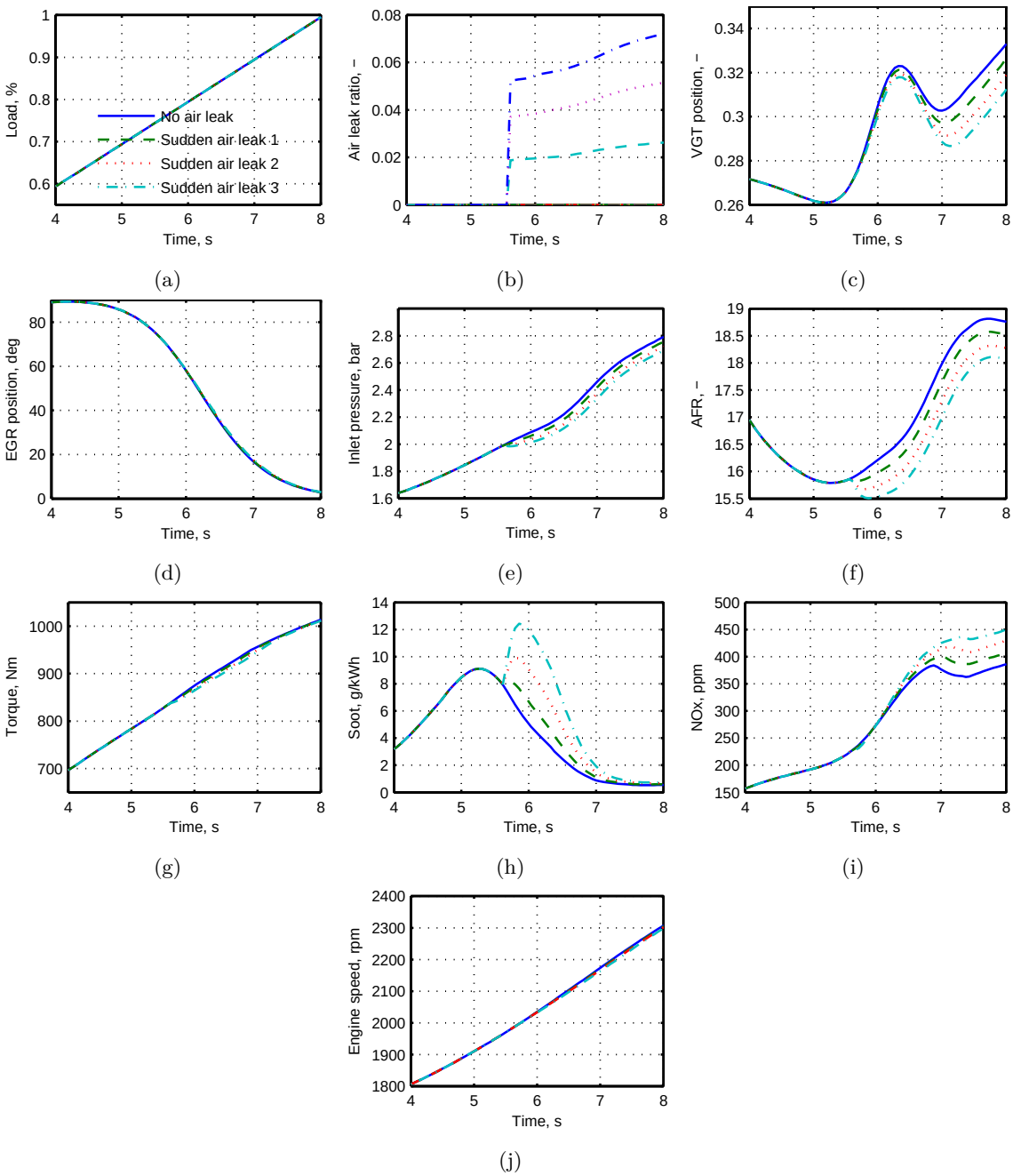

Figure 5.2: Robustness evaluation of the fuzzy logic controller when an air leak suddenly happens in the intake pipe area while the engine is accelerating.

when the air leak happens but they gradually return to the original value in less than 2 s after the air leak.

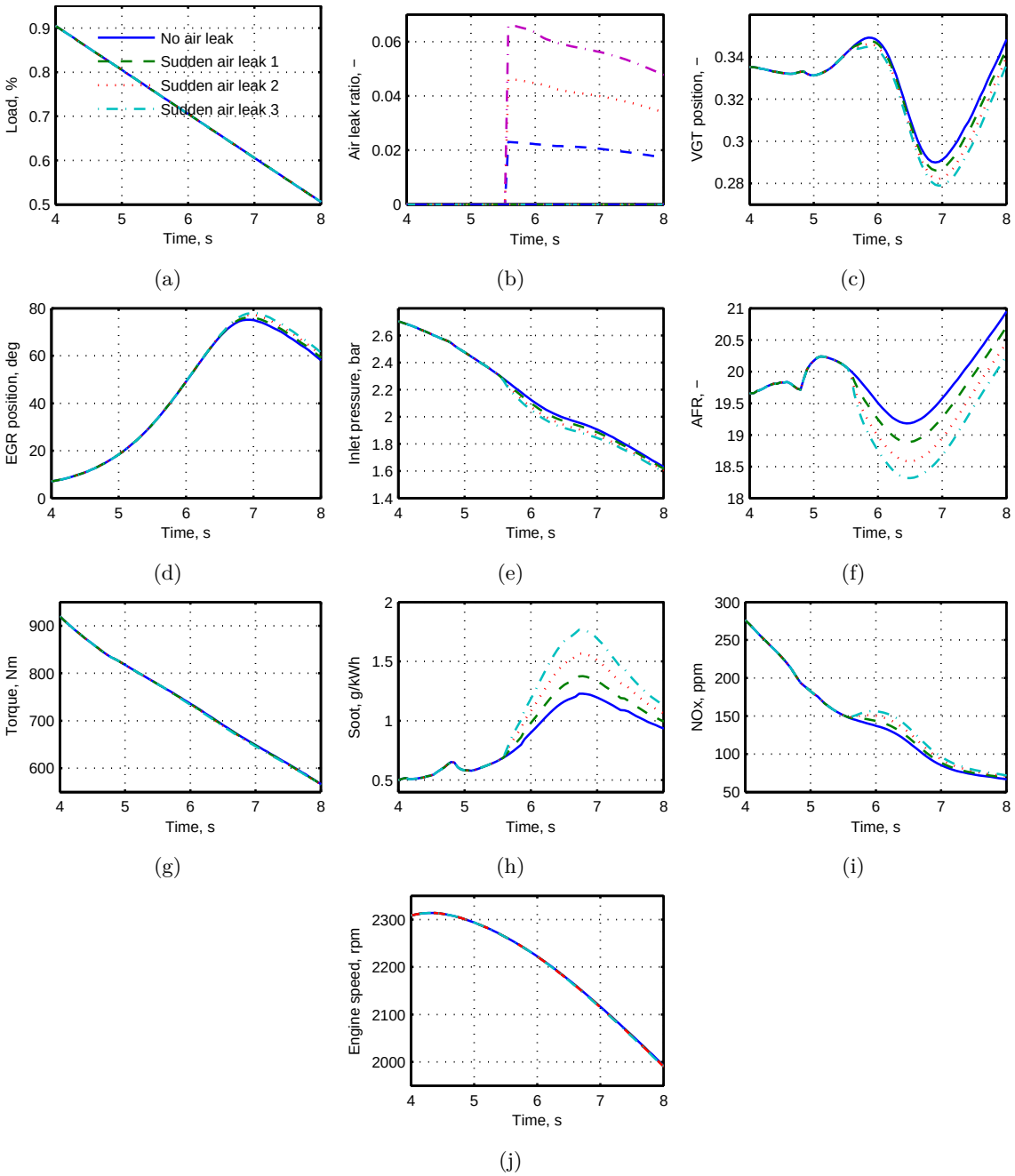

Figure 5.3: Robustness evaluation of the fuzzy logic controller when an air leak suddenly happens in the intake pipe area while the engine is decelerating.

Constant load demand

When the load demand is constant, the results (Fig. 5.4) are similar to the results when the load demand is increasing and decreasing. Fig. 5.4 a shows the load demand has been set as constant at 0.5 between 4 s and 8 s of the test. Engine speed (Fig. 5.4 j) is

still climbing slowly from about 1770 rpm to 1790 rpm because the torque produced by the engine is still greater than the torque of the mechanical consumer. A sudden air leak happens again at about 5.5 s and it can be seen that the air leak ratios of these 3 tests start to increase from 0 to about 2%, 4%, and 6% respectively. The air leak then stays constant because the load demand is constant.

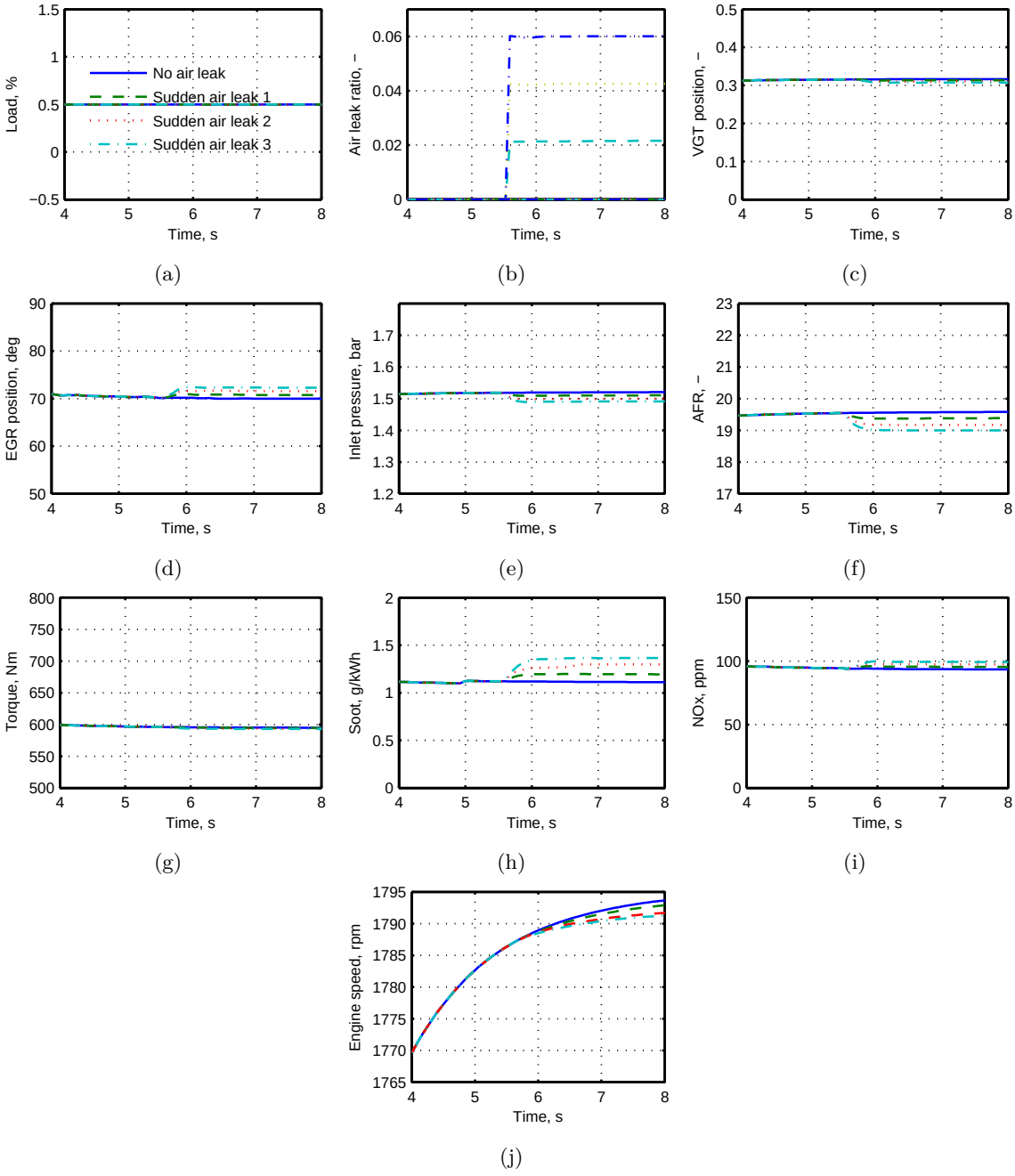

Figure 5.4: Robustness evaluation of the fuzzy logic controller when an air leak suddenly happens in the intake pipe area while the engine is cruising.

5.2 Turbocharger Mechanical Efficiency Change

5.2.1 Simulation design

The mechanical efficiency of the turbocharger may drop slightly over time due to unsatisfied oil conditions and mechanical wear and tear. The controller should be able to adapt to this change.

Four separate simulations have been carried out using the transient engine model. The only parameter that changes these four simulations is the mechanical efficiency of the turbocharger. The mechanical efficiency has been set to 98%, 94%, 90%, and 86% for these four simulations, respectively. This is to find out whether the fuzzy logic controller is able to adapt to the changes in the mechanical efficiency of the turbocharger.

5.2.2 Simulation results

Fig. 5.5 shows the simulation results of the comparison between these four different mechanical efficiencies. The same load demand curve (Fig. 5.5 a) was fed to all four simulations, which include acceleration and deceleration (Fig. 5.5 j). This is to find out how the engine behaves with the fuzzy logic VGT and EGR controller under different engine running conditions. It can be seen that, since the mechanical efficiency of the turbocharger drops from 98% to 86% (Fig. 5.5 b) the VGT position (Fig. 5.5 c) has been set lower by the fuzzy logic controller to compensate for the loss of inlet pressure. When the load demand suddenly starts to decrease at about 18 s into the test, a peak drop of inlet pressure (Fig. 5.5e) happens as well as the AFR (Fig. 5.5 f), and this is when the VGT position has been set further lower compared to the stage before. The drop of inlet pressure has been recovered gradually since then. A sudden increase of the soot (Fig. 5.5 h) also happens around that time due to the drop in inlet pressure, though it gradually decreases because the VGT position has been adjusted by the fuzzy logic controller to provide additional inlet pressure that needed NOx (Fig. 5.5, which i) is not very sensitive to the mechanical efficiency drop of the turbocharger. Thus, there are only minor adjustments made to the EGR positions. Also, because of the adjustments of the VGT positions, the engine torque (Fig. 5.5 g) has not been significantly affected by the drop in the mechanical efficiency of the turbocharger.

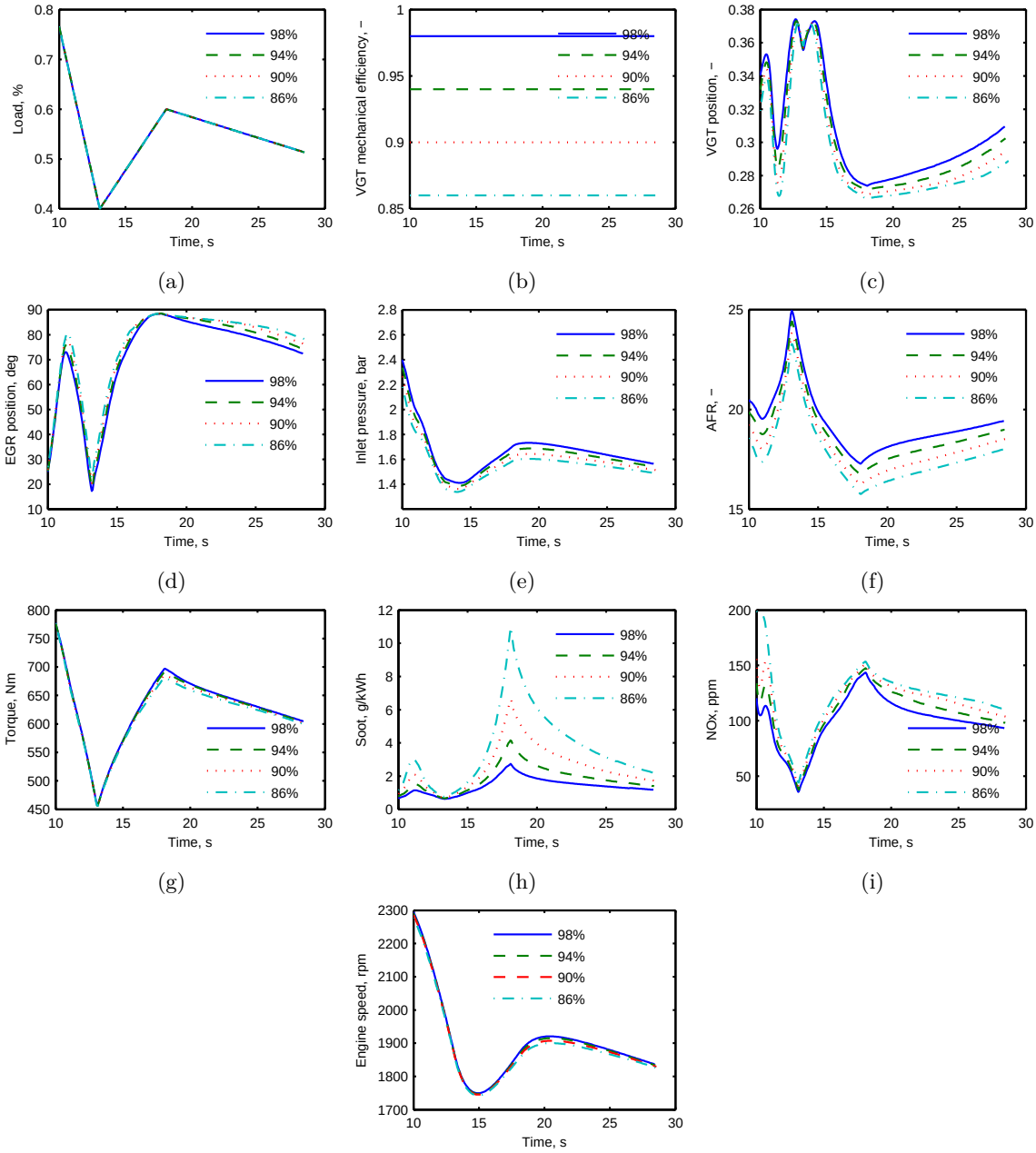

Figure 5.5: Robustness evaluation of the fuzzy logic controller when the mechanical efficiency of the turbocharger is deteriorated over time.

5.3 Chapter Summary and Conclusions

In this chapter, robust evaluation of the fuzzy logic controller is reported. The evaluation includes a sudden air leak test and a mechanical efficiency deterioration test. The sudden air leak test investigates whether the fuzzy logic controller can make necessary adjustment to compensate for the inlet pressure and flow loss caused by the air leak. The mechanical efficiency deterioration test is to find out whether the fuzzy logic controller is able to adapt to the change of the turbo mechanical efficiency.

Simulations were carried out using the AVL-BOOST transient engine model. Results show that the fuzzy logic controller is able to make necessary adjustments in both tests. It is able to compensate for the inlet pressure and flow loss either due to the air leak or the efficiency drop without losing engine torque and producing increased soot and NOx.

Chapter 6

Comparison and Discussion

In Chapter 4, the development of four real-time VGT and EGR controllers was detailed. In summary, these controllers are:

1. PI controllers which include Vgt-independent control (PID controller 1) and Vgt-independent control (PID controller 2) ;
2. Fuzzy logic controller (FLC1) ;
3. Fuzzy logic controller with emission predictor (FLC2) ;
4. ANFIS controller.

In this chapter, the comparisons of transient performance between FLC1 and the other three controllers were described and discussed.

6.1 Comparison between FLC1 and PID Controller

Due to some hardware limitations (for example, the noise signal cannot be removed from the output of pressure sensors and this will affect the stability of the PIC control), the PID controller was only tested using the transient engine model developed in AVL-BOOST. For this reason, the comparison was based on transient simulation results.

Fig. 6.1 shows the comparison between transient simulation results of FLC1 and PID controller 1 tested using the transient engine model running under the same load demand. The comparison investigates the differences in performances and emissions of the engine between the FLC1 and PID controller. The fuzzy logic controller controls the VGT and EGR based on predefined fuzzy logic rules; while the PID controller tries to achieve the predefined optimal inlet pressure and EGR mass fraction by regulating the VGT and EGR positions.

In transient simulation mode, the change in engine speed is proportional to the difference between the torque produced by the engine and the torque of load. A positive difference induces an increase in engine speed, whereas a negative difference induces a decrease in engine speed. Fig. 6.1 a shows the comparison of engine speed between FLC1 and PI controllers. It can be seen that at 5 seconds and between 20 and 30 seconds of the test, the engine speed of fuzzy logic controller is higher than that of the PID controller. This indicates that the torque produced is higher when controlled by FLC1 (see Fig. 6.1 i). Noticeably, the amount of fuel injected are the same (see Fig. 6.1 d) and BSFC (Fig. 6.1 j) of FLC1 is less than that of PID controller. This is because the fuel injected was burnt more completely when controlled by FLC1 than that of PID controller. Hence soot production (Fig. 6.1 k) of FLC1 is much less than that of PID controller. The reason to this is when the VGT and EGR is controlled by FLC1, inlet pressure is higher than that of PID controller, and hence more air is supplied to the engine and AFR of FLC1 is higher as well (see Fig. 6.1 g). The fundamental reason is the VGT position difference between FLC1 and PID controller. Fig. 6.1 e shows that the VGT position controlled by FLC1 is lower than that when controlled by PID controller. Moreover, the turbo efficiency is also higher when the VGT is controlled by FLC1 (see Fig. 6.1 h).

The comparison of EGR position controlled by FLC1 and PI controllers is shown in Fig. 6.1 f. Fig. 6.1 c shows the EGR mass fraction varies with the EGR position. It can be seen that the EGR mass fraction is maintain at about 7% which is the predefined optimal value when controlled by PID controller, while the EGR mass fraction is not fixed when controlled by FLC1, but changes with the EGR position controlled based fuzzy logic control rules. Results show that the NOx production of the engine when controlled by FLC1 is less than the NOx production of the engine when controlled by PID controller (see Fig. 6.1 l).

The comparison shows that the fuzzy logic controller is superior to that of the PID controller.

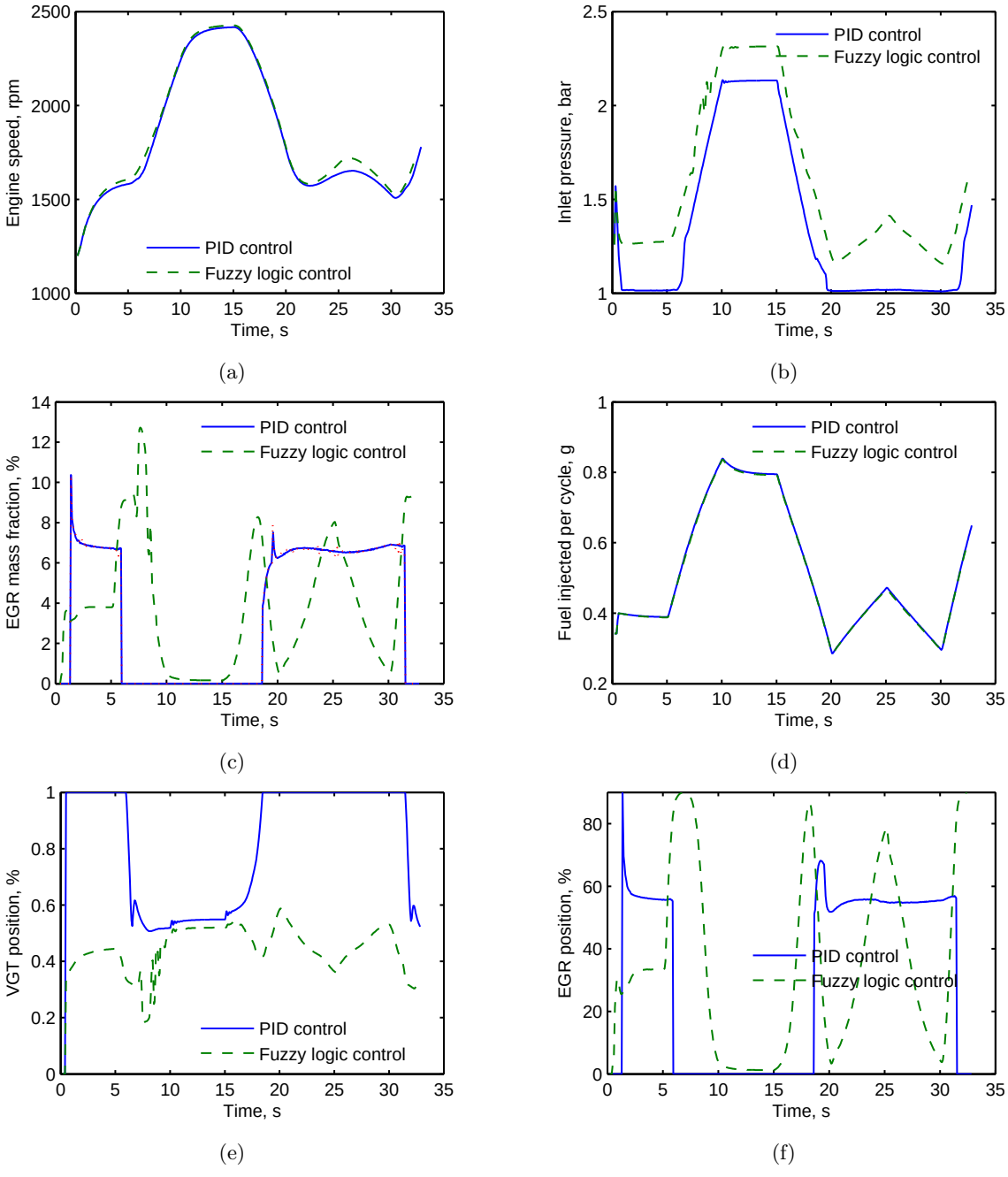

Figure 6.1: Comparison between FLC1 and PID controller 1, simulation results.

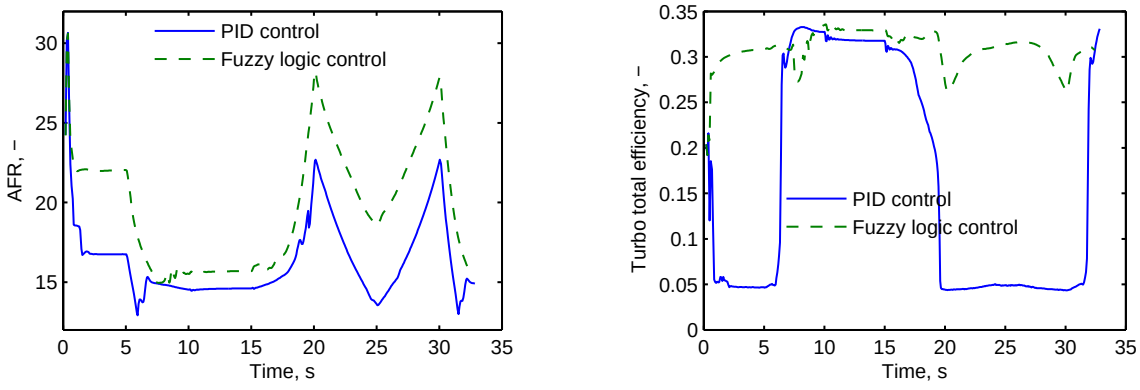

(g)

(h)

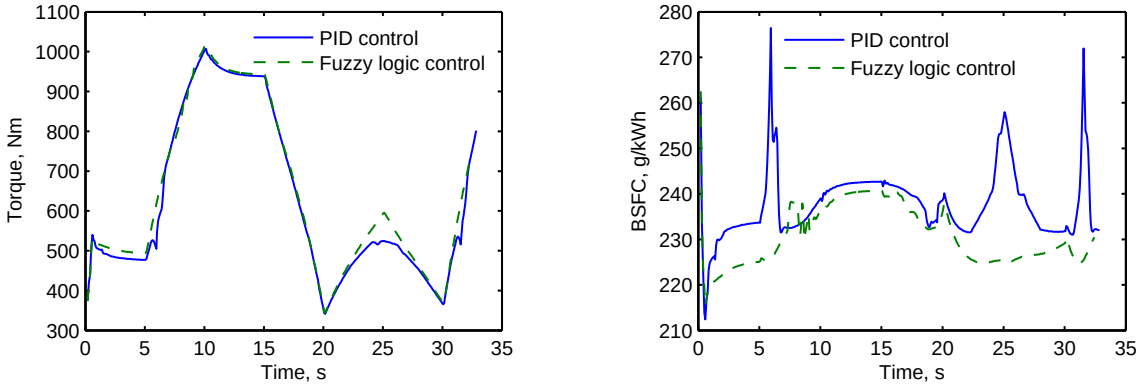

(i)

(j)

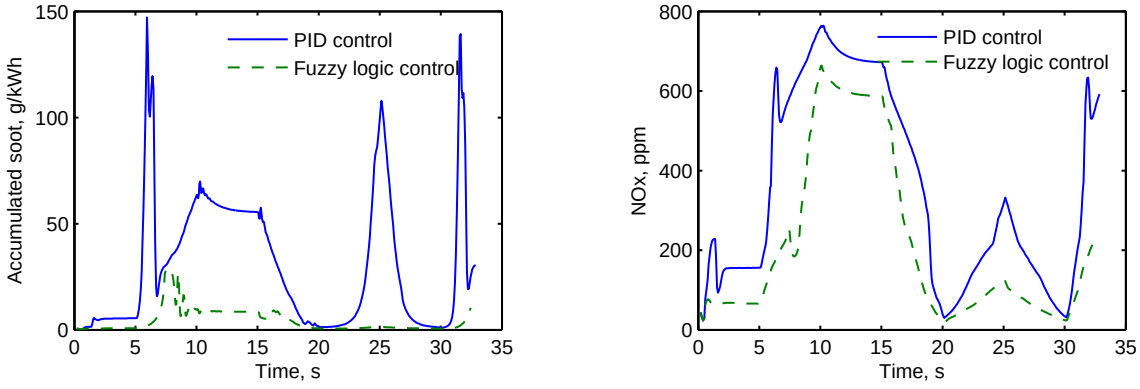

(k)

(l)

Figure 6.1: (continued)

6.2 Comparison between FLC1 and FLC2

In this section, the engine performances and emissions when VGT and EGR were controlled by FLC1 are compared with those when controlled by FLC2. The comparison investigates the performance of the fuzzy logic controller using emission predictors instead of real emission analysers under transient running conditions. The comparison was carried out on the CAT3126B test bed using the NRTC driving cycle.

Fig. 6.2 shows the experimental results of the comparison. When the engine is governed by a driving cycle, the load demand is adjusted by a PID controller, which makes the engine running under the engine speed and torque profiles defined by the driving cycle. It can be seen that when the VGT and EGR were controlled by FLC2, engine speed (Fig. 6.2 a), torque (Fig. 6.2 b), and load (Fig. 6.2 c) curves exactly match the engine speed curve when controlled by FLC1. This means that when the VGT and EGR are controlled by FLC2, the engine can produce the same torque as controlled by FLC1. Due to remaining differences between the predicted emission levels and the measured ones, the VGT and EGR position curves (Fig. 6.2 d and e) when controlled by FLC2 are not aligned with those when controlled by FLC1. However, the inlet pressure curves (Fig. 6.2 f) when controlled by FLC1 and FLC2 are similar, and these differences did not make the engine produce more emissions when compared to the emissions produced by the engine when controlled by FLC2, but reduced the emissions at some points of the test (see Fig. 6.2g and h).

During the period from 190s to 200s of the test, it can be seen that NOx production (Fig. 6.2 h) is slightly lower when the VGT and EGR are controlled by FLC2 compared to the NOx production when the VGT and EGR are controlled by FLC1. However, opacity of the exhaust gas (Fig. 6.2 g) is slightly higher when the VGT and EGR are controlled by FLC2 compared to that when controlled by FLC1. This is because the predicted opacity value is slightly lower than the measured value of opacity, and hence the VGT position (Fig. 6.2 d) controlled by FLC2 is slightly higher than that when controlled by FLC1.

In conclusion, because the performances and emission levels of the engine when controlled by FLC2 are similar to those of the engine when controlled by FLC1, emission predictors can be used to replace the real emission analysers when real emission analysers are not available.

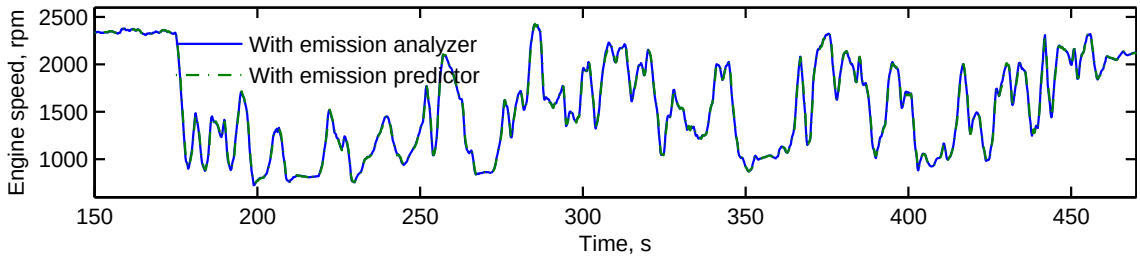

(a)

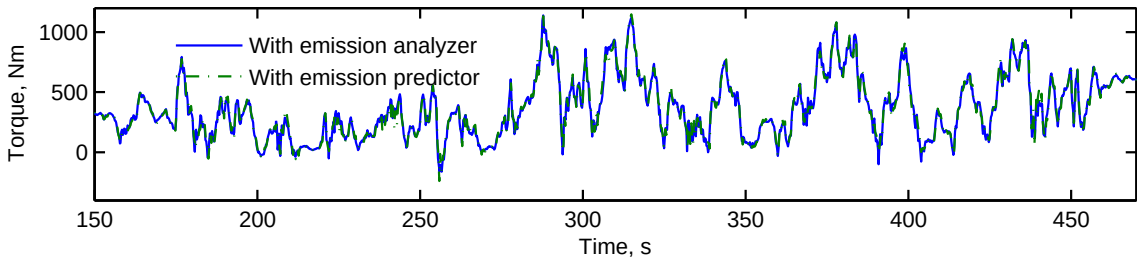

(b)

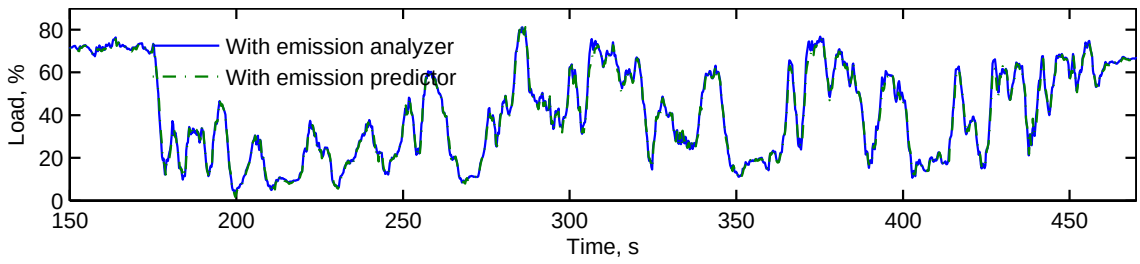

(c)

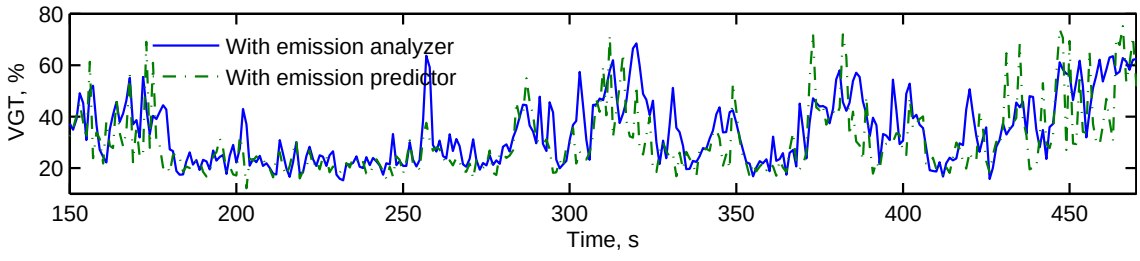

(d)

Figure 6.2: Comparison between FLC1 and FLC2, experimental results.

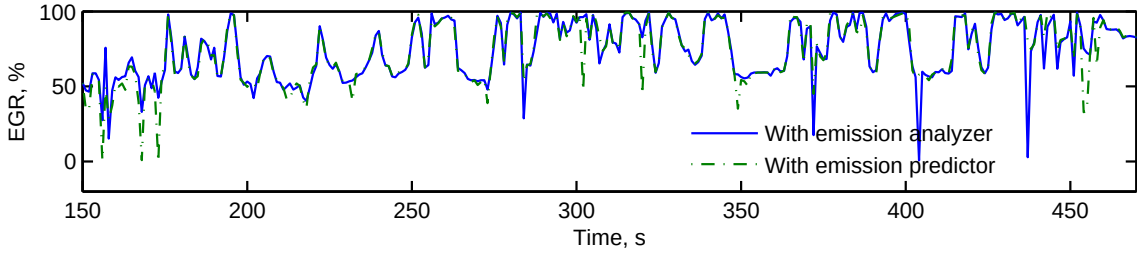

(e)

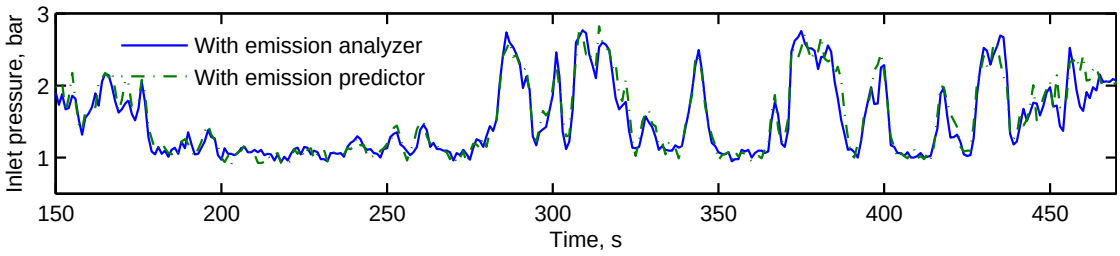

(f)

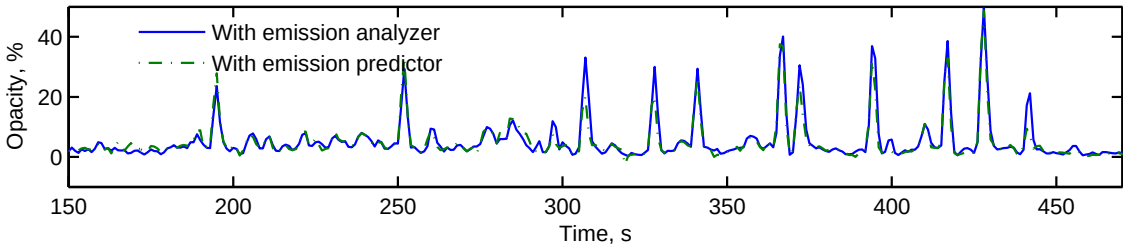

(g)

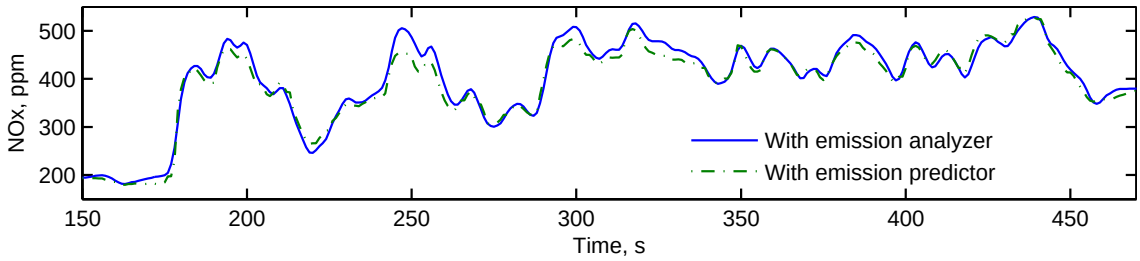

(h)

Figure 6.2: (continued)

6.3 Comparison between FLC1 and ANFIS Control

In this section, the performances and emissions of the engine when the VGT and EGR are controlled by FLC1 are compared with that of the engine when the VGT and EGR are controlled by ANFIS controller. The comparison is to assess the performance and effectiveness of the ANFIS controller compared to that of the FLC1 under transient running condition.

6.3.1 Simulation

Simulations of the VGT and EGR controlled by the fuzzy logic controller and ANFIS controller were carried out using the transient engine model. Using the same load demand signal, engine speed, VGT position, EGR position, inlet pressure, torque, soot and NOx of the engine were compared between these two types of control. Results show that when the VGT and EGR were controlled by the ANFIS controller, there are not any noticeable differences between the engine speed (Fig. 6.3 a) and torque (Fig. 6.3 f) curves, which means the performances of the engine between these two types of control are the same. However, there are slight differences between the inlet pressure (Fig. 6.3 e) curves. Between 8 to 13 seconds and 23 to 30 seconds of the test, the inlet pressure (Fig. 6.3 e) of the engine when controlled by the ANFIS controller is slightly higher than that of the engine when controlled by the fuzzy logic controller. This is because during those periods, the VGT position (Fig. 6.3 c) when controlled by ANFIS controller is lower than the VGT position when controlled by the fuzzy logic controller. As a result, soot production (Fig. 6.3 g) when controlled by the ANFIS controller is lower than the soot produced when controlled by the fuzzy logic controller. Similarly, NOx production (Fig. 6.3 h) when controlled by the ANFIS controller is also slightly lower than that when controlled by the fuzzy logic controller. This is because during those time periods, EGR position (Fig. 6.3 d) when controlled by the ANFIS controller is slightly higher than the EGR position when controlled by the fuzzy logic controller.

In conclusion, by learning from the data sets generated by running the engine with fuzzy logic controller, the performance of the engine when running with ANFIS controller is very similar to the performance of the engine when running with fuzzy logic controller. Soot and NOx productions of the engine when running with ANFIS controller is slightly better than that of the engine when running with fuzzy logic controller.

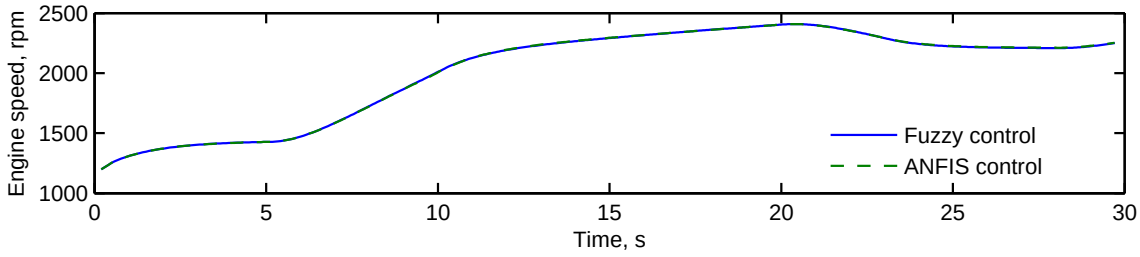

(a)

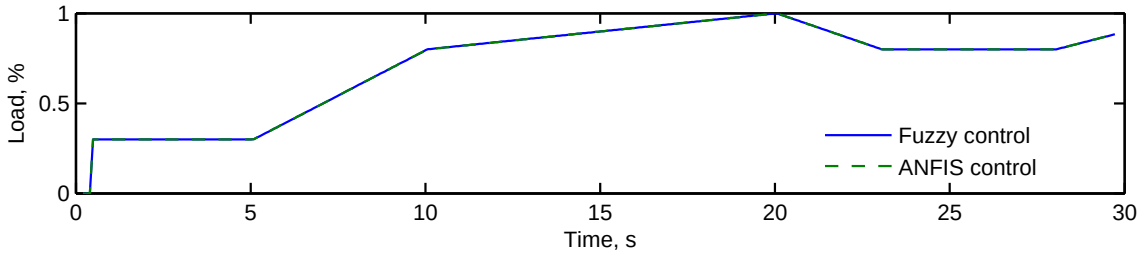

(b)

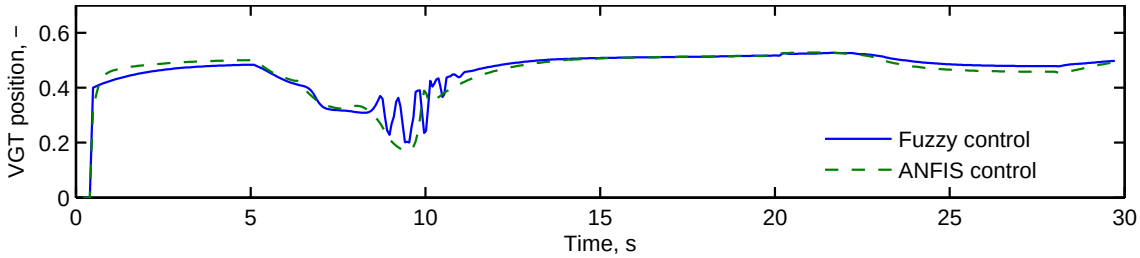

(c)

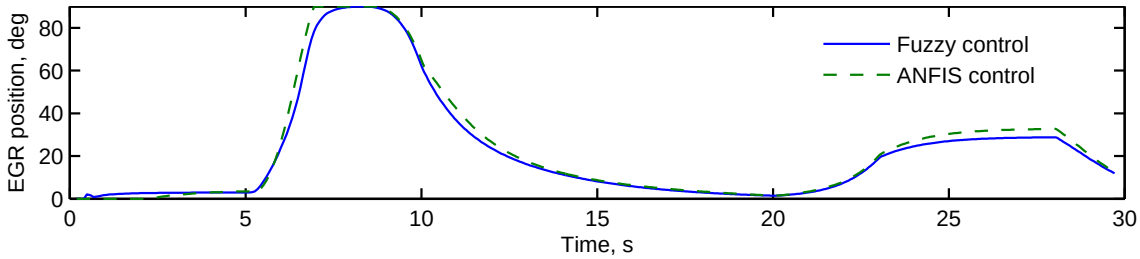

(d)

Figure 6.3: Comparison between FLC1 and ANFIS controller, simulation results.

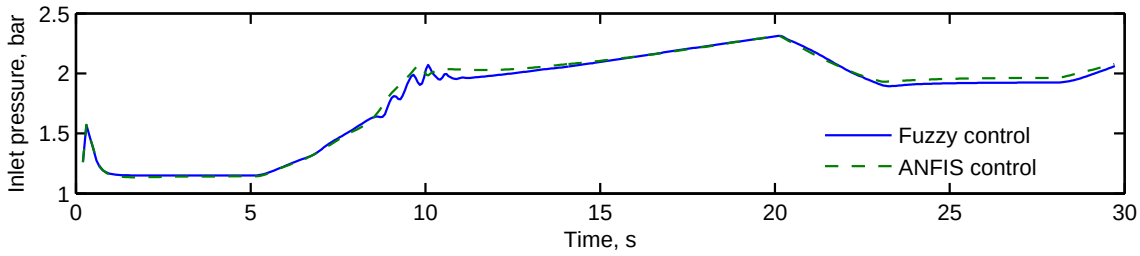

(e)

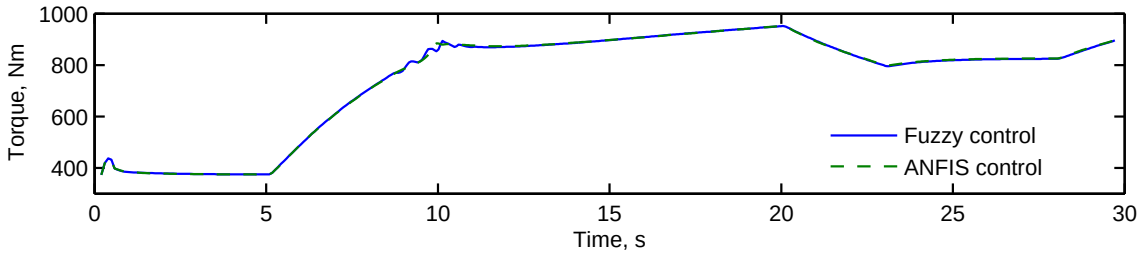

(f)

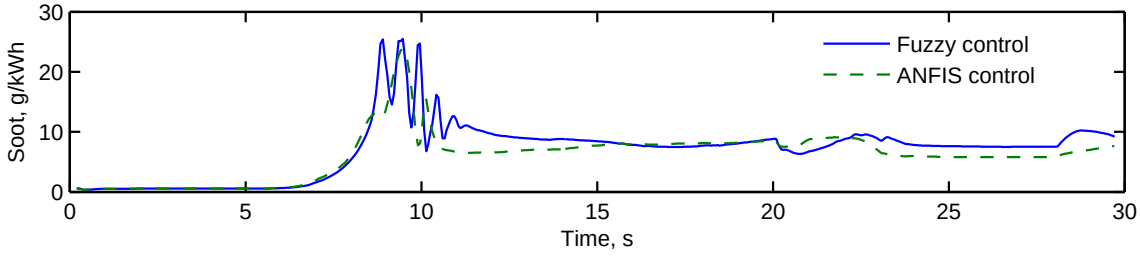

(g)

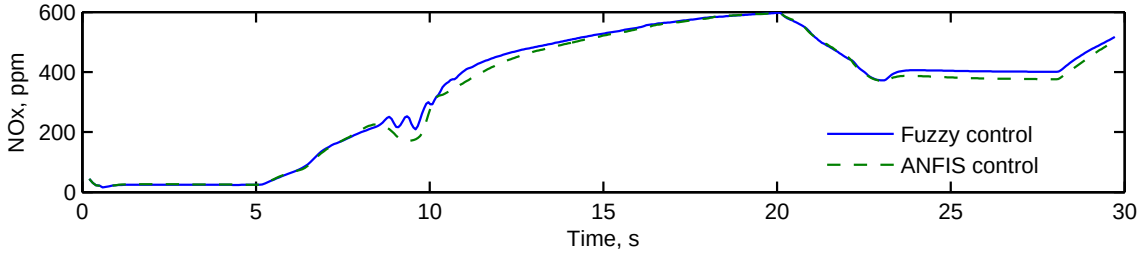

(h)

Figure 6.3: (continued)

6.3.2 Experiment

The ANFIS controller has also been tested on the test bed. Due to a hardware limitation, only the ANFIS VGT controller has been tested and compared with the fuzzy logic controller (FLC1). Fig. 6.4 shows the comparison between engine speed, load, VGT position, inlet pressure, and opacity of the engine when the VGT position is controlled by the ANFIS controller and the FLC1. At each second, the dynamometer governs the engine to run at the predefined engine speed profile. Load demand (pedal position) is controlled by a feedback controller which makes the engine provide the predefined torque at that second. It can be seen that, the load demand curve of the engine when the VGT position is controlled by the ANFIS controller is very close to the load demand curve when the VGT position is controlled by the FLC1. Because the VGT position controlled by the ANFIS controller is higher than the VGT position controlled by the FLC1 between 20 s and 26 s, the inlet pressure of the engine when the VGT position is controlled by the ANFIS controller is lower than the inlet pressure when the VGT position is controlled by FLC1. As a result, the opacity of the engine exhaust gas when the VGT position is controlled by the ANFIS controller is higher than the opacity of the exhaust gas when the VGT position is controlled by FLC1. Between 27 s and 71 s, the VGT position controlled by the ANFIS controller is lower than the VGT position controlled by FLC1, and hence the inlet pressure of the engine when the VGT position is controlled by the ANFIS controller is higher than the inlet pressure when the VGT position is controlled by FLC1, and the opacity of the exhaust gas when the VGT position is controlled by the ANFIS controller is lower than that of the opacity of exhaust gas when the VGT position is controlled by the FLC1. The difference between the VGT position controlled by the ANFIS controller and FLC1 is caused by the error of the ANFIS model trained for the ANFIS controller. The error of the ANFIS model can be further reduced by removing the signal noises from the data used to train the ANFIS model.

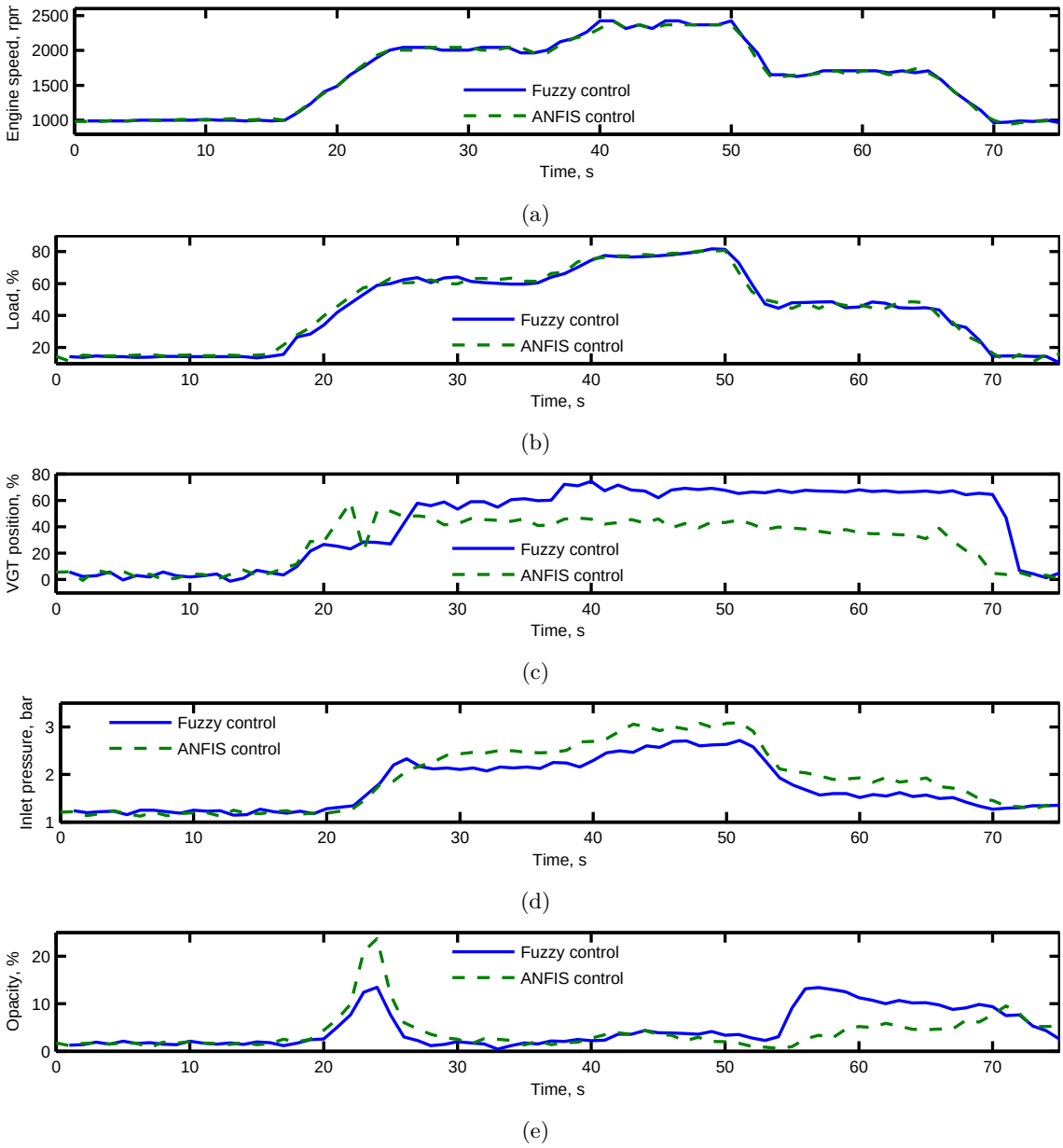

Figure 6.4: Comparison between FLC1 and ANFIS controller, experimental results.

6.4 Chapter Summary and Conclusions

In this section, the fuzzy logic controller was compared with the PID controller and ANFIS controller under transient running conditions. Simulation results show that engine fuel consumption is better when the VGT and EGR is controlled by the fuzzy logic controller compared to the engine fuel consumption when the VGT and EGR is controlled by the PID controller. Meanwhile, the soot and NOx productions when the VGT and EGR is controlled by the fuzzy logic controller are both less than the soot and NOx productions when the VGT and EGR is controlled by the PID controller. The ANFIS controller is able to control the VGT and EGR without online emission measurement, and the engine performances and emissions are slightly better than that when the VGT and EGR is controlled by the fuzzy logic controller. Thus, the fuzzy logic controller can be replaced with the ANFIS controller when online emission measurement is not available.

Moreover, the engine performances and emissions when the VGT and EGR are controlled by the fuzzy logic controller with emission analysers were compared with those when the VGT and EGR are controlled by the fuzzy logic controller with emission predictors. The experimental results show that when the VGT and EGR are controlled by the fuzzy logic controller with the emission predictors, the engine performances and emissions are very close to those when the VGT and EGR are controlled by the fuzzy logic controller with emission analysers. Thus, the developed emission predictors can replace the emission analysers to work with the proposed fuzzy logic controller when preferred.

Chapter 7

Conclusions and Future work

7.1 Summary of the work

Briefly, this work aims to develop real-time controllers for the control of VGT and EGR in a diesel engine under transient running conditions of the engine. To fulfill this task, a transient engine model is also needed to be developed as part of the project. The engine model is used to test and validate the controllers before they can be tested on the test bed.

The real-time controllers developed in this work include PID controller, fuzzy logic controller, and ANFIS controller. Engine performances and emissions will be balanced and optimized when the VGT and EGR are controlled by these controllers. Moreover, on-board emission predictors have been developed using the ANFIS modelling technique. The emission predictors can be used to provide the fuzzy logic controller with estimated emission productions of the engine when online emission measurement is not available.

7.1.1 Transient engine model

The transient engine model was developed using AVL-BOOST simulation software based on the specifications of the CAT3126B engine test bed located at the University of Sussex. The code is a 1D simulation tool which can provide highly reliable simulation results of an IC engine in both steady-state and transient running condition.

The main configurations of the model include: the combustion behaviour of the engine which uses the Vibe 2-Zone model, the friction characteristic of the engine which uses SLM model, the heat transfer behaviour of the engine, the geometry of the cylinders, initial running conditions, the intake and exhaust valves timing and lift curves, the ECU which defines the fuel injection map, the VGT sub-model which uses the OEM maps of the

turbo, the EGR valve flow coefficients, and the pipes and manifolds layout and geometries.

After the configurations, the engine model was validated against the CAT3126B test bed. It is firstly validated based on the same inlet pressure and then validated based on the same VGT and EGR positions. The validation based on the same inlet pressure has shown good agreement between the simulation results and the experimental results. However, there are greater differences between the simulation results and the experimental results when validated based on the same VGT and EGR positions. This is because the maps of the turbine when the vanes are between the fully open and fully closed positions are interpolated from the maps of the turbine when the vanes are at fully open and fully closed positions.

7.1.2 PID controller

PID controller is currently widely used for VGT and EGR control in automotive industry. In order to assess the performances of the proposed fuzzy logic controller, PI controllers were developed so that it can be used to compare with the proposed fuzzy logic controller.

PID controllers for VGT and EGR control require predefined set-points of inlet pressure and EGR gas mass fraction. The set-points of inlet pressure are used to regulate the VGT turbine positions using a feedback control loop, the set-points of EGR mass fraction are used to regulate the EGR valve position using a feedback control loop. Investigations have been carried out using the transient engine model to find out the optimized set-points of inlet pressure and EGR mass fraction. In order to simplify the problem, the inlet pressure has been set the value, which will make the AFR about 14.7 which is the stoichiometric value for diesel engine. A trade-off has been made to determine the EGR gas mass fraction between the soot and NOx productions. The following step is to tune the coefficients of the P and I terms (It is found out that, for this application, only P and I terms are sufficient enough to achieve the required control performances which include rise time, overshoot, settling time, steady-state error and stability).

Because EGR will have a negative effect on engine performance and running stability, the EGR valve will only be operated at medium engine speed and under low load. In addition, it will be kept closed under all other conditions. Considering the interactive effects between the VGT and EGR, VGT vanes will be kept fully open when the EGR valve is under control (PID controller 1). In order to investigate the interactive effects between the VGT and EGR, another PID controller with VGT and EGR independently controlled (VGT position is controlled regardless of the status of EGR valve) has also been

developed (PID controller 2). The engine performances and emissions when the VGT and EGR are controlled by these two PI controllers have been compared and discussed. Simulation results show that the engine performances and emissions when the VGT and EGR are controlled by PID controller 1 are slightly better than those when the VGT and EGR are controlled by PID controller 2. But due to the interactive effects between the VGT and EGR, the stability of the control was affected when both VGT and EGR are under operation.

7.1.3 Fuzzy logic controller

Using a fuzzy logic control technique, the RFLC controller is able to address the trade-off issue in the VGT and EGR control problem. In order to develop effective fuzzy logic control rules, the influences between a VGT and EGR have been investigated in a diesel engine test bed, the impact of the VGT and EGR position changes to a diesel engine has also been examined. The control targets, which are the level of soot and NO_x emissions, were chosen as control input variables. This allows the RFLC controller to monitor and control the emission levels in real time.

To develop the fuzzy logic controller, input variables need to be defined. The input variables for VGT control are engine speed, load demand, inlet pressure, exhaust opacity and EGR position. The input variable for EGR control are engine speed, load, and NOx. Moreover, fuzzy logic control rules need to be created. These rules were determined by observing the experimental investigation of the effects of the VGT and EGR positions to the performances and emissions of the diesel engine. Based on these rules, the fuzzy logic controller is able to determine the VGT and EGR positions in real time with respect to the instant status of the input variables. The fuzzy logic controller is developed based on the CAT3126B engine. For other engines, if the specifications are quite different, some necessary adjustments to the membership functions of input variables and fuzzy logic control rules would be required.

By encoding in real time code and uploading to a MicroAutoBox, the proposed controller has been implemented and validated in a diesel engine test bed. The experimental results show that compared to the baseline engine, the proposed RFLC controller can significantly reduce soot and NO_x emissions of the engine running on an off-road driving cycle. The specific fuel consumption of the engine can also be reduced. It was also discovered that, despite the trade-off effect existing between the soot and NO_x production, they were reduced at the same time by the RFLC controller compared to that of the

baseline engine. Furthermore, the proposed controller can also avoid the time-consuming process of building the reference maps required by traditional controllers. Consequently, the development time and cost can be reduced. Finally, the controller requirements are compatible with the capabilities offered by a standard ECU, and hence it has the potential to be rapidly implemented on mass-produced ECUs.

A repeatability test of the fuzzy logic controller has been carried out on the CAT3126B test bed. Experimental results show that each redundant test has good agreement with each other and the standard deviation of the mean values of each key engine parameter are trivial. This demonstrates that this control scheme is repeatable and reliable.

Robustness evaluation of the fuzzy logic scheme has been carried out using the AVL-BOOST transient engine model developed. The evaluation includes a sudden air leak test and a turbocharger mechanical efficiency deterioration test. Simulation results have demonstrated that the fuzzy logic controller is able to adapt to the uncertainties, and compensate for the loss of inlet pressure due to the sudden air leak and the loss of the performance of the turbocharger due to the mechanical efficiency deterioration.

7.1.4 ANFIS controller

The ANFIS controller is developed to replace the fuzzy logic controller when online measurement of engine exhaust emissions are not available. By learning from a data set generated by running transient test of the engine when the VGT and EGR are controlled by the fuzzy logic controller, the ANFIS model is able to determine the positions of VGT and EGR as the fuzzy logic controller does. Because the data set used to train the ANFIS model was generated from engine tests which are running in highly transient condition, the data set would cover all possible engine running conditions. As a result, the developed ANFIS controller is capable of working under any other transient conditions.

The input variables of the ANFIS VGT controller are engine speed, load demand, inlet pressure, and EGR position, output is VGT position; the input variables of the ANFIS EGR controller are engine speed and load demand, output is EGR position. Both simulation and experimental results show that when the engine is tested using the same test profile, the ANFIS controller is able to determine the VGT and EGR positions as they are controlled by the fuzzy logic controller. Thus, when online emission measurement is not available, the fuzzy logic controller can be replaced by the corresponding ANFIS controlled.

7.1.5 On-board emission predictor

On-board emission predictors which can predict emission outputs in real-time running conditions were also developed in this work. The predictor can be used to provide the fuzzy logic controller with the required emission input signals when online emission measurement is not available. The predictor is developed using ANFIS modelling technique, which is more efficient than neural networks. The ANFIS model trained using an experimental data set is able to predict the emission outputs such as soot and NOx based on the engine running conditions such as engine speed, load, intake oxygen level, and intake air flow. Similar to that of the fuzzy logic controller, the data set used to train the ANFIS model was collected from experimental tests performed on the CAT3126B test bed. These experimental tests have included as much running conditions as possible, so it is able to predict emission outputs under transient running condition.

7.2 Novel Contributions

This work demonstrated the following novel contributions:

(a) A transient diesel engine model has being created using AVL-BOOST simulation software. The model was configured based on the specifications of the CAT3126B engine, and it is able to simulate the engine in both steady state and transient running conditions. The timings and lifts of intake and exhaust valves were derived from the profiles of the intake cam and exhaust cam. The timing and lift were further tuned by calibrating them for the best performances of the engine. The fuel injection map for the ECU sub-model was created based on the natural air intake curve. The VGT sub-model was configured using the OEM maps of the compressor and turbine, the EGR valve was simulated by defining a look-up table between the flow coefficients and valve positions. The engine model was validated against the CAT3126B engine, the results show that the engine model is able to represent the CAT3126B engine with relatively small differences. There is a full range of parameters of the engine are accessible across engine. Temperatures, pressures and heat transfer are accessible by adding measuring points to the positions where needed. The combustion behaviour and energy analysis are also available. More interested results would be BMEP, engine torque, BSFC, soot and NOx productions of the engine. The PID controller, fuzzy logic controller, ANFIS controller can be tested and validated using the engine model before they can be tested in the real engine, also the performance of the

on-board emission predictors can also be assessed using the engine model.

(b) Traditional PID controllers are good at resolving the control target at a predefined value (set-point) precisely when running in steady state. However, diesel engines usually run at highly transient conditions, such as the NRTC cycle used in this work. Hence, a map of predefined values for the control target has to be defined firstly. Because the set-point of the control target changes rapidly under transient running conditions as defined in the map, the PID controller with fixed coefficients may struggle to track the change of the set-points and the stability of the control would not be guaranteed, especially in this particular problem where there is interactive effect between the VGT and EGR as demonstrated in Section 4.1.3. The proposed real-time fuzzy logic controller is a novel approach to control the VGT and EGR in a diesel engine. Instead of regulating the VGT and EGR positions to achieve the predefined set-points of the inlet pressure and EGR mass fraction, the fuzzy logic controller is able to rapidly determine the optimized positions of the VGT and EGR by monitoring the engine running conditions and emission outputs in real time. Hence, the fuzzy logic controller is much more robust compared to the traditional PID controllers. There are still PID controllers working in the inner loop to position the VGT vanes and EGR valves at the positions determined by the fuzzy logic controller, but compared to regulating the VGT and EGR positions to achieve the set-points of inlet pressure and EGR mass fraction, this local position control has fewer nonlinearities, the hysteresis for example. Hence, the PID control is adequate. Results have shown that compared to the engine performances and emissions when the VGT and EGR are controlled by the PID controller, the engine performances has been improved when the VGT and EGR are controlled by the fuzzy logic controller, the fuel consumption and emissions have been reduced.

(c) ANFIS controllers have been developed in this work. By learning from a data set collected from transient experimental tests on the CAT3126B engine when the VGT and EGR are controlled by the fuzzy logic controller, the ANFIS controller is able to determine the VGT and EGR positions without monitoring the emission outputs from the engine, and hence the ANFIS controller can replace the fuzzy logic controller when online emission measurement is not available. It has been anticipated that the performances and emissions of the engine when the VGT and EGR are controlled by the ANFIS controller should be very close but not better than the engine performances and emissions when the VGT and EGR are controlled by the fuzzy

logic controller. However, both simulation and experimental results show that the performances of the engine when the VGT and EGR are controlled by the ANFIS controller can be improved compared to the performances of the engine when the VGT and EGR are controlled by the fuzzy logic controller, emissions can also be slightly reduced when the VGT and EGR are controlled by the ANFIS controller.

(d) On-board emission predictors for soot and NOx have also been developed in this work, and the predictors are used to provide the fuzzy logic controller with predicted emission outputs as the control inputs required by the fuzzy logic controller. The ANFIS modelling technique is used to develop the predictors by learning from a data set collected from transient experimental tests that include engine speed, inlet oxygen concentration, intake air flow, and load as input variables, with the soot and NOx as the output variables for soot predictor and NOx predictor, respectively. Experimental results show that the engine performances and emissions when the VGT and EGR are controlled by the fuzzy logic controller with emission predictors are very close to those of the engine when the VGT and EGR are controlled by the fuzzy logic controller with emission analysers. Most of the time during the tests, the engine performances and emissions are slightly better with emission predictors than those with emission analysers. This is caused by the differences between predicted values and measured values of soot and NOx, and the predicted values are generally slightly higher than the measured values.

7.3 Recommendation of Future Work

Future work should address the following points:

(a) Although the transient engine model has been carefully calibrated according to the specifications, performances and emissions of the CAT3126B engine, the accuracy of the model can be further improved by undertaking the following work:

- refining of the combustion model by measuring the in-cylinder pressure and calculating the heat release curve;
- refining the turbine sub-model by building more maps at more positions of vanes. Currently, the turbine maps are only available at fully closed and fully opened positions. The maps at other vane positions are derived by means of the interpolation technique, and hence the accuracy of the turbine model

is affected. Similarly, the EGR sub-model is simulated by a simplified map between the EGR flow coefficients and valve positions. Further improvement to the EGR sub-model can be done by actually mapping the EGR valve. This can be noticed from the second scheme of validation of the model, which is validated based on the same VGT and EGR positions;

- the intake and exhaust valve lifts and timings are derived from the intake and exhaust cam profiles and further calibrated to achieve the best engine performances and emissions. There should be some differences between these calibrated values and the actual values of the lifts and timings;
- in this work, the fuel injection map of the ECU sub-model is created based on the air intake behaviour (valve timings and lifts) of the engine model, with considerable differences from the actual fuel injection map of the CAT3126B engine. Further improvement to the fuel injection map can be made by accessing the ECU of the CAT3126B model and building the fuel injection map of the ECU sub-model accordingly.

(b) The performance of the fuzzy logic controller is largely determined by the fuzzy logic control rules, the design of the membership functions, and the number of input variables. Therefore, the performance of the RFLC controller can be further developed by further tuning the fuzzy control rules, adjusting the membership functions and adding more relevant control input variables if necessary;

(c) The ANFIS models for the ANFIS controller and on-board emission predictors can be further improved by removing the signal noise from the experimental data used to train the models;

(d) In this work, the proposed fuzzy logic controller with emission analysers and with emission predictors has been tested on the NRTC cycle, and more tests of the proposed controllers could be carried out using other driving cycles, such as the world-wide harmonized heavy-duty certification (WHDC). This would further assess the performance of the proposed controllers;

(e) The comparison between the proposed fuzzy logic controller and PID controller has only been performed on the transient engine model developed due to some hardware limitations of the CAT3126B test bed at the moment. Comparison of the PID controller with the fuzzy logic controller on the test bed is recommended when it is

possible to do so. It is anticipated that there will be greater overshoot and more oscillations of the PI control.

(f) In the current work, all the simulations and experimental tests were carried out when the engine has been warmed up completely. Further studies may include cold start tests of the engine running with the proposed controllers.

Bibliography

[1] ABB (2013). Orimaster fpd500 compact orifice flowmeter. Cited on xviii, 164

[2] Abidi, I., BOSCHE, J., HAJJAJI, A. E., and AITOUCHE, A. (2012). Control of a turbocharged diesel engine with egr system using takagi-sugeno¡¯s approach. In *20th Mediterranean Conference on Control & Automation (MED), Barcelona, Spain, July 3-6*, page 960. Cited on 21

[3] Ahmed, F. S., Laghrouche, S., Mehmood, A., and Bagdouri, M. E. (2014). Estimation of exhaust gas aerodynamic force on the variable geometry turbocharger actuator: 1d flow model approach. *Energy Conversion and Management*, 84:436. Cited on 15

[4] Alfieri, E. and Alois Amstutz, L. G. (2009). Gain-scheduled model-based feedback control of the air/fuel ratio in diesel engines. *Control Engineering Practice*, 17:1417. Cited on 21

[5] Ali, S. A., Bada, N'doye, and Nicolas, L. (2012). Sliding mode control for turbocharged diesel engine. *2012 20th Mediterranean Conference on Control & Automation (MED) Barcelona, Spain, July 3-6, 2012*. Cited on 23

[6] Ammann, M., Fekete, N. P., Guzzella, L., and Glattfelder, A. H. (2003). Model-based control of the vgt and egr in a turbocharged common-rail diesel engine: Theory and passenger car implementation. *SAE Journal of Engines 2003-01-0357*. Cited on 5

[7] Arnold, J.-F., Langlois, N., and Chafouk, H. (2009). Fuzzy controller of the air system of a diesel engine: Real-time simulation. *European journal of operational research*, 193(1):282–288. Cited on 20, 25

[8] Astrom, K. and Hagglund, T. (2001). The future of pid control. *Control Engineering Practice*, 9(11):1163–1175. Cited on 61

[9] AVL (2010). Avl opacimeter 439. online PDF. Cited on 166

[10] AVL (2011a). Avl-boost users guide. Cited on 29

[11] AVL (2011b). Theory - avl boost. Cited on 32, 33, 34

[12] Bauer, H. (2004). *Diesel - Engine Management, 3rd.* Wiley-Blackwell, 3rd edition. Cited on xii, 2, 8, 10, 11, 12

[13] Bohbot, J., Miche, M., Pacaud, P., and Benkenida, A. (2009). Multiscale engine simulations using a coupling of 0-d/1-dmodel with a 3-d combustion code. *Oil & Gas Science and Technology - Rev. IFP.* Cited on 16

[14] Bolla, M., Farrace, D., Wright, Y. M., and Boulouchos, K. (2014). Modelling of soot formation in a heavy-duty diesel engine with conditional moment closure. *Fuel*, 117:309. Cited on 15

[15] Brace, C., Wijetunge, R., Hawley, J., Vaughan, N., Wallace, F., Horrocks, R., and Bird, G. (1999). Transient investigation of two variable geometry turbochargers for passenger vehicle diesel engines. *SAE 991241.* Cited on 5

[16] Burke, R. D., Baumann, W., Akehurst, S., and Brace, C. J. (2014). Dynamic modelling of diesel engine emissions using the parametric volterra series. *Proceedings of the Institution of Mechanical Engineers, Part D: Journal of Automobile Engineering.* Cited on 1

[17] Ceccarelli, R., Moulin, P., and Canudas-de Wit, C. (2009). Robust strategy for intake leakage detection in diesel engines. *Control Applications, (CCA) & Intelligent Control, (ISIC), 2009 IEEE.* Cited on 113

[18] Challen, B. and Baranescu, R., editors (1999). *Diesel engine reference book: second edition.* ELSEVIER - BUTTERWORTH HEINEMANN. Cited on 3, 8, 17, 19, 24, 25

[19] Cheng, X., Chen, L., Hong, G., Yan, F., and Dong, S. (2014). Modeling study of soot formation and oxidation in di diesel engine using an improved soot model. *Applied Thermal Engineering*, 62(2):303. Cited on 15

[20] Cieslar, D., Dickinson, P., Darlington, A., Glover, K., and Collings, N. (2014). Model based approach to closed loop control of 1-d engine simulation models. *Control Engineering Practice*, 29:212–224. Cited on 15

[21] Clarke, D. W., Mohtadi, C., and Tuffs, P. S. (1987). Generalized predictive control - part ii extensions and interpretations. *Automatica*, 23(2):149–160. Cited on 21

[22] Cornolti, L., Onorati, A., Cerri, T., Montenegro, G., and Piscaglia, F. (2013). 1d simulation of a turbocharged diesel engine with comparison of short and long egr route solutions. *Applied Energy*, 111:1–15. Cited on 15

[23] Cui, H., Li, M., and Han, Y. (2010). The steady flow test and cfd numerical simulation on improving research of locomotive diesel engine helical intake port. *2010 WASE International Conference on Information Engineering*, page 255. Cited on 14

[24] Dambrosio, L., Camporeale, S. M., and Fortunato, B. (2000). Performance of gas turbine power plants controlled by one step ahead adaptive technique. In *ASME Turbo Expo 2000: Power for Land, Sea, and Air. ASME Paper 2000-C T-037.* Cited on 25

[25] Dambrosio, L., Pascazio, G., and Fortunato, B. (2003). Vgt turbocharger controlled by an adaptive technique. *Mechatronics, IEEE/ASME Transactions on*, 8(4):492–499. Cited on 25

[26] dAmbrosio, S., Finesso, R., Fu, L., Mittica, A., and Spessa, E. (2014). A control-oriented real-time semi-empirical model for the prediction of nox emissions in diesel engines. *Applied Energy*, 130:265–279. Cited on 21

[27] Dickmann, H.-P., Wimmel, T. S., Szwedowicz, J., Filsinger, D., and Roduner, C. H. (2005). Unsteady flow in a turbocharger centrifugal compressor: Three-dimensional computational fluid dynamics simulation and numerical and experimental analysis of impeller blade vibration. *Journal of Turbomachinery*, 128(3):455. Cited on 14

[28] DieselNet (2012). Heavy-duty truck and bus engines: Emission standards. Online webpage. Cited on x, 9, 84

[29] Djemili, I., Aitouche, A., and Cocquempot, V. (2011). Adaptive observer for intake leakage detection in diesel engines described by takagi-sugeno model. *2011 19th Mediterranean Conference on Control & Automation (MED).* Cited on 113

[30] ECM (2003). Ecm oxy6200 engine oxygen monitor. Cited on xviii, 164, 165

[31] Finesso, R., Misul, D., and Spessa, E. (2014). Development and validation of a semi-empirical model for the estimation of particulate matter in diesel engines. *Energy Conversion and Management*, 84:374–389. Cited on 21

[32] Flardh, O., Ericsson, G., Klingborg, E., and Martensson, J. (2014). Optimal air path control during load transients on a spark ignited engine with variable geometry

turbine and variable valve timing. *Control Systems Technology, IEEE Transactions on*, 22(1):83–93. Cited on 24

[33] Gad, S. (2014). *Diesel Fuel, In Encyclopedia of Toxicology (Third Edition)*. Academic Press, Oxford. Cited on 8

[34] Gems (2013). 2200 series/2600 series - general purpose industrial pressure transducers. Cited on xviii, 161

[35] Grahn, M., Johansson, K., and McKelvey, T. (2014). Model-based diesel engine management system optimization for transient engine operation. *Control Engineering Practice*, 29:103–114. Cited on 15

[36] Hawley, J., Wallace, F., Cox, A., Horrocks, R., and Bird, G. (2000). Reduction of steady-state nox levels from an automotive diesel engine using optimised vgt/egr schedules. *SAE990835*. Cited on 5

[37] Hengstler (2001). Incremental encoders. online. Cited on xviii, 162

[38] Heywood, J. B. (1988). *Internal Combustion Engine Fundamentals*. McGraw-Hill. Cited on 12

[39] Hosoz, M., Ertunc, H. M., Karabektas, M., and Ergen, G. (2013). Anfis modelling of the performance and emissions of a diesel engine using diesel fuel and biodiesel blends. *Applied Thermal Engineering*, 60(1-2):24–32. Cited on 16

[40] Hosoz, M. and H. M. Ertunc, H. B. (2011). An adaptive neuro-fuzzy inference system model for predicting the performance of a refrigeration system with a cooling tower. *Expert Systems with Applications*, 38(11):14148–14155. Cited on 99

[41] Isodori, A. (1995). *Nonlinear control systems, 3rd edn.* Springer Verlag, Englewood Cliffs, New York. Cited on 23

[42] Jankovic, M., Jankovic, M., and Kolmanovsky, I. (2000). Constructive lyapunov control design for turbocharged diesel engines. *IEEE TRANSACTIONS ON CONTROL SYSTEMS TECHNOLOGY*, 8(2):288. Cited on 21

[43] Jantzen, J. (2013). *Foundations of Fuzzy Control : A Practical Approach, second edition.* Wiley. Cited on 26, 72

[44] Jayashankara, B. and Ganesan, V. (2010). Effect of fuel injection timing and intake pressure on the performance of a di diesel engine - a parametric study using cfd. *Energy Conversion and Management*, 51(10):1835. Cited on 15

[45] Kegl, B., Kegl, M., and Pehan, S. (2013). *Green Diesel Engines : Biodiesel Usage in Diesel Engines.* Springer, 1st edition. Cited on 1

[46] Kim, S., Jin, H., and Choi, S. (2014). Pressure and flow based control of a turbocharged diesel engine air-path system equipped with dual-loop egr and vgt. *2014 American Control Conference (ACC) June 4-6,2014. Portland, Oregon, USA*. Cited on 22

[47] Kolmanovsky, I. and Stefanopoulou, A. (2001). Optimal control techniques for assessing feasibility and defining subsystem level requirements: an automotive case study. *Control Systems Technology, IEEE Transactions on*, 9(3):524–534. Cited on 24

[48] Kuzmych, O., Aitouche, A., and Cheng, L. (2013). Robust nonlinear control design for turbocharged biodiesel engine. In *Proceedings of the 3rd International Conference on Systems and Control, Algiers, Algeria, October 29-31*. IEEE. Cited on xvii, 22, 154

[49] Labcell (2012). Meriam laminar flow elements - labcell ltd. Cited on 163

[50] Lopez, J. J., Garcia-Oliver, J., Garcia, A., and Domenech, V. (2014). Gasoline effects on spray characteristics, mixing and auto-ignition processes in a ci engine under partially premixed combustion conditions. *Applied Thermal Engineering*, 70(1):996. Cited on 16

[51] Maiboom, A., Tauzia, X., and Hetet, J.-F. (2008). Experimental study of various effects of exhaust gas recirculation (egr) on combustion and emissions of an automotive direct injection diesel engine. *Energy*, 33(1):22–34. Cited on 2, 3

[52] Martin, F. (2001). *Robotic Explorations: A Hands-On Introduction to Engineering.* Prentice-Hall. Cited on xii, 20

[53] McGranahan, G. and Murray, F. (2012). *Air Pollution and Health in Rapidly Developing Countries.* Taylor and Francis. Cited on 1

[54] Mtui, P. L. (2013). Performance and emissions modeling of natural gas dual fuelling of large diesel engines. *INTERNATIONAL JOURNAL OF SCIENTIFIC & TECHNOLOGY RESEARCH.* Cited on 16

[55] Nelson-Gruel, D., Chamaillard, Y., Charlet, A., and Colin, G. (October 8-10, 2014). Robust control applied to minimize nox emissions. *2014 IEEE Conference on Control Applications (CCA), Part of 2014 IEEE Multi-conference on Systems and Control, Antibes, France*. Cited on 23

[56] Nyberg, M. (2003). Using hypothesis testing theory to evaluate principles for leakage diagnosis of automotive engines. *Control Engineering Practice*. Cited on 113

[57] Omran, R., Younes, R., and Champoussin, J.-C. (2009). Optimal control of a variable geometry turbocharged diesel engine using neural networks: Applications on the etc test cycle. *IEEE TRANSACTIONS ON CONTROL SYSTEMS TECHNOLOGY*, 17(2):380–393. Cited on 25

[58] Oustaloup, A. (1999). *La commande CRONE, 2nd edition*. HERMES. Cited on 23

[59] Pierburg (2013). Exhaust gas recirculation and control - with pierburg components. KSPG Automotive. Cited on 3

[60] Pisano, A. and Usai, E. (2011). Sliding mode control: A survey with application in math. *Mathematics and Computers in Simulation, vol 81 pp. 954-979*. Cited on 23

[61] Poloni, T., Roha-Ilkiv, B., and Johansen, T. A. (2014). Mass flow estimation with model bias correction for a turbocharged diesel engine. *Control Engineering Practice*, 23:22–31. Cited on 15

[62] Porter, B., Ross-Martin, T., and Truscott, A. (1996). Control technology for future low emissions diesel passenger cars. *IMechE Publication C517/035/96*. Cited on 5

[63] Powers, M. J. (2002). Gems sensors series 2200/2600 - operating & installation instructions. Cited on 160

[64] Rakopoulos, C. D. and Giakoumis, E. G. (2009). *Diesel Engine Transient Operation: Principles of Operation and Simulation Analysis*. Springer Science Business Media. Cited on 3

[65] Roy, S., Banerjee, R., and Bose, P. K. (2014). Performance and exhaust emissions prediction of a crdi assisted single cylinder diesel engine coupled with egr using artificial neural network. *Applied Energy*, 119:330–340. Cited on 17

[66] R.S.Wijetunge, C.J.Brace, J.G.Hawley, and N.D.Vaughan (2000). Fuzzy logic control of diesel engine turbocharging and exhaust gas recirculation. *Proceedings of the UKACC International Conference on Control*. Cited on 5

[67] SCHRENK, H. H., F.A.P.H.A., and BERGER, L. B. (1941). Composition of diesel engine exhaust gas. *AmericanJournal ofPblic Health and THE NATION'S HEALTH*, 31(7):669. Cited on xii, 11

[68] Shayler, P. J., Leong, D. K. W., and Murphy, M. (2005). Contributions to engine friction during cold, low speed running and the dependence on oil viscosity. *SAE Technical Paper 2005-01-1654*. Cited on 29

[69] Speight, J. G. (2006). *The Chemistry and Technology of Petroleum*. Taylor & Francis Group, fourth edition edition. Cited on xii, 10

[70] Stefanopoulou, A. G., Kolmanovsky, I., and Freudenberg, J. S. (2000). Control of variable geometry turbocharged diesel engines for reduced emissions. *IEEE TRANSACTIONS ON CONTROL SYSTEMS TECHNOLOGY*, 8(4):733–745. Cited on 21

[71] Steinhauser, M. O. (2012). *Computer Simulation in Physics and Engineering*. De Gruyter. Cited on 14

[72] Sugeno, M. (1985). *Industrial Applications of Fuzzy Control*. Elsevier Science Inc., New York, NY, USA. Cited on 83

[73] Tan, P., Hu, Z., Deng, K., Lu, J., Lou, D., and Wan, G. (2007). Particulate matter emission modelling based on soot and sof from direct injection diesel engines. *Energy Conversion and Management*, 48(2):510. Cited on 15

[74] Tao, F., Reitz, R. D., Foster, D. E., and Liu, Y. (2009). Nine-step phenomenological diesel soot model validated over a wide range of engine conditions. *International Journal of Thermal Sciences*, 48(6):1223. Cited on 15

[75] Totten, G. E., Westbrook, S. R., and Shah, R. J. (2003). *Fuels and Lubricants Handbook - Technology, Properties, Performance, and Testing*. ASTM International. Cited on 12, 13

[76] Tsai, M.-C. and Gu, D.-W. (2014). *Robust and Optimal Control : A Two-port Framework Approach*. Springer. Cited on 22

[77] Tschanz, F., Amstutz, A., Onder, C. H., and Guzzella, L. (2013). Feedback control of particulate matter and nitrogen oxide emissions in diesel engines. *Control Engineering Practice*, 21(12):1809–1820. Cited on 21

[78] Tu, J., Yeoh, G. H., and Liu, C. (2012). *Computational Fluid Dynamics : A Practical Approach*. Elsevier Science. Cited on 14

[79] Utkin, V. (1977). Variable structure systems with sliding mode: A survey. *IEEE Trans.Autom. Control, vol. AC-22, pp. 212-222, 1977*. Cited on 23

[80] Uzun, A. (2014). Air mass flow estimation of diesel engines using neural network. *Fuel*, 117:833–838. Cited on 16

[81] Van Nieuwstadt, M., Kolmanovsky, I., Moraal, P., Jankovic, M., and Stefanopoulou, A. (2000). Egr vgt control schemes: Experimental comparison for a high speed diesel engine. *IEEE Control Systems Magazine*, pages 64–79. Cited on 5

[82] Vinsonneau, J., Shields, D., King, P., and Burnham, K. (2002). Improved si engine modelling techniques with application to fault detection. *Control Applications, 2002. Proceedings of the 2002 International Conference on (Volume:2)*. Cited on 113

[83] Watanabe, H., Suwa, Y., Matsushita, Y., Morozumi, Y., Aoki, H., Tanno, S., and Miura, T. (2007). Spray combustion simulation including soot and no formation. *Energy Conversion and Management*, 48(7):2077. Cited on 15

[84] Wijetunge, R., Brace, C., Hawley, J., and Vaughan, N. (2000). Dynamic behaviour of a high speed direct injection diesle engine. *Proceedings of the SAE, Journal of Engines*, 108(3):1120–1129. Cited on 5

[85] Wijetunge, R. S., Hawley, J. G., and Vaughan, N. D. (2004). Application of alternative egr and vgt strategies to a diesel engine. *SAE International*, 2004-01-0899. Cited on 3

[86] Zhang, J., Shen, T., and Marino, R. (2010). Model-based cold-start speed control scheme for spark ignition engines. *Control Engineering Practice*, 18(11):1285. Cited on 21

[87] Zhong, J. (2006). *PID controller tuning: A short tutorial*. Purdue University. class lesson. Cited on x, 62

[88] Zhou, Y. and Chen, Q. (2012). Optimization of muffler of engines by computers and analysis method. *International Conference on Industrial Control and Electronics Engineering*. Cited on 16

[89] Zinober, A. (1990). *Deterministic control of uncertain systems*. London: Peter Peregrinus Press. Cited on 23

Appendix A

Experiment preparation

A.1 Test Bed Overview

The test bed illustrated in Fig. A.1 is built with a CAT3126b truck engine coupled to a SCHORCH dynamometer. The engine is equipped with a Garrett GT3782VA variable geometry turbocharger and a Pierburg high pressure EGR valve. Two water cooled intercoolers have been installed on the test bed for intake air and EGR gas respectively. The main specifications of the engine are listed in Table A.1.

Table A.1: Specifications of CAT3126B engine.

Model	CAT3126B	**Intake manifold**	5L
Type of engine	Inline, 4 stroke	**Exhaust manifold**	0.945L
Cylinders number	6	**Type of combustion**	HEUI* direct injection
Inlet valves number	2	**Injection pressure**	145-200bar
Exhaust valves number	1	**Injection orifices number**	6
Firing order	1-5-3-6-2-4	**Maximum torque**	1166Nm@ 1440rpm
Bore * stroke	110 * 127mm	**Maximum power**	224kW@ 2200rpm
Compression ratio	16 : 1	**Idle speed**	700rpm
Total displacement	7.25L	**Maximum speed**	2640rpm

*hydraulically actuated electronically controlled unit injector

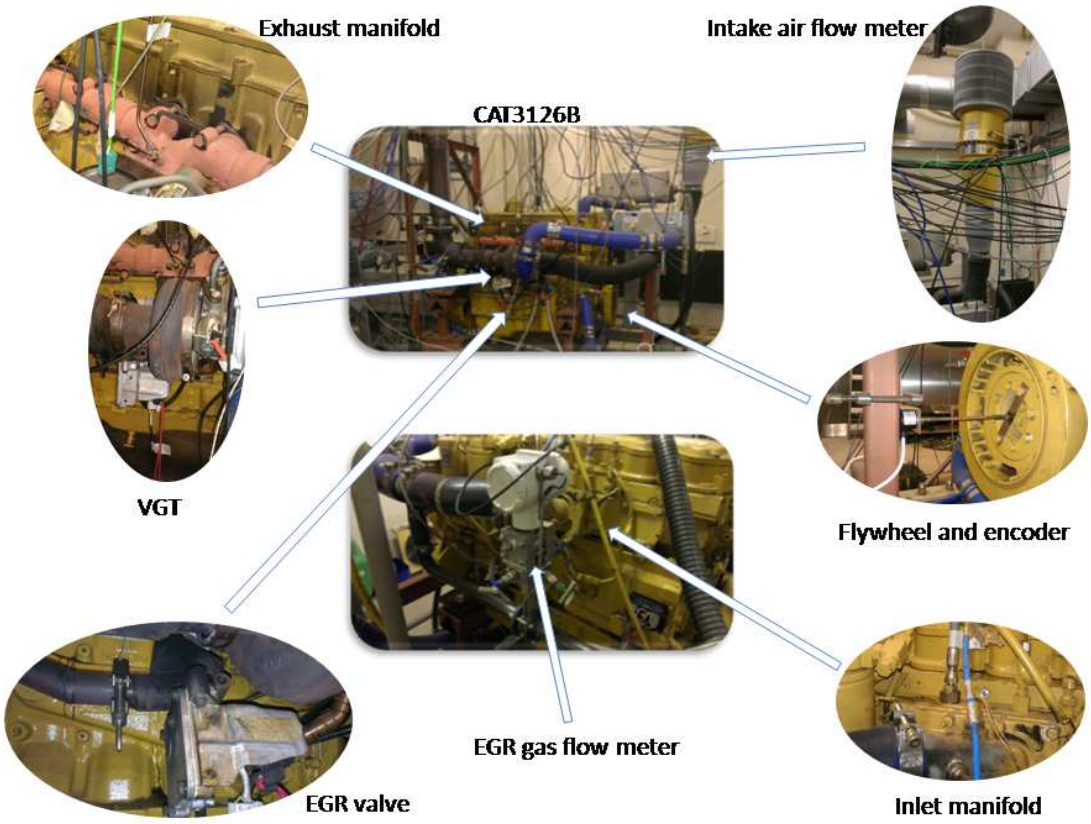

(a)

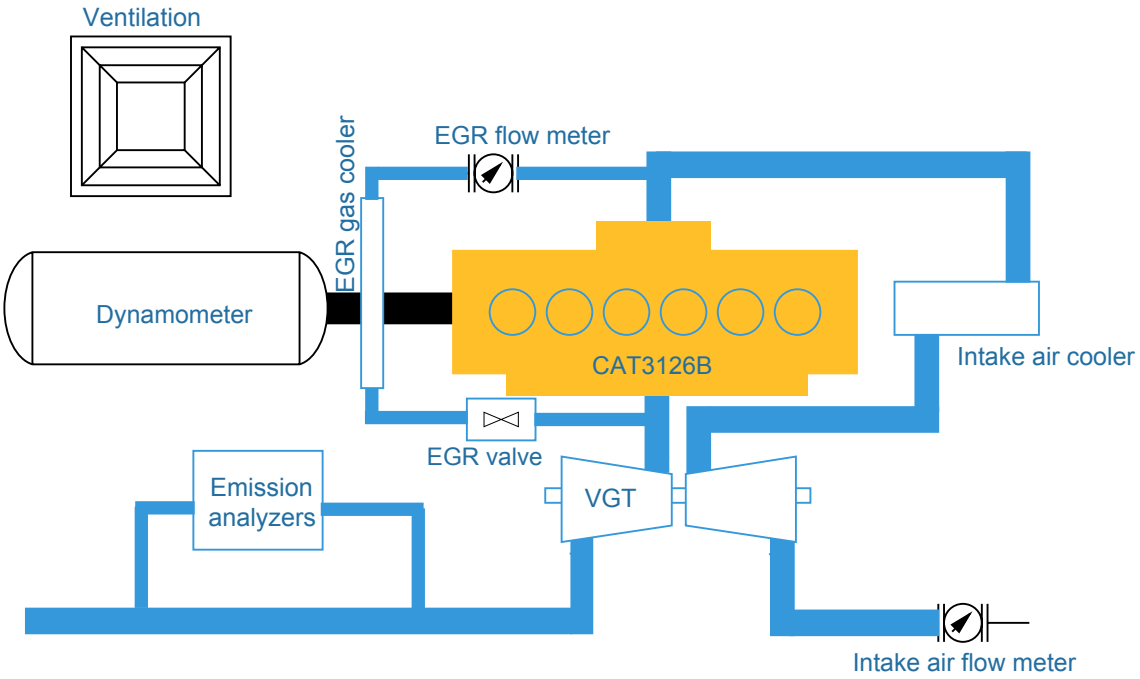

(b)

Figure A.1: Test bed illustrations. (a) photograph of the main components of the test bed, (b) sketch of test bed layout.

Apart from the existing sensors built in for ECU and dynamometer control, additional sensors have been installed around the engine and have been wired to a dSPACE MicroAutoBox 1401/1501. These sensors include two flow meters for measuring the intake air and EGR gas flows, two pressure sensors for measuring the inlet and exhaust manifold pressures, two oxygen sensors for measuring the oxygen concentration in the intake air and exhaust gas flows, an acceleration pedal position sensor for controlling the load, an encoder for measuring the engine speed, and two emission analysers for measuring the soot and NO_x levels in the exhaust gas. Additionally, the installed VGT and EGR valve are equipped with position feedback sensors.

The overall systematic structure of the test bed is illustrated in Fig. A.2. As shown in the figure, the engine is connected with two control platforms, which are the CP Cadet and the dSPACE control desk. The engine tests are governed by the CP Cadet Platform, which will allow the engine to run against a predefined driving cycle and also log test conditions and results. The dSPACE control desk is able to communicate with the MicroAutoBox, so that the data from the MicroAutoBox can be stored and it can also send control signals to the MicroAutoBox while running tests.

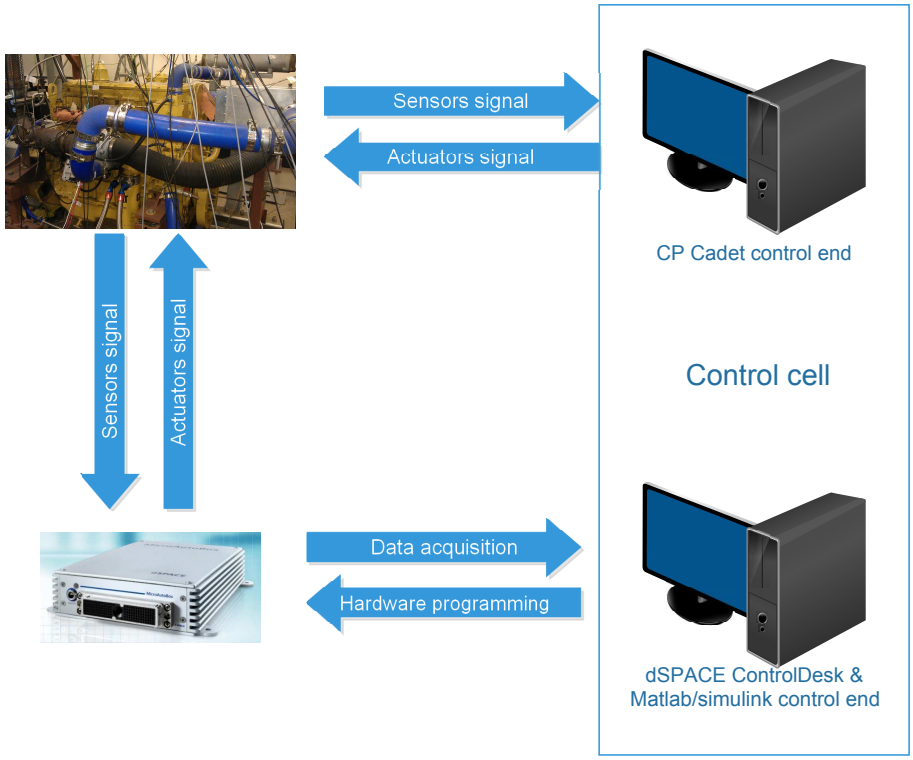

Figure A.2: Test bed overall structure [48]

A.2 MicroAutoBox Setup

MicroAutoBox is a compact, stand-alone prototyping unit. It works like an ECU and can be used for real-time control prototyping applications. The specifications of the MicroAutoBox used in this work is listed in Table A.2 below. It can be seen that the MicroAutoBox is composed of seven basic components: processor, memory, interfaces, analog input channels, analog output channels, digital I/O channels, and signal conditioning modules. The processor is used for calculating and processing commands. The memory is used for storing the real-time code and calculation results at each step. The interfaces are used to connect the MicroAutoBox to computers or other devices as required. The analog and digital I/O channels are used to connect the MicroAutoBox to sensors and actuators. The signal conditioning modules are used for regulating signal levels and electric circuit protection. As it is shown in Fig. A.2, the MicroAutoBox is linked to a PC which is used for compiling and data acquisition, wired to all the sensors required for control, and connected to the actuators which need to be controlled (see Fig. A.3).

Figure A.3: MicroAutoBox connections to PC, sensors and actuators.

As mentioned in Section A.1, additional sensors were installed on the engine and connected to the MicroAutoBox for control and data acquisition. These sensors are connected through either analog or digital input channels. As actuators, the VGT and EGR drives are connected through analog output channels.

Table A.2: Specifications of MicroAutoBox 1401/1501

MicroAutoBox		1401/1501
Processor		IBM PPC 750FX, 800 MHz
Memory		8 MB main memory 4 MB memory exclusively for communication between MicroAutoBox and PC/notebook 16 MB nonvolatile flash memory containing code section and flight recorder data Clock/calendar function for time-stamping of flight recorder data
Interfaces	**CAN interface**	Dual CAN interface; 2 CAN channels in total
	Serial interface	1 x RS232 interface
		1 x serial interface usable as K/L - Line or LIN interface
	ECU inteface	Dual-port memory interface, 16 K x 16-bit DPRAM
Analog input	**Resolution**	16 12-bit channels
	Sampling	4 to 1 multiplexed Simultaneous sample & hold
	Input voltage range	0 ... 5 V
Analog output	**Resolution**	8 12-bit channels
	Output voltage range	0 ... 4.5 V
	Output current	5 mA max. sink/source current
Digital I/O	**General**	Digital I/O on 68336 slave processor, 20 MHz, with time processor unit (TPU) I/O software support for different applications
	Bit I/O	16 discrete inputs 10 discrete outputs, 5 mA output current 16 shared discrete inputs/outputs, bit-selectable 16 TPU channels Up to 16-bit resolution
	PWM generation/ measurement	4 shared inputs for frequency or PWM 4 PWM outputs, PWM frequency 2.5 Hz ... 100 kHz, duty cycle 0 ... 100% Up to 16-bit resolution
Signal conditioning		Signal conditioning for automotive signal levels, no power driver included Overvoltage protection Overcurrent and short circuit protection

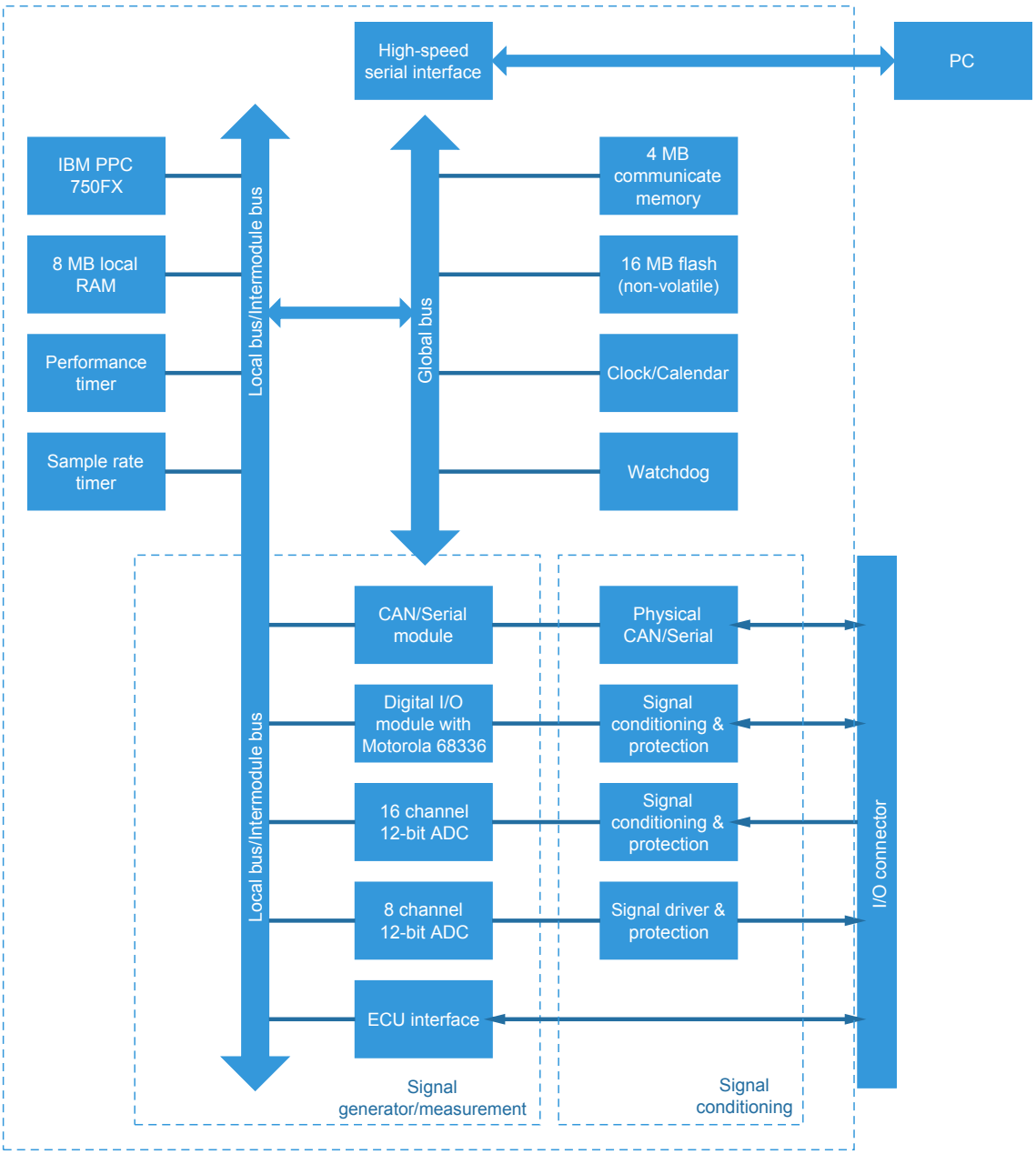

Figure A.4: Block diagram of MicroAutoBox 1401/1501

A.3 Sensors Configuration in Matlab/Simulink

In order to correctly read the measuring signals from sensors, each sensor needs to be configured in Simulink by assigning the correct input and output type to it, such as analog digital converter (ADC) type, digital analog converter (DAC), time processor unit (TPU). Fig. A.5 shows the I/O channels and pins connected. Table A.3 shows the wires and PIN connections to the sensors and actuators.

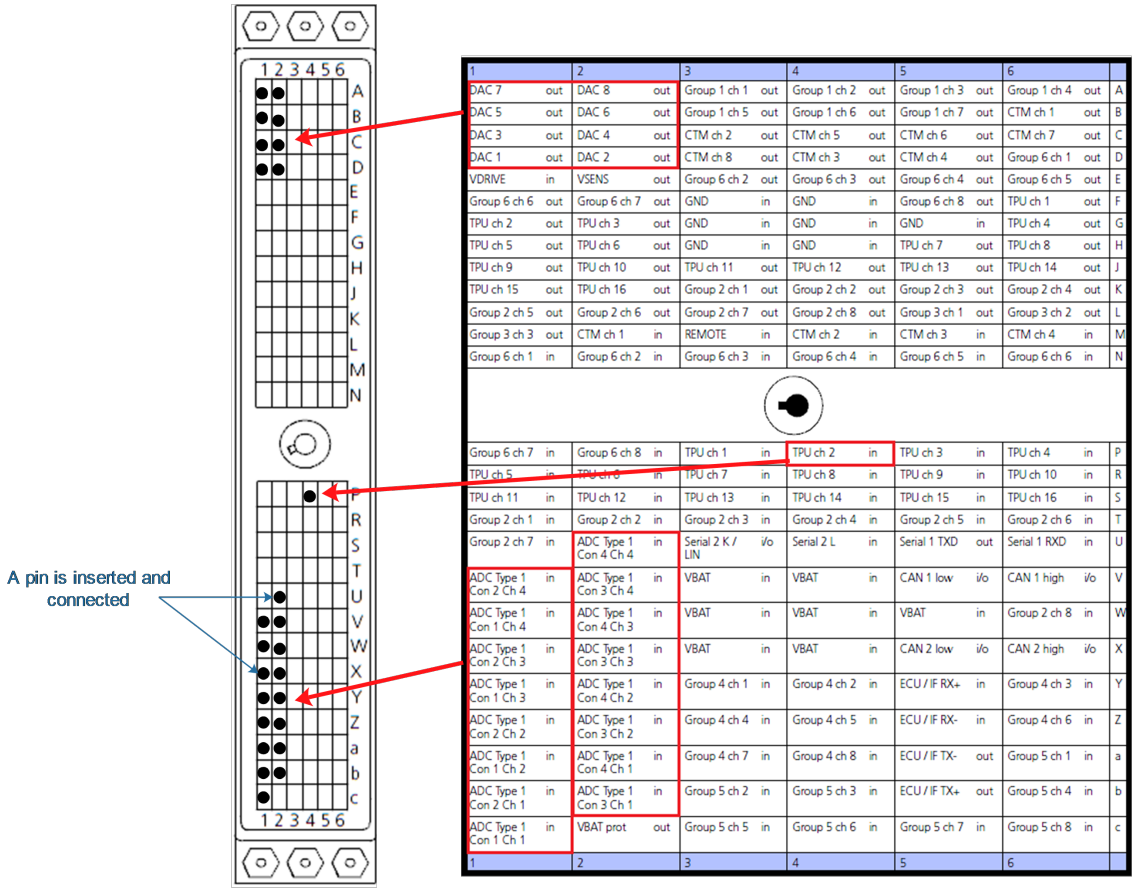

Figure A.5: MicroAutoBox I/O channels connected.

Sensors have to be calibrated before they can measure correctly. Some sensors have been previously calibrated by their manufacturers and the calibration information is available, so they do not need to be calibrated again. However, some sensors do not supplied with calibration information, so they need to be calibrated before use. The sensors require calibrations in this work include temperature sensor and pressure sensor, and the calibration methods have been described below. Calibration information is available for all the other sensors used in this work.

Temperature sensor used is thermocouple type. A thermocouple (see Fig. A.6) is a temperature-measuring device consisting of two dissimilar conductors that contact each

Table A.3: MicroAutoBox PIN connections

Wire colour pattern	Sensors connected to	PIN position	PIN type
orange(o)	EGR feedback	W1	ADC con1 ch4 in
green(g)	encoder speed (B)	M2	CTM ch1
violet(v)	temperature	b2	ADC con3 ch1 in
pink(p)	Smoke+	V1	ADC con2 ch4 in
yellow-r	Smoke-	Z1	ADC con2 ch2 in
g-brown	EGR drive	D2	DAC 2 out
yellow-blu	pressure 2+	a1	ADC con1 ch2 in
r-brown	pressure 1+	c1	ADC con1 ch1 in
r-black	VGT feedback	b1	ADC con2 ch1 in
r-blu	VGT Drive	D1	DAC 1 out
white-blu	flow meter+	Y1	ADC con1 ch3 in
white-r	flow meter-	X1	ADC con2 ch3 in
grey	accer pedal position	M5	CTM ch3
white	EGR meter	Z2	ADC con3 ch2
yellow	O2 - 2 - exhaust	Y2	ADC con4 ch2

other at one or more spots. It produces a voltage when the temperature of one of the spots differs from the reference temperature at other parts of the circuit. This change of voltage produced is proportional to the temperature changes. To calibrate a thermal couple, two reference temperature are required. For example, 100℃ (boiling water) and 0℃ (ice and water mixture). Record the voltage at 100℃ and 0℃ respectively and make a look-up table with these two points (see Fig. A.7).

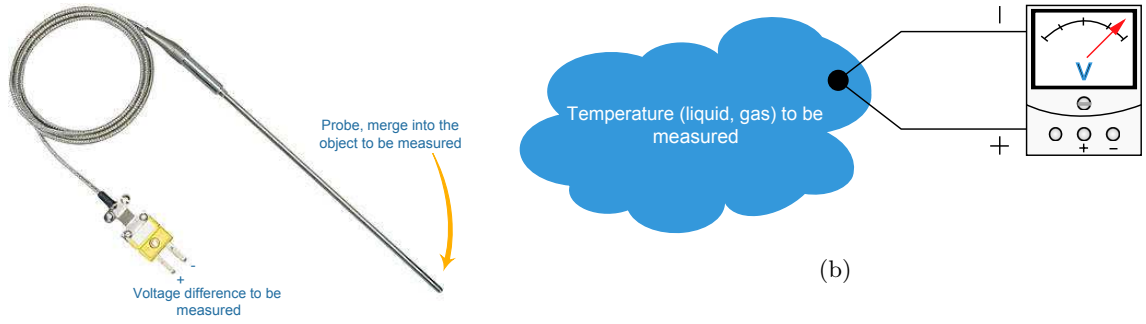

Figure A.6: Illustration of a thermal couple. (a) a real photo, (b) measuring principle of thermal couple.

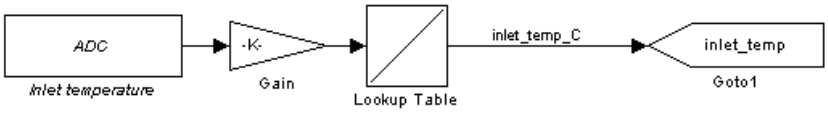

Figure A.7: Thermal couple configuration and calibration model created in Simulink

Pressure sensor used is Gems 2200 series, they are molecularity bonded high output strain gauges to provide 100mV output for full range pressure when used with a 10V d.c. power supply [63]. The change of voltage output is proportional to the change of pressure. To calibrate these pressure sensors, a pressure generator is needed. Connect a pressure sensor to the pressure generator, record two voltage readings at two different pressures generated by the pressure generator, and then make a look up table in Simulink (see Fig A.9).

Because the voltage output variations from a thermal couple and a pressure sensor are comparatively small compared to the 0 -5V voltage input range of the Analog input channel, so the temperature and pressure reading would not be accurate enough if directly connect the sensor to MicroAutoBox. A electric signal amplifier card (see Fig. A.10) is used to amplify the voltage variation range of these sensors to match the range of the MicroAutoBox analog input range 0 - 5V.

Engine speed is measured by a Hengstler rotary incremental shaft encoder (see Fig.

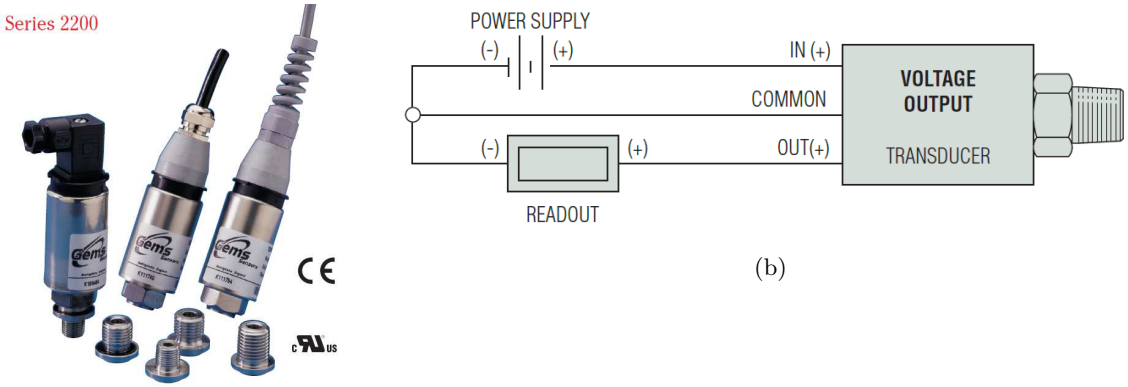

(a) (b)

Figure A.8: Gems 2200 series pressure transducer. (a) photos of pressure transducers, (b) illustration of the measuring circuit. [34]

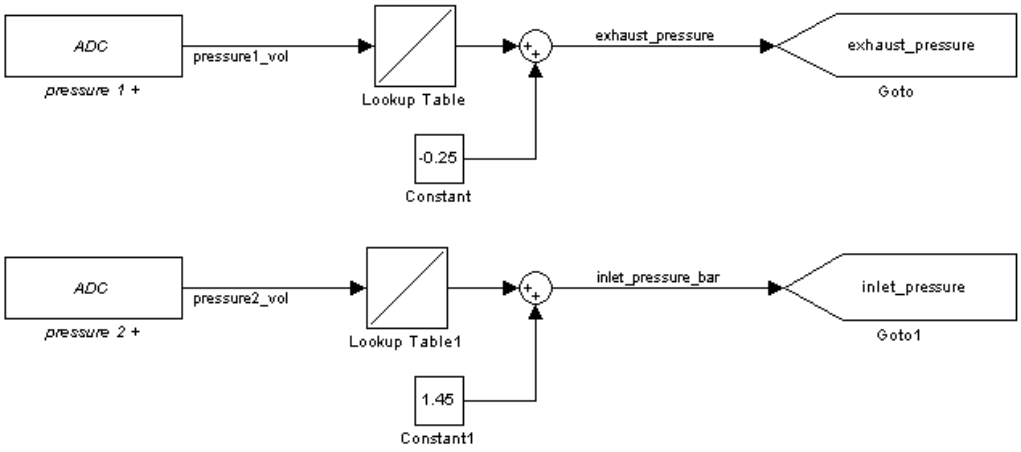

Figure A.9: Pressure sensors configuration and calibration models created in Simulink

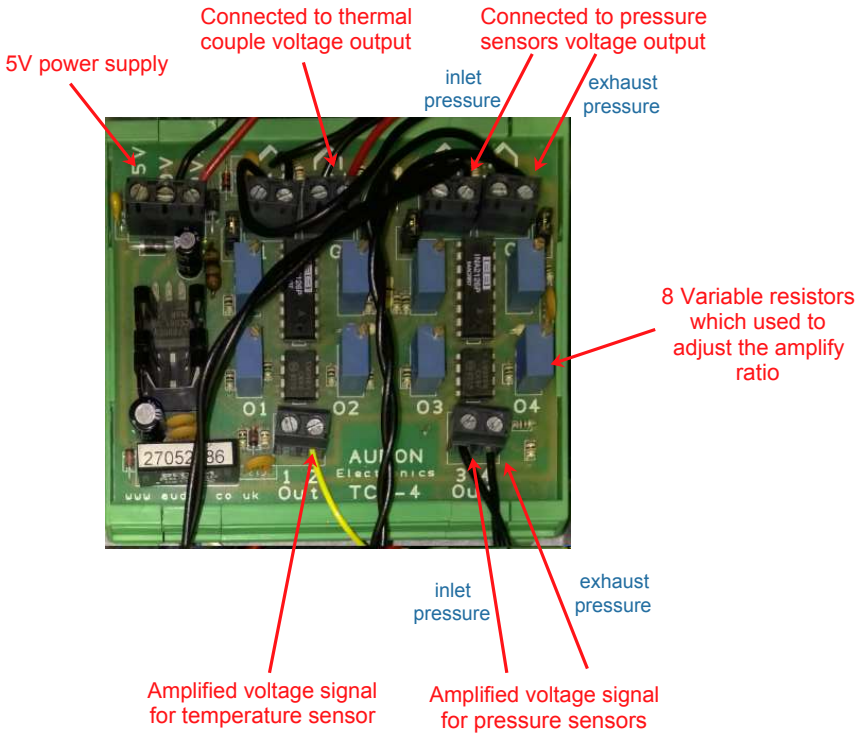

Figure A.10: Amplifier card used for thermal couple and pressure sensors.

A.11). Incremental encoders are sensors capable of generating signals in response to rotary movement. The shaft encoder generates a signal for each incremental change in position. Fig. A.12 shows the Simulink model created.

Figure A.11: Hengstler rotary incremental shaft encoder (RI32-0/360ER.14KB) [37].

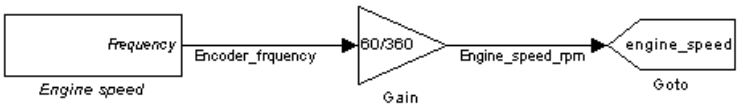

Figure A.12: Shaft encoder configuration and calibration model created in Simulink

The intake fresh air flow was measured using a Labcell Meriam laminar flow element

(see Fig. A.13) which measures the volume flow rate of gas based on capillary flow principles. In order to obtain the mass air flow, a formula governed by the ideal gas law was used to translate the volume flow rate to mass flow rate. According to the manual [49], the measurement has an accuracy of ±0.72 LPM of reading. The configuration and calibration model created in Simulink is shown in Fig. A.14.

(a)

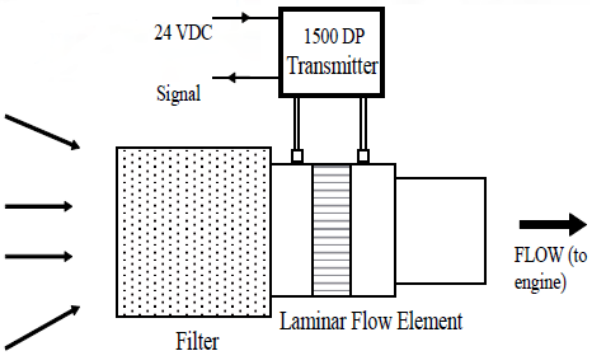

(b) [49]

Figure A.13: Labcell Meriam laminar flow meter for measuring the intake air flow.

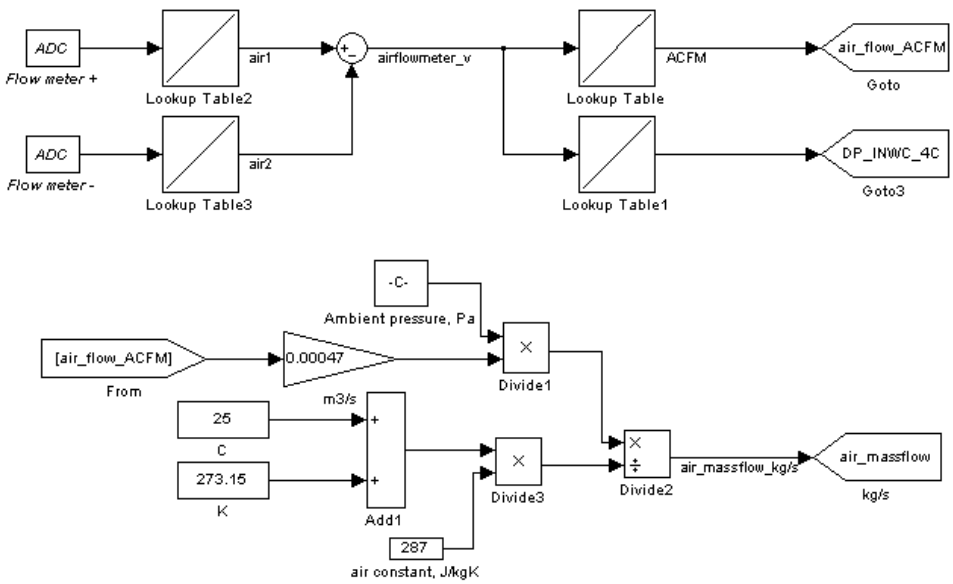

Figure A.14: Intake flow meter configuration and calibration model created in Simulink.

The EGR gas flow was measured using an ABB OriMaster FPD500 orifice flow meter (Fig. A.15 a). This flow meter measures the volume flow rate based on the orifice fluid measuring principle (Fig. A.15 b). The principle is that the fluid flow rate is a function of the pressure difference across the restriction. This flow meter has a built-in transferring module which takes gas temperature into account, therefore the output from this meter is directly mass flow rate. According to the specifications of the flow meter [1], the system accuracy of a calibrated meter at reference conditions (for Re>10^5) is ±1% of flow rate with a repeatability of 0.1%. The configuration and calibration model created in Simulink is shown in Fig. A.16.

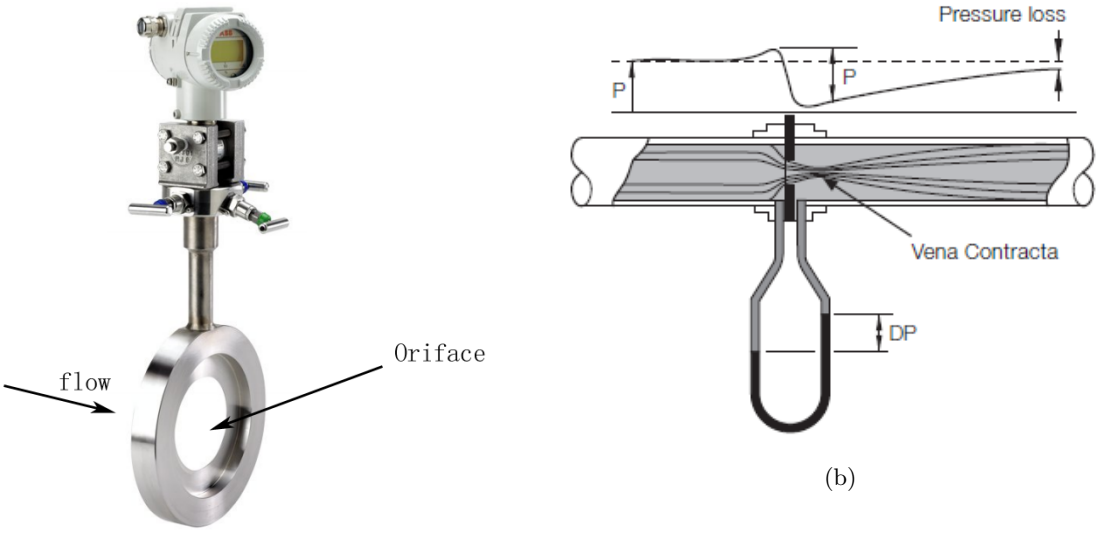

(a) (b)

Figure A.15: ABB OriMaster FPD500 compact orifice flow meter. (a) Flow meter body, (b) Orifice measuring principle. [1]

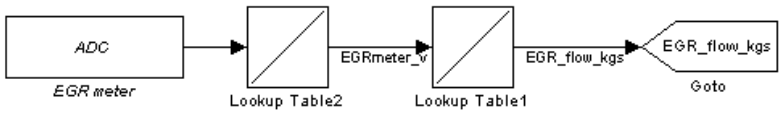

Figure A.16: EGR flow meter configuration and calibration model created in Simulink.

The oxygen level in the exhaust manifold was measured by an ECM OXY6200 oxygen sensor. With a input power range from 11VDC to 28VDC, the output analog signal is from 1.0V to 5.5V which is linearized in oxygen percentage 0.0% to 25.0% [30]. The configuration and calibration model created in Simulink is shown in Fig. A.18.

Pedal position sensor uses a PWM signal ranges from 0 to 100%. The configuration model created in Simulink is shown in Fig. A.19.

Figure A.17: OXY6200 oxygen sensor used for measuring the exhaust manifold oxygen level [30].

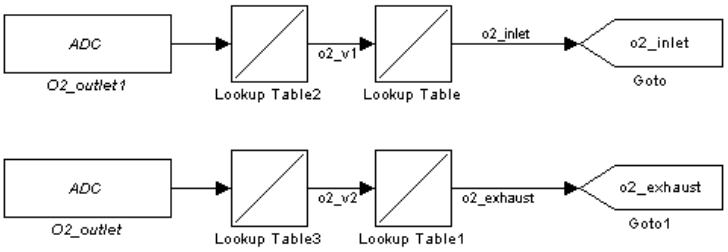

Figure A.18: Oxygen sensors configuration and calibration model created in Simulink.

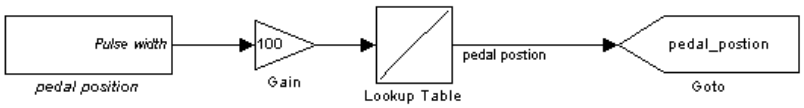

Figure A.19: Pedal position configuration model created in Simulink.

Soot was measured using an AVL 439 opacimeter. The measurement principle, the zero-level stability and the signal rise time can be found in Fig. A.20 [9]. The figure shows that the zero-level stability is within 0.2% in terms of opacity of the gas and the rise time from 10% to 90% is 100 ms. The configuration and calibration model created in Simulink is shown in Fig. A.21.

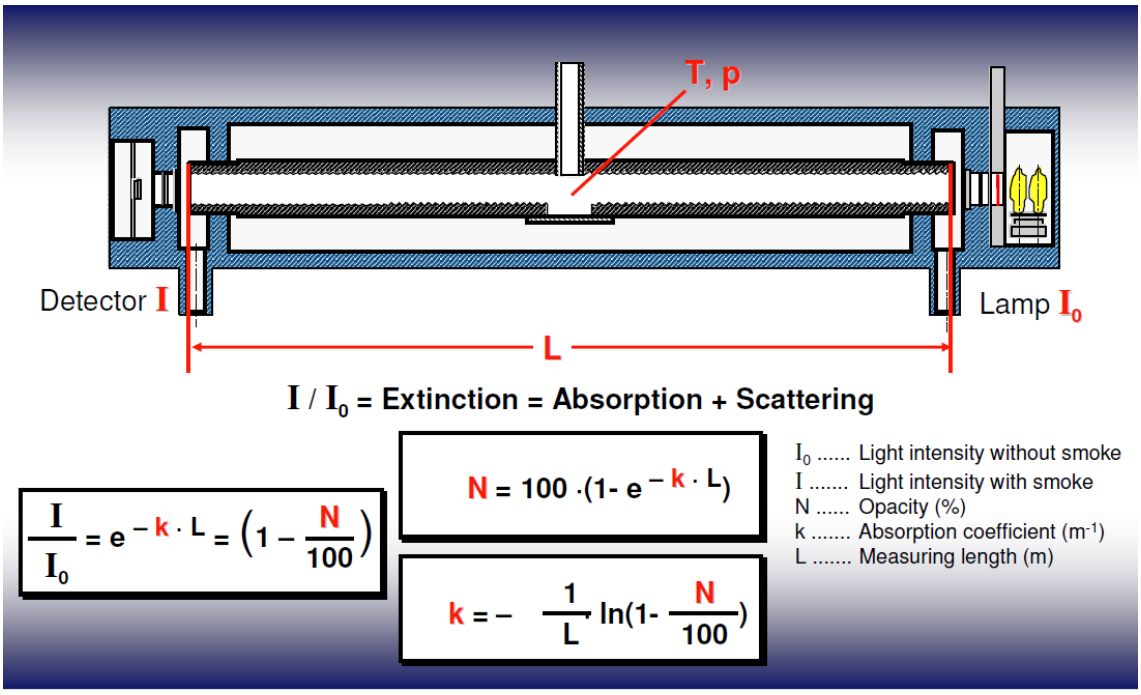

(a)

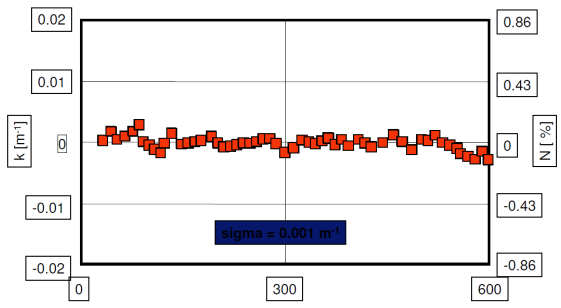

(b)

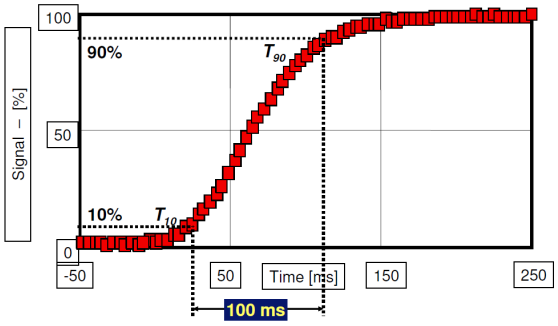

(c)

Figure A.20: AVL 439 opacimeter. (a) Measurement principle, (b) Zero-level stability, and (c) Signal rise time.

NO_x was measured by a Testo 350 emission analyser. The measurement range and the rise time information are listed in Table A.4.

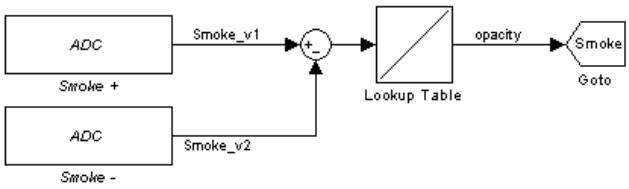

Figure A.21: AVL 439 opacimeter configuration model created in Simulink.

Table A.4: Testo 350 emission analyser

Gases	Measurement range	Resolution	Accuracy	Response time
NO	0 - 4000ppm	1ppm	±5% of reading (100 - 1999ppm)	<30s (t90)
NO_2	0 - 500ppm	0.1ppm	±5% of reading (100 - 500ppm)	<40s (t90)

A.4 VGT & EGR Local Position Control

The VGT vanes and EGR valve are driven by electric motors. A positive voltage supplied to the motors will make them turn in one direction, a negative voltage supplied will make them turn in the other direction. With this mechanism, the VGT vanes and EGR valve can be moved either ways as needed. The VGT and EGR also have position feedback signals available, the voltage feedback signals can be interpreted as positions of the VGT vanes and EGR valve (see Fig. A.22 a, c). With these position feedback signals, it is possible to built close-loop controllers (see Fig. A.22 b, d) to position the VGT vanes and EGR valve at any positions.

Two electronic cards are used to drive the VGT vanes and EGR valve. Fig. A.23 a shows the card used to drive the VGT vanes. As marked, the card is powered by a 12V DC supply. The DC output signal that drives the VGT vanes is controlled by the control signal sent from the MicroAutoBox. If the control signal sent from MicroAutoBox is 0V, the DC output will be 0V, and the vanes will be moved towards the open position; if the control signal is 4.5V, the DC output will be 12V, and the vanes will be moved towards closed position. The schematic diagram of the NPN-type transistor is shown in Fig. A.23 c.

The card used to drive the EGR valve is shown in Fig. A.23 b. Similarly, the card requires a 12V DC power supply and it takes a control signal sent from MicroAutoBox. The difference is that this card can generate a pulse-width modulation (PWM) signal, which can vary the voltage output between 2.25V and 4V. When the control signal sent from MicroAutoBox varies from 0V to 4.5V, the left pin output varies from 0V to 12V,

and the right pin output varies from 12V to 0V. In this way, the output voltage signal level and direction can be varied. When the voltage signal is positive, the EGR valve is driven towards the open position; when the voltage signal is negative, the EGR valve is driven towards the closed position.

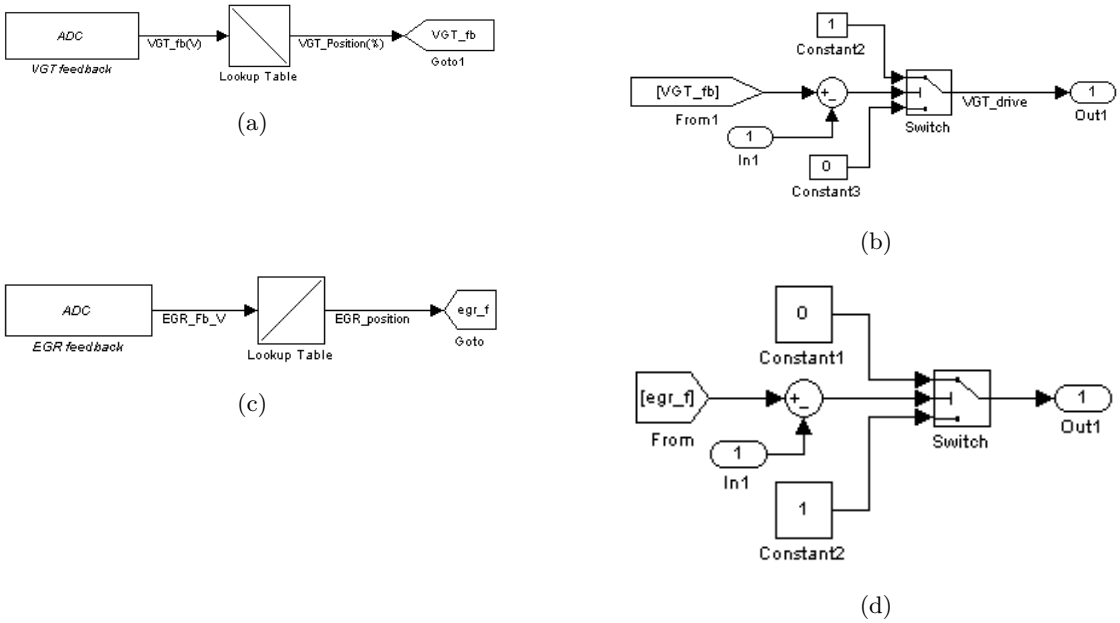

Figure A.22: VGT and EGR position feedback and local control models built in Simulink. (a) VGT feedback signal configuration and calibration, (b) VGT local position control model, (c) EGR feedback signal configuration and calibration, (d) EGR local position control model.

A.5 Control Panels in ControlDesk

ControlDesk is software developed by dSPACE to provide an interactive development environment. Basically, by setting up an experiment in ControlDesk, it allows you to configure, start, and stop an experiment, to view the readings of sensors in real time, to manipulate actuators, and to record experimental results for data analysis. Fig. A.24 and A.24 shows dashboards created in ControlDesk for VGT and EGR control.

A.6 Chapter Summary and Conclusions

In this chapter, the test bed preparation work was documented in detail including detailed descriptions of the hardware and software involved. At first, the specifications of the test bed was given, followed by the setup of the MicroAutoBox, wiring, configuration and calibration of the sensors and actuators in Matlab/Simulink. The sensors include thermal

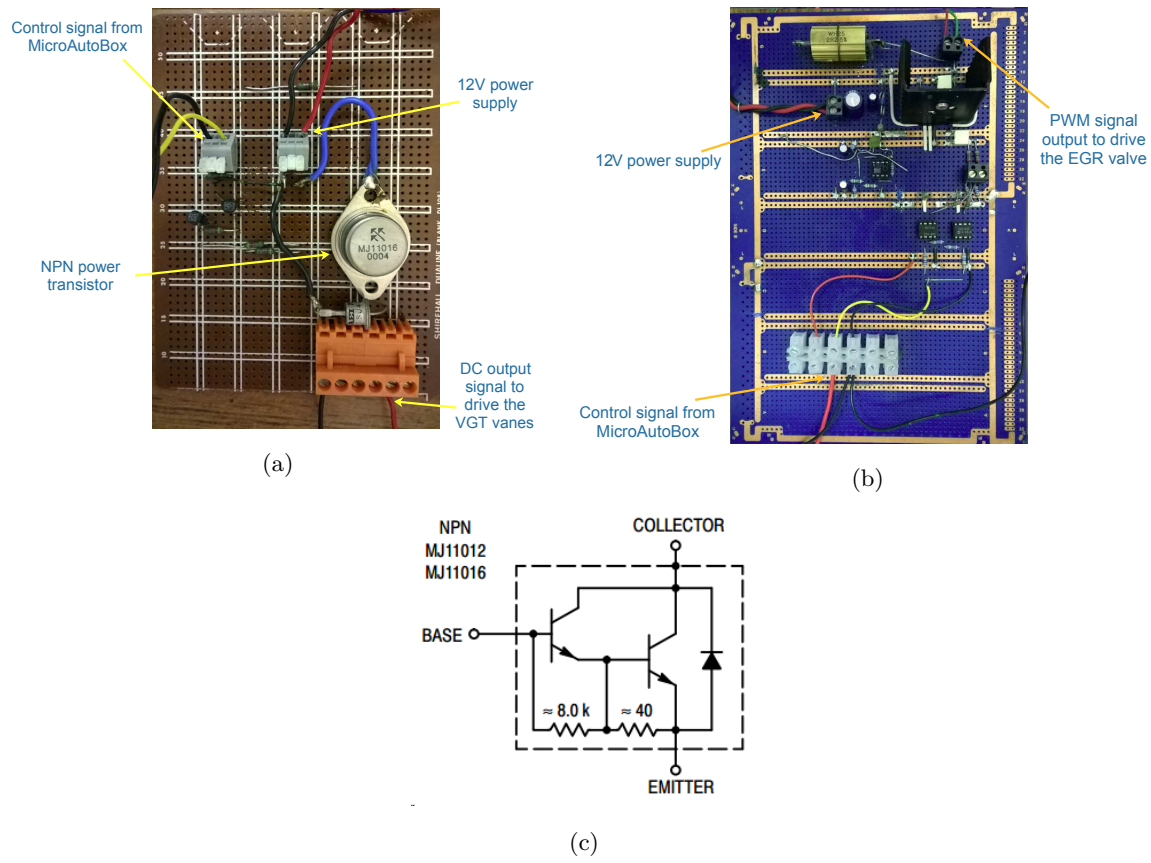

Figure A.23: Electronic cards used to drive the VGT and EGR. (a) NPN card used to drive the VGT vanes, (b) PWM signal card to drive the EGR valve, (c) NPN transistor schematic diagram.

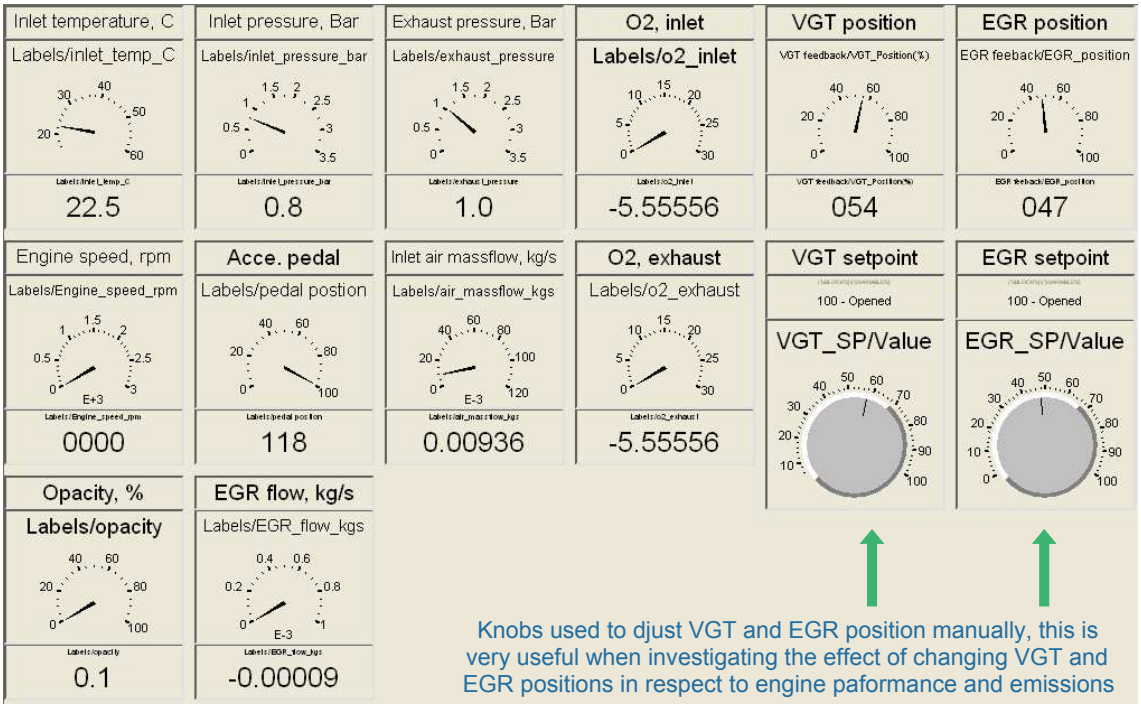

(a)

Figure A.24: Experiment dashboard created in ControlDesk. (a) VGT and EGR manual control, (b) VGT and EGR fuzzy logic control.

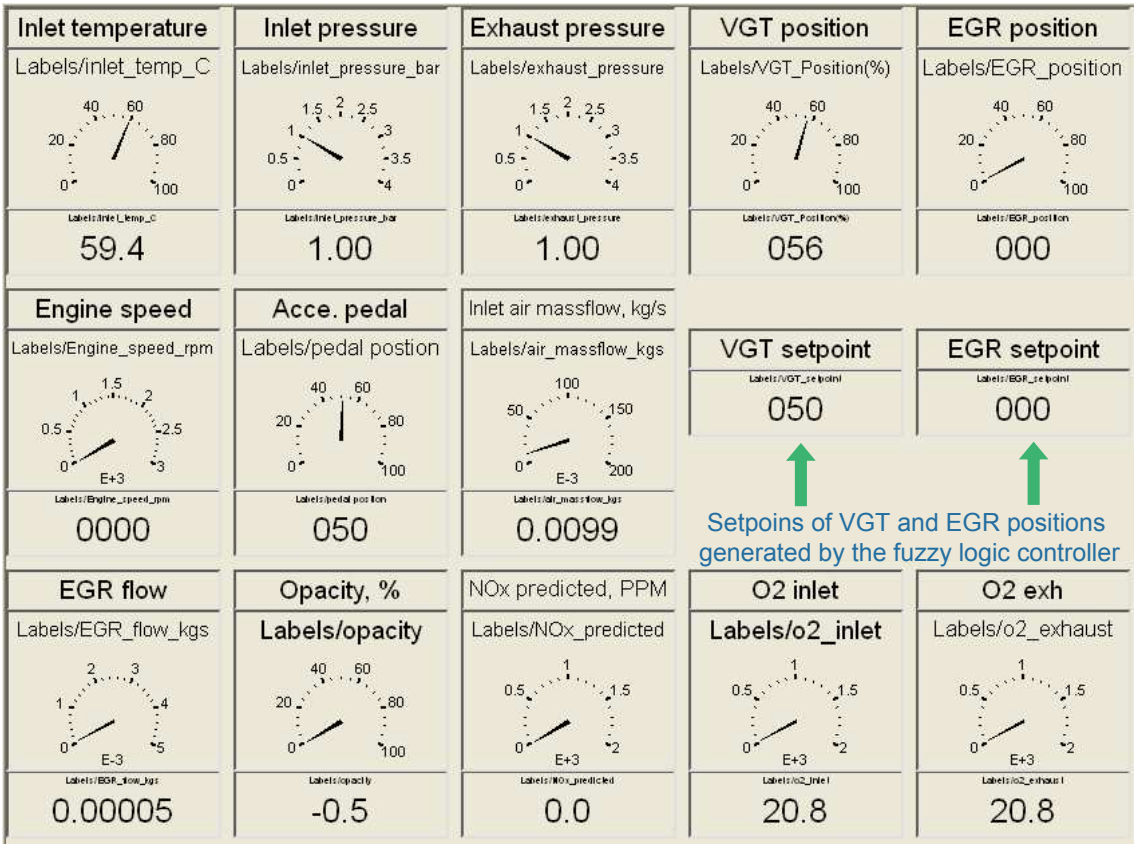

(b)

Figure A.24: (continued)

couples, pressure transducers, encodes, flow meters, lambda sensors, emission analysers, and VGT and EGR position feedback sensors. Actuators include VGT and EGR drives. Three electronic cards for signal conditioning are also described. In the end, the interface created in ControlDesk which are used for engine testing control and data acquisition were presented and explained.

Appendix B

Research Publications

The following publications have been created during the study:

1. Li Cheng, William Wang, Abdel Aitouche. Robustness evaluation of real-time fuzzy logic control of the VGT and EGR on a diesel engine. 23rd Mediterranean Conference on Control and Automation, June 16th to 19th, 2015.

2. Li Cheng, William Wang, Zhijun Peng, Abdel Aitouche. Construction and experimental implementation of a novel real-time fuzzy logic controller for VGT and EGR control in a heavy-duty diesel engine. Submitted to Control engineering practice, Elsevier.

3. Li Cheng, Jun Peng, William Wang, Abdel Aitouche. Simulation investigation of the performance and cost of pure electric vehicle power train with Ultracapacitor. 4th International Conference on Systems and Control, Tunisia, April 28th to 30th, 2015.

4. Zhijun Peng, Li Cheng, Weiji Wang, Bo Gao and Abdel Aitouche. An ANFIS solution for Real-time control of the EGR&VGT in a diesel engine. Advanced Materials Research Vols. 732-733 (2013).

5. Boulaid Boulkroune, Abdel Aitouche, Vincent Cocquempot, Li Cheng, and Zhijun Peng. Actuator Fault Diagnosis with Application to a Diesel Engine Testbed. Mathematical Problems in Engineering, vol. 2015, Article ID 189860, 15 pages, 2015. doi:10.1155/2015/189860

6. Olena Kuzmych, Abdel Aitouche, Li Cheng. Robust nonlinear control design for turbocharged biodiesel engine. 3rd international conference on systems and control, Oct 29-31, 2013, Algiers.

7. Dimitriou, P., Wang, W., Peng, J., Cheng, L. et al., Analysis of Diesel Engine In-Cylinder Air-Fuel Mixing with Homogeneity Factor: Combined Effects of Pilot Injection Strategies and Air Motion. SAE Int. J. Engines 7(4) :2014, doi:10.4271/2014-01-9052

A large part of the content in Chapter 3, 4, and 6 has yet to be published in international journals.

Appendix C

Test bed photos

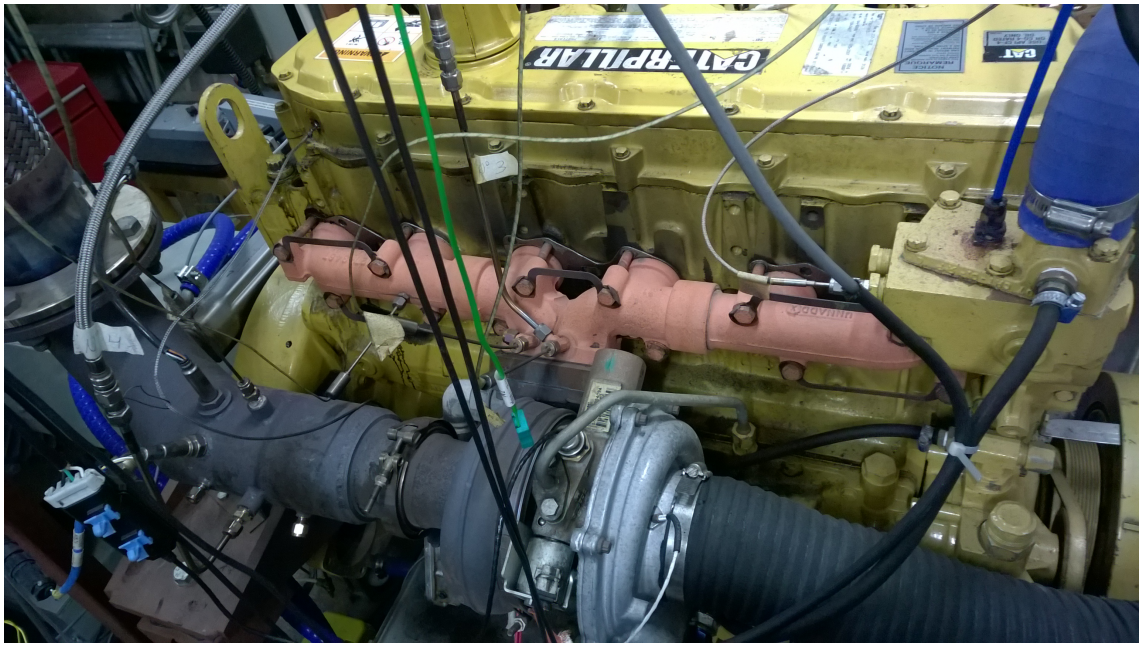

Figure C.1: Exhaust manifold and the variable geometry turbocharger.

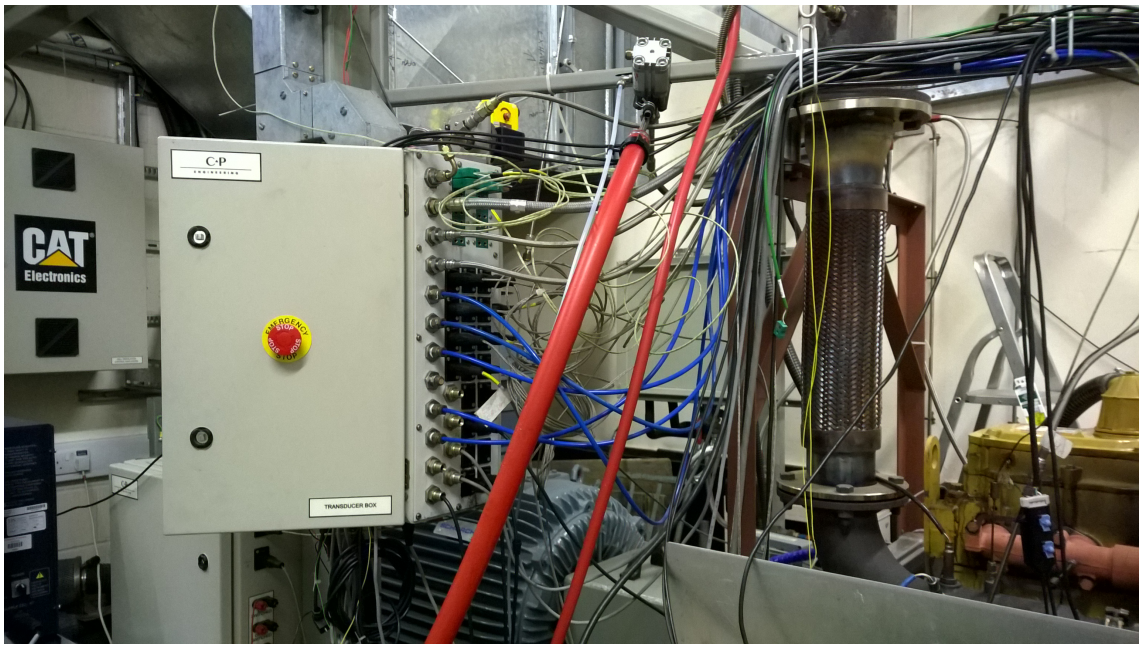

Figure C.2: Pressure transducers cluster.

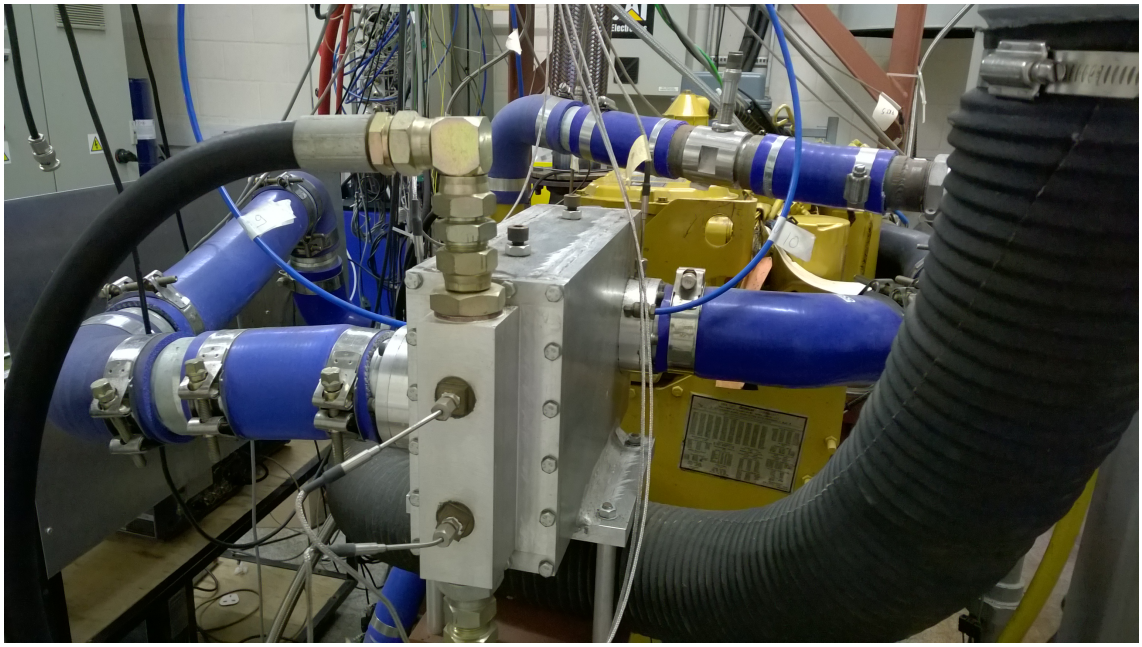

Figure C.3: Intake air inter-cooler.

Figure C.4: Control panel of the dynamometer.

Figure C.5: AVL 439 opacimeter.

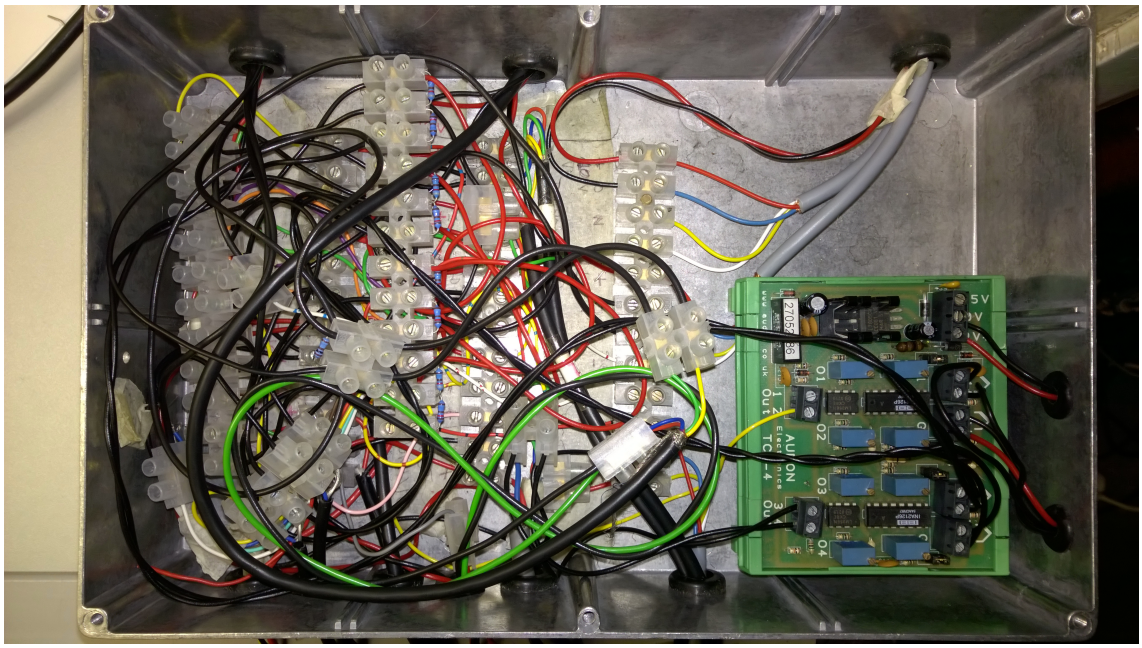

Figure C.6: Wring box for connecting sensors with the dSPACE MicroAutoBox.

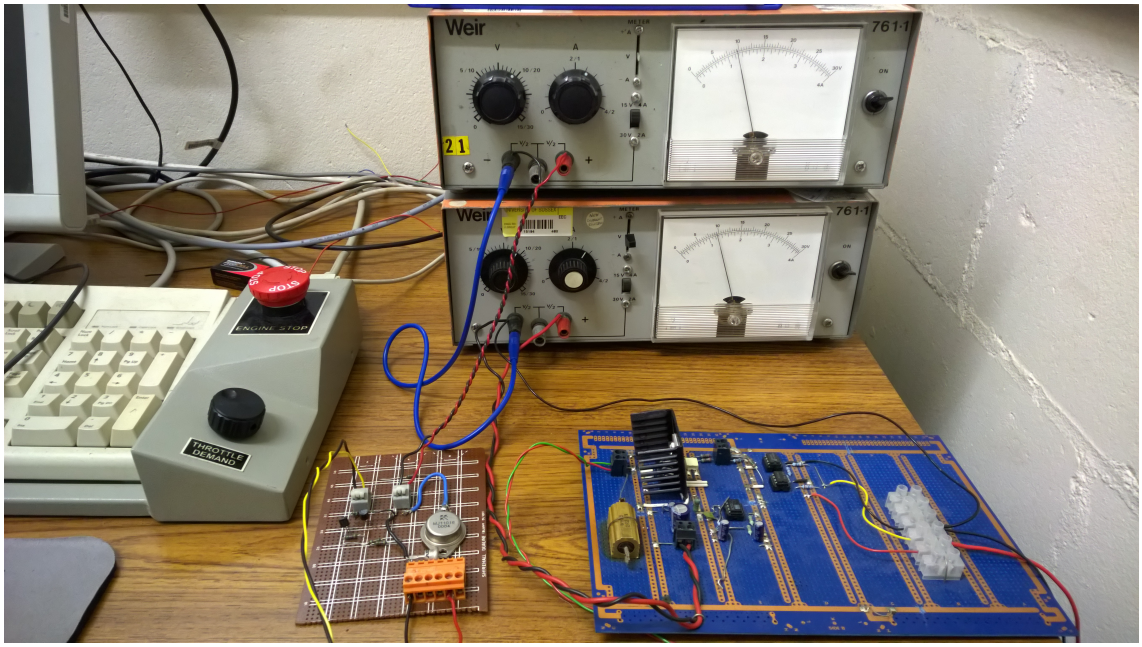

Figure C.7: Printed circuit board control cards for the positioning of the VGT and EGR.

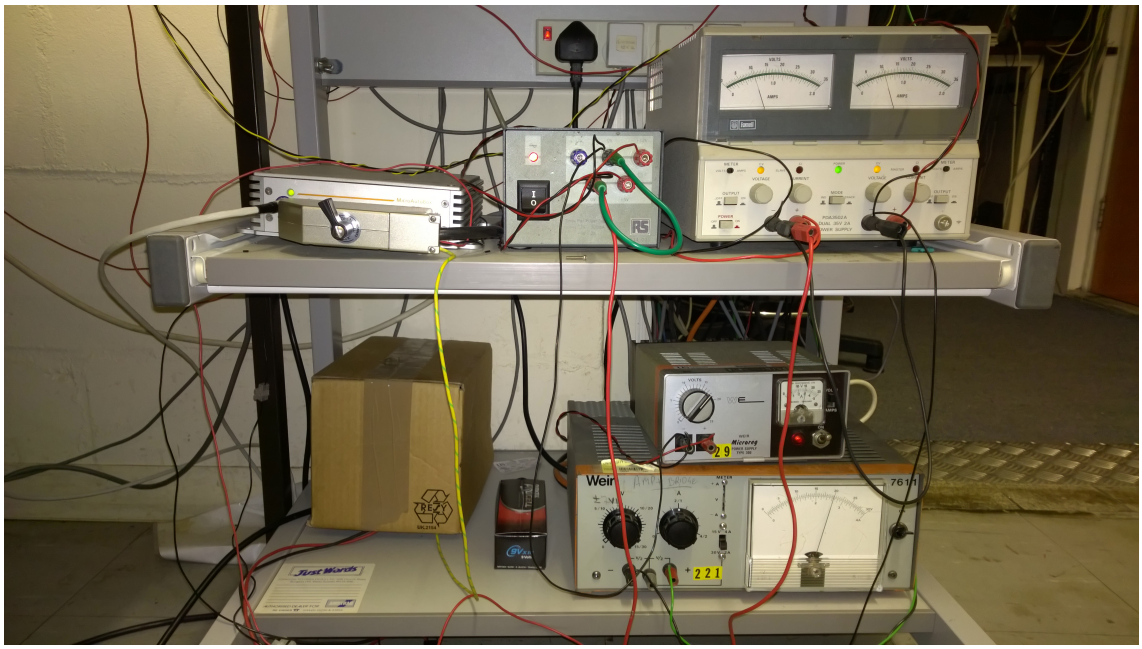

Figure C.8: Power supplies for sensors and MicroAutoBox.